How do the large-scale dynamics of galaxy interactions trigger star formation in the Antennae galaxy merger?

Cinthya Natalia Herrera Contreras

Institut d'Astrophysique Spatiale

École doctorale d'Astronomie et d'Astrophysique d'Ile de France

How do the large-scale dynamics of galaxy interactions trigger star formation in the Antennae galaxy merger?

PHD THESIS

submitted and publicly defended on November 5th, 2012

to obtain the title of

Docteur de l'Université de Paris Sud-XI

Spécialité Astrophysique et Astrophysique

by

Cinthya Natalia Herrera Contreras

Composition of the jury :

President :	Guillame Pineau des Forêts	-	Institut d'Astrophysique Spatiale
Reviewers :	Jérôme Pety	-	IRAM, LERMA
	Christine D. Wilson	-	Depatment of Physics and Astronomy McMaster University
Examiners :	Pierre-Alain Duc	-	CEA Saclay
	Mónica Rubio	-	Departamento de Astronomía Universidad de Chile
Thesis Director :	François Boulanger	-	Institut d'Astrophysique Spatiale

Université Paris-Sud XI

Institut d'Astrophysique Spatiale

École doctorale d'Astronomie et d'Astrophysique d'Ile de France

Comment la dynamique à grande échelle déclenche la formation d'étoiles dans les galaxies des Antennes?

THÈSE DE DOCTORAT

présentée et soutenue publiquement le 5 novembre, 2012

pour l'obtention du grade de

Docteur de l'Université de Paris Sud-XI

Spécialité Astrophysique et Astronomie

par

Cinthya Natalia Herrera Contreras

Composition du jury :

Président :	Guillame Pineau des Forêts	-	Institut d'Astrophysique Spatiale
Rapporteurs :	Jérôme Pety	-	IRAM, LERMA
	Christine D. Wilson	-	Depatment of Physics and Astronomy McMaster University
Examinateurs :	Pierre-Alain Duc	-	CEA Saclay
	Mónica Rubio	-	Departamento de Astronomía Universidad de Chile
Directeur de thèse :	François Boulanger	-	Institut d'Astrophysique Spatiale

Université Paris-Sud XI

Acknowledgments

During these three years that I spent in Orsay/Paris doing my PhD, I received the help, company and support of a lot of people, that was essential to me for finishing my thesis. I would like to give a big THANKS all of them.

I am extremely grateful to my supervisor Dr. François Boulanger. Thanks François for all of the time that you spent teaching me and helping me (including french bureaucracy things). By your side, I learned plenty of things about work, science and life. Thanks for always encouraging me, and for working together sometimes until very late (thanks Pascale too for your patience!). This thesis is mainly the result of your excellent guidance.

In addition, I want to thank Dr. Nicole Nesvadba, with whom I also worked during these three years. Thanks Nicole for helping me to see my work from a more extragalactic point of view and for teaching me both science and communicational skills. The dynamism between you and François taught me a lot. Also, thank you very much for correcting my english in this manuscript and in the papers too.

Thanks to the members of the jury of my thesis, Dr. Christine Wilson, Dr. Jêrome Pety, Dr. Mónica Rubio, Dr. Pierre-Alain Duc and Dr. Guillaume Pineau de Forêts, for reading carefully my thesis. Also, I thanks the MIS group, with whom I was able to develop my speaker skills, by presenting my work and getting useful feedback. I am also very grateful to the CNRS-CONICYT 2009 scholarship that gave me the opportunity of doing my PhD at the IAS.

Three years away from your family is a lot and, if you are very attached to them as I am, it can be very hard. I was able to complete my PhD work because I found support and company in Paris. I want to thanks to all my friends that I shared beautiful and funny moments with. I think I was very lucky for finding such a bunch of beautiful people. Many of them became an important part of my life.

My chilean friends, Vivi and Vale, who were there with me since almost the very beginning, and then Celia who joined us. Thanks that you are/were here my friends, I didn't lose my chilean spirit! An IAS (and gym, pubs, wine, pizzas, and a thousand things more) without M.I.R. Alves wouldn't be the same for me. Thanks Marta for your valuable friendship, support and help in improving my english skills.

A PhD is full of lunches, coffees, seminars, *pots*, conferences, *la pause*, etc. I want to thank to many other students and post-docs at the IAS. Specially, thanks to Andrea, Tuhin, Antoine, Melanie, Beth, Niraj, Gonzalo, Leo, Marco, Lapo, Nathalie, Dan, Claudia, Anna and Martine.

Because of my french classes, I had the chance of meeting non-astronomical people. I want to thank my friends that changed my parisian life: my dear good friend Qian, Adam, Denis, Denise, Liz and Alex. We had such a good time/soirées in Paris (and Belgium!). In particular, thanks Mehdi for taking care of me and supporting me during the final stage of my thesis and in all my decisions after that.

During all my life, my family has been there with and for me, supporting me and encouraging me. I want to thank my beloved mom Cecilia and two sisters Evelyn and Karla, and to my dad Juan Carlos. Your support was fundamental for me. Thanks for being always present.

Abstract

The Antennae (22 Mpc) is one of the most well-known mergers in the nearby Universe. Its distance allow us to observe and study the gas at the scales of stellar cluster formation. It is an ideal source to understand how the galaxy dynamics in mergers trigger the formation of stars. Most of the stars in the Antennae are formed in compact and massive stellar clusters, dubbed super-star clusters (SSCs). The most massive ($> 10^6$ $M_\odot$) and youngest (< 6 Myr) SSCs are located in the overlap region, where the two galaxies collide, and are associated with massive (several 10^8 $M_\odot$) and super-giant (few hundred of pc) molecular complexes (SGMCs). The formation of SSCs must involve a complex interplay of merger-driven gas dynamics, turbulence fed by the galaxy interaction, and dissipation of the kinetic energy of the gas. Within SGMCs, a hierarchy of structures must be produced, including dense and compact concentrations of molecular gas massive enough to form SSCs, pre-cluster clouds (PCCs). For star formation to occur, the mechanical energy of PCCs must be radiated away to allow their self-gravity to locally win over their turbulent gas pressure. Specific tracers of turbulent dissipation are therefore key inputs to test the validity of this theoretical scenario.

In my thesis, I studied the Antennae overlap region. My work is based on observations with the SINFONI spectro-imager at the VLT, which includes H_2 rovibrational and Brγ line emission, and with ALMA, which includes the CO(3−2) line and dust continuum emission. Both data-sets have the needed sub-arcsecond angular resolution to resolve the scales of SSC formation. The spectral resolutions are enough to resolve motions within SGMCs. Combining CO and H_2 line emission is key in my PhD work. I use CO as a tracer of the distribution and kinematics of the molecular gas, and H_2 as a tracer of the rate at which the gas mechanical energy is dissipated.

My thesis focuses on diverse sources in the Antennae overlap region which trace different stages of star formation: the gathering of mass necessary to form SGMCs, the formation of PCCs within SGMCs and the disruption of a parent cloud by a newly formed SSC. I show that at each stage turbulence plays a key role. I found that the kinetic energy of the galaxies is not thermalized in large scale shocks, it drives the turbulence in the molecular ISM at a much higher level than what is observed in the Milky Way. Near-IR spectral diagnostics show that, outside of SSCs embedded in their parent clouds, the H_2 line emission is powered by shocks and traces the dissipation of the gas turbulent kinetic energy. I relate the H_2 emission to the loss of kinetic energy required to form gravitationally bound clouds. This interpretation is supported by the discovery of a compact, bright H_2 source not associated with any known SSC. It has the largest H_2/CO emission ratio and is located where the data show the largest velocity gradient in the interaction region. To our knowledge, this is the first time that an extragalactic source with such characteristics is identified. We would be witnessing the formation of a cloud massive enough to form a SSC. The data also allow us to study the disruption of a parent molecular cloud by an embedded SSC. Its matter is loosely bound and its gravity would be supported by turbulence, which makes it easier for feedback to disrupt the parent cloud.

I end my manuscript presenting two projects. I propose to establish additional energy dissipation tracers observable with ALMA, which gives us the high spatial and spectral resolution needed to isolate scales at which clusters form. This is a Cycle 1 proposal accepted in first priority. I also plan to expand my work to other nearby extragalactic sources by investigating the turbulence-driven formation of stars in different extragalactic sources by combining near-IR and submillimeter observations.

Résumé

Les Antennes sont une des fusions de galaxies les plus connues dans l'Univers proche. Sa proximité nous permet d'observer et d'étudier ses gaz à l'échelle de la formation des amas stellaires. C'est une source idéale pour comprendre comment la dynamique dans les fusions de galaxies déclenche la formation d'étoiles. La plupart des étoiles dans les Antennes sont formées dans des amas stellaires compacts et massifs, surnommés *super-star clusters* (SSC). Les SSC les plus massifs ($> 10^6$ $M_\odot$) et les plus jeunes (< 6 Myr) sont situés dans la région de collision entre les deux galaxies et sont associés aux complexes moléculaires massifs ($\sim 10^8$ $M_\odot$) et super-géants (des centaines de pc) (*super-giant molecular clouds*, SGMCs). La formation de SSC doit impliquer une intéraction complexe entre la dynamique des gaz et une turbulence entraînée par la fusion des galaxies, et la dissipation de l'énergie cinétique des gaz. Dans les SGMC, une hiérarchie de structures doit être produite, incluant des concentrations denses et compactes de gaz moléculaires qui sont suffisamment massifs pour former un SSC, des nuages *pre-cluster clouds* (PCC). La formation des étoiles se produira si l'énergie mécanique des PCC est émise dans le lointain, permettant à l'auto-gravité de gagner localement les pressions thermique et turbulente du gaz. Des diagnostics spécifiques de dissipation turbulente sont donc des éléments essentiels pour tester la validité de ce scénario.

J'étudie la région d'intéraction des Antennes. J'utilise des observations avec le spectro-imageur SINFONI sur le VLT (raies rovibrationnelles de H_2) et ALMA (raie CO(3–2) et l'émission du continuum de la poussière). Les données ont des résolutions angulaires pour résoudre les échelles de la formation des SSC et des résolutions spectrales pour résoudre les mouvements à l'intérieur du SGMC. La combinaison des raies CO et H_2 est essentielle dans mon travail. J'utilise le CO comme traceur de la distribution et de la cinématique du gaz moléculaire, et H_2 comme traceur du taux de dissipation d'énergie mécanique de gaz.

Ma thèse se concentre sur des sources traçant des différentes étapes de la formation d'étoiles : le rassemblement des gaz pour former des SGMCs, la formation des PCC dans les SGMCs et la destruction des nuages moléculaires par les SSC. Je montre que la turbulence joue un rôle essentiel à chaque étape. J'ai trouvé que l'énergie cinétique de rencontre des deux galaxies n'est pas thermalisée dans les chocs aux échelles où elle est injectée. Elle entraîne une turbulence dans l'ISM moléculaire à un niveau beaucoup plus élevé que celui observé dans la Voie Lactée. Sauf dans les SSC encore intégrés dans les nuages moléculaires, la raie de H_2 est produite par des chocs et trace la dissipation de l'énergie cinétique turbulente du gaz. J'associe l'émission de H_2 à la perte d'énergie cinétique nécessaire pour former des nuages gravitationnellement liés. Cette interprétation est étayée par la découverte d'une source lumineuse et compacte en H_2, qui n'est associée à aucun SSC connu, située là où les données montrent le plus grand gradient de vitesse. À notre connaissance, c'est la première fois qu'une source extragalactique avec ces caractéristiques est identifiée. Nous observons la formation d'un nuage suffisamment massif pour former un SSC. Les données montrent également la destruction d'un nuage moléculaire par un SSC récemment formé. Sa matière est faiblement liée. Sa gravité serait soutenue par la turbulence, ce qui rend plus facile pour les mécanismes de rétroaction de perturber le nuage parent.

Enfin, je présente deux projets. Je propose d'établir d'autres traceurs de dissipation d'énergie observables avec ALMA, proposition du Cycle 1 acceptée en première priorité. Je propose également d'étendre mon travail pour étudier la formation des étoiles entraînées par la turbulence dans différentes sources extragalactiques en combinant les observations dans le proche infrarouge et submillimétrique.

Contents

List of Figures

List of Tables

Chapter 1

Introduction

Contents

Star formation is an essential process which drives galaxy evolution (Kennicutt 1998a), and likewise, galaxy evolutionary processes determine the characteristics of star formation in galaxies. However, the physical processes that trigger and regulate the formation of stars out of the interstellar matter are not fully understood (e.g. Elmegreen 2012). Although today numerical simulations of galaxies have the resolution to resolve the size scales of star forming clouds, they remain schematic in their description of the interstellar medium physics. They cannot resolve the wide range of physical scales, densities and temperatures of the multi-phase interstellar medium. Observations must guide theoretical studies. This is the approach I have

followed in my thesis work. To start, I was given spectral-imaging observations in the near-IR of the overlap region in the Antennae galaxy merger. The observations were successful, revealing unexpected results which provided me with the ingredients to focus my thesis on one main question, how do the large-scale galaxy dynamics in mergers trigger the formation of stars? Encouraged by these first results, I prepared my own observing proposals to extend my work. The ALMA observations of the Antennae carried out as part of the Science Verification gave me the opportunity to have an early access to one of the first data taken with that interferometer. I had the elements to go deeper in the study of star-formation in the Antennae galaxies and to investigate the dispersal of parent clouds by newly born super star clusters. In this manuscript, I gather the research I have done during my three years of PhD work at the IAS in Orsay.

In this chapter, I give the global astrophysical context of my PhD work. A more specific introduction to my research is given in the following thesis chapters, together with the relevant parts of my work. I start in Section 1.1 with a summary of the current cosmological framework of our Universe. In Section 1.2, I summarize our knowledge of galaxies in the Universe, and present the two main theories for galaxy formation and evolution. Section 1.3 gives a view of galaxy interactions and mergers in the local Universe. A general introduction to the multiphase nature of the ISM is given in Section 1.4. Section 1.5 introduces the star formation process, its main properties and observables. In Section 1.6, I describe the role of turbulence in the interstellar medium. Finally, in Section 1.7, I describe the method which I followed in my PhD work and the structure of this manuscript.

1.1 Cosmological framework

On the largest scales, our Universe is observed to be homogeneous and isotropic. The most accepted model to explain the origin of our Universe is the *Big Bang* model. It describes a Universe which originated from a dense and hot singularity in space-time, and is in expansion since then. The Big Bang accounts for three observational facts: the expansion of the Universe (first observational evidence presented by Hubble 1929), the abundance of light elements (i.e. H, He and Li, Alpher et al. 1948), and the Cosmic Microwave Background[1] (CMB, first detected by Penzias & Wilson 1965). The CMB represents the surface of last scattering of photons and free electrons prior to recombination about 300,000 years after the Big Bang. It is therefore the most direct observable of the primordial density fluctuations of the Universe, from which galaxy clusters and galaxies formed. Fig. 1.1 illustrates the timeline of the Universe.

Detailed studies of the CMB fluctuations also give us information about the total matter and energy content of the Universe, including in particular the dark

[1]This thermal radiation is the fossil of the Big Bang. It is characterized by a black body radiation at a temperature of 2.73 K. The CMB is not completely defined by an uniform single temperature, but it presents small fluctuations of less than 1 mK, the so-called anisotropies.

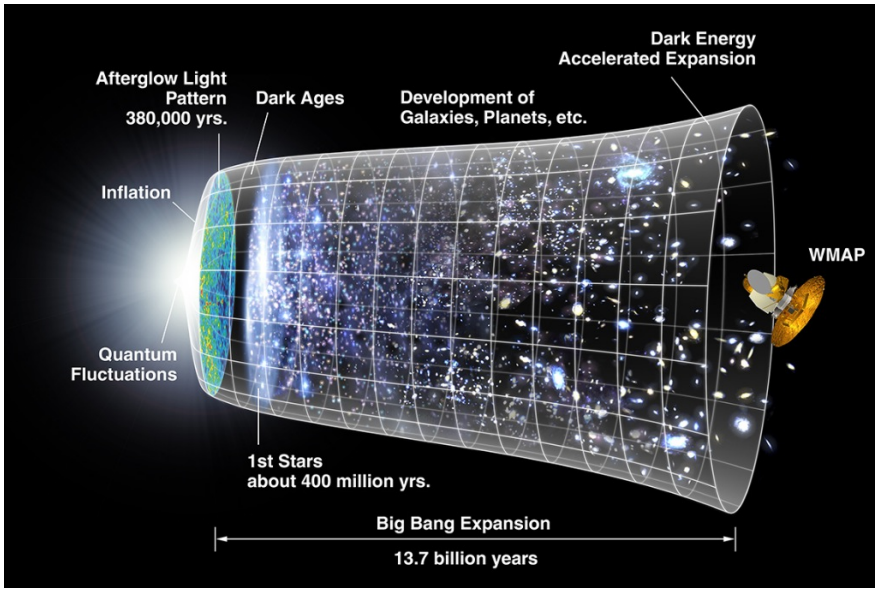

Figure 1.1: Timeline of the Universe, from the Big Bang (left side of the image) to the present day (right side). Our Universe originated 13.75 billion of years ago. It experienced a phase of rapid exponential acceleration and growth known as the Inflation. While the Universe expanded and cooled, elementary particles acquired mass and then combined to form hadrons (i.e. protons, neutrons). Inflation was slowed down by the gravity of the newly formed matter. After the formation of the first structures, they grew in mass in a hierarchical way by the merging of smaller structures into larger ones. *Credits: NASA/WMAP Science Team.*

matter[2] and dark energy[3]. The main results from the WMAP (Wilkinson Microwave Anisotropy Probe, Bennett et al. 2003) 7-years program infer that: the matter/energy in the Universe consists of 22.7% of Cold Dark Matter (CDM), 72.8% of Dark energy and that the remaining 4.6% is matter visible to us (baryonic matter, i.e. stars, gas, etc.), and it predicts that the Universe is not curved but flat (values taken from Tab. 8 in Jarosik et al. 2011). WMAP results support the ΛCDM *model*, that is the current accepted cosmological model for our Universe, which includes the presence of dark matter and dark energy. New maps of the CMB, more sensitive and at higher spatial resolution capable to probe the CMB anisotropies at much smaller scales, are expected to be released in January 2013 as part of the Planck satellite project.

[2]Dark matter consists of elementary particles of so far unknown type, which interact with normal matter only through gravity. In the cosmological framework, the dark matter is needed to account for the growth of the primordial perturbations in the Universe that led to the formation of large-scale structures.

[3]Dark energy is a theoretical form of energy predicted to account for observations that showed that our Universe is in accelerated expansion (e.g. deduced by measuring distances to galaxies using supernovae as candles Riess et al. 1998). It would be homogeneous in the Universe, having a gravitationally repulsive effect (negative pressure). In the cosmological framework, one way of parameterizing dark energy is by introducing a cosmological constant Λ, explaining the flatness and acceleration of the Universe. More details about dark energy can by found in the review by Frieman et al. (2008).

1.2 Galaxy formation and evolution

When we talk about galaxy evolution it is inevitable to talk about galaxy formation. These two processes are connected with the cosmological scenario, the initial conditions for galaxy formation in the Universe and the physical processes that regulate galaxy evolution.

1.2.1 Galaxies in the Universe

Large-scale surveys of the spatial distribution of galaxies, as the Sloan Digital Sky Survey[4] and the 2dF Galaxy Redshift Survey[5], revealed the large-scale structure in the Universe. Most galaxies are along relatively low-density filaments surrounding voids of sizes of hundreds of Mpc, and in high-density clusters at the junctions of these filaments (York et al. 2000; Colless et al. 2001).

It is estimated that there are about 170 Billions of galaxies in the observable Universe (Gott et al. 2005). Galaxies show a wide range of morphologies, from *elliptical* galaxies which have a dominant spherical or ovoid bulge, *spiral galaxies* which present a fainter bulge, and thin and flat spiral arms, to *irregular* morphologies which can have different origins, for example, gravitational influence of nearby galaxies or primitive state of the galaxy formation. Table 1.1 compares the basic properties of elliptical and spiral galaxies. For instance, our galaxy the Milky Way is a barred spiral galaxy, and our neighbors the Magellanic Clouds are dwarf irregular galaxies. Fig. 1.2 shows the variety of individual galaxies in the Universe. They have been historically classified according to the Edwin Hubble galaxy morphological classification (Hubble 1926), which is shown in Fig. 1.2 with real examples of observed galaxies.

Table 1.1: Characteristics of typical elliptical and spiral galaxies.

Characteristic	Ellipticals	Spirals
Sizes	$1 - 150$ kpc	$6 - 100$ kpc
Masses	$10^6 - 10^{13}$ $M_\odot$	$10^9 - 10^{12}$ $M_\odot$
Luminosities	$10^6 - 10^{12}$ $L_\odot$	$10^8 - 10^{11}$ $L_\odot$
Bulge	Prominent	Faint
	(old, low-mass stars)	(old stars)
Disk	Not present	Prominent (stars + gas + dust)
	-	Young stars
	-	Active star formation
Kinematics	Stars have radial kinematics	Rotational disk
Others	- Gas and dust poor	Morphologies of their bulges are similar to
	- Low star formation activity	morphologies of ellipticals galaxies

There is evidence that galaxies are associated with extended dark-matter halos. Its presence accounts for the unseen galactic masses that several observations sug-

[4] http://www.sdss.org/
[5] http://magnum.anu.edu.au/~TDFgg/

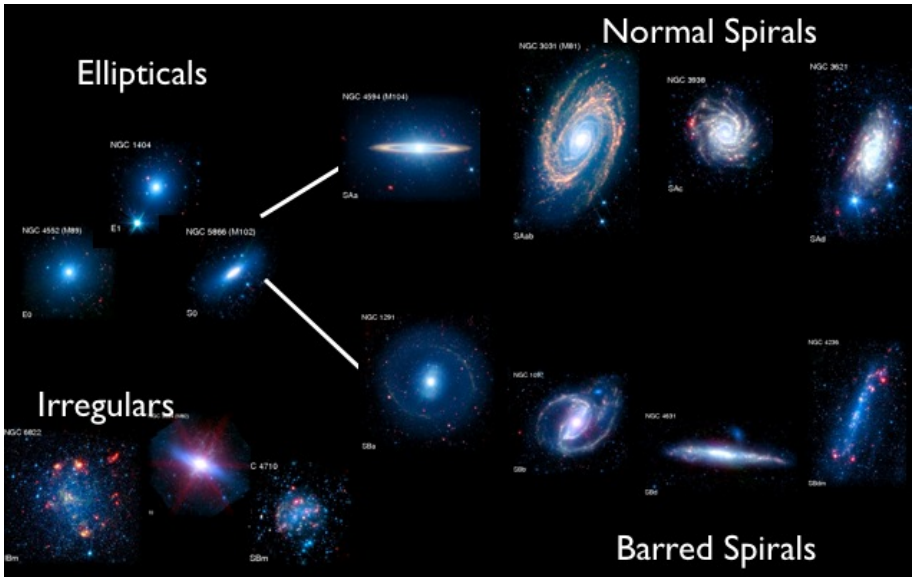

Figure 1.2: Hubble's classification of galaxies in the Universe. From the left, elliptical galaxies, to the right, spiral galaxies which can present or not a bar connecting the bulge and the spiral arms. Not included in this classification are the irregular galaxies, which are located on the left-bottom part of the diagram. Figure adapted from the Spitzer Infrared Nearby Galaxies Survey (SINGS) Hubble tuning fork poster.

gest, for instance observations of galaxy rotation curves (pioneering work by Rubin et al. 1980) or weak gravitational lensing in galaxy clusters (e.g. Tyson et al. 1990, or quantified by Clowe et al. 2004 for the Bullet galaxy cluster). It is now commonly accepted that galaxies, besides being constituted of their visible features, also have a massive dark matter halo that extends beyond the visible galaxy.

1.2.2 Hierarchical model of dark matter halo collapse and galaxy evolution

The current accepted theory for the formation of dark matter halos is the hierarchical merging scenario (Lacey & Cole 1993). The formalism of a non-linear hierarchical formation of structures was first given by Press & Schechter (1974), and it has been developed, modeled and modified since then, keeping the basic formalism (e.g. White & Rees 1978; Lacey & Cole 1993; Cole et al. 2000; Bower et al. 2006). In this model, the primordial small density fluctuations are the progenitors of galaxies. The model predicts that these density perturbations, dominated by dark matter, collapsed to form small virialized dark matter halos. Halos grow gradually, 'hierarchically', through the merging of smaller halos. Fig. 1.3 shows a diagram of this merger-tree model also called the 'bottom-up' model (Lacey & Cole 1993). In this diagram, each branch represents a dark matter halo. Time evolves from the top to the bottom of the image, while the widths of the branches represent the masses of the halos. Numerical simulations of large numbers of dark matter halos broadly agree with the observed distribution of galaxies revealed by the previously

mentioned surveys.

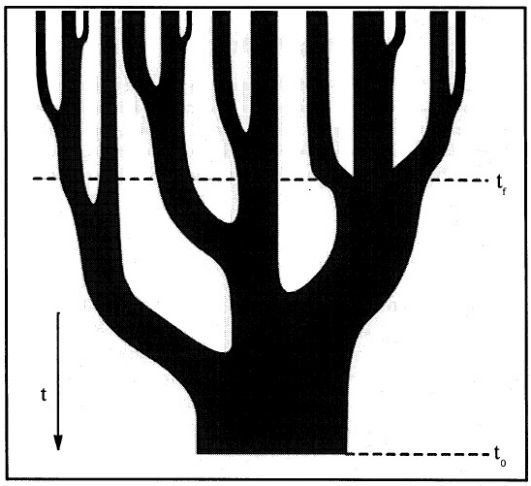

Figure 1.3: Diagram of the hierarchical merger of dark matter halos scenario. This model predicts that small halos of dark matter interact and merge into larger halos, in a hierarchical way. Figure extracted from Lacey & Cole (1993, their Fig. 6)

There is a clear difficulty to translate the dark matter collapse into a robust model of galaxy formation and evolution. Simulations of dark matter are relatively far advanced. The problem lies in the modeling of the baryonic matter. Such models must cover realistic ranges of sizes, gas densities and temperatures, and accurate physical descriptions of gas cooling and heating, subsequent star formation, dust, etc. This is beyond current computational limitations. Moreover, many of these processes are not yet understood. As a consequence, all of the simulations make simplistic assumptions and/or rely on empirical relationships without clear physical interpretation. For example, in my thesis I would like to understand how galaxy mergers trigger star formation. Detailed numerical simulations of the Antennae merger exist (e.g. Bournaud et al. 2008; Teyssier et al. 2010), but they must be compared and guided by high angular resolution observations where we can *resolve* (at scales of a few tens of parsecs) the star formation process.

In the following two sections, I describe the two major groups of models to account for the growth of galaxies, (1) hierarchical, merger-driven growth, and (2) galaxy growth through rapid 'monolithic' collapse or cold accretion of gas onto galaxies leading to a single, intense burst of star formation.

1.2.3 Hierarchical, merger-driven growth of galaxies

As its name indicates, in this theory mergers are the most important phenomenon. Within the framework of the ΛCDM model and the hierarchical merger formation of dark matter halos, this theory is the standard and natural model for galaxy formation.

In the theory of hierarchical merging as driver of galaxy formation and evolution, baryons follow the fate of the dark matter halos, connecting the galaxy formation

process with the hierarchical scenario. First, galaxies, each tracing their own dark matter halo, would form within the merger-tree model for dark matter introduced before (Kauffmann et al. 1993). The primordial Gaussian density fluctuations presented in the CMB were constituted by a mixture of dark matter and primordial gas (light elements produced in the Big Bang). When virialized dark matter halos form, the gas within them collapses, accumulates and condenses in their centers to form the visible counterparts of the dark matter halos, galaxies and stars (see for instance Cole et al. 2000). Therefore, galaxies are the result of the primordial quantum fluctuations. While dark matter halos were merging, their host galaxies could also interact and merge. It is in this way how the hierarchical growing of dark matter halos is extended to their host galaxies.

Hierarchical merging explains the formation of elliptical galaxies. However, it predicts too many dwarf galaxies (Moore et al. 1999) and cannot account for the observed number of spiral galaxies (Steinmetz & Navarro 2002). Major mergers (Section 1.3) are violent, destroying the disks of the collapsing galaxies, leading to the formation of elliptical galaxies. There is also a problem with the star formation rate of galaxies. The hierarchical model predicts a gradual star formation, but recent observations have shown that massive galaxies in the early Universe have high star formation rates (Smail et al. 2004), with very little star formation over the last 10 Gyr. Many researchers believe now that this is the result of heating by energy released during the accretion of matter onto supermassive black holes (active galactic nuclei feedback, e.g. Croton et al. 2006). However, more subtle difficulties with our understanding of gas cooling are not ruled out (Birnboim et al. 2007).

1.2.4 Galaxy formation by cold accretion and 'monolithic' collapse of baryons

An alternative to the 'bottom-up' approach given above is quantified by models where galaxies formed most of their mass in a single giant star-forming event triggered by rapid gas infall. Such a scenario of 'monolithic' collapse was first proposed to explain the formation of our own galaxy. Eggen et al. (1962) proposed that the monolithic collapse of gas of a proto-galactic cloud yields the observed characteristics of the Milky Way, these are the bulge, disk and halo, where the halo was formed in the initial phase of the collapse. However, it was later disfavored since its predictions did not match with observations of velocities of halo stars and globular clusters (Searle & Zinn 1978), and the relatively young ages of disk stars.

In the past few years, the basic idea behind the 'monolithic' collapse scenario has become more popular again, challenging at least one aspect of the hierarchical model, the preponderance of major galaxy mergers in driving the formation and evolution of galaxies. Dekel et al. (2009) argue that the collapse of cold gas through narrow, dense streams within the dark matter halos onto forming galaxies could be the main mechanism of how galaxies form in the early Universe. Cold accretion models de-emphazise the role of mergers for early galaxy growth.

Dark matter halos are distributed along large-scale dark matter filaments. These

filaments trigger shocks in the gas falling from the periphery to the central regions of massive dark matter halos. The gas is heated by these shocks producing an internal energy that balances gravity, the gas is in virial equilibrium with the dark matter. In the standard hierarchical model, if the gas falls onto halos above a certain mass, it will not be able to cool rapidly enough to be available as new 'fuel' for star formation in the central galaxy (White & Rees 1978). However, motivated by the results of high-resolution hydrodynamical simulations (Kereš et al. 2005), modelers believe that accretion occurs through filaments, where the enhanced density allows the gas to cool faster. This may allow gas to cool and thereby be accreted onto the forming galaxy. The predicted outcome are immerse narrow streams of cold gas fueling intense star formation in high redshift galaxies. Figure 1.4 displays an illustration of this scenario. The colors refer to the inflow rate per solid angle. The low-flux medium in the dark matter halo is penetrated by three cold, narrow, dense streams, which converge radially at the center of the halo.

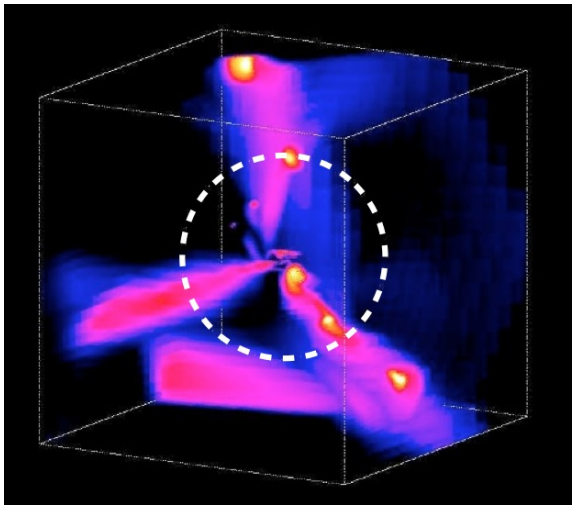

Figure 1.4: MareNostrum simulation of a monolithic collapse of the gas within a dark matter halo. The figure illustrates a 3-D view of the galaxy formation. The colors correspond to the inflow rate per solid angle of point-like tracers at the centers of cubic-grid cells. The white dashed-circle delimits the virial mass of the halo. In this simulation, three cold, narrow streams are radially penetrating the dark matter halo. The galaxy will form at the center of the halo. Figure extracted from Dekel et al. (2009, their Fig. 2).

This scenario de-emphasizes the role of mergers between galaxies of comparable sizes (major mergers, see Section 1.3) in the formation of massive galaxies at high redshift. Gas clumps falling along filaments resemble minor mergers (see Section 1.3). Encouraged by the results of Dekel et al. (2009), modelers and observers have proposed that the irregular, clumpy morphologies of many high-redshift galaxies may be explained by fragmentation of intensely star-forming, rapidly accreting, and very gas-rich disks in the early Universe (e.g. Bournaud et al. 2008). This would be an alternative of considering clumpiness as a sign of merger activity, although both are difficult to distinguish observationally (Robertson et al.

2006). However, by itself, the cold accretion model of Dekel et al. (2009) does not reproduce the early presence of galaxies with low star formation rate. It also requires either implausibly high gas accretion rates or star-formation efficiencies that are near 100%, about two orders of magnitude greater than what is found locally (Section 1.3).

1.3 Galaxy interactions and mergers in the local Universe

As I just discussed previously, it is not so clear anymore whether galaxy mergers are the only mechanism that shapes galaxies in the early Universe. However, what is certain is that mergers are a common phenomenon in the nearby Universe and play a large role in determining the morphologies of galaxies and the properties of their stellar populations along the Hubble sequence, in particular in early-type galaxies. Moreover, 'pair studies', surveys of close galaxy pairs seen in projection, suggest that the number of mergers increases with increasing redshift out to at least $z \sim 1$ (Le Fèvre et al. 2000; Conselice et al. 2003; de Ravel et al. 2009; Darg et al. 2010).

Interacting galaxies with moderate relative velocities, where the kinetic energy does not exceed the binding energy, will finally merge, after orbiting around each other several times. Dynamical friction, tidal forces, and dissipation of kinetic energy in the gas of the two galaxies will make them lose more and more kinetic energy with each orbit, until they fall to the center of the gravitational potential and coalesce. Depending on the merger configuration, the total merger time is likely to be few 100 Myr, and up to about 1 Gyr (e.g. Di Matteo et al. 2008).

In the local Universe, there are many examples of galaxy interactions that have been observed at high angular resolution, e.g., with the *Hubble Space Telescope* (HST), like the Antennae or the "Mice" galaxies (see Figure 1.5). Efforts to associate individual galaxy mergers with a given merger stage from the first encounter to the final coalescence date back to Toomre & Toomre (1972) and Toomre & Toomre (1977). The Milky Way is currently undergoing several mergers. The Leading Arm Feature observed on the Southern hemisphere is perhaps the most prominent feature showing that the Milky Way will ultimately swallow its two low-mass companions, the Magellanic Clouds (Putman et al. 1998). In the local Universe, there are famous galaxies used as prototypical examples, where it is possible to study the gas and dust morphology and kinematics. Probably the best studied merger in the nearby Universe are the Antennae galaxies, NGC 4038 and NGC 4039, at 22 Mpc, which are still in an early merger state. My thesis work is based on this merger.

Based on the masses of the interacting galaxies mergers are commonly split into two regimes. Major mergers involve two roughly equal-mass galaxies, where the galaxy mass ratio ranges from 1:1 to 1:3. Major mergers change the morphology and subsequent evolution of galaxies most strongly, in particular if the two merging galaxies are gas-rich. In addition to galaxy mass, other parameters, for example

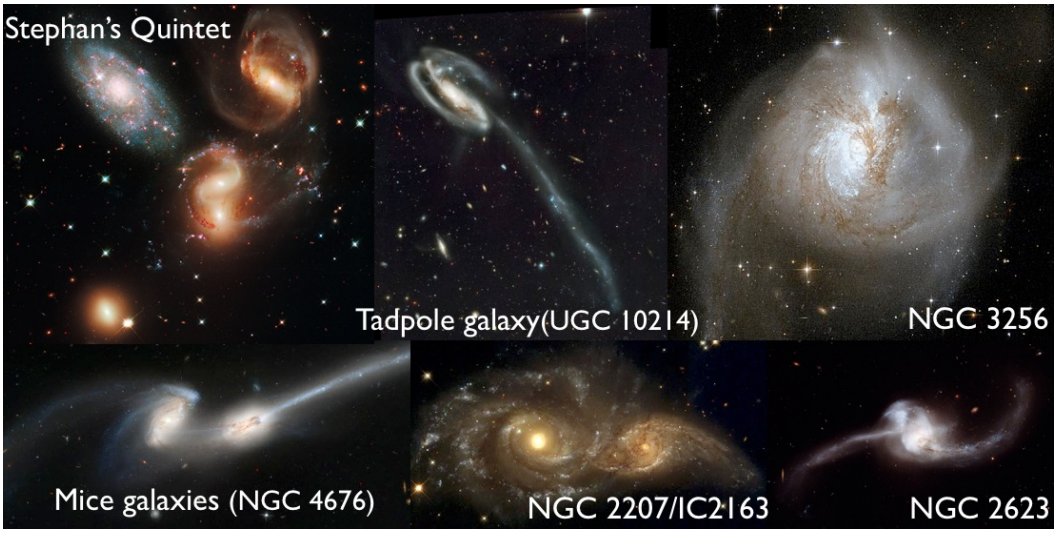

Figure 1.5: Examples of interacting galaxies in the local Universe, observed by the *Hubble Space Telescope*. Merger and interacting galaxies can be found at different stages from early encounters, where the two galaxies can be easily resolved, to more evolved merging. *Credits.* Stephan's Quintet: NASA, ESO and the Hubble SM4 ERO Team. Tadpole galaxy: NASA, H. Ford (JHU), G. Illingworth (UCSC/LO), M.Clampin (STScI), G. Hartig (STScI), the ACS Science Team, and ESA. NGC 3256: NASA, ESA, the Hubble Heritage (STScI/AURA)-ESA/Hubble Collaboration, and A. Evans. Mice galaxies: NASA, H. Ford (JHU), G. Illingworth (UCSC/LO), M.Clampin (STScI), G. Hartig (STScI), the ACS Science Team, and ESA. NGC 2207/IC2163: NASA and The Hubble Heritage Team (STScI). NGC 2623: NASA, ESA and A. Evans.

the orientation of the galaxy rotation relative to the merger orbit, play a role (e.g. Di Matteo et al. 2008). "Pro-grade" mergers where the galaxy rotation and merger orbital axis are aligned, are most effective, because a given part of each galaxy will be strongly influenced by the merger for a longer time-scale. The remnant of a major merger of two gas-rich galaxies is an elliptical galaxy (e.g. Barnes & Hernquist 1991). In the standard merger scenario, most of the gas in the two merging galaxies will either be consumed by star formation or removed from the galaxy through galactic superwinds driven by star formation or active galactic nuclei (AGNs), so that the merger remnant is not expected to show much star formation afterwards (e.g. Hopkins et al. 2006).

In minor mergers, one galaxy is considerably less massive that the other. Typical ranges are from 1:3 to 1:10. During the merger, the less massive galaxy will be 'swallowed' by the more massive galaxy, in a process similar to the satellite accretion scenario proposed for galaxy formation (Searle & Zinn 1978). Extended low surface-brightness tails around nearby galaxies show that the lower-mass galaxies can be entirely disrupted during the interaction, whereas the more massive galaxy remains almost unchanged (e.g., NGC 5907, Martínez-Delgado et al. 2008). The Magellanic clouds are an example of two irregular dwarf galaxies being accreted onto the Milky Way, and surveys including the Sloan Digital Sky Survey have revealed multiple almost fully disrupted satellite galaxies of the Milky Way (e.g. Belokurov et al.

2007). Some scientists suggest that stars in the halo of the Milky Way could be made almost entirely from such satellite galaxies, whereas others suspect that at least some globular clusters in the Milky Way may be the remnants of satellite galaxies accreted early on (e.g. Lee et al. 1999). Phases of rapid accretion of multiple satellite galaxies have recently been suggested to form the extended low-surface brightness envelopes around massive elliptical galaxies, and to cause several other structural parameters of these galaxies (Johansson et al. 2009).

Galaxy interactions and mergers of gas-rich galaxies are often associated with high infrared luminosities (Sanders & Mirabel 1996) from dust heated by star formation. They can build more massive galaxies, and trigger bursts of star formation (Mihos & Hernquist 1996) and/or non-thermal nuclear activity (AGN, Springel et al. 2005). Infrared observations performed by IRAS (Infrared Astronomical Satellite, launched in 1983), revealed the presence of ∼75000 *starburst galaxies*[6], which are defined by their high star formation rates (SFR). For instance, the Milky Way has a moderate SFR of ∼1 $M_{\odot}$ yr^{-1} (Robitaille & Whitney 2010). In starburst galaxies, the SFR goes from a few to about a thousand times the Galactic value (Kennicutt 1998b). Depending on their far-IR luminosities, such galaxies are referred to as LIRGs (luminous infrared galaxies, with $L_{\rm FIR}$ of-order 10^{10} $L_{\odot}$, or ULIRGs (ultraluminous infrared galaxies, $L_{\rm FIR} > 10^{11}$ $L_{\odot}$). In these galaxies, the formation of stars is triggered by the condensation of a large amount of cold molecular gas which, in most cases, is likely to be driven by the interaction of galaxies that perturbs the gravitational potential of the merging galaxies, leading to the collapse of the required immense amount of gas to fuel the star formation.

First numerical simulations of gas-rich mergers tried to reproduce the morphologies of the mergers, going back to the successful modeling of the tidal arms of the Antennae merger through Toomre & Toomre (1972). However, they did not have the computational power to include the effects of gas, which unlike the stars rapidly dissipates kinetic energy and therefore responds most strongly to the merger. This was only done by Barnes & Hernquist (1991) who modeled the collision between two gas-rich galaxies. Tidal forces produce not only extended tails of stars and gas, but also drive gas flows inwards producing nuclear starbursts, in a time scale of ∼100 Myr. This nuclear emission may account for the most luminous IR galaxies in the local and distant Universe. Later, the ISO (Infrared Space Observatory, launched in 1995) with much higher resolution and sensitivity, provided observations of starburst galaxies with much more details.

The study of the star formation process in galaxies, and in particular in starbursts, provide the evidence of their evolution. In the following of this Chapter, I focus on the star formation process. I start by describing the medium from where stars form, the interstellar medium.

[6]Most of the observed starburst galaxies are mergers. Individual galaxies with a high star formation rates are also observed, but their number and IR luminosity are lower than those of mergers.

1.4 The interstellar medium

The matter between stars in galaxies, the interstellar medium (ISM), links stellar and galactic scales. The ISM rules the life cycle of stars, connecting their birth and death. Stars form out of this matter and, when they die, they return their processed matter to the ISM. The ISM is best quantified in our Galaxy. Its mass is composed by 99% of gas and 1% of dust. In turn, the most abundant gas element is hydrogen ($\sim$ 89%) followed by helium ($\sim$ 9%). The remaining 2%, is composed by heavier elements, the so-called metals. Even though its mass corresponds to only 10% of the stellar mass in the Milky Way, the ISM is crucial for star formation and galaxy evolution because it is the matter from which new stars form.

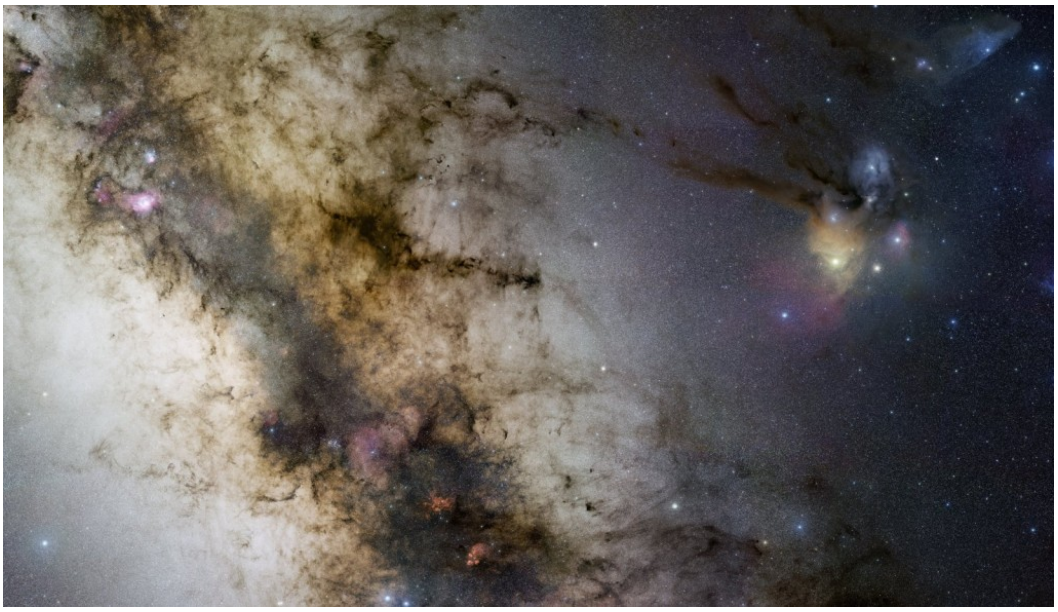

Figure 1.6: The galactic interstellar medium. The image corresponds to the central part of our Milky Way in the constellation of Sagittarius, observed in the optical. This image illustrates the richness of the ISM. The main feature is the dust lane which runs obliquely through the image. The bright source to the right is the Rho Ophiuchi cloud complex, a star-forming region. *Credit Image: ESO/S Guisard.*

We observe the ISM through gas emission and absorption lines. These lines give us information on the gas kinematics, and physical conditions such as density, temperature and pressure. The first evidence of the presence of dust in the ISM in our Milky Way came from observations of open star clusters that indicated reddening and absorption of the light (Trumpler 1930).

Today, powerful telescopes at all wavelengths, the modeling of interstellar processes and numerical simulations, shape our current picture of the ISM. In this section, I describe the characteristics of the ISM as we understand it today.

1.4.1 The multiphase ISM

Field et al. (1969) suggested that the gas in the ISM could be found in two stable phases in pressure equilibrium, cold clouds and warm gas. This theory evolved to the current multiphase ISM theory (McKee & Ostriker 1977; Burkert & Lin 2000), in which interstellar gas is distributed over a wide range of temperatures with a mean pressure $P_{\rm eq}/k_{\rm B}$ of a few 10^3 K cm^{-3}. Figure 1.7 illustrates the three-phase model of the ISM proposed by McKee & Ostriker (1977). In this model the cold, warm and hot phases are in pressure equilibrium. Numerical simulations have since quantified a dynamical view of the ISM including turbulent cycling of matter between gas phases (de Avillez & Breitschwerdt 2005).

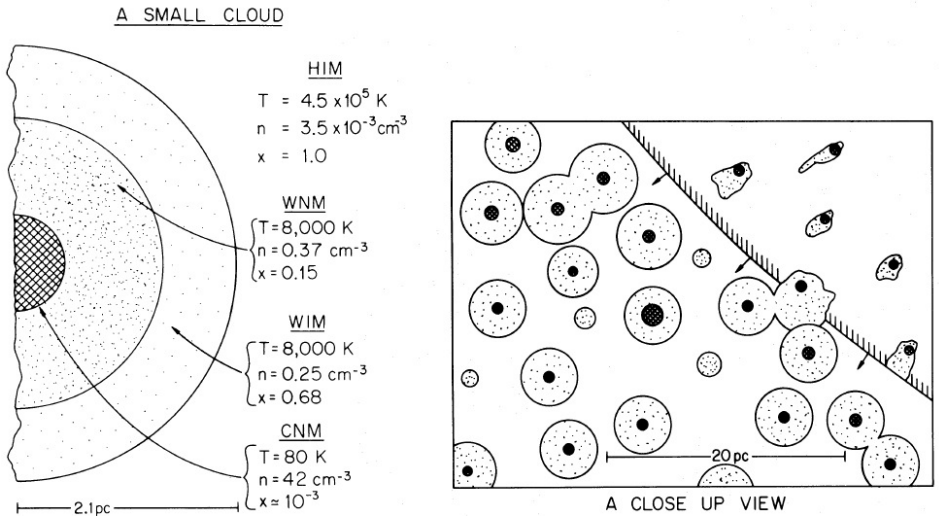

Figure 1.7: This figure illustrates the three-phase ISM model of McKee & Ostriker (1977, their Figure 1). The left panel zooms on a cloud, embedded in the hot plasma produced by supernova explosions. The cold neutral medium (CNM) at the center of the cloud is surrounded by layers of warm neutral and ionized medium (WNM and WIM). The right panel gives a more extended view of a supernova blast wave impacting interstellar clouds.

The ISM is classified according to the state of its most abundant element – molecular, atomic and ionized state – , hydrogen (H), which depends on the gas temperature and density. Table 1.2 summarizes the characteristics of the different phases of the ISM (adapted from Table 1.1 in Tielens 2005).

Molecular gas is mainly found in molecular clouds, which have low temperatures and high densities (see Table 1.2). It is the densest and coldest phase of the ISM. Interstellar chemistry leads to the formation of diverse sets of molecules, with CO being the most abundant after H_2. The distribution of molecular gas in galaxies is typically traced through CO transition lines and dust far-IR emission.

The *neutral gas* consists of atoms, essentially neutral hydrogen H I. It is traced by the hyperfine transition of the hydrogen at $\lambda = 21$ cm[7], in absorption or emission. There are two thermally stable phases in the neutral gas, *cold neutral medium* (CNM)

[7]This line emission is created by the transition of two hyperfine levels of H.

and *warm neutral medium* (WNM). The gas temperature and density of these two phases vary by about two orders of magnitude (Table 1.2). While the molecular gas is confined in molecular clouds, the neutral gas emission is much more diffuse and extended across galaxies.

The *ionized gas* is much lighter than the molecular and neutral gas. It presents temperatures high enough to convert the gas into a plasma formed by protons and electrons (i.e. ionized hydrogen H II). The typical tracers of the ionized gas are the hydrogen recombination lines, such as Hα or Brγ, the thermal free-free radio emission and X-rays. The ionized gas can be classified according to the gas temperature and density in two phases, *warm ionized medium* (WIM) and *hot ionized medium* (HIM). The hot ionized gas is produced in high velocity shocks driven by supernovae explosions and stellar winds, and also at larger scales in galaxy interactions. The warm ionized medium is generally found surrounding massive and young stars (O or B type), but it also extends to a thick disk component in disk galaxies.

Table 1.2: Characteristics of the phases of the ISM. Adapted from Tielens (2005).

State of the gas	Phase	Temperature [K]	Density [part. cm^{-3}]
Molecular	Molecular Clouds	10	$>10^2$
Neutral	Cold Neutral Medium (CNM)	10^2	50
	Warm Neutral Medium (WNM)	8×10^3	0.5
Ionized	Warm Ionized Medium (WIM)	8×10^3	0.1
	Hot Ionized Medium (HIM)	$\sim 10^5 - 10^6$	10^{-3}

Numerical simulations on the scales of galaxies are now including the multiphase ISM. However, this is a computational challenge due to the amount of processes that shape it and regulate its energetics. Our observational knowledge has grown from the Milky Way to nearby galaxies and is moving into the interpretation of observations of distant galaxies.

1.4.2 Interstellar environments

The ISM is complex. To model the observations and quantify physical processes, we need to introduce simplified descriptions of interstellar environments. In this section, I detail the two environments, PDRs and shocks, to which I will refer in my thesis work. For each of them, I describe the mechanism of excitation of the H_2 molecule.

1.4.2.1 Massive star forming regions

In the following, I describe the different components of massive star forming regions.

a. Molecular Clouds. They are concentrations of dense molecular gas and dust, associated with dark nebulae. They have a wide range of sizes, starting from

$\sim$ 10 pc, to Giant Molecular Clouds (GMC) with sizes up to $\sim$ 100 pc. Dense cores within molecular clouds have sizes $\sim$ 1 pc, densities of 10^4 cm^{-3} and masses of $10-10^3$ $M_\odot$. These cores are the potential sites of star formation in molecular clouds (see Section 1.5 for a more extended view of the star formation process). In the simplistic picture, molecular clouds are assumed to be spherical or ovoidal. In reality, observations in the Milky Way have shown that they can have diverse morphologies. Since we cannot resolve the internal structures of extragalactic molecular clouds, the galactic view is normally extrapolated to these galaxies.

Recent observations obtained with the *Herschel Space Observatory* have revealed the filamentary structure of the star forming regions. The internal structure of molecular clouds is filamentary, where star formation occurs only in the densest parts (e.g. Könyves et al. 2010 in the Aquila cloud and Arzoumanian et al. 2011 for the IC 5146 cloud).

b. Photodissociation Regions (PDRs). PDRs are created on the surface of molecular clouds where they are exposed to far-UV radiation. In these regions the physics and chemistry of the gas are driven by the interaction of matter with far-UV photons. Since PDRs are the interface between the molecular and ionized gas they are composed by a mix of neutral and ionized atoms, and molecules (Fig. 1.8). The transitions from H to H_2 and from C^+ to CO take place within PDRs. The depth at which these transitions occur, depends on the radiation field (UV-photons) and the gas density. Models quantify physical and chemical processes in PDRs. The comparison of observed gas line emission from PDRs with model results yields constraints on physical parameters.

The typical tracers of PDRs are the fine-structure lines of [C II] (at 158μm) and [O I] (at 63 and 145μm), and the far-IR continuum emission from dust. In the Milky Way, the spatial structure of PDRs is resolved. For instance, in the two prototypical PDRs, the Orion bar and the Horsehead mane (Pety et al. 2008). Arab et al. (2012) present Herschel observations of the Orion Bar, at an angular resolution of 0.″05 pc, where they spatially resolve the PDR and its various components. The Horsehead nebula has also been observed at several molecular transitions, which allowed to describe in detail its structure (i.e. Gerin et al. 2009). In extragalactic molecular clouds, we cannot observe the structure of PDRs, and even more it is very difficult (if not impossible for more distant galaxies) to isolate them from the molecular clouds.

c. H II Regions. When massive stars are formed in molecular clouds, their UV emission starts heating and ionizing its surrounding cloud creating a region where the hydrogen is fully ionized. Initially, H II regions are compact and dense ($\sim$ 0.5 pc, $10^3 - 10^4$ cm^{-3}). Due to their high pressure they expand into diffuse extended H II regions. H II regions are mainly traced by thermal radio emission, and hydrogen recombination lines. Theoretically, the sizes of H II regions are defined by the Strömgren sphere, which is determined by the balance between the number of recombinations and ionizations in the simple case where the gas

density is uniform.

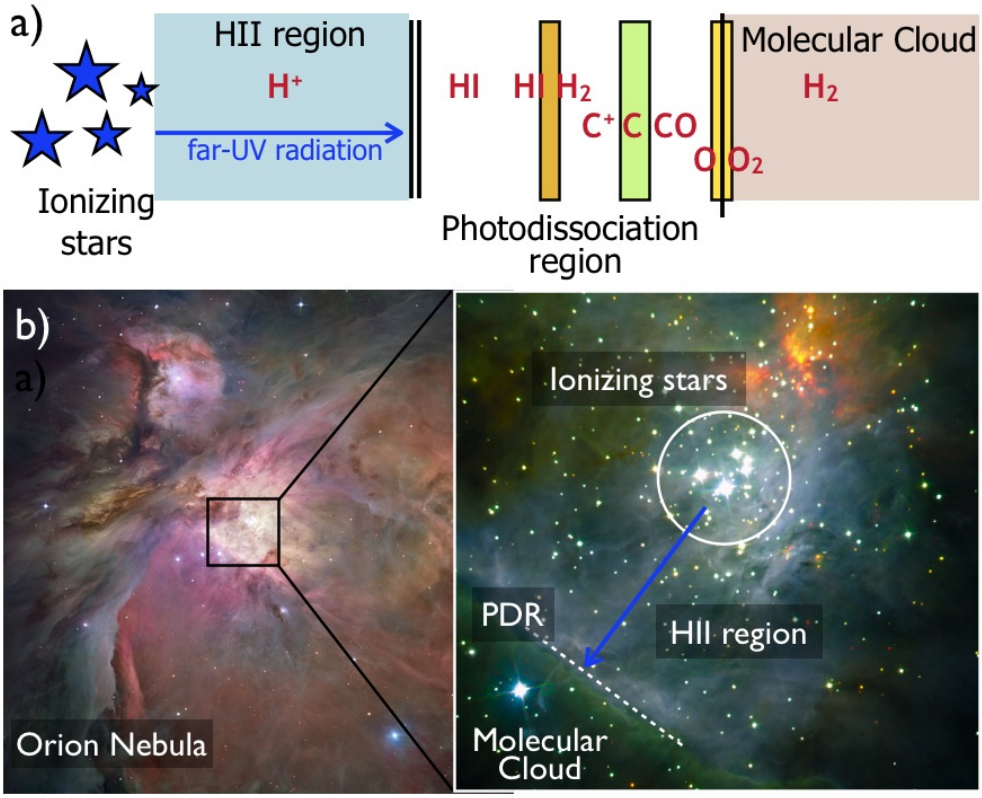

Figure 1.8: a) The H II region corresponds to the blue area and the molecular cloud to the pink area. The PDR is the interface between them and here it is illustrated as different layers which are defined by the elements transitions. Note: Diagram not scaled. b) The Orion Nebula. The left panel displays the whole nebula as seen by the Hubble Space Telescope. The picture in the right panel was obtained with the near-IR camera ISAAC at the VLT, and it zooms the central part of the nebula where the Trapezium stellar cluster is ionizing its surrounding. (*Image credits. Left: NASA,ESA, M. Robberto (STSI/ESA) and the HST Orion Treasury Project Team Hubble. Right: McCaugrean, Alves, Zinnecker, Palla*).

Fig. 1.8a displays a simple 1-D diagram that explains the link between molecular clouds, PDRs and H II regions. The H II region corresponds to the blue area in which the hydrogen is ionized by the stellar UV radiation. The density of the gas and the strength of the stellar radiation will define the extent of the H II region. The PDR corresponds to the interface between the H II region and the molecular cloud. At the ionizing front the PDR starts. This region can be decomposed in several layers that limit the dissociation and/or ionization of the different elements. These processes depend on the photon energy. In Fig. 1.8a, the color boxes represent the transitions between the elements. In orange the transition from neutral to molecular hydrogen ($\sim 10^2$ K), in green the triple transition from ionized to neutral carbon and from neutral carbon to CO (at several tens of K) and in yellow from neutral to molecular oxygen (at a few tens of K). Fig. 1.8b shows a well known Galactic PDR, the Orion

Nebula. In the left, the Orion Nebula observed with the HST. In the right, an IR image obtained with the Very Large Telescope that zooms onto the central part of the nebula, where the Trapezium open star cluster is observed. In this diagram, I highlighted this ionizing cluster, and one of the multiple PDRs that are found in this region, the *Orion Bar*. This is a beautiful example where all the components, H II region, PDR and molecular cloud, can be isolated.

How is H_2 excited in PDRs? Where the molecular gas is exposed to UV radiation, the low J levels of the ground vibrational state of H_2 are excited by collisions, but the H_2 vibrational states are populated by a fluorescent cascade following UV pumping to an electronic excited state (e.g. Sternberg & Dalgarno 1989). Figure 1.9 illustrates the *UV pumping* of the H_2 molecule. The H_2 molecules absorb UV photons in the Lyman and Werner bands, with energies in the range $h\nu = 11.2-13.6$ eV. This absorption produces the electronic excitation of the molecule. The excited state of H_2 will rapidly decay with two possible consequences: in $\sim 10\%$ of the cases, the decay leads to the dissociation of the molecule, while in $\sim 90\%$ of the cases the molecule decays into bound ro-vibrational levels of the ground electronic state (Black & Dalgarno 1976; Black & van Dishoeck 1987). PDR models quantify the H_2 line intensities based on this physics.

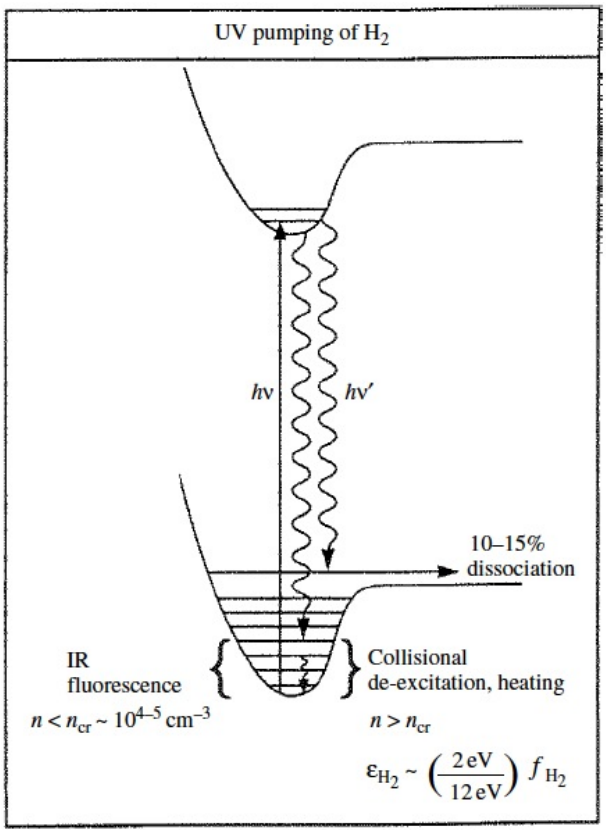

Figure 1.9: Diagram illustrating the UV pumping of the H_2 molecule. From Tielens (2005).

1.4.2.2 Shocks

A shock occurs when gas moves with a velocity higher than the speed of sound in the surrounding medium. For example, this occurs after a supernova explosion (see Figure 1.10). The high pressure region created by the explosion expands supersonically into the ISM. Shocks are also present in wind-blown bubbles and in the early expansion of H II regions.

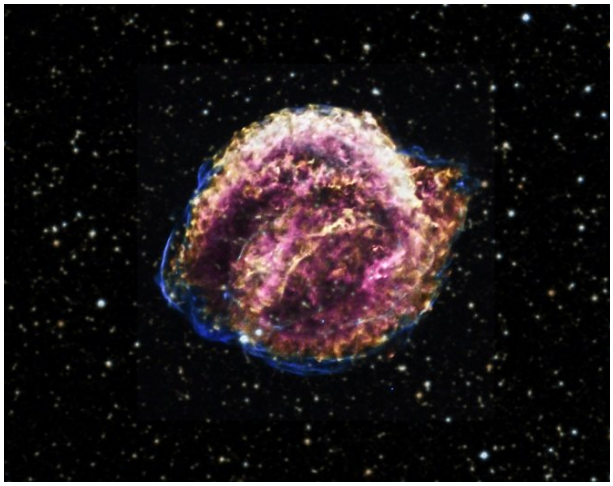

Figure 1.10: Kepler's supernova remnant. Composite image in the X-ray and optical regions of the electromagnetic spectrum obtained with the Chandra X-ray Observatory and the Digitized Sky Survey, respectively. The X-ray emission shows the very hot gas particles with very high energy. *Credits Image: X-ray: NASA/CXC/SAO/D.Patnaude, Optical: DSS.*

Shocks are created by supersonic turbulent motions over a range of scales in molecular clouds (see Section 1.6.1). In these shocks, the gas kinetic energy is dissipated into heat. The heated gas can radiate away this energy. The chemistry of the gas is also affected by the shock. In the Milky Way, emission associated with shocked gas can clearly be identified in Supernova Remnants (SNR) and the environments of young stellar objects (YSOs). These objects are used as template sources to model interstellar shocks. Two main types of shocks are considered, depending on the strength of the magnetic field. When the shock velocity is larger than the magneto-sonic velocity, the kinetic energy is dissipated viscously in a very sharp velocity jump. These shocks are called J (*jump*) type shocks. For lower shock velocities the kinetic energy is gradually dissipated into heat through ion-neutral friction (e.g. Lesaffre et al. 2013). These shocks are called C (*continuum*) type shocks. The structure of a C-shock wave (temperature and velocity) is described in Figure 1.11.

The post-shock temperature depends on the shock velocity. Shocks with velocities larger than 50 $\mathrm{km\,s^{-1}}$ ionize the pre-shock gas. For shocks in molecular clouds, the observations may be accounted for with lower velocity shocks where the H_2 molecule is not dissociated and is the main cooling agent. The H_2 lines are thus the main tracer of the kinetic energy dissipated in shocks within molecular clouds.

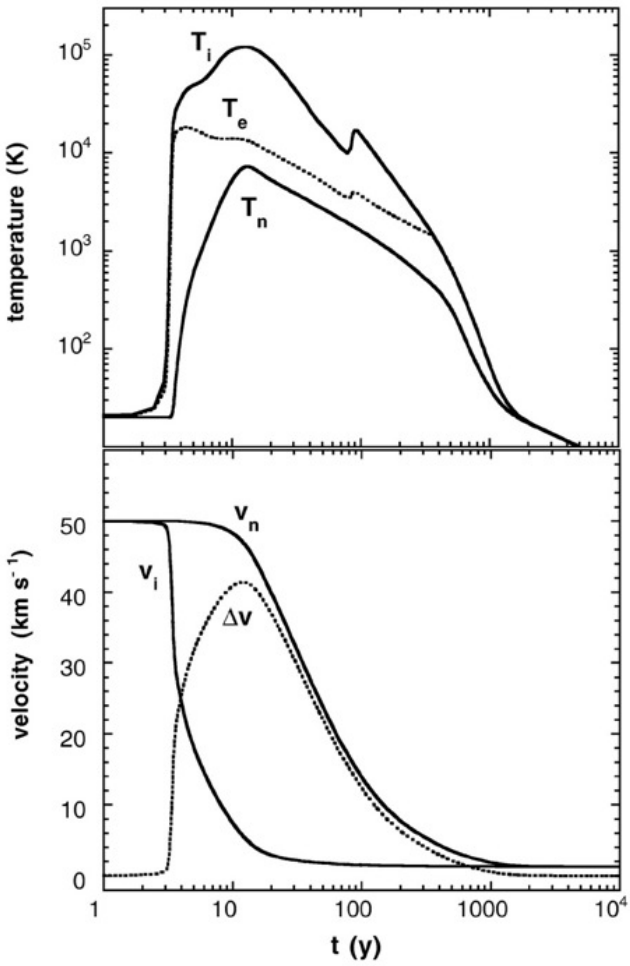

Figure 1.11: Temperature (upper panel) and velocity (lower panel) profiles through a C-type shock wave of speed $v_{\rm shock} = 50$ km s^{-1}, pre-shock density $n_{\rm H} \simeq n({\rm H}) + 2n({\rm H_2}) = 10^4$ cm^{-3} and magnetic induction $B = 100$ μG. The x-axis t correspond to the flow time of the neutral fluid. The subscripts i, n and e stand for ion, neutral and electrons. Taken from Fig. 2 in Flower & Pineau des Forêts (2003).

The contribution of other species to the gas cooling depends on the gas composition (see Figure 1.12).

The models take into account the detailed molecular chemistry occurring across the shock. The erosion of grain mantles and relative motions between ionized and neutral species enhances the abundance of some specific molecules. For example, SiO and HNCO are complementary tracers of shocks in molecular clouds. Fast ($v_{\rm shock}$ >15 km s^{-1}) shocks can destroy the grain cores, liberating refractory elements to the gas phase such as Si to form SiO, while slow ($v_{\rm shock}$ <15 km s^{-1}) shocks can process the icy grain mantles, releasing molecules formed on grains such as H_2CO, CH_3OH and HNCO (Flower & Pineau des Forêts 2003).

In shocks, all levels of H_2 are excited by collisions. However, the interpretation of the H_2 excitation diagram is not simple because the gas temperature varies across

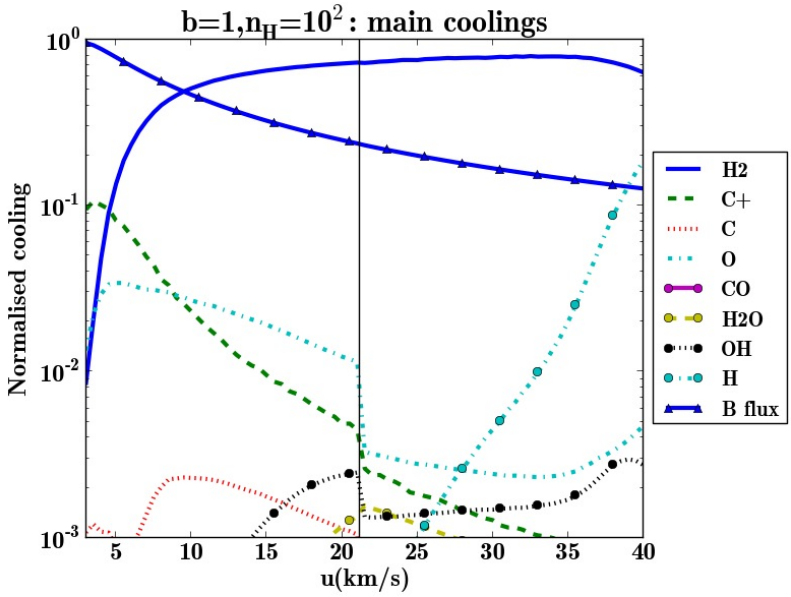

Figure 1.12: Cooling integrated along the wave of a weakly magnetized shock, for a gas density of $n_{\rm H} = 10^2$ cm^{-3}. The color lines correspond to different cooling agents. The H_2 line cooling is the straight blue line. H_2 is the main cooling species for shock velocities commensurate with turbulent motions in molecular clouds. Taken from Lesaffre et al. (2013), their Fig. 8.

the shock. The rotational mid-IR and the ro-vibrational near-IR H_2 lines do not come from the same post-shock gas. Models are needed to interpret the data. They predict line ratios between ro-vibrational lines which are different from those of PDRs. In PDRs, near-IR line emission is dominated by fluorescence following UV excitation while in shocks the gas is hot enough for the vibrational levels to be excited by collisions.

1.5 Star formation

In this section, I introduce the present understanding of star formation from an observer's point of view.

The only galaxies where we can observe the star formation process at small scales (less than a few parsecs) are the Milky Way and the Magellanic Clouds. Galactic observations provide the necessary spatial resolution to isolate the different stages and scales associated with the star formation process. For instance, we can observe the early stages of the formation of single stars (i.e. protostars), and study how YSOs interact with their environment. Figure 1.13 present an example of this. The "Pillars of Creation" is a region in the Eagle star-forming nebula where we observe single protostars.

Extragalactic observations provide a complementary perspective on star formation. These observations may be used to characterize the relation between SFR and gas content for the full diversity of galaxy types.

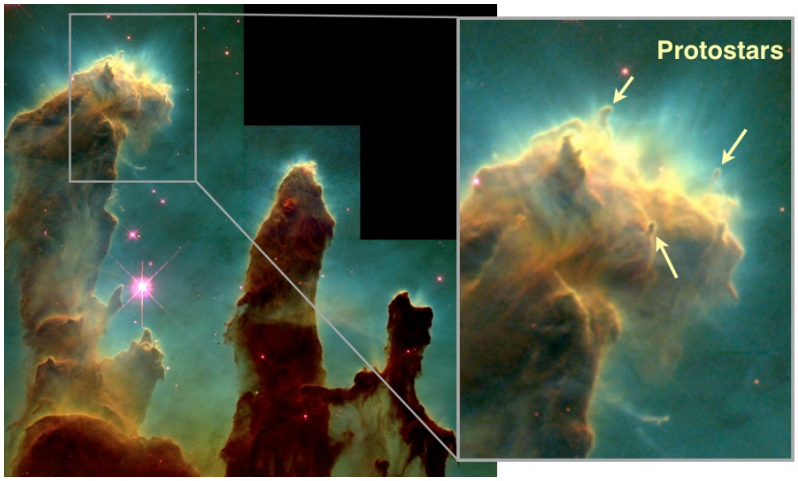

Figure 1.13: Birth of stars in the Pillars of Creation region in the Eagle star-forming nebula, as seen by the HST (at optical wavelengths). It is thought that protostars (or YSO) are located in the center of the photo-evaporated gaseous globules. *Image credit: NASA, ESA, STScI, J. Hester and P. Scowen (Arizona State University).*

1.5.1 Tracing the star formation

Since massive stars ionize their surrounding gas, star formation sites are traced by the emission from ionized gas. The optical and near-IR hydrogen recombination lines are the most common tracers of massive star formation. Among them the most used is Hα, in the visible region of the electromagnetic spectrum. Recombination lines emitting in the near-IR (i.e. Brγ), unlike Hα, trace star formation in dusty regions. The free-free emission (Bremsstrahlung) at radio wavelengths is also a tracer of the star formation. This emission is produced by the scattering of free electrons with ions. The electrons are free before and after the interaction, however, they do exchange energy and momentum with the ion. Far-IR dust emission is an alternative tracer of star formation. Interstellar dust absorbs efficiently the UV radiation from O and B stars. It re-emits this power as continuum emission in the mid and far-IR parts of the electromagnetic spectrum.

1.5.2 Molecular gas, the fuel to form stars.

Star formation is related to the formation and the dynamical evolution of molecular clouds. Molecular clouds form in different ways in different types of galaxies. In galactic disks, the formation of giant molecular complexes is thought to be initiated by gravitational instabilities in spiral arms (Jog & Solomon 1984; Elmegreen 1989). This is supported by observations which show that GMCs are located in the spiral arms (e.g. Stark & Lee 2006; Schinnerer et al. 2010). In irregular galaxies like the Large Magellanic Cloud (LMC), observations show molecular clouds in shells around massive star forming regions. In this context, it is likely that the expansion of wind-blown bubbles and SNRs trigger the formation of molecular clouds. In interacting galaxies, large-scale compression of the gas can trigger gravitational instabilities and

the formation of molecular clouds (Teyssier et al. 2010).

Many observations have been done to quantify the molecular gas content of galaxies. For instance, in the Milky Way by Dame et al. (1987), Solomon et al. (1987) and Dame et al. (2001), and in the Magellanic Clouds by Fukui et al. (2008) and Hughes et al. (2010). With these observations, astronomers have characterized the molecular clouds, the progenitors of stars. They have found that the properties of GMCs (i.e. sizes, velocity dispersions and masses) are correlated. Solomon et al. (1987) present a study of galactic clouds and Bolatto et al. (2008) of extragalactic clouds, where it is shown that the correlations for Galactic and extragalactic clouds are alike.

GMCs have masses within a wide range of values ($\sim 10^4 - 10^6\ M_\odot$, Fukui & Kawamura 2010). One of the main characteristics of an ensemble of molecular clouds within a galaxy is their distribution of masses, which defines the cloud population. Observations show that the distribution of GMC masses may be fitted by a power law:

$$\frac{dN}{dM} \propto M^\alpha, \tag{1.1}$$

where N is the number of clouds that can be found with a mass within M and $M + dM$. The canonical value for α is -1.5. It corresponds to the value for the inner Milky Way (Solomon & Rivolo 1989). This value differs in other environments. In the outer Milky Way and in local Galaxies, α is steeper. It reaches values up to -2.1 for clouds in the outer Galaxy, -1.7 in the LMC and -2.9 in M33 (Rosolowsky 2005). The origin of these differences is not yet understood.

1.5.3 Star formation rate

The rate at which stars are formed out of their parent molecular clouds can be estimated from observations of hydrogen recombination lines or dust emission in the mid and far-IR (Section 1.5.5). The global SFR of galaxies is observed to vary by 3 orders of magnitude, depending on gas content and galaxy type (Section 1.3).

The first observational evidence of the correlation between the gas density and the SFR was given by Schmidt (1959). He found that the SFR surface density $\Sigma_{\rm SFR}$ = SFR/Area and the gas (H I+H_2) surface density $\Sigma_{\rm gas} = M_{\rm gas}$/Area were correlated as $\Sigma_{\rm SFR} \propto \Sigma^2_{\rm gas}$. Later, Kennicutt (1998b) calibrated this relation for a set of normal disk and starburst galaxies. Using both populations, he found that the spectral index is more similar to 1.4. This relationship is the so-called Kennicutt-Schmidt law, which infers a global star formation law:

$$\frac{\Sigma_{\rm SFR}}{M_\odot\ {\rm yr}^{-1}\ {\rm kpc}^{-2}} = (2.5 \pm 0.7) \times 10^{-4} \left(\frac{\Sigma_{\rm gas}}{M_\odot\ {\rm pc}^{-2}}\right)^{1.4\pm0.15}. \tag{1.2}$$

Fig. 1.14 illustrates the correlation between the SFR per unit area and the gas surface density in normal disk galaxies (circles) and starburst galaxies (squares). Starbursts and normal disk galaxies populate different ranges in this relation. From this correlation, it is clear that galaxies with high SFR also present high surface

gas density. Since the relation between SFR and gas density has a slope larger than 1, starburst galaxies turn gas into stars in a more efficient way than normal disk galaxies. Many other studies of the star formation law have been done (see

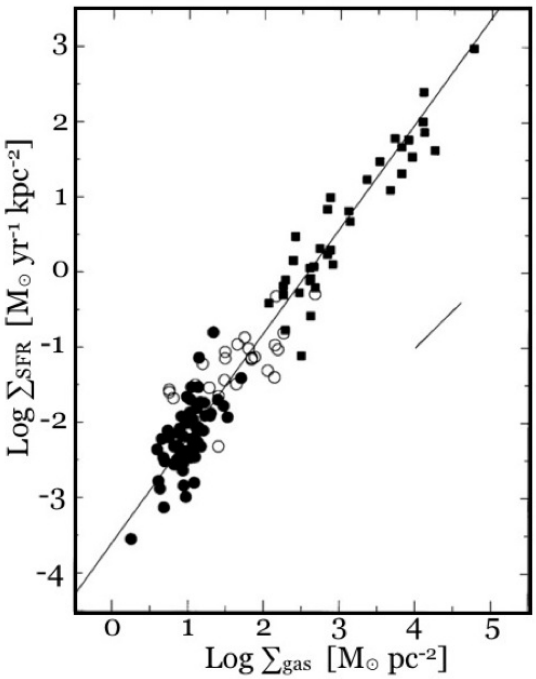

Figure 1.14: Illustration of the Kennicutt-Schmidt law. Gas surface density versus global star formation rate per unit area for normal disk (filled circles) and starburst galaxies (squares). Open circles represent the center of normal disk galaxies. The fit to the observations corresponds to the Eq. 1.2. The short line illustrate the spectral index equals to 2 estimated by Schmidt (1959). Figure adapted from Kennicutt (1998b, his Fig. 6).

compilation by Elmegreen 2011). Bigiel et al. (2008) gathered observations for nearby galaxies (7 spirals and 11 H I-dominated dwarfs). They found two different correlations, for gas surface densities larger and smaller that $\sim 10\,M_\odot$ pc^{-2}. For values of Σ_{gas} smaller than this threshold, all the gas is atomic. The threshold value corresponds to the transition from H I to H_2. For H I the relation is not linear, the index is more or less 1.5. For H_2 the relation is linear. This study suggests that H_2 forms stars with the same efficiency for all normal galaxies.

1.5.4 Overview of the star formation process

Within molecular clouds, we can observe the different stages of the star formation process: molecular clouds which have not yet formed stars and may still be accreting matter from the diffuse ISM, pre-stellar cores where stars will form, H II regions produced by embedded massive stars, and last, evolved star clusters still associated with their parent clouds. Figure 1.15, adapted from Fukui & Kawamura (2010), illustrates this process coming from observations.

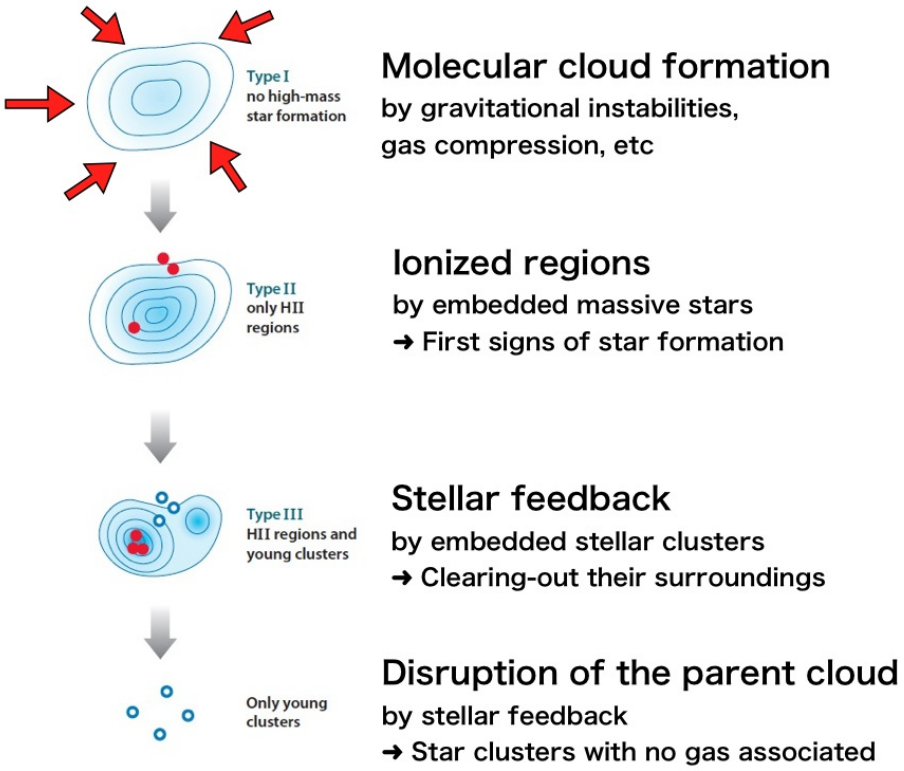

Figure 1.15: Evolutionary sequence of molecular clouds. Figure adapted from Fukui & Kawamura (2010). Blue emission represents the molecular gas. Red and open blue circles correspond to H II regions and young stellar clusters, respectively. From top to bottom: The formation of molecular clouds through gravitational instabilities or other triggering mechanisms. Newly formed stars ionize their surrounding creating bubbles of ionized gas, H II regions. The newly formed stars disrupt their parent molecular cloud. At the end of this evolutionary process, all of the molecular cloud is photo-ionized or photo-dissociated, and expelled back to the ISM by stellar feedback.

In a given cloud, different regions may be at different stages of this evolutionary scheme as illustrated in Figure 1.16, borrowed from Klessen (2011). Turbulence creates a hierarchy of clumps within the molecular cloud. Where turbulence is dissipated, the matter collapses to form stars. This does not occur at the same time everywhere across the cloud. Once massive stars are formed they have a global impact on the molecular cloud. Eventually, stellar feedback disrupts the cloud and stops star formation. The newly formed embedded stellar clusters impact their surroundings in several ways. Gas ionization creates regions of high pressure that expand. Stellar winds and supernova explosions can also contribute to push matter away. The impact of radiation is also important. UV light photodissociates molecules and radiation pressure can be the main force pushing matter away (Krumholz & Matzner 2009; Murray et al. 2010; Lopez et al. 2011). The end result of feedback, is a star cluster that has dispersed its parent molecular cloud. The image in Figure 1.16 represents the open cluster NGC 602, which is close to having dispersed all of its parent cloud.

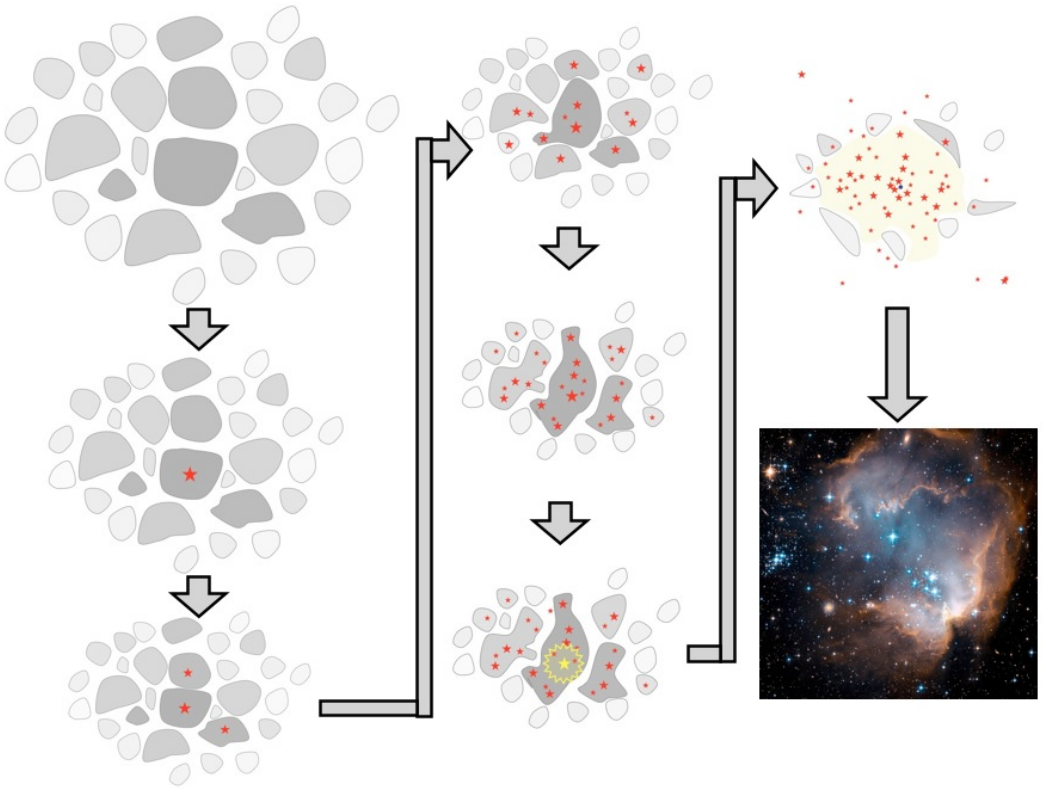

Figure 1.16: Formation of a stellar cluster from a turbulent molecular cloud. The shaded areas correspond to fragmented molecular gas, where the grey scale represent its density (more dense more obscured). Red stars correspond to newly formed stars. Yellow star represent the ionizing stars that stop the star formation through stellar feedback. Light yellow area is the ionized region surrounding the stellar cluster. The color figure is an astronomical object (NGC 602) to be compared with the cartoon diagram. Figure adapted from Klessen (2011).

1.5.5 Star formation efficiency

Stars form by gravitational fragmentation and collapse of gas within GMCs. It is a cloud of an ideal gas. For the gas to collapse, the gravitational force must dominate all opposing forces. If we consider only the competition between gravity and gas thermal pressure, for a spherical cloud of radius R, mass M and temperature T, the condition for collapse is:

$$\frac{3GM^2}{5\,R} > 3\,N\,k_{\rm B}\,T. \tag{1.3}$$

For an homogeneous cloud of density ρ, the radius is

$$R = \left(\frac{M}{4/3\pi\rho}\right)^{\frac{1}{3}}. \tag{1.4}$$

Thus, this balance leads to critical values for the mass and the radius, the so-called Jeans mass $M_{\rm Jeans}$ and radius $R_{\rm Jeans}$ (Jeans 1902). The gravitational collapse will

occur after gathering a Jeans mass of:

$$M_{\rm Jeans} = \left(\frac{5\,k_{\rm B}\,T}{G\,\mu\,m_{\rm H}}\right)^{3/2} \times \left(\frac{3}{4\,\pi\,\rho}\right)^{1/2}. \tag{1.5}$$

The Jeans mass depends on the gas temperature and density. The collapse will occur in a free-fall time-scale, $\tau_{\rm ff}$:

$$\tau_{\rm ff} = \sqrt{\frac{3\,\pi}{32\,G\,\rho}} = 3.6 \times 10^7 \times \sqrt{\frac{1}{n_{\rm gas}}}\ {\rm yr}. \tag{1.6}$$

For molecular clouds with typical densities of about 10^{2-3} cm^{-3}, the free-fall time is about 1 Myr. For the gas densities and temperatures listed in Table 1.2, the Jeans mass is $M_{\rm Jeans} \sim 150\ M_{\odot}$, a value much smaller than masses of GMCs (e.g. Blitz 1993; Heyer et al. 2009). Thus, clouds should be collapsing and forming stars efficiently. However, this is not what observations indicate. The average of star formation efficiency in the Milky Way is low. Only a few percent of the molecular gas is converted into stars in a free-fall time (Murray 2011).

Why only some of the observed molecular clouds form stars and others not?
This is a much debated question since GMCs were discovered in the early eighties. The Jeans criterion only takes into account gravity and gas thermal pressure. Astronomers have tried to account for the observations by introducing magnetic and turbulent pressures to prevent the cloud collapse. For much time it was thought that star formation is controlled by the rate at which material can escape the magnetic support by ambipolar diffusion (Mouschovias 1991; Bertoldi & McKee 1992). Observations and numerical simulations are challenging this view. Today, there is an increasing consensus that the lifetime of molecular clouds is much less than has been previously assumed, and that molecular clouds form, produce stars and disperse all within a few dynamical timescales. Within this new paradigm, turbulence regulates star formation.

In the next section, I introduce the concept of turbulence and its role in the ISM.

1.6 The role of turbulence

Turbulence is everywhere! Figure 1.17 gives examples of turbulence in diverse natural contexts: a pan of boiling water; the smoke from an ignited match; ocean waves, portrayed in an ancient woodblock printing; clouds in the Earth's atmosphere shaped by Kelvin-Helmholtz instabilities[8]; solar magnetic flares; outflowing gas in the starburst galaxy M82. In the following, I focus on interstellar turbulence.

1.6.1 Interstellar turbulence

A general account of the importance of turbulence in astrophysics was given by Chandrasekhar (1949) where he suggested that the motions inside interstellar clouds

[8]This instability occurs when there is a velocity shear in a fluid.

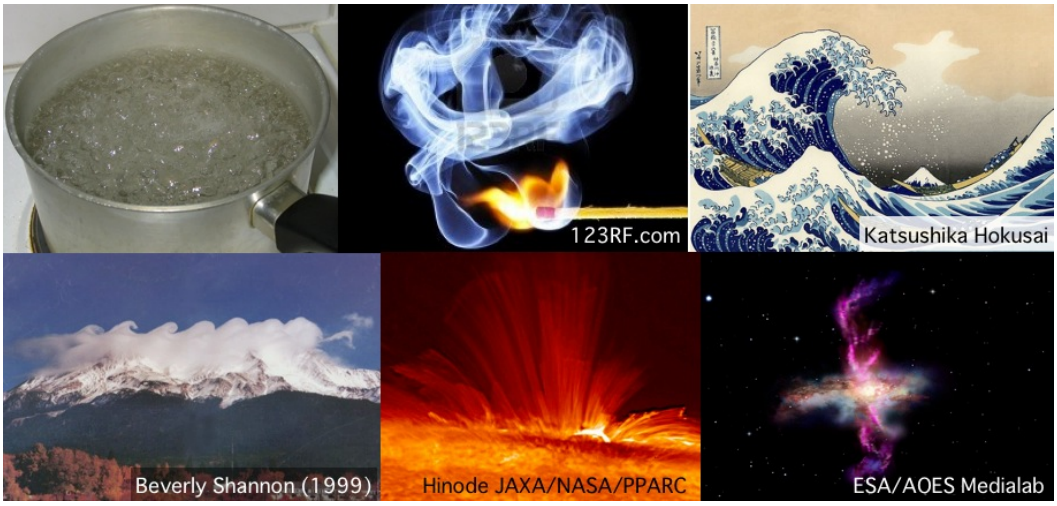

Figure 1.17: Examples of turbulence in nature. From small scales (in your own kitchen!) to astronomical scales.

must be turbulent because the Reynolds number[9] is high (10^5). The Reynolds number depends on the characteristic length of the flow (largest turbulent fluctuation) L, the flow velocity at that scale v_s and the kinematic viscosity ν_s, $Re = \frac{v_\mathrm{s}\, L}{\nu_\mathrm{s}}$. Chandrasekhar introduced a visionary idea, which is today widely accepted, saying *we may regard the clouds of various dimensions in interstellar space as eddies in a medium occupying the whole of galactic space.* Quoting him again, he describes turbulence in these terms: *in a turbulent medium there are eddies which spontaneously form and disintegrate; this process goes on continuously; each eddy travels a certain average distance with a certain average speed before it looses it identity.*

1.6.2 Turbulent energy cascade and dissipation

In turbulence, motions at various scales are coupled. The multi-scale nature of turbulence was first introduced by Richardson (1922). Kolmogorov (1941) described in dimensional terms the energy cascade across scales. The energy injected on the scale of the largest eddies decays into smaller eddies down to the scale where dissipation occurs (Figure 1.18). For incompressible turbulence, the rate at which energy is transferred is constant across scales.

In molecular clouds turbulence is characterized by observations which establish scaling laws between the gas velocity dispersion and the cloud size. Larson (1981) was the first to highlight the existence of scaling laws in molecular clouds. Many papers have now added information on these laws (e.g. Bolatto et al. 2008; Heyer et al. 2009). Figure 1.19 shows the relation between velocity dispersion and size for galactic and extragalactic GMCs, where is observed that the amplitude of turbulent

[9]The Reynolds number corresponds to the ratio between the convection and the viscous terms in the Navier-Stokes equation for incompressible flows. Laboratory experiments show that flows become turbulent for Reynolds number larger than about a few thousand.

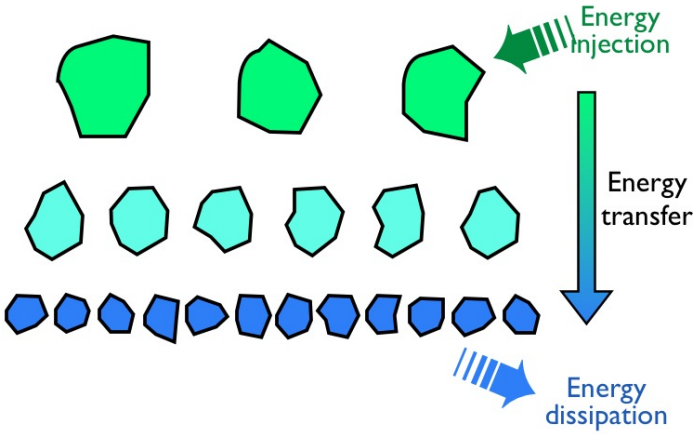

Figure 1.18: This diagram illustrates the cascade of kinetic energy in turbulent flows. Kinetic energy injected on large scales is transferred to smaller scales down the scale where dissipation occurs.

motions σ_v increases with the cloud radius R as $\sigma_v \propto R^{1/2}$.

The turbulent motions in molecular clouds are supersonic. For a temperature of $T = 20$ K, the sound speed is

$$c_{\rm s} = \sqrt{\frac{\gamma\, k_{\rm B}\, [T/20\ {\rm K}]}{\mu\, m_{\rm H}}} = 0.3\ {\rm km\ s^{-1}} \tag{1.7}$$

where γ is the adiabatic index. I have used a value of $5/3$ which is appropriate for cold molecular gas. This value is much smaller than turbulent motions observed in GMCs (Figure 1.19). In supersonic turbulence, unlike in the Kolmogorov theory of incompressible turbulence, dissipation can occur at all scales in shocks. This may explain why the observed spectral index of the velocity scaling law of $1/2$ is larger than the value of $1/3$ for Kolmogorov turbulence.

Dissipation can also occur in vortices (Godard et al. 2010) through ion-neutral friction like in C-shocks (Section 1.4.2.2). The relative importance between shocks and vortices depends on the distribution of energy between compressible and incompressible modes, and thereby the nature of the forcing of turbulence (Federrath et al. 2010). In vortices, like in shocks, H_2 is the main cooling agent of gas heated by dissipation of mechanical energy.

The turbulent energy of interstellar clouds dissipates over a dissipation time scale comparable to the cloud crossing time $t_{\rm cross} = R/\sigma_v$ (McKee & Ostriker 2007). The existence of turbulent motions implies continuous supply of energy to balance dissipation over this time scale. In star-forming clouds, the energy may come from stellar feedback (Tan et al. 2006; Krumholz et al. 2006). Mass accretion can also drive turbulence (Klessen & Hennebelle 2010). On larger scales, galactic dynamics are also a source of kinetic energy that can drive turbulence. In rotating disk galaxies, simulations indicate that gravitational and thermal instabilities under the influence of galactic rotation contribute to the formation of the turbulent velocity

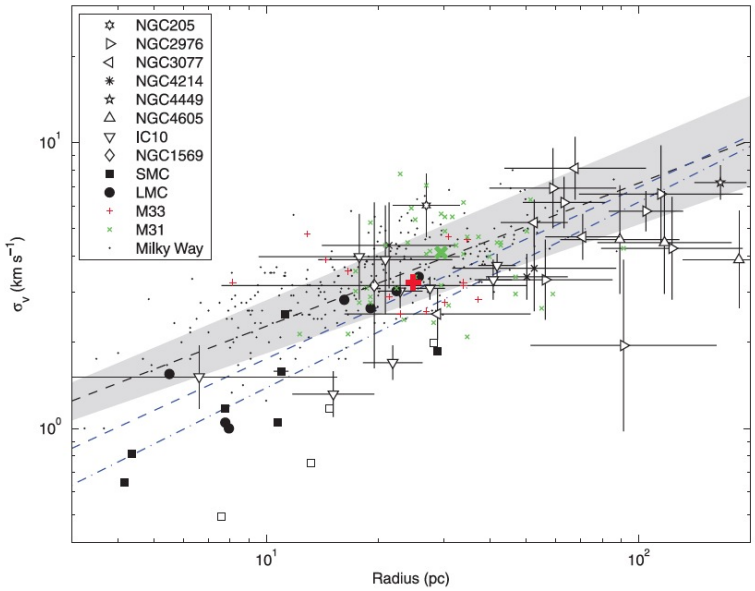

Figure 1.19: Velocity dispersion-size relation for galactic and extragalactic GMCs. The canonical relation found in galactic molecular clouds, $\sigma_v \propto R^{0.5}$, which is marked as the shaded area including uncertainties. From Bolatto et al. (2008).

field. Together with the self-gravity of the gas, they can be the energy sources which drive turbulence in the ISM of galaxies (e.g. Wada et al. 2002).

Hydro and MHD simulations of interstellar clouds suggest that turbulence plays a dual role in star formation. On the one hand, it prevents clouds to collapse globally. On the other hand, shocks create density enhancements that allow local collapse. In several papers the results of simulations are integrated into an analytical theory of star formation. These models quantify the star formation rate as the function of three main parameters, the virial parameter, the sonic Mach number and the Alfvén Mach number[10] (Krumholz & McKee 2005; Padoan & Nordlund 2011; Hennebelle & Chabrier 2011). Federrath & Klessen (2012) also discuss the impact of the turbulent forcing parameter[11]. All models agree that turbulence can account for the low SFE observed in molecular clouds (Section 1.5.5).

1.7 Aim and structure of this thesis

Within the broad astrophysical context I have introduced, in my thesis I address the two following questions:

(1) **How do the large-scale dynamics of galaxy interactions trigger star formation on much smaller scales?**

[10] The ratio between the turbulent velocity on large scales and the Alfvén speed. The Alfvén velocity is the velocity at which magnetic perturbations propagate in the direction of the magnetic field.

[11] Measure of the the ratio of compressible-to-solenoidal modes in the velocity field.

(2) **What is the impact of the stellar feedback from super-star clusters on their surrounding matter?**

To do that, I study one emblematic example of galaxy merger in the local Universe, the Antennae galaxies. This galaxy pair is close enough to resolve star-forming structures with ground-based telescopes. The investigation that I have done during my three PhD years is mainly based on the analysis of two tracers of the molecular gas. The combination of these two tracers is key to my work.

(a) **Molecular mass.** I use CO observations to trace the distribution and kinematics of molecular gas.

(b) **Energy dissipation.** I use H_2 line emission to trace the rate at which the gas mechanical energy is dissipated. The H_2 observations also provide information on the gas kinematics.

My manuscript is structured as follows. In Chapter 2, I present the Antennae galaxy merger where I summarize the most significant observational results and numerical simulations. I present the observations I have worked on and my observational results in Chapter 3. In Chapter 4, I argue that the H_2 emission traces the dissipation of turbulent kinetic energy. Chapter 5 proposes an interpretation where the loss of turbulent kinetic energy associated with the formation of gravitationally bound gas within convergent gas flows driven by the galaxy interaction. In Chapter 6, I quantify the different feedback processes using data on a super stellar cluster still embedded in its parent molecular cloud. A summary of the results and conclusions obtained in my PhD work are provided in Chapter 7, where I also detail some perspectives for future research. In Appendix A I introduce a recently identified source which is not included in the main chapters of the thesis. Appendix B includes my two refereed publications. Appendix C presents the press release of the results of my second paper which uses ALMA data. Finally, Appendices D and E list the physical constants and their abbreviations that were used through this thesis.

Chapter 2

The Antennae galaxies

Contents

Figure 2.1: The Antennae galaxy merger, located in the Corvus constellation. In the left panel, as seen by a ground-based telescope (*Image credits: R. Gendler*) and, in the right panel, a zoom onto the central part taken with the HST. The northern and southern galaxies are NGC 4038 and NGC 4039, respectively. Image is composed by the emission observed in the filter F435W (broadband, ∼B) in blue, F550M (medium-width filter, ∼V) in green, and the combinations of F819W (broadband, ∼I) and Hα in red.

The Antennae galaxy merger (also known as NGC 4038/39, Arp 224) is one of the most outstanding objects in the local Universe. Discovered by W. Herschel in

1785, the Antennae consist of two gas-rich interacting spiral galaxies (see Fig. 2.1), the northern galaxy NGC 4038 at $\alpha : 12^{\rm h}01^{\rm m}53\overset{\rm s}{.}0$, $\delta : -18°52'10''$ and the southern galaxy NGC 4039 at $\alpha : 12^{\rm h}01^{\rm m}53\overset{\rm s}{.}6$, $\delta : -18°53'11''$ (coordinates extracted from NED[1]). At a distance of 22 Mpc (Schweizer et al. 2008), and with a nearly face-on geometry, the Antennae are one of the best studied mergers. They were named 'the Antennae' because of their prominent tidal arms which resemble the antennae of an insect (see left panel in Fig. 2.1).

2.1 The molecular gas in the overlap region: super-giant molecular complexes

Observations of the molecular gas content in the Antennae galaxy merger date back to the mid-1980s when Sanders & Mirabel (1985) pointed the 12 m NRAO single-dish telescope to this merger. With a beam of FWHM $\sim 60''$, they quantified the total CO emission of the pair. A few years later, IRAS observations revealed that mergers of gas-rich galaxies are IR-luminous. In the Antennae, the merger triggers not only nuclear star formation. With that idea in mind, Stanford et al. (1990), using the Owens Valley Radio Observatory (OVRO), observed the Antennae with much higher angular resolution than before (FWHM = $6''$). These interferometric observations revealed that the CO emission is concentrated in three regions, the two nuclei and the "overlap region" where the two galaxies are colliding (see Fig. 2.2). At the end of the nineties, ISO observations revealed bright mid-IR emission from the overlap region in the Antennae, confirming the importance of star formation activity outside the nuclei (Mirabel et al. 1998). A little earlier, HST observations have revealed the presence of a large number of massive star clusters, dubbed Super Star Clusters (SSCs), in the Antennae pair (Section 2.2). These new data motivated new high-resolution observations of CO to determine the spatial distribution and the kinematics of the molecular gas. Wilson et al. (2000, 2003) presented the observations of the Antennae merger in the CO$(1-0)$ transition at 115 GHz. These observations were obtained with the OVRO interferometer between 1998 and 1999, with a final synthesized beam size of $3\overset{''}{.}15 \times 4\overset{''}{.}91$ (336 pc $\times$ 524 pc at the distance of the Antennae). The channel size of these observations was 5.2 km s^{-1}, and the sensitivity in one channel was 0.33 K.

The new CO observations revealed that the molecular gas in the overlap region fragments into Super-Giant Molecular Complexes, SGMCs. Fig. 3.17 presents the CO$(1-0)$ emission in the Antennae, in which the SGMCs are labeled. The brightest CO emission is found in both nuclei and in the overlap region, where the SGMCs are located. About 50% of the total CO emission comes from the overlap region. There is some CO emission in the western spiral arm of NGC 4039. The SGMCs with masses larger than 10^8 $M_\odot$ are larger and more massive than GMCs observed in normal galaxies, as the Milky Way.

[1] http://ned.ipac.caltech.edu

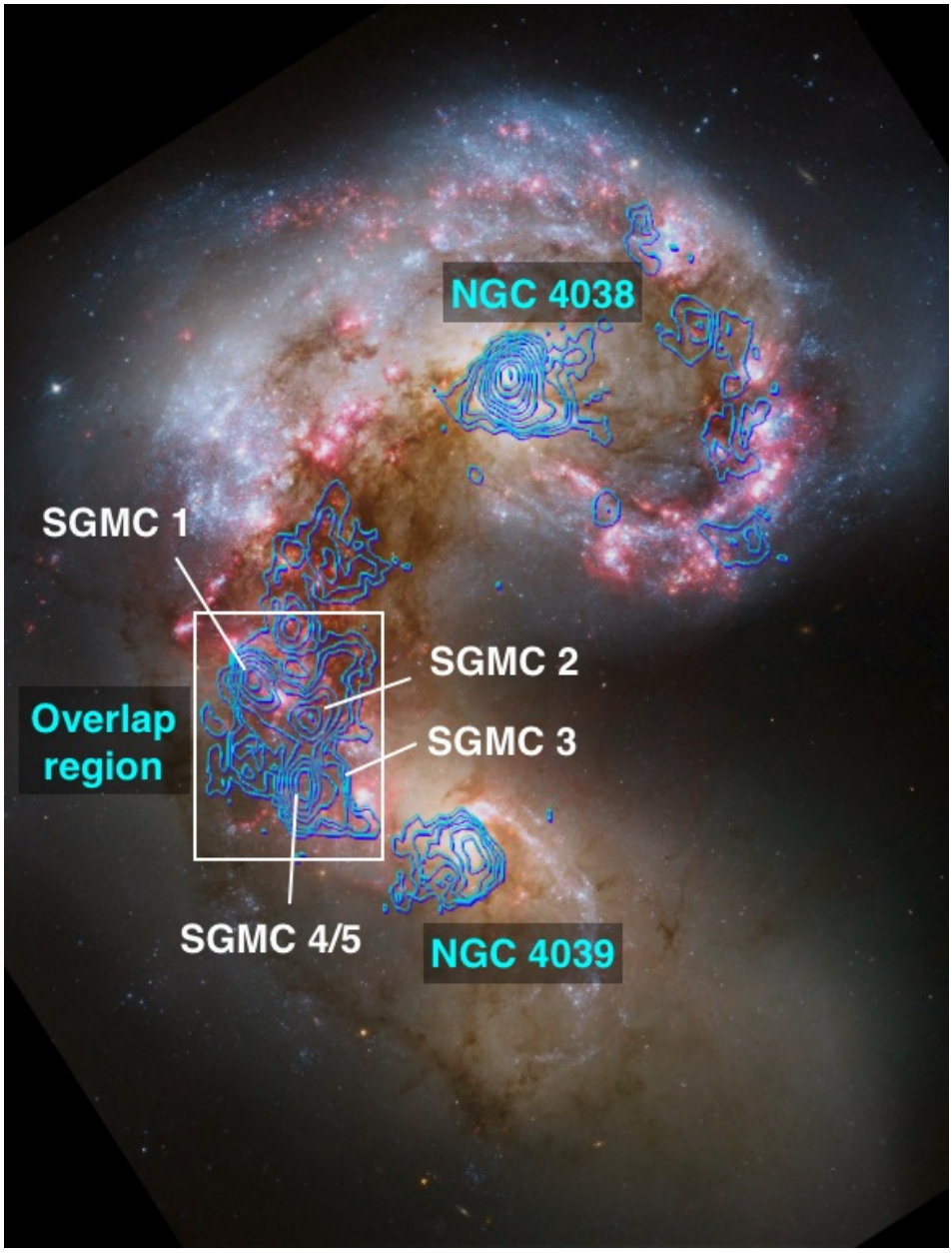

Figure 2.2: Super Giant Molecular Clouds in the Antennae galaxy merger. The color image corresponds to the HST image presented in Fig. 2.1. Contours are extracted from Wilson et al. (2000) and correspond to CO(1−0) emission obtained with the OVRO interferometer. Both nuclei and the overlap region between them are highlighted. I indicate the location of the SGMCs which were first identified by Wilson et al. (2000). The white box highlights the overlap region.

Ueda et al. (2012) showed the distribution of the $CO(3-2)$ emission line from observations obtained with the Submilimeter Array (SMA), with an angular resolution of $\sim 1''$. $CO(3-2)$, that traces warmer gas than $CO(1-0)$, is clumpy and it presents a complex velocity structure (Fig. 2.3). Wei et al. (2012) presented $CO(2-1)$ observations of the Antennae galaxies obtained with the SMA and the

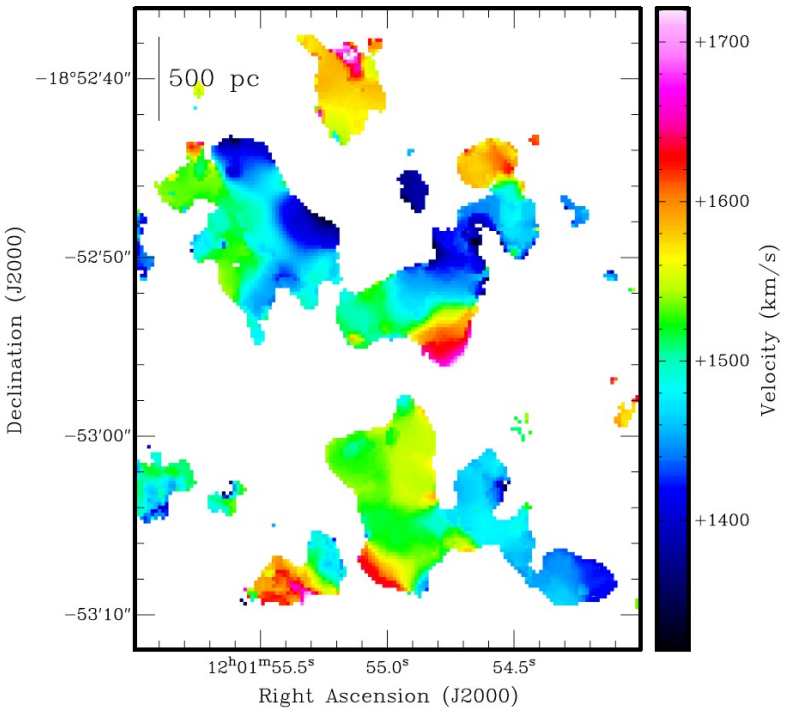

Figure 2.3: CO(3−2) velocity field of the Antennae overlap region, observed with the SMA. Taken from Ueda et al. (2012).

Plateau de Bure (IRAM). These observations have an angular resolution of 1.″5. The authors report a distinct break in the mass function around $log(M/M_{\odot}) \sim 6.5$, which separates the molecular clouds into two distinct populations. The smaller, less massive clouds reside in more quiescent areas, while the larger, more massive clouds cluster around regions of intense star formation.

2.2 The star formation: super-star clusters

In the Antennae galaxies, most of the recently formed stars are observed in SSCs. The masses of SSCs identified with HST and ground based follow-up observations are in the range between a few 10^4 to several 10^6 $M_{\odot}$. The larger masses are two orders of magnitude higher than those of stellar clusters in quiescent galaxies like the Milky Way. One of the closest nearby examples of massive stellar clusters is the R136 cluster in the 30 Doradus nebula in the Large Magellanic Cloud, which has a mass of $\sim 5 \times 10^4$ $M_{\odot}$, a core size of 0.5 pc and an age of $\sim$ 3 Myr (Hunter et al. 1995).

One of the first studies of stellar clusters in the Antennae galaxies was done by Whitmore & Schweizer (1995). By analyzing observations obtained with the *Wide Field Camera* (WFC) on board the *Hubble Space Telescope*, they detected more than 700 objects in the visible range that they identified as young star clusters. The age of SSCs range from a few to a few hundred Myr. They must have formed at different

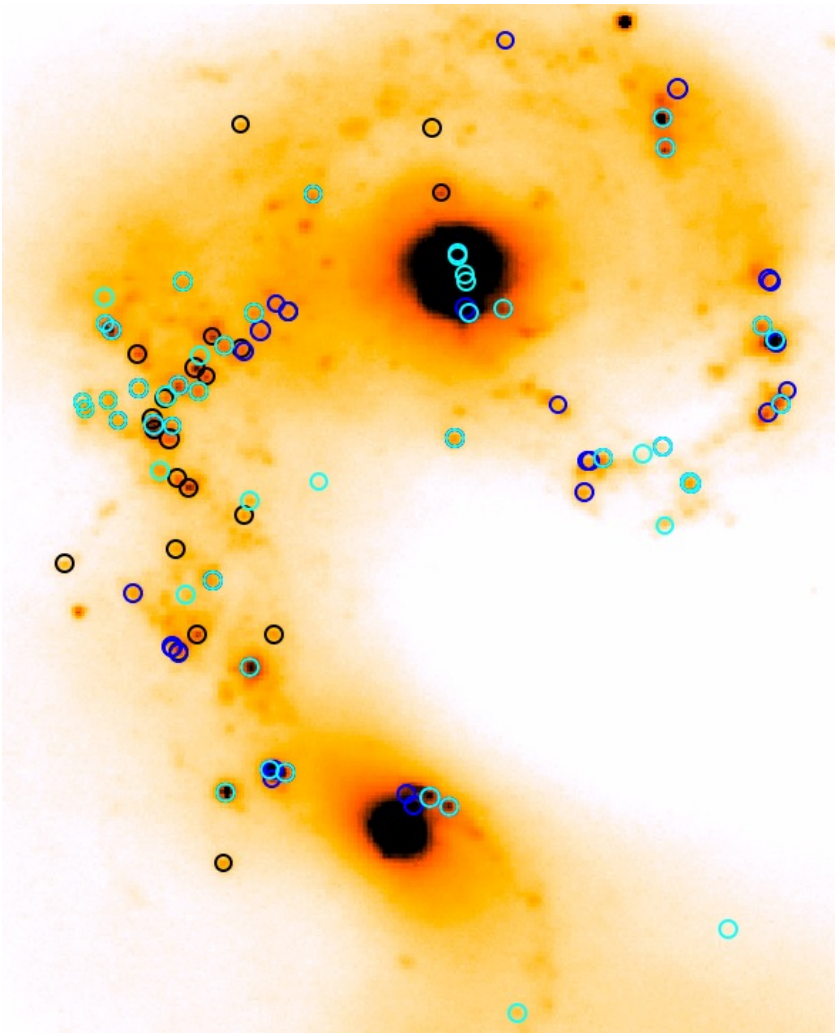

Figure 2.4: Super stellar clusters in the Antennae galaxy merger, listed in Table 7, 8 and 9 of Whitmore et al. (2010). Cyan, blue and black circles represent the most massive ($> 5 \times 10^5$ $M_\odot$), optical luminous and IR luminous SSCs.

stages of the merging process (Whitmore et al. 1999). It is not straightforward to infer the star-formation history from the age distribution of clusters, because a large fraction of them do not remain bound (Mengel et al. 2005). The median age of the clusters is about 10 Myr, which Fall et al. (2005) interpret as evidence for rapid disruption of the clusters. The youngest clusters seems to be located in the overlap region. Mengel et al. (2005) studied the infrared images obtained with ISAAC at the VLT and SOFI at the NTT. These observations gave a good statistics of the SSCs in the Antennae, confirming that most of the massive ($\geq 10^5$ $M_\odot$) stellar clusters are younger than 10 Myr and are located in the overlap region. With the Near Infrared Camera and Multi-Object Spectrometer (NICMOS) mounted on the HST, Whitmore et al. (2010) were able to better distinguish between individual stars and stellar clusters than what was done with the earlier WFC observations.

Figure 2.4 shows the position of these SSCs in the Antennae. They estimated that the distribution function of the cluster masses follows a power-law with a spectral index of $\beta = -2.1$[2].

2.3 The Antennae across the electromagnetic spectrum

The Antennae galaxies are amongst the best studied galaxy mergers in the local Universe, and they have been observed at almost all wavelengths.

Chandra observations revealed spatially and spectrally complex *X-ray* emission from the Antennae. About 120 point-like X-ray sources are identified (Fabbiano et al. 2004; Zezas et al. 2006). About 40 of these sources are associated with IR-stellar clusters (Clark et al. 2011). Some of the emission is diffuse emission from hot plasma showing large bubbles that may have been created by the starburst. Figure 2.5 displays the X-ray Chandra observations.

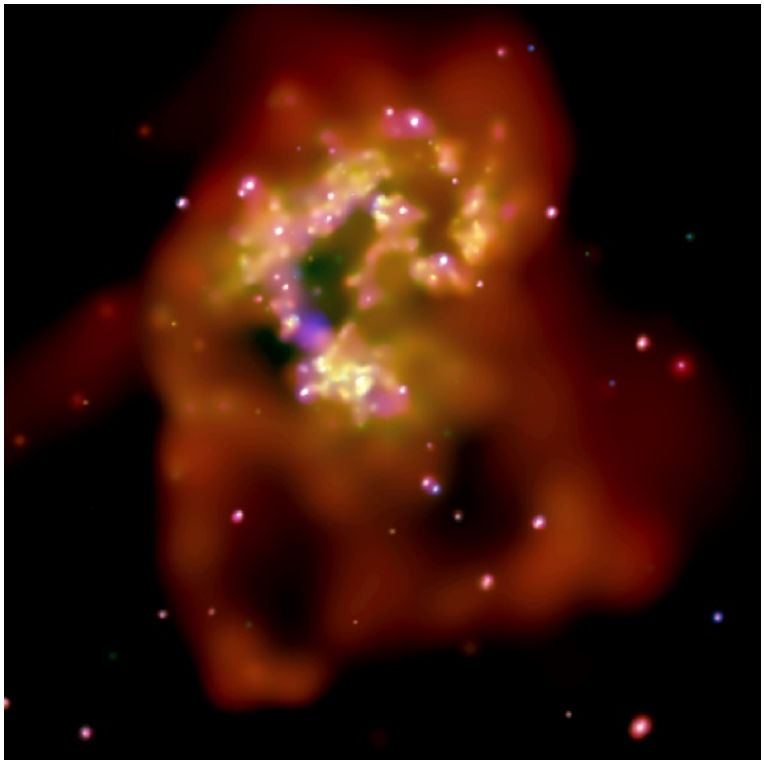

Figure 2.5: Composite image of the X-ray emission observed with Chandra. The red, green and blue emission correspond to low, medium and high energy X-rays, respectively. The image reveals loops of hot gas spreading out from the Antennae southern part into the intergalactic space, large clouds and bright point-like sources. *Credit: NASA/CXC/SAO/Fabbiano et al. (2004).*

The emission in the *optical* captured by the HST, displayed in Figure 2.1, shows the starlight emission from the whole galaxy pair and the zones obscured by the interstellar dust.

[2]Mass function defined as a single power law $dN/dM \propto M^{\beta}$

Infrared observations with the Infrared Space Observatory (Mirabel et al. 1998), the Spitzer Telescope (Brandl et al. 2009) and the Herschel Space Telescope (Klaas et al. 2010) revealed the location of newly formed massive stars, which are heating their surrounding gas and dust (see Figure 2.6). In the mid- and far-IR we see dust emission. The overlap region is the brightest region in this pair. Spitzer spectroscopic observations showed that warm molecular gas, traced by the mid-IR rotational transitions of H_2, is concentrated in the overlap region (Brandl et al. 2009).

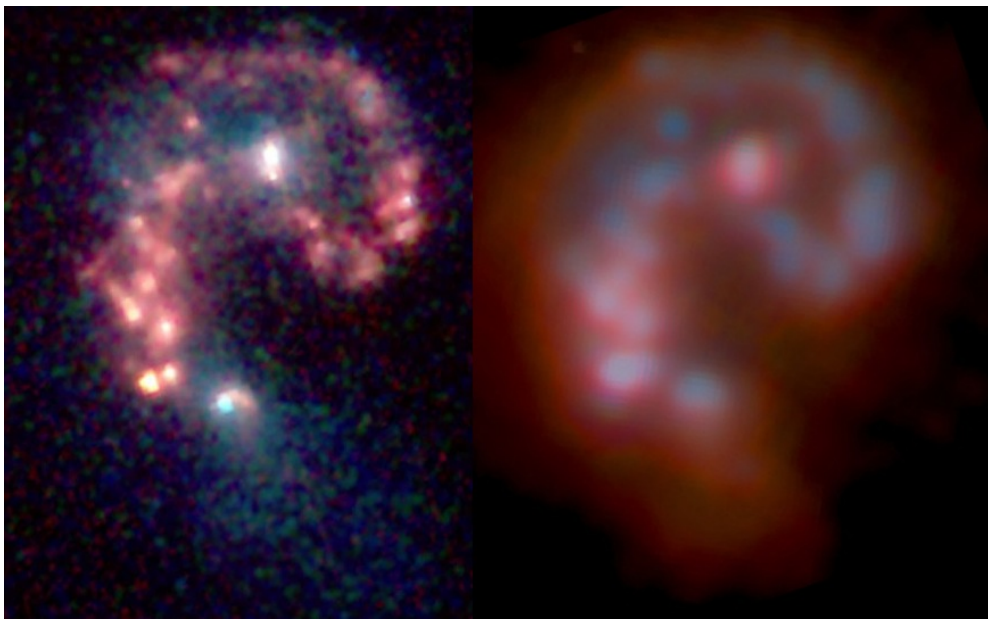

Figure 2.6: IR emission from dust reveals the sites of star formation in the overlap region. *Left image:* IR composite image of the Antennae galaxies observed by Spitzer. Colors represent the emission ranging from 3.6 microns (shown in blue) to 8.0 microns (shown in red). *Image credit: NASA/JPL-Caltech/Z. Wang (Harvard-Smithsonian CfA). Right image:* the far-IR emission as observed by Herschel/PACS, composed by dust emission at 70, 100 and 160 μm in blue, green and red, respectively. *Image credit: ESA / PACS / SHINING / U. Klaas.*

Radio observations at 4 and 6 cm obtained with the *Very Large Array* were presented by Neff & Ulvestad (2000). These observations showed diffuse as well as compact emission (see Figure 2.7). One third of the compact sources are associated with H II regions, thermal radio emission. The other sources have a non-thermal emission spectrum. They are likley to be supernovae remnants. The strongest thermal compact sources are all associated with mid-IR sources.

Hibbard et al. (2001) presented *centimeter* observations of the Antennae at low angular resolution (40″). They observed H I in its hyperfine structure line at 21 cm. These observations display the distribution and kinematics of diffuse atomic gas over the galaxy disks and the overlap region. They show a good correspondence of the H I tidal tails with optical observations (Figure 2.8).

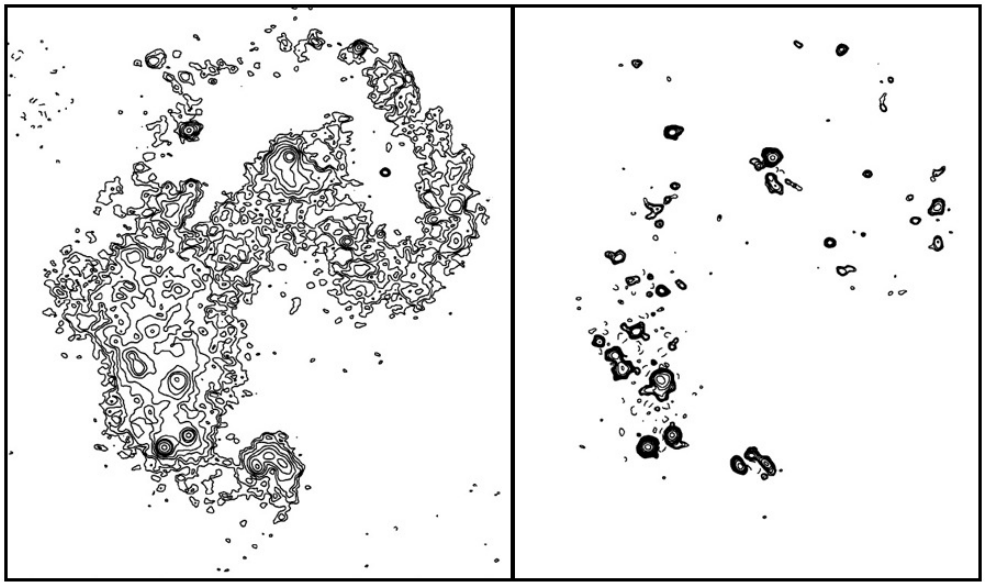

Figure 2.7: Radio emission at 6 cm as observed with the VLA. The left image shows the total emission at 6 cm, where diffuse gas is observed. The right image present a high filter of the total emission at 6 cm, revealing the compact emission. From Neff & Ulvestad (2000).

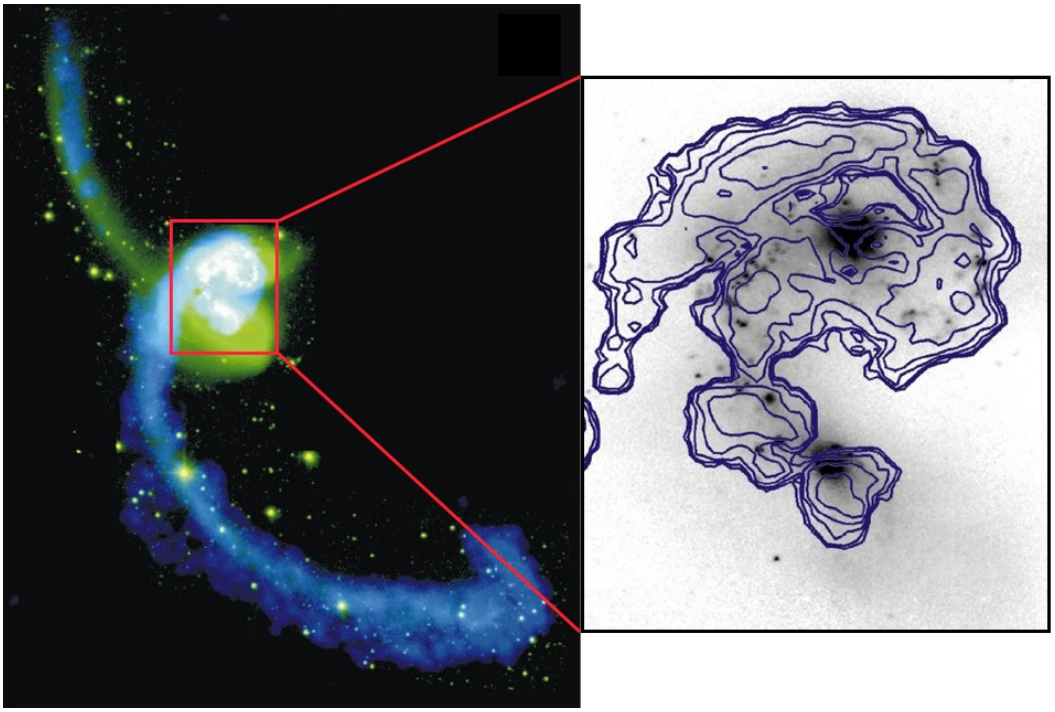

Figure 2.8: *Left image:* Large-scale distribution of the H I emission. The blue color represents the H I emission, and green and white are a combined image using the filters B, V and R. The diffuse H I emission extends over the whole interacting disks and the tidal arms. *Right image:* Details of the H I emission in the disks. Contours represent the H I (21 cm emission), which is overlaid on a K-band image. From Hibbard et al. (2001).

2.4 Numerical simulations

Historically, simulations of galaxy mergers were first done to reproduce their morphologies (e.g. Toomre & Toomre 1972). Later, H II observations provided kinematic information which allows to better constrain the merger parameters and history (e.g. Karl et al. 2010). The most recent hydrodynamical simulations also include the multiphase ISM in an attempt to account for the observed properties of the star formation. In this section, I briefly introduce the history of the numerical simulations based on the Antennae galaxy merger, until their current state.

Toomre & Toomre (1972) performed the first numerical simulation to reproduce the morphology of the Antennae galaxy, among other mergers. The aim of these simulations was to reproduce the long tails of the Antennae that are seen in visible light (left panels in Figures 2.1 and 2.8). Based on 3-body simulations, Toomre & Toomre (1972) found that this morphology could be recovered by assuming an interaction of two galaxies with the same mass which are slightly past apocenter[3] passage. The long visible tails are the result of gravitational tidal effects. Barnes (1988) presented the first 3-dimensional N-body simulation of interacting galaxies including bulge, disks and massive halos. They corroborated the importance of gravity in forming such tidal tails.

Almost 40 years after the first attempt to model the Antennae galaxy merger, computers now allow to do numerical simulations including gas physics down to the size of star-forming regions. At the same time, high angular resolution observations have become available. Both simulations and observations allow us to study the impact of the large-scale galaxy dynamics on star formation.

Renaud et al. (2008) fairly recently performed N-body stellar simulations designed to match the Antennae morphology. They showed that, at pericenter passage[4], a significant fraction (about 15%) of the disk material undergoes compressive tides. This must play a role in accounting for the present efficiency of star formation in the Antennae. The correlation between compressive modes and star formation is illustrated in the upper panel in Fig. 2.9. The time interval spent by individual particles embedded in a compressive mode follows a log-normal distribution of characteristic time $\tau \sim$10 Myr.

Karl et al. (2010) made N-body+hydrodynamical simulations (stars plus gas) including radiative cooling, star formation, and feedback from Type II SNe, to study star formation in relation to the merger history. Their simulation reproduces remarkably well the velocity field of the gas as measured with H I observations. Figures 2.10 and 2.11 illustrate the comparison of the H I observations presented by Hibbard et al. (2001) and their simulation. The simulations and the H I data highlight regions where the galaxies interaction is driving converging flows of matter. The high observed SFR of 20 $M_{\odot}$ yr^{-1} (Zhang et al. 2001) is obtained in a particular moment: in a 20 Myr time interval around the pericenter passage. Karl et al. (2011) compare the SFR time dependence in recent numerical simulations of the Antennae.

[3]The furthest point in the orbit between both galaxies

[4]The closest approach between both galaxies during the merger process.

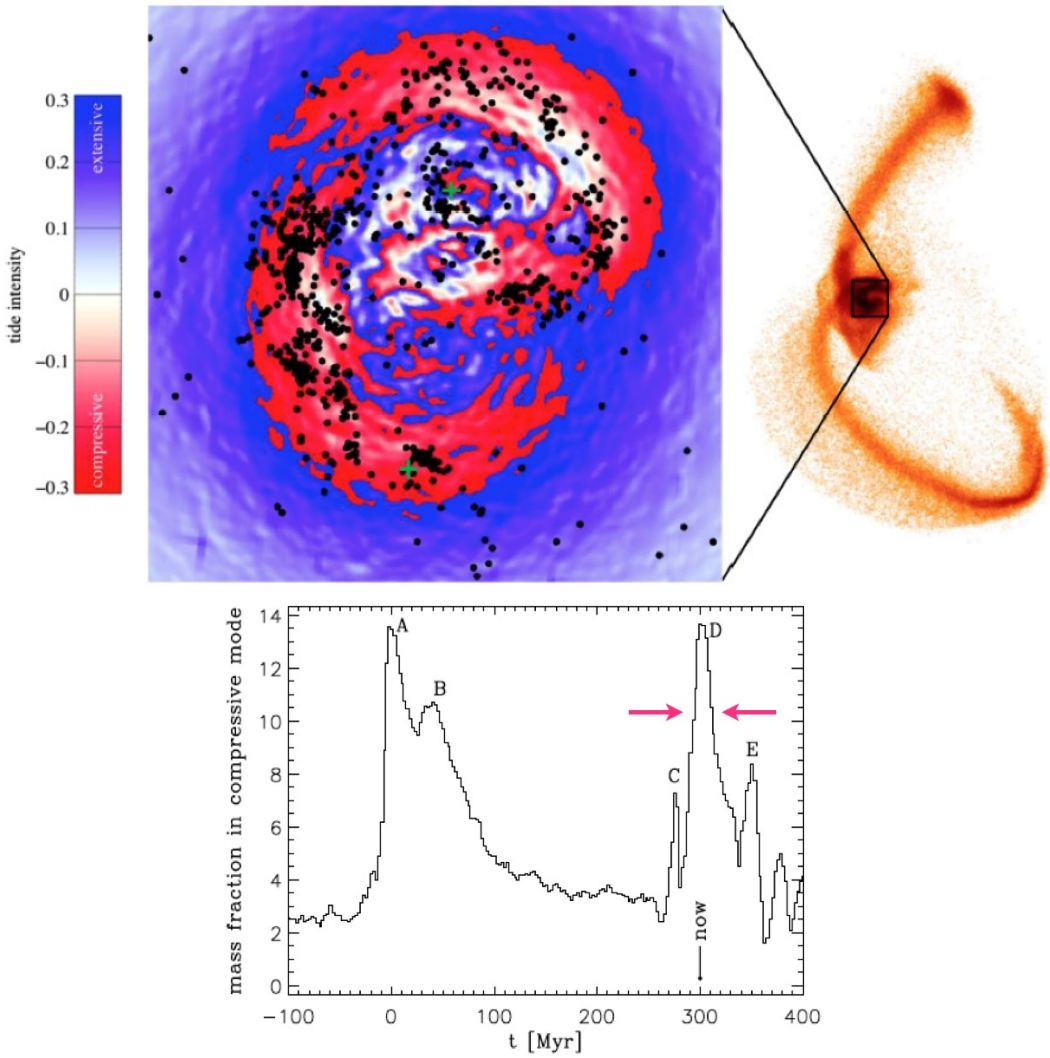

Figure 2.9: N-body simulation of Renaud et al. (2008). The upper panel shows the compressive modes in red, which spatially coincide with the observed SSCs in the Antennae (black dots Mengel et al. 2005). The lower panel shows the mass fraction of the gas in the compressive mode. At the current time, a significant fraction of the mass (15%) is in the compressive mode, over a the time-scale of $\tau \sim 10$ Myr.

All simulations predict a significant enhancement of the star-formation efficiency, relative to its value in the two spirals prior to interaction, after pericenter passage. In the simulations, the enhancement of the star formation efficiency is caused by the gas compression and subsequent gas cooling. For several runs this enhancement is one order of magnitude or more, depending on the feedback recipe. Karl et al. (2011) claim that the observations are best reproduced with weak feedback.

Teyssier et al. (2010) present AMR hydrodynamical simulations for low (96 pc, 10^6 $M_\odot$) and high (12 pc, 4×10^4 $M_\odot$) spatial and mass resolution, based on the N-body simulations of Renaud et al. (2008). In the high-resolution model, they solve

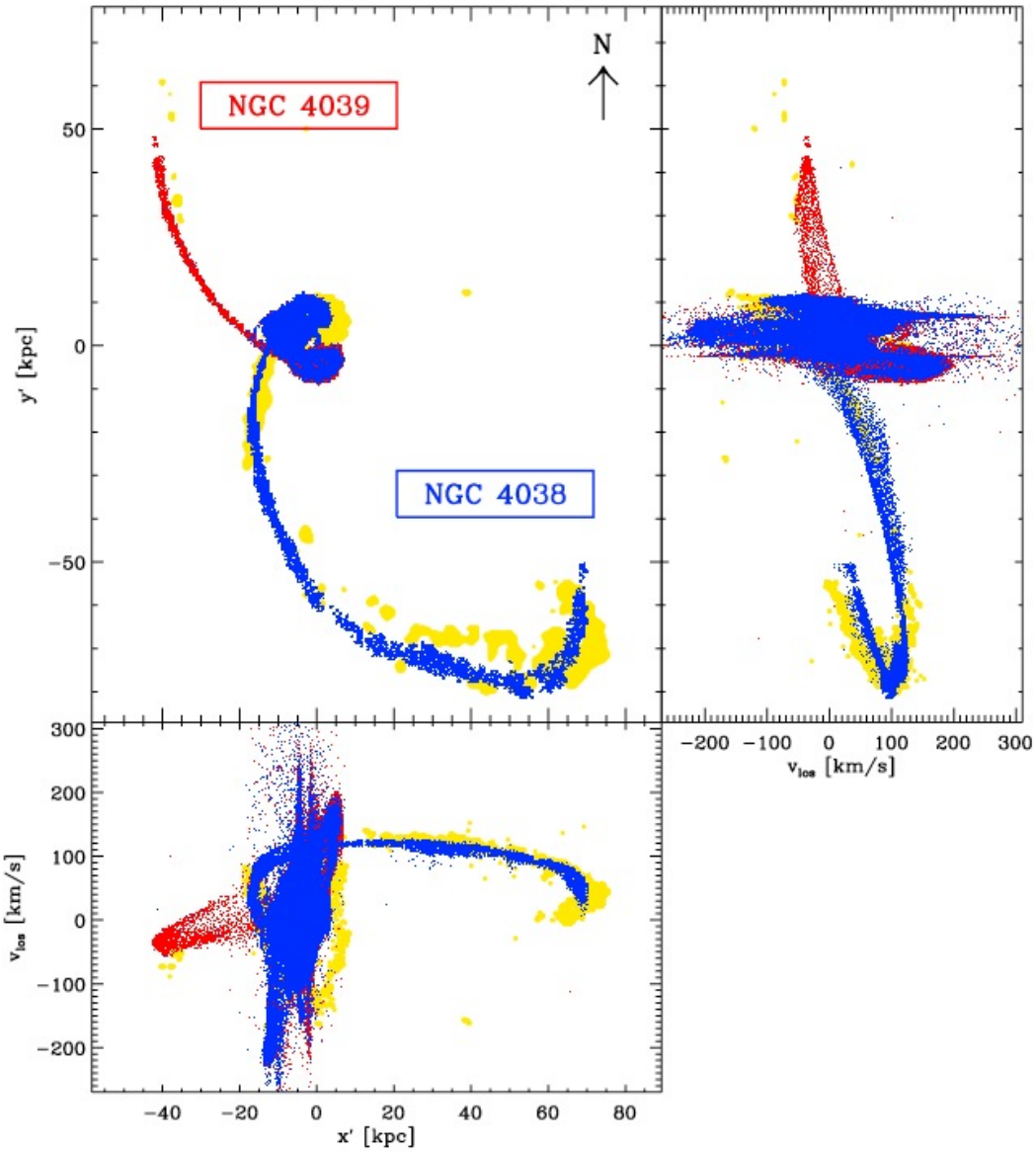

Figure 2.10: Gas properties of the H I estimated from the simulation, and compared with observations by Hibbard et al. (2001). Blue and red dots are the simulated gas particles from the northern galaxy NGC 4038 and for the southern NGC 4039, respectively. Yellow dots correspond to the observations. From Karl et al. (2010), their Fig. 1.

and reproduce the turbulent cloudy structure of the cold ISM. The resolution has a significant impact on the SFR, which is 5 times higher for the high-resolution than the low-resolution model. Whereas in the low-resolution model the gas structures are stable, in the high-resolution model massive dense clumps are formed due to the Jeans instability. Contrary to the results by Karl et al. (2010), the models by Teyssier et al. (2010) estimate that the observed high SFR can be produced during a long period of ~ 300 Myr.

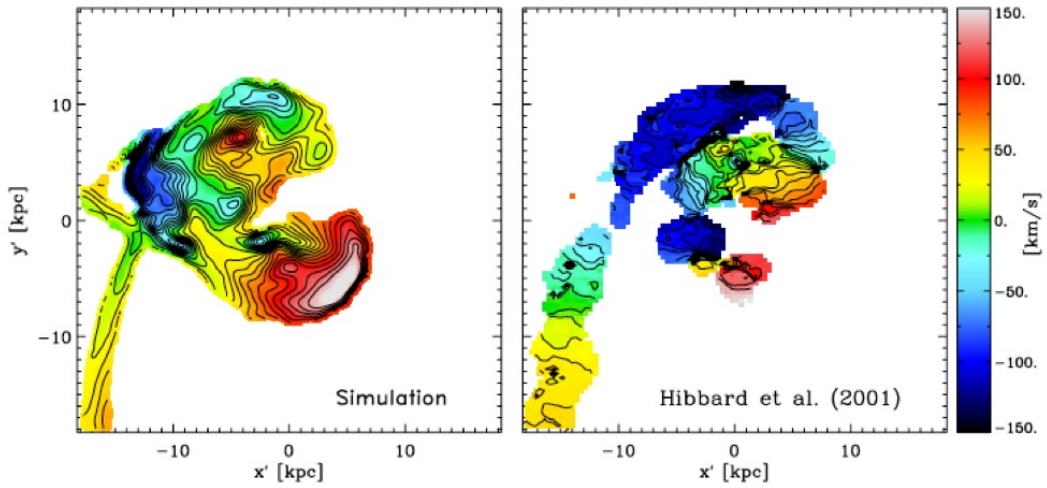

Figure 2.11: Comparison of the density-weighted velocity map from the simulation (left panel) and intensity-weighted H I observed velocity field (right panel) in the central part of the Antennae merger. From Karl et al. (2010), their Fig. 2.

Hence at present, simulations do not yet paint a consistent picture of the star formation history in the Antennae galaxy merger.

Chapter 3

Observations, data reduction and observational results

Contents

This thesis is based on a set of observations of the Antennae galaxy merger at different wavelengths of the electromagnetic spectrum. The observations consist of a combination of new data, public and obtained by us, and published datasets, which are presented in this chapter. First, our own observations, taken in the near-infrared region, were obtained with two instruments at the VLT/ESO and with WIRCam at the CFHT. Second, we used observations taken with the ALMA interferometer in the millimeter domain. Other ancillary data that were also used are described in Chapter 2. These data include observations with the OVRO interferometer and the Spitzer Space Telescope (Section 2.3).

In this chapter, I present the near-IR observations and data reduction (Section 3.1). In Section 3.2, I introduce the interferometric radio ALMA observations and their comparison with single-dish data. Finally, in Section 3.3 I present the observational results obtained from these observations, characterizing the molecular and ionized gas across the Antennae overlap region.

3.1 Near-Infrared observations

Spectroscopic observations in the near-Infrared (near-IR, ranging from $0.8-2.5$ μm) region of the electromagnetic spectrum were obtained with SINFONI and CRIRES, two instruments at the Very Large Telescope (VLT) of the European Southern Observatory (ESO) in Paranal, Chile (Figure 3.1). These observations were obtained with two different proposals that were carried out in service mode. The first proposal was to observe with SINFONI. It included pointings at both nuclei of the Antennae galaxies and one pointing in the overlap region (ID383.B-0789, PI Nicole Nesvadba). These three pointings were selected exclusively for their bright H_2 emission in the mid-IR (Brandl et al. 2009). The success of the first observations prompted a second proposal with both SINFONI and CRIRES instruments (ID386.B-0942, PI Cinthya Herrera). With SINFONI, we observed three additional pointings in the overlap region, and with CRIRES we obtained a high-resolution spectrum of the compact H_2 source discovered with the first SINFONI observations (Herrera et al. 2011).

Figure 3.1: The Very Large Telescope at the Paranal Observatory in the north of Chile. This image shows the four telescopes that constitute the VLT, Antu, Kueyen, Melipal and Yepun. *Credit image: ESO/S. Guisard.*

Broad and narrow-band imaging of the whole Antennae galaxy merger were obtained with the Wide-field InfraRed Camara (WIRCam) at the Canada-France-Hawaii Telescope (CFHT), located in Hawaii. The observations were carried out in March of 2009 as part of the program ID 09AF98 (PI Nicole Nesvadba). We observed the Antennae with the Brγ and H_2 $1-0$ S(1) narrow-band filters, and the Ks-band broad filter. The sampling of WIRCam is $0\farcs3$, and the angular resolution was about $0\farcs8$. Small corrections in the astrometry ($\lesssim 0\farcs8$) were performed by aligning the Ks-band image to the K-band 2MASS (Two Micron All Sky Survey) image of the Antennae galaxies. Figure 3.2 displays the combination of the Ks-band, Brγ and H_2 $1-0$ S(1) emission as seen by the CFHT.

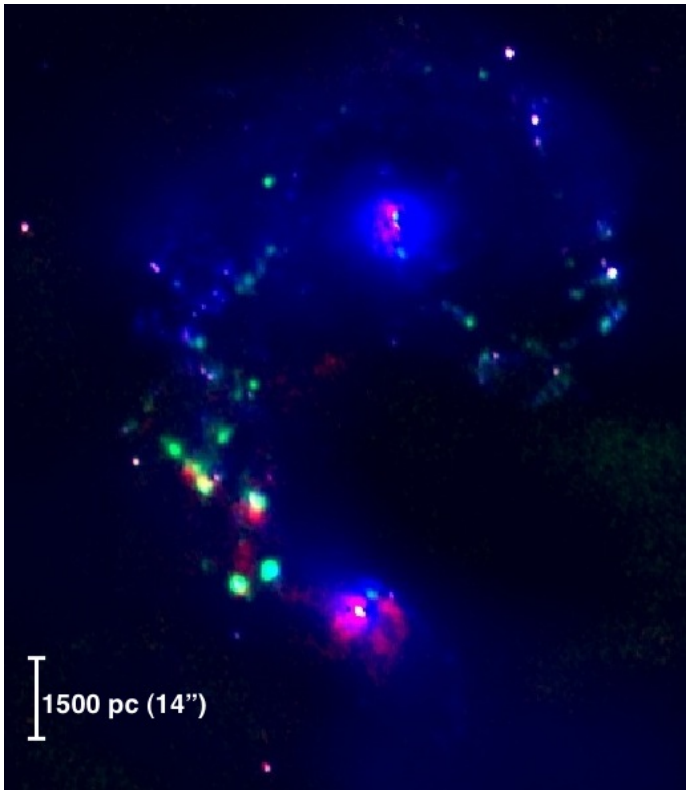

Figure 3.2: The Antennae galaxy observed with the CFHT. The Ks broad band and Brγ and H_2 $1-0$ S(1) narrow-band images are shown in blue, green, and red, respectively. Brγ and H_2 $1-0$ S(1) images are continuum subtracted.

3.1.1 SINFONI observations

We observed several pointings within the Antennae overlap region with the Spectrograph for INtegral Field Observations in the Near Infrared, SINFONI (Eisenhauer et al. 2003; Bonnet et al. 2004) in the K-band ($\sim$ 2.0 - 2.5 μm). SINFONI is mounted at the Cassegrain focus of the UT4 telescope (Yepun) at the VLT (see Fig. 3.4). SINFONI is a near-IR integral field spectrograph fed by an adaptive optics module. The spectrograph operates with 4 gratings (J, H, K, H+K) providing a spectral resolution around 2000, 3000, 4000 in J, H, K, respectively, and 1500 in H+K. The SINFONI field-of-view (FOV) on the sky is cut into 32 slices. The pre-slit optics allows to choose the width of the slices. The choices are 250 milliarcsecond (mas), 100 mas and 25 mas, leading to FOVs on the sky of $8''\times8''$, $3''\times3''$, or $0.8''\times0.8''$respectively. Each one of the 32 slitlets is imaged onto 64 pixels of the detector. Thus one obtains 32x64 spectra of the imaged region on the sky [1].

Observations of different regions in the Antennae galaxy were done with the largest FOV provided by SINFONI. The spectral resolving power in the K-band is $R = \lambda/\Delta\lambda = 4490$ (SINFONI User's manual). The SINFONI observations were

[1] From http://www.eso.org/sci/facilities/paranal/instruments/sinfoni/overview.html

carried out in two different runs under good and stable atmospheric conditions. The first observations were taken in June and July 2009 with 30 minutes of ON-source exposure time. The second dataset was observed in February 2011 in 40 minutes ON-source integration time. In both, the exposure time was split into individual exposures of 600 seconds. We adopted a dither pattern where one sky frame was taken in-between two object frames to allow for an accurate subtraction of the night sky. Figure 3.3 shows the different SINFONI FOV pointings in the Antennae galaxies, four in the overlap region and one in each nucleus. This work focuses on the overlap region.

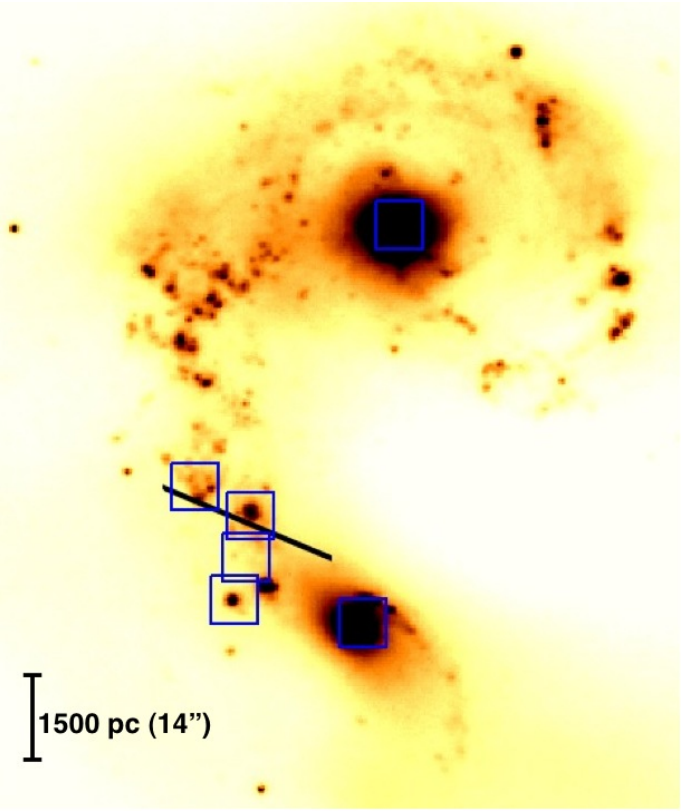

Figure 3.3: The color figure corresponds to the K-band emission from the Antennae galaxies, obtained with the CFHT. The blue squares represent the FOV of the six observations done with SINFONI. The black line represents the slit used for the CRIRES observation, at a position angle of 67°.

Data reduction was done with the standard IRAF tools to reduce longslit spectroscopy (Tody 1993), complemented by a set of SINFONI-specific IDL routines prepared by N. Nesvadba (e.g. Nesvadba et al. 2011). For each observation, these routines subtract the dark-field, and correct for the flat-field and bad pixels. They combine the images and apply a wavelength calibration. Finally, sky images were used for sky subtraction to the science observations. The telluric contamination by the Earth's atmosphere was corrected using bright ($K \sim 6-8$ mag) stars observed at a similar air mass as our target. We used the light profiles of these stars to measure

the point spread function (PSF) of our data, FWHM = 0.″7 × 0.″6. Comparison with high-resolution HST/NICMOS imaging retrieved from the MAST archive[2], and part of the data presented by Whitmore et al. (2010), shows that our PSF estimate is robust. Since the SINFONI FOV is just a few arcsecs, its size does not allow to align the observations with astrometry catalogs. The astrometry was performed by comparing the continuum emission from the SINFONI observations with the Ks-band image obtained with the CFHT. Each of the four SINFONI pointings in the overlap region was aligned separately to the CFHT image. Corrections were smaller than 0.″7.

All of the four pointings in the overlap region were observed in different days and/or night spans. I corrected the spectral information for the Earth velocity with respect to the local standard of rest (LSR) at the moment of the observation. The observations taken in 2009 were corrected by -30.10 km s^{-1}, and the observations taken in 2011 by $+19.17, +20.31$ and $+20.45$ km s^{-1}.

3.1.2 CRIRES observations

Figure 3.4: Pictures at the left and right panels show the CRIRES and SINFONI instruments mounted at the VLT, respectively.

The CRyogenic high-resolution Infrared Echelle Spectrograph (CRIRES, Kaeufl et al. 2004), installed on the UT1 telescope (Antu) at the VLT (see Fig. 3.4), is a high-resolution grating spectrometer that covers the entire near-IR spectrum accessible from ground-based observations, 0.95−5.12 μm. We observed one position in the Antennae overlap region at the central wavelength of ∼2.1313 μm, which corresponds to the H_2 1−0 S(1) line (2.1218 μm rest frame) redshifted to the velocity of the source of 1550 km s^{-1}. Figure 3.3 shows, as black line, the position of the slit in the Antennae galaxies, with a position angle of PA = 67°. The observations were obtained at the end of January 2011, under good and stable atmospheric conditions. The slit length was 40″and the width was 0.″4. For the chosen slit width, the spectral resolving power is $R = 50000$, which corresponds to a velocity resolution of 6 km s^{-1}

[2] http://archive.stsci.edu/

at 2.13 μm. The observations where done for two positions of the slit to allow for sky subtraction. The slit length is large enough to keep the source on the slit during the two pointing observations, which permitted us to increase the signal-to-noise ratio by using all of the integration time on source (Figure 3.5). This is a difficult observation which required a total exposure time of 4.8 hours. The source cannot be seen in individual exposures.

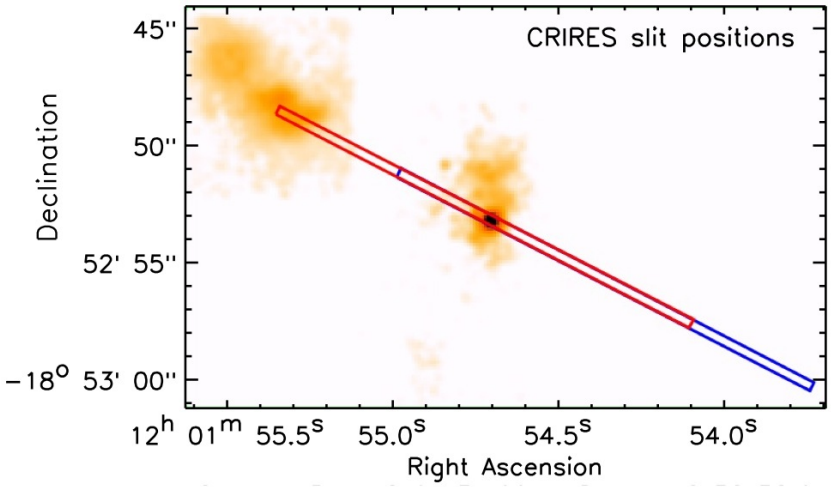

Figure 3.5: The figure zooms into Figure 3.3 and shows the region of which the CRIRES spectroscopy was obtained. The two boxes represent the the CRIRES slit positions on the Antennae overlap region. The black emission in the center of the image is our target.

The data reduction was performed in IDL. Data were dark-subtracted and flat-fielded. The observations were done over four different nights within a week. The data of the four nights were averaged together after weighting by the noise. Sky subtraction is done after data averaging, by subtracting the two averaged images at the two slit positions. On this final image, we have two independent spectra of the source, corresponding to the two positions of the slit on the sky. The final spectrum is obtained by subtracting the map from itself, offset by the distance between the two pointings. The photometric calibration was done using as the reference the H_2 $1-0$ S(1) emission detected with SINFONI for the same source. This is not a critical step because the goal of the CRIRES observations was to obtain the spectral profile of the line, not to measure its flux. Wavelength calibration was applied to the final spectrum by using three telluric atmospheric OH lines close to the reference wavelength of 2.1313 μm. Gaussian curves were fitted to these OH lines. The central position of the lines were matched to the real wavelengths of the sky lines by doing a linear fit. We applied this fit to the wavelength axis. Finally, to have the velocities in the LSR frame, we corrected by the Earth movement that, at the moment of the observations, was +22 km s^{-1}.

3.2 Radio observations: ALMA

I used radio observations obtained with the new Atacama Large Millimeter/submillimeter Array (ALMA[3]), which is located in Llano Chajnantor at 5000 m of altitude in the Atacama Desert in the north of Chile (see Fig. 3.6). ALMA is an interferometer still under construction. Its complete construction is foreseen for 2013. When ALMA is complete, it will have a total of 66 antennas with dishes of 7 and 12 meters of diameter. These antennas can be moved to have different baselines, which allows to reach sub-arcsec spatial resolutions. The ALMA wavelength range will be 320 μm $-$10 mm, divided into 10 Bands, which can be observed in Figure 3.7 overlaid to the atmospheric transmission curve on Llano de Chajnantor.

Figure 3.6: The Atacama Large Millimeter/submillimeter Array, ALMA, located on Llano Chajnantor in Chile, at the beginning of 2012. Credit: W. Garnier, ALMA (ESO/NAOJ/NRAO)

The observations were obtained during Science Verification, in which the ALMA capabilities are demonstrated to produce data of the required quality, by comparing them with images obtained previously with other telescopes. The Antennae galaxies were observed in the Band 7 at 345 GHz (i.e. CO$(3-2)$ line emission). A mosaic was constructed by observing several pointings across the galaxies. The observations were taken between May and June 2011, with 10 to 13 antennas and baselines from 25 to 200 m. This configuration yielded an angular resolution of $0\farcs6\times1\farcs1$ (66 pc$\times$115 pc, at a distance of 22 Mpc). The intrinsic spectral resolution corresponds to 0.85 km s^{-1}, which was binned into channels of 10 km s^{-1}. I use the reduced data cube and continuum image provided by the ALMA team, in units

[3]ALMA is an international project between Europe, East Asia and North America in cooperation with the Republic of Chile

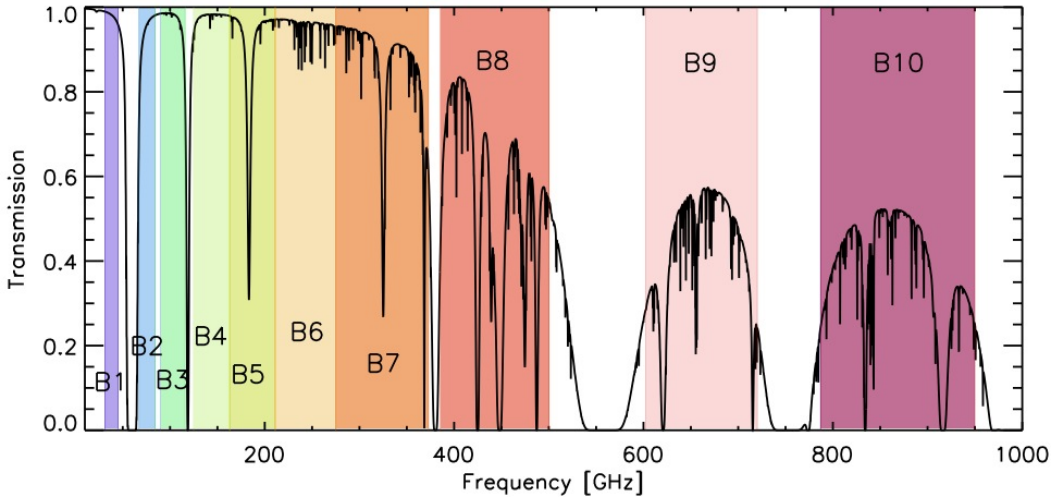

Figure 3.7: The 10 bands of the ALMA telescope overlaid on the atmospheric transmission curve on Llano Chajnantor, with a precipitable water vapour of 0.5mm.

of km s^{-1} vs Jy beam^{-1}, which is publicly available on the ALMA website[4] since August 2011. The detailed description of the data reduction, done with Common Astronomy Software Applications (CASA), was provided by the ALMA team and can be found in the CASA Guides web page by the National Radio Astronomy Observatory (NRAO)[5]. These data were corrected for the primary beam attenuation.

Low spatial frequencies are filtered out because of missing short spacings which cause the loss of extended structures larger than 4″ and negative sidelobes adjacent to bright emission. To measure fluxes I used a clipped cube where all pixel values smaller than 2σ (6 mJy beam^{-1}) were set to zero. I quantify the missing flux from the extended sources by comparing the clipped ALMA dataset with single dish observations. For that, I use the CO$(3-2)$ spectra presented by Zhu et al. (2003) and Schulz et al. (2007). From Zhu et al. (2003), I extract the spectrum in their Fig. 5, which is in units of mean brightness temperature ($T_{\rm mb}$). These observations were obtained with the James Clerk Maxwell Telescope in Hawaii, during 1998. The FWHM of the observations is 14″. The line emission in the figure corresponds to a pointing in the overlap region at α =12^{h}01^{m}54^s.8, δ −18°52′55″. From Schulz et al. (2007), I use the spectrum in their Fig. 1 in units of $T_{\rm mb}$. This spectrum was taken with the Heinrich Hertz Telescope in Arizona, between 1999 and 2003. The FWHM of the observations is 22″. The spectrum in the figure corresponds to a pointing in the overlap region at α =12^{h}01^{m}55^s.2, δ −18°52′53″. To compare the ALMA observations with the two single dish data-sets, I convolve the clipped ALMA data to the resolution of the JCMT and HHT observations. Then, I extract the ALMA spectrum at the coordinates of the two different pointings of the single dish observations. Fig. 3.8 displays the comparison between the interferometric

[4] http://almascience.eso.org/alma-data/science-verification
[5] http://casaguides.nrao.edu/index.php?title=AntennaeBand7

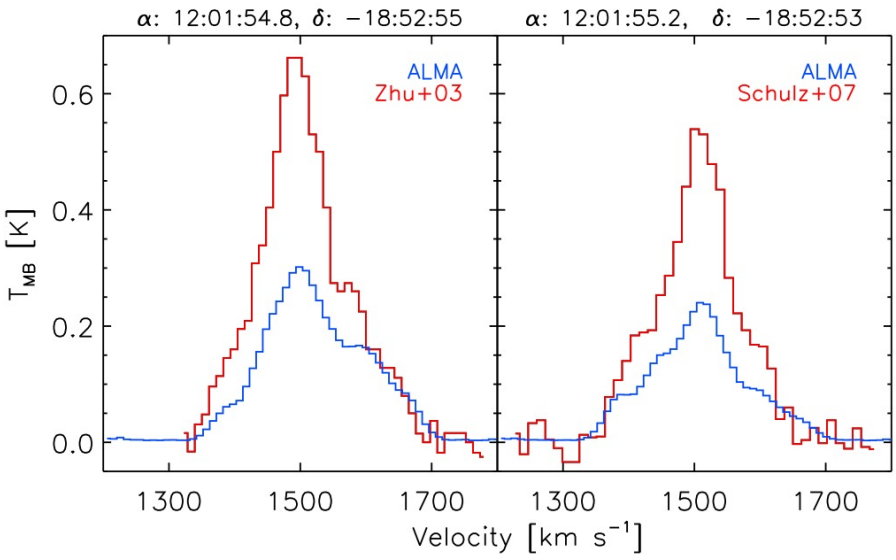

Figure 3.8: Comparison between the ALMA and single dish observations of the CO(3 − 2) line. The blue lines in the left and right frames correspond to the spectra extracted from the convolved ALMA data-cube to a resolution of 14″ and 22″, respectively. Red lines represent the emission observed by single-dish telescopes.

ALMA and single dish observations. On the left, the comparison with Zhu et al. (2003) and, on the right, with Schulz et al. (2007). The line profiles are similar, but the ALMA observations are clearly missing flux. In the overlap region, the flux observed with ALMA corresponds to 57% and 56% of the flux observed by the single dish observations performed by Zhu et al. (2003) and Schulz et al. (2007), respectively.

3.3 Data analysis

The observations previously presented give us information on the molecular and ionized gas in the Antennae overlap region. From these data, I am able to characterize the gas in this zone and study its physical state and kinematics. In this section, I present the direct results obtained from these observations for the extended emission across the overlap region. First, I start by explaining how I obtained the K-band continuum images and the measurement of the line emission within the K-band. Second, I describe the measurements in the ALMA observations. Third, I present the morphology and kinematics of the molecular gas across the overlap region, and compare the H_2 and CO emission maps. Forth, I introduce the morphology and kinematics of the ionized emission. Fifth, I examine and compare the ionized (Brγ) and molecular (H_2 and CO) gas emission from each of the four SGMCs. And finally, I highlight the presence of a compact molecular source in the overlap region.

3.3.1 Measuring the near-IR continuum and line emission

As mentioned before, SINFONI observations cover the full K-band from which the continuum emission and several line emission can be extracted. The K-band continuum image is computed pixel-by-pixel. In order to remove the emission lines and *bad channels*, the continuum emission is measured in an iterative way by excluding the channels with emission higher than a certain threshold value. In each pixel, the threshold value used is the mean value plus 3 times he standard deviation. After masking, a new standard deviation value is computed from the remaining channels. I proceed in this way, iteratively, until there is no more channels larger than 3σ. As a result, the K-band continuum and standard deviation images are obtained. Figure 3.9 displays the contours of the SINFONI K-band image overlaid on the K-band image of the Antennae overlap region, obtained with the CFHT (see section 3.1.1).

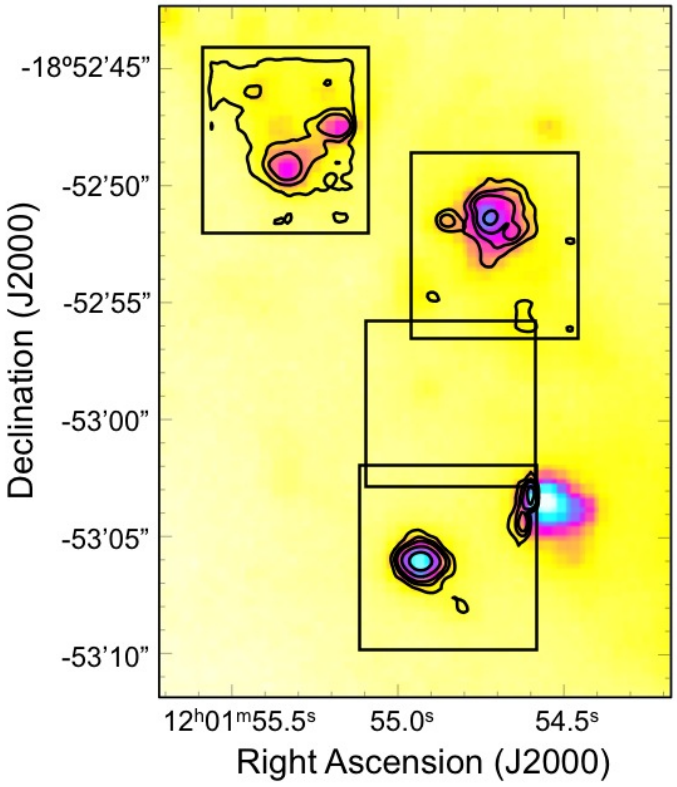

Figure 3.9: K-band continuum emission from the Antennae overlap region. The color image represents the CFHT K-band emission and the contours the K-band continuum obtained with SINFONI. The values for the contours are 5, 10, 15, 30 and 70×10^{-20} erg s^{-1} cm^{-2} Å^{-1}. Boxes mark the four SINFONI fields.

I also measure the emission lines covered by the SINFONI observations to create intensity, velocity and line-width maps. The SINFONI wavelength range includes several ro-vibrational H_2 and ionized lines (see Table 3.1), where the H_2 $1-0$ S(1) line at 2.12 μm and the Brγ line at 2.17 μm are the strongest ones.

To measure the SINFONI spectrum of a given source (e.g. SGMCs), I use spatial

Table 3.1: Main emission lines within the SINFONI wavelength coverage

Molecular lines		Ionized lines	
Line	Rest Wavelength[a] [μm]	Line	Rest Wavelength[a] [μm]
H_2 $v = 1 - 0$ S(0)	2.22329	He I ($2p^1P^0 - 2s^1S$)	2.05869
H_2 $v = 1 - 0$ S(1)	2.12183	He I ($4s^3S - 4s^3S$)	2.1127
H_2 $v = 1 - 0$ S(2)	2.03376	Brδ	1.94509
H_2 $v = 1 - 0$ S(3)	1.95756	Brγ	2.16612
H_2 $v = 2 - 1$ S(1)	2.24772		
CO v=2−0 bandhead	2.29353		

[a] Values were taken from Allen (1973).

masks defined from the integrated emission in one of the brightest lines. Only the pixels above some intensity thresholds are co-added. This increases the signal-to-noise of the emission of the weakest lines. To do that, two different masks are created, one for the ionized and the other for the molecular gas. First, I compute line emission images for H_2 $1 - 0$ S(1) and Brγ by integrating the emission in the wavelength range where the emission lines were defined after subtracting the nearby continuum. Second, I compare the line intensity images with the K-band continuum standard deviation image. The masks are defined where the line intensity is 3 times larger than the K-band continuum standard deviation. Finally, the two masks were applied to the SINFONI data-cube, to produce two masked cubes. Intensity, velocity and line-width maps for each line emission were obtained by fitting, pixel-by-pixel, Gaussian curves to the masked data-cubes with the MPFIT routine written in IDL (Markwardt 2009). With the limited spectral resolution of SINFONI, the emission lines are well fitted by one Gaussian curve.

3.3.2 Measuring the sub-mm continuum and line emission

For the continuum emission at 230 and 345 GHz observed with ALMA, I use reduced images directly provided by the ALMA team (see section 3.2). Figure 3.10 presents the continuum emission seen by ALMA. The left and right color images show the continuum emission at 230 GHz and 345 GHz, respectively, with CO$(2 - 1)$ and CO$(3 - 2)$ contours overlaid, respectively.

Now I explain how I measure the CO emission lines from the observations to create intensity, velocity and line-width maps. The ALMA Band 6 and 7 data are focused on the CO$(2 - 1)$ and CO$(3 - 2)$ lines at 60 μm (345 GHz) and 1.3 mm (230 GHz), respectively. These observations were masked by using the 2σ threshold discussed in Section 3.2. Intensity maps for each emission line were obtained by fitting, pixel-by-pixel, Gaussian curves to the masked data-cubes with the MPFIT routine. The ALMA data show emission lines with several velocity components, where up to three Gaussian components were fitted. Thus, the final images correspond to the addition of all the Gaussian fits. Since the spectra have more than one

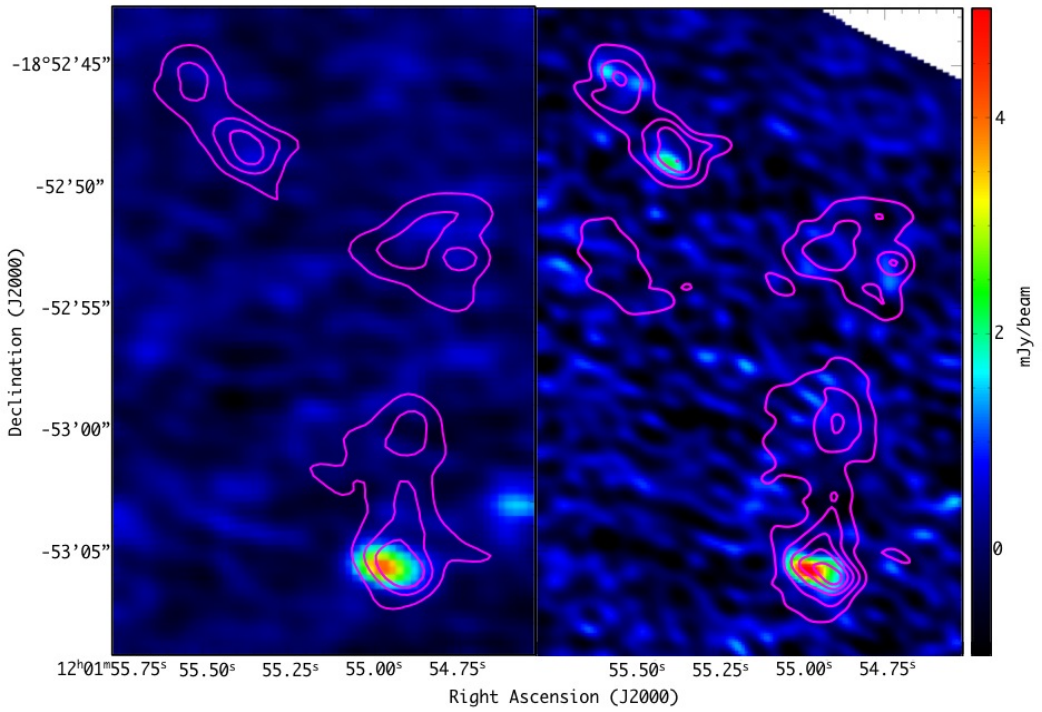

Figure 3.10: Color images correspond to the continuum emission of the overlap region at 230 GHz and 345 GHz for left and right images, respectively, as seen by ALMA. Contours represent the CO$(2-1)$ and CO$(3-2)$ emission lines.

component, the velocity and line-width maps are the first and second moments of the data-cube.

3.4 Observational results

In this section, I present the observational results obtained from the SINFONI and ALMA observations. Sections 3.4.1 and 3.4.2 present the morphology and kinematics of the molecular and ionized gas, respectively. In Section 3.4.3, I compare these data in each SGMC. In Section 3.4.4, I highlight the presence of a compact molecular source, PCC1, with bright H_2 line emission associated with an emission peak in the ALMA CO observations, which shows no Brγ, nor continuum emission in the K-band.

3.4.1 CO vs H_2 emission

Our SINFONI observations target the brightest sources in H_2 pure-rotational line emission by Brandl et al. (2009, Spitzer observations). The maximum angular scale of our CO$(3-2)$ ALMA observations corresponds to the sizes of supergiant molecular cloud complexes observed in CO$(1-0)$ by Wilson et al. (2000). Here, I compare the morphology and kinematics of the H_2 and CO lines.

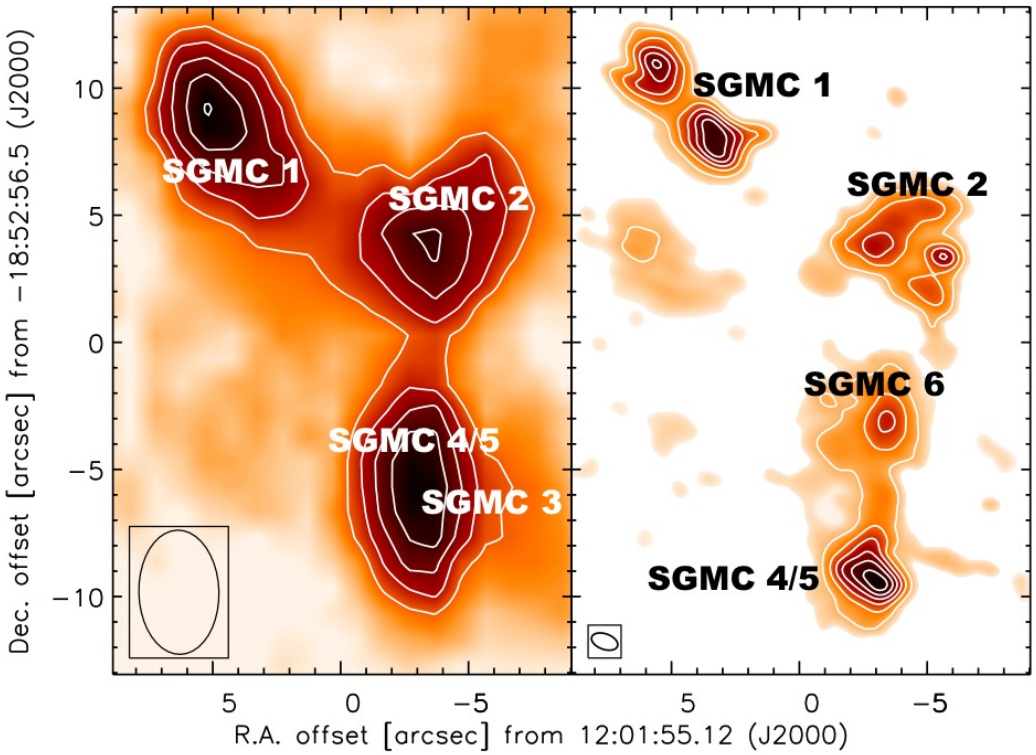

Figure 3.11: Overall CO morphology of the Antennae overlap region. Comparison of the OVRO CO$(1-0)$ and ALMA CO$(3-2)$ observations. OVRO contours are from 1 to 3 every 0.5 Jy arcsec^{-2} km s^{-1} and ALMA contours from 10 to 60 every 10 Jy arcsec^{-2} km s^{-1}. The beam size for both observations is indicated inside a box at the bottom left part of each panel.

I start by comparing the CO$(3-2)$ morphology with that previously known from the CO$(1-0)$ emission (Wilson et al. 2000), obtained with the OVRO interferometer and presented in Section 2.1. The right and left panels in Fig. 3.11 present the morphology of the CO$(3-2)$ and CO$(1-0)$ emission lines, respectively. The ALMA channel maps are very similar to the SMA observations in Ueda et al. (2012), who also observed the CO$(3-2)$ transition. We identified all SGMCs discovered by Wilson et al. (2000) except for SGMC 3, which is not covered by ALMA.

The new data show two velocity components in SGMC 1 and 2. We also decomposed SGMC 4/5 into two smaller complexes at positions (−3,−9.5) and (−3,−3.5) in Fig. 3.11, each of which has two velocity components. We kept the name SGMC 4/5 for the first complex, and labeled the northern extension SGMC 6 a and b.

Fig. 3.12 displays the morphology of the H_2 $1-0$ S(1) emission line (right panel) of our SINFONI observations and the rotational H_2 S(2) line (in the left panel) as seen by the Spitzer Space Telescope (Brandl et al. 2009, angular resolution of $\sim 4''$). The overlap region is very bright in the rotational and ro-vibrational H_2 lines. The H_2 gas in the overlap region comes from the SGMCs, identified with the CO observations.

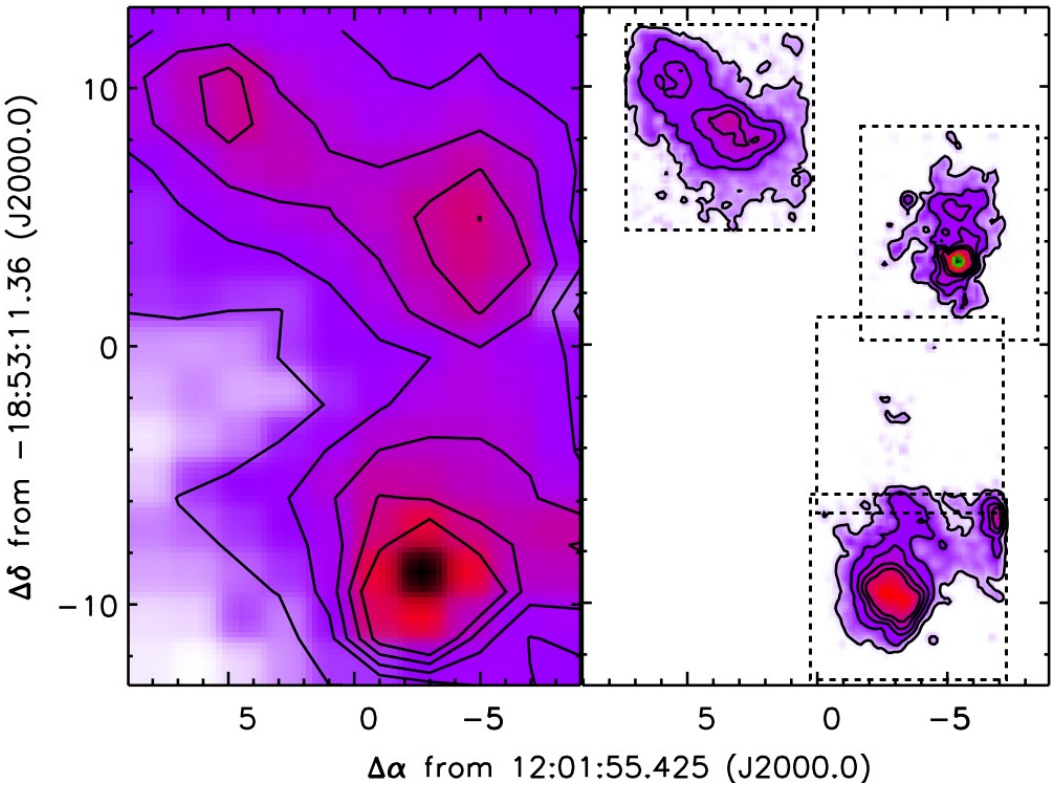

Figure 3.12: H_2 morphology of the Antennae overlap region. The left panel displays the H_2 S(2) line at 12.28 μm as observed with Spitzer. The right panel presents the H_2 $1-0$ S(1) line as observed with SINFONI.

In Figure 3.13 I compare the velocity maps of the H_2 $1-0$ S(1) and CO$(3-2)$ emission lines. The range of velocities is large $\sim$1400$-$1650 km s^{-1}. Individual spectra for each SGMC are displayed in Figure 3.14. Owing to the higher spectral resolution of the ALMA data (final resolution of 10 km s^{-1}) in comparison with the SINFONI data ($\sim$107 km s^{-1}), I can identify more velocity structures in the CO data than in the H_2 data. For each SGMC, I fit two Gaussian curves to the CO$(3-2)$ spectra in Figure 3.14. Table 3.2 lists, for each SGMC, the CO properties of the velocity components, the total H_2 $1-0$ S(1) line emission and the ratio between H_2 and CO fluxes. Error bars include only fit uncertainties, not the systematic errors owing to the missing short spacings. We see that the H_2-to-CO luminosity ratio varies among SGMCs.

Fig. 3.15 shows, in the left panel, the CO emission from the Antennae covered by ALMA, which is overlaid to the WIRCam K-band continuum emission. Right panel zooms on the overlap region. This figure shows the spatial distribution of the H_2 and CO emission in the Antennae overlap region at an angular resolution of $\leq 1''$ (100 pc). The color image is the H_2 $1-0$ S(1) emission and the contours are the CO$(3-2)$ emission. Asterisks represent young ($<$5 Myr) and massive ($>10^5$ $M_\odot$) SSCs in the SINFONI fields, which are associated with SGMCs. I highlight a compact molecular

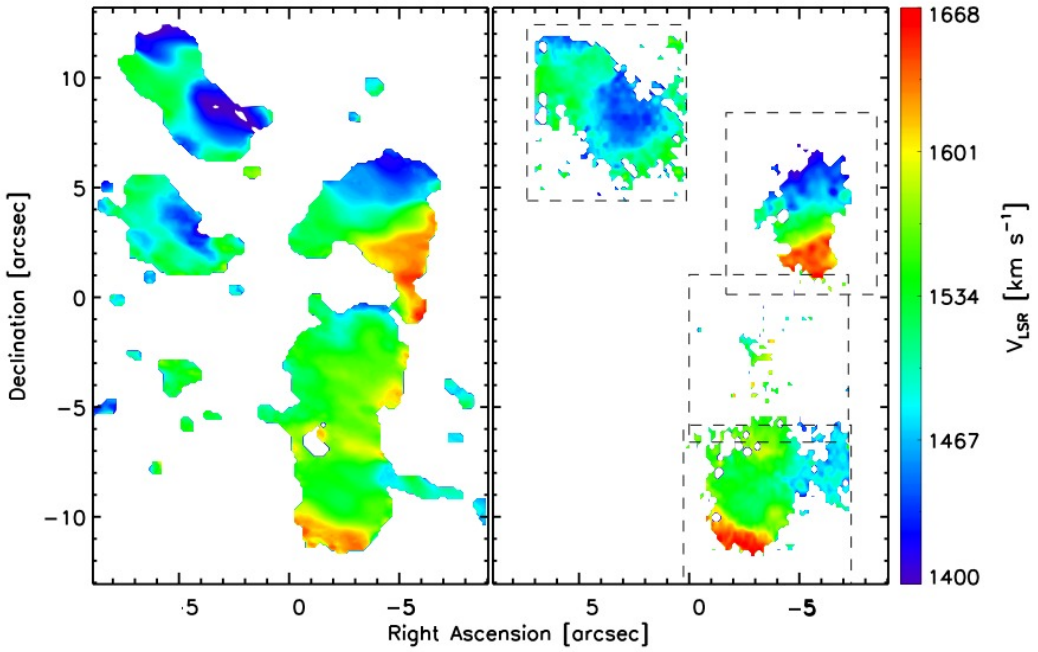

Figure 3.13: First-moment map of CO(3 − 2) and velocity map of H_2 1 − 0 S(1) of the Antennae overlap region in the left and right panels, respectively. Velocities are relative to the LSR. The four SINFONI fields are marked with dashed squares.

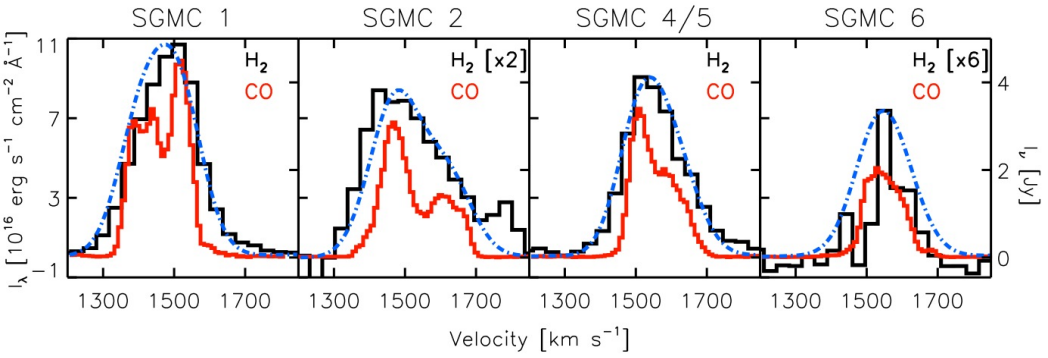

Figure 3.14: Emission-line spectra for each SGMC. The figures display the H_2 1 − 0 S(1) line in black and the CO(3 − 2) line in red. Left and right y-axis correspond to the H_2 and CO lines, respectively. The H_2 emission in SGMC 2 and 6 is scaled by a factor 2 and 6, respectively. Blue spectra are the CO spectra convolved to the SINFONI spectral resolution and scaled to the H_2 emission.

source (PCC1) observed in both emission lines.

3.4.2 The ionized gas emission: Brγ

The ionized gas is traced by the Brγ emission line. Fig. 3.16 displays the morphology and kinematics of Brγ across the overlap region as seen by SINFONI. All SGMCs

Table 3.2: CO(3 − 2) properties of the SGMCs and their velocity components. We include the integrated H_2 1 − 0 S(1) fluxes and H_2/CO flux ratios (Herrera et al. 2012).

Source	V_{LSR} km s^{-1}	Δv km s^{-1}	S_{CO} Jy km s^{-1}	$F_{H_2\ 1-0\ S(1)}$ erg s^{-1} cm^{-2}	$\frac{H_2\ 1-0\ S(1)}{CO(3-2)}$
SGMC 1	1417±2	105±6	380±24	1.6×10^{-14}	2.1
	1521±1	63±3	289±16		
SGMC 2	1469±1	90±2	289±8	8.3×10^{-15}	1.6
	1613±2	114±5	176±10		
SGMC 4/5	1505±1	58±2	171±9	1.3×10^{-14}	2.6
	1586±3	126±6	256±12		
SGMC 6	1506±2	50±8	48±12	6.7×10^{-16}	0.2
	1561±5	113±6	216±15		

emit in Brγ. The morphology of the ionized gas does not correlate with neither the H_2 nor the CO emission. The left panel of Fig. 3.16 shows that SGMC 4/5 is the brightest ionized source in the overlap region. This source also corresponds to the brightest source observed by ISO in the mid-IR (Mirabel et al. 1998). The velocity field of the ionized gas does not match that of the molecular gas. The associated velocities of the ionized gas are in the range of 1300 to 1570 km s^{-1}, about 100 km s^{-1} smaller than those measured in the molecular gas.

3.4.3 SGMCs in the overlap region

As observed in Fig. 3.11, in the overlap region the CO(3 − 2) gas is fragmented into four SGMCs. Each of them presents substructures in the molecular as well as the ionized gas. In this section, I compare the morphologies of the K-band continuum, H_2 1 − 0 S(1), CO(3 − 2) and Brγ emission lines for each SGMC.

Figure 3.17 displays the gas emission lines for the SGMCs in the overlap region. From the top to the bottom, SGMC 1, 2 4/5 and 6. The images at the left show the K-band continuum contours overlaid on the H_2 1 − 0 S(1) flux map. In the central and right columns, the color images are the CO(3 − 2) and Brγ flux maps, respectively. Both of them are compared with the H_2 1 − 0 S(1) contours. These images reveal substructures within each SGMC. In the same figure, I highlight the K-band sources identified by Gilbert & Graham (2007) and new sources unveiled by the different emission lines, that will be introduced below. Generally, the K-band continuum emission correlates with the Brγ emission line, and the CO line with the H_2 line.

SGMC 1: H_2 and CO morphologies in this molecular complex are comparable. The ionized emission extends over the same area as the molecular gas but with a different structure, in which the emission peaks do not match. Gilbert & Graham (2007) identified three sources in the K-band, D, D1 and D2, which can be seen in

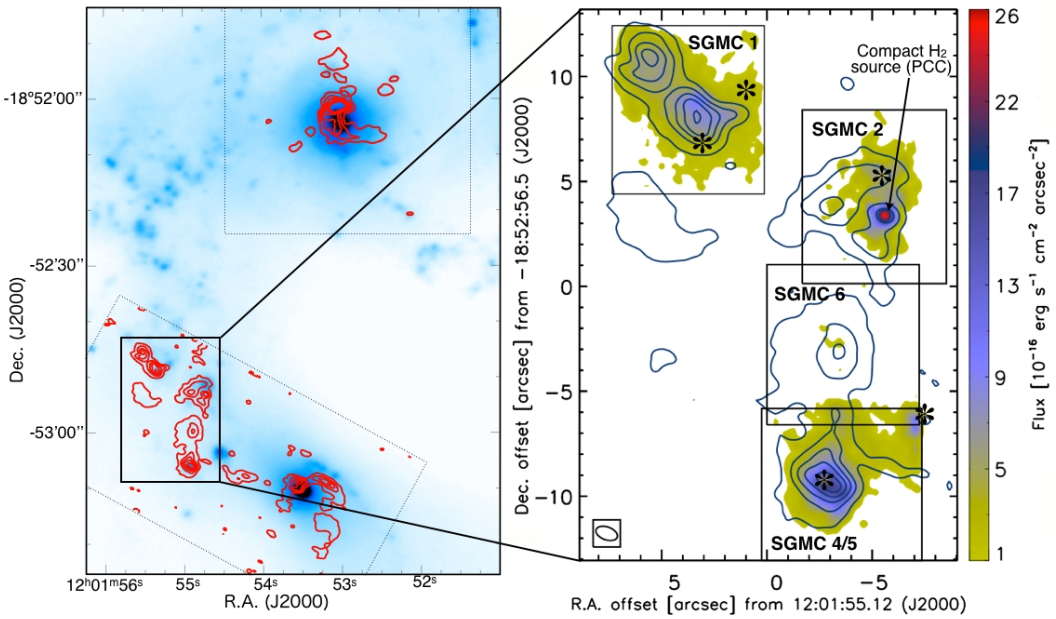

Figure 3.15: *Left.* ALMA CO morphology shown on top of our CFHT K-band continuum image (Herrera et al. 2011). Dotted boxes mark the two ALMA mosaics, the solid box marks the overlap region. *Right.* H_2 $1-0$ S(1) morphology as seen with SINFONI. Boxes mark individual SINFONI fields-of-view, contours show $CO(3-2)$ from 2 to 42 Jy km s^{-1} beam^{-1} in steps of 8 Jy km s^{-1} beam^{-1}. The inset at the bottom right of the right panel shows the ALMA beam. We also mark massive and young SSCs (asterisks), and the compact H_2 source PCC discussed in Seccion 3.4.4.

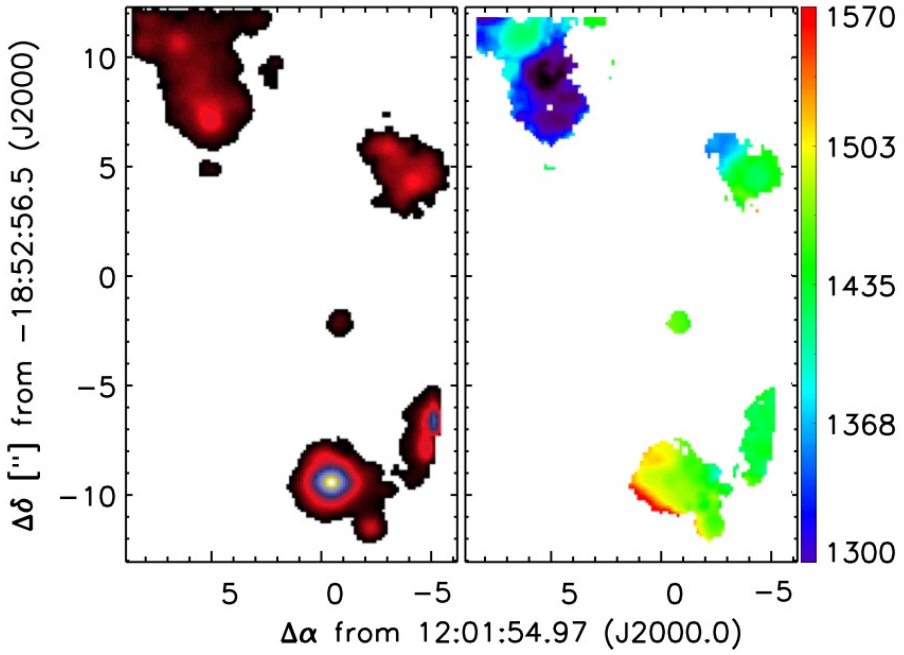

Figure 3.16: Brγ morphology and kinematics across the overlap region. It is observed that all SGMCs are associated with ionized gas.

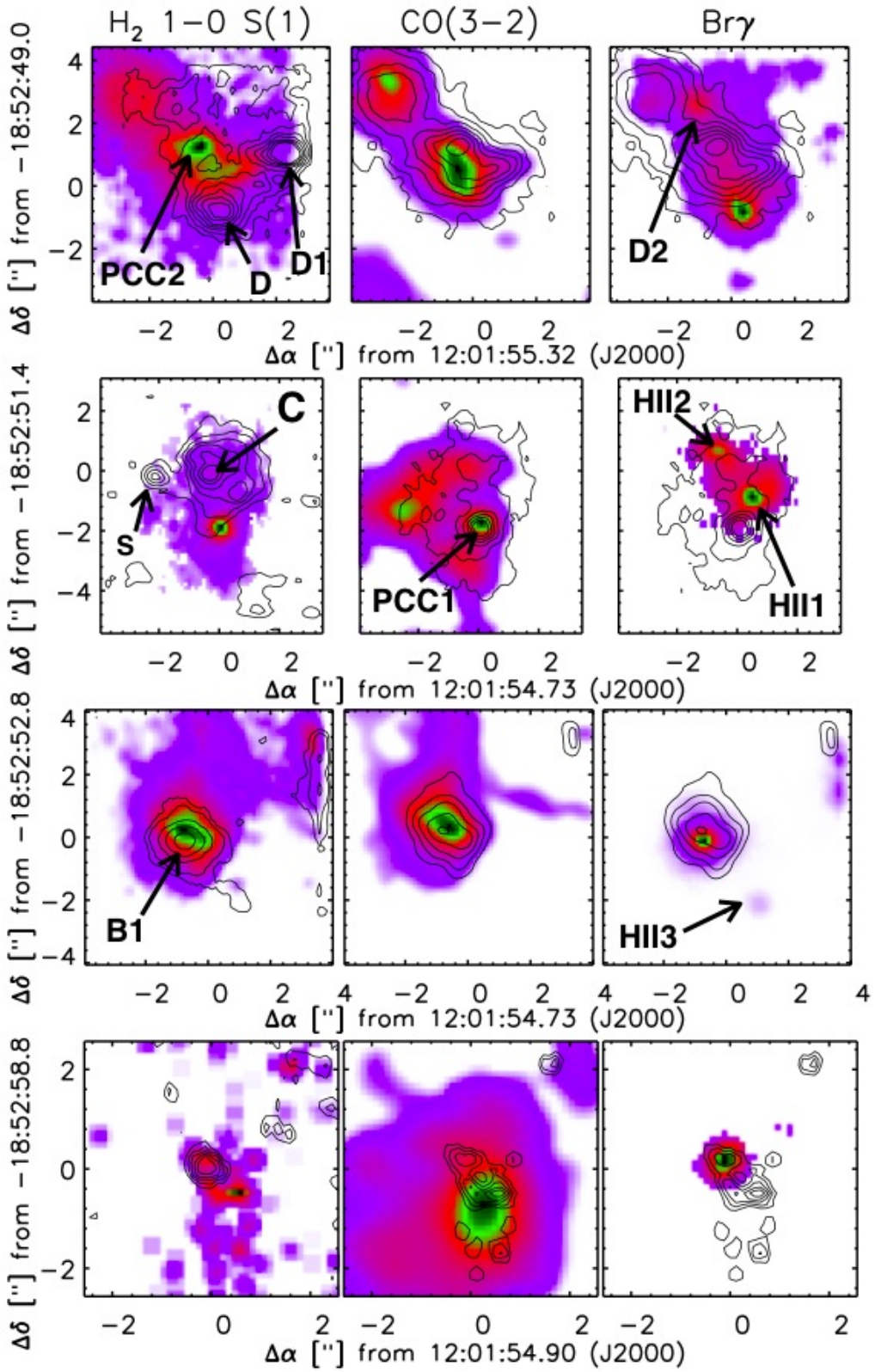

Figure 3.17: Intensity maps of each SGMC. From top to bottom, SGMC 1, SGMC 2, SGMC 4/5 and SGMC 6. From the left to the right, K-band continuum emission contours overlaid on the H_2 $1-0$ S(1) emission line, H_2 contours overlaid on the $CO(3-2)$ emission line and H_2 contours overlaid on the Brγ emission line. I highlighted the different sources found in the SGMCs. The images are not in the same flux scale.

the top panels in Fig. 3.17. D and D1 are very luminous in the continuum emission. D and D2 have a counterpart in Brγ but not in the molecular gas. D1 does not have a clear association with any of the gas lines. The H_2 emission lines reveals the existence of a compact H_2 source, labeled as PCC2. This source will be further discussed in Chapter 4.

SGMC 2: The Brγ and H_2 gas morphologies are dissimilar. H_2 emission is composed of both extended emission and a compact source (Herrera et al. 2011), which is labeled as PCC1. This source was previously introduced in Figure 3.15. Brγ emission is more spatially confined, showing two ionized compact sources (labeled as H II1 and H II2 in Fig. 3.17) which have no counterpart in the molecular gas. The PCC1 source has a clear counterpart in the $CO(3-2)$ emission line. The CO gas shows more substructures than the H_2 gas.

SGMC 4/5: The H_2 $1-0$ S(1) and $CO(3-2)$ lines in SGMC 4/5 have similar morphologies. They are more extended than the ionized gas, which is mainly concentrated in one luminous source associated with a SSC and that coincides with the peak emission of the molecular gas. SGMC 4/5 presents the only H_2 peak associated with a SSC across the overlap region. Towards the south-west of the brightest ionized peak, there is a fainter ionized source with no associated molecular gas, which is labeled as H II3.

SGMC 6: This molecular complex has the fainter H_2 emission among the SGMCs in the overlap region. Unexpectedly, the CO emission is much brighter and extended than the H_2 emission. Brγ emission has a morphology like the continuum emission. Both are localized in a compact source that has associated H_2 gas.

3.4.4 Compact molecular source, PCC1

Within the SGMCs there are compact sources in both molecular and ionized gas. In this section, I focus on the most spectacular source in the overlap region which is observed in H_2, named PCC1, which is the one that I have studied the most. I will come back to the other compact sources in Chapters 5 and 6.

PCC1 is localized in the SGMC 2 (see Fig. 3.17). Its size is measured from its emission profiles across the right ascension and declination axis, at the position $\alpha : 12^{\rm h}01^{\rm m}54\overset{\rm s}{.}72, \delta : -18°52'53\overset{''}{.}4$, where the compact source peaks. Figure 3.18 shows these emission profiles, in the left panel at a fixed declination, and in the right panel at a fixed right ascension. Gaussian curves are fitted to both profiles. The geometrical observed FWHM size corresponds to $0\overset{''}{.}82$ (∼88 pc). To estimate the intrinsic FWHM size of the source, the observed FWHM size is corrected for the seeing of $0\overset{''}{.}65$. The source size is $0\overset{''}{.}51$, which corresponds to 50 pc.

I compare the emission from PCC1 and the SGMC in which it is embedded. Fig. 3.19 presents the K-band spectra of PCC1 and the diffuse extended emission of SGMC 2. To construct the spectrum of the extended emission, I integrate over the full spatial extent where H_2 $1-0$ S(1) emission is observed, and subtract the contribution from the compact source. For PCC1, I integrate within a circular aperture of $0\overset{''}{.}8$ that corresponds to its observed size. The nearby background was subtracted

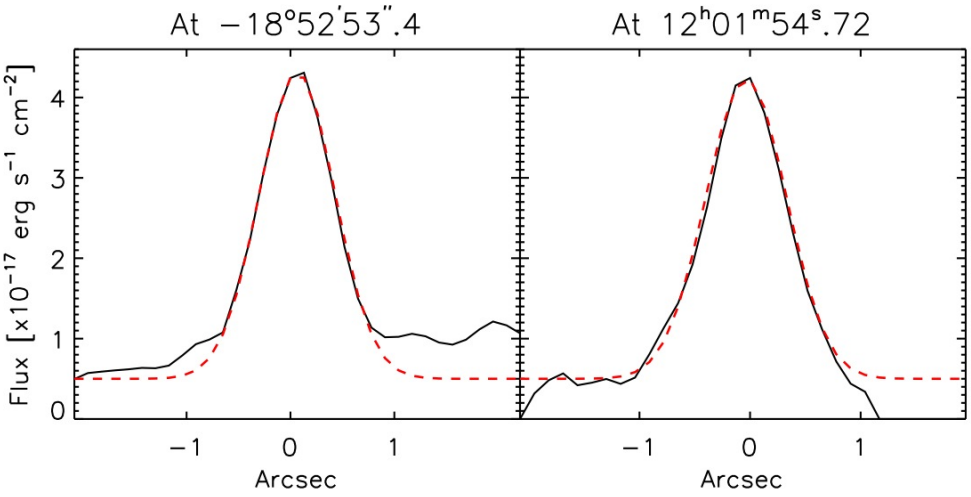

Figure 3.18: Emission profiles of PCC1 along the x- and y-axis at the peak of the source. Red lines correspond to the Gaussian fit to the profiles, from where the source size is estimated.

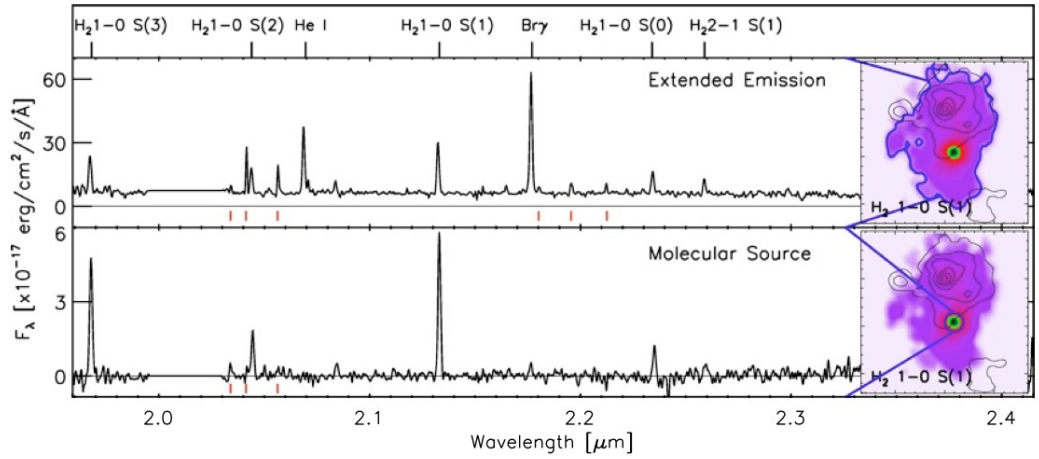

Figure 3.19: Integrated SINFONI spectra for the extended emission from SGMC 2 and the compact molecular source PCC1. The spectra are smoothed by 3 bins in wavelength. Around 2.0 μm the atmospheric transmission is very low so we did not plot this part of the spectra. I mark in red the wavelengths of the strong night sky lines seen in the spectra (OH lines). In the right panel, blue contours mark the aperture from which each spectrum was extracted.

using an outer annulus. The PCC1 intensity lines are measured from this spectrum by Gaussian fit. Table 3.3 lists these values. The spectra suggest that the astrophysical nature of these sources must be very different. For the extended emission from SGMC 2, we observe emission lines from both molecular and ionized gas. PCC1 shows only H_2 lines. Fig. 3.20 presents a zoom onto the Brγ and H_2 $1-0$ S(1) lines for the extended emission-line region and the compact molecular source to illustrate the differences in line intensities and kinematics. For the extended emission, the velocities of the molecular and ionized gas are offset by ~ 100 km s^{-1}.

I obtain high spectral resolution measurements of the line profile of PCC1 with

Table 3.3: Line parameters measured from PCC1 and the extended emission from SGMC 2

	PCC1			Extended emission[a]		
Line	Flux×10^{16}	Velocity	FWHM	Flux×10^{15}	Velocity	FWHM
H_2 1 − 0 S(3)	6.5±0.2	1515±16	167±7	6.1 ± 0.4	1490 ± 17	225 ± 14
H_2 1 − 0 S(2)	2.3±0.1	1538±17	140±11	3.3 ± 0.3	1461 ± 18	234 ± 18
H_2 1 − 0 S(1)	7.6±0.1	1547±16	146±2	6.9 ± 0.3	1493 ± 17	215 ± 9
H_2 1 − 0 S(0)	1.6±0.2	1554±18	140±22	2.8 ± 0.2	1465 ± 18	118 ± 16
H_2 2 − 1 S(1)	0.9±0.2	1530±26	243±44	1.7 ± 0.2	1450 ± 18	146 ± 20
Brγ	<0.06	1443		9.5 ± 0.2	1408 ± 16	133 ± 4
HeI				5.2 ± 0.2	1410 ± 16	131 ± 7
CO(3 − 2)[b]	7.6 ± 0.4	1534 ± 2	93 ± 4	289 ± 8	1469 ± 1	90 ± 2
				176 ± 10	1613 ± 2	114 ± 5

Fluxes are given in erg s^{-1} cm^{-2}, and velocities and FWHM in km s^{-1}. [a] CO emission for the extended source is measure for two velocity components. [b] CO fluxes are in units of Jy km s^{-1}.

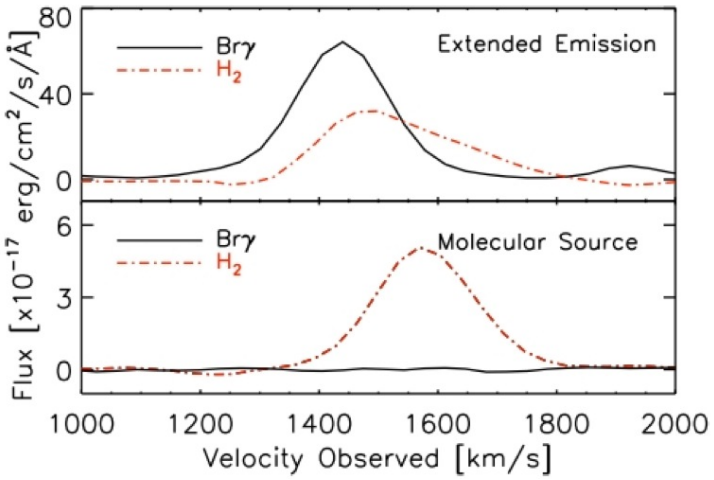

Figure 3.20: Emission line profiles of molecular and ionized gas for the extended emission from SGMC 2 and PCC1. Solid lines correspond to Brγ and dot-dashed lines to H_2 1 − 0 S(1). The kinematics of the extended molecular and ionized gas are different with an offset of ∼ 100 km s^{-1}. PCC1 shows broad H_2 line emission and no Brγ emission.

CRIRES (Fig. 3.21). Fitting this profile requires two Gaussian components with different line widths at a common velocity, with FWHM = 50 km s^{-1} and FWHM = 160 km s^{-1}, respectively. I illustrate this by showing fits with one and two Gaussians in Fig. 3.21. In the two-Gaussian fit, the narrow component contributes 25% to the total H_2 line flux. I verified that I recover the line profile measured with SINFONI after convolution with the line spread function of SINFONI.

PCC1 is very bright in H_2, but it does not have any counterpart in the Brγ emission. It is located in the SGMC with the largest velocity gradient (see Fig. 3.13), and where the velocity gradient is the steepest. The position-velocity diagram in Fig. 3.22 clearly shows the large velocity gradient in SGMC 2 of ∼ 200 km s^{-1} where PCC1 is embedded. The left panel in Figure 3.23, shows in colors the CO(3 − 2)

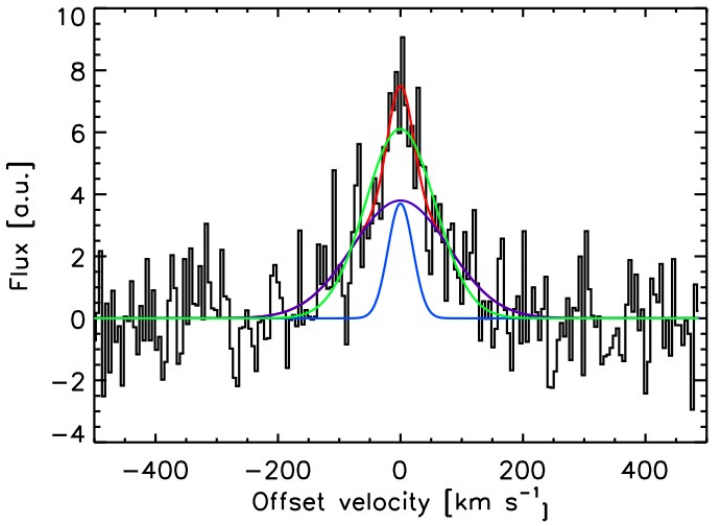

Figure 3.21: Integrated spectra of PCC1 observed with CRIRES. Fitting the data with a single Gaussian (green line) shows significant residuals. An adequate fit (red line) requires 2 Gaussian curves (blue lines), corresponding to a narrow and a broad component, respectively.

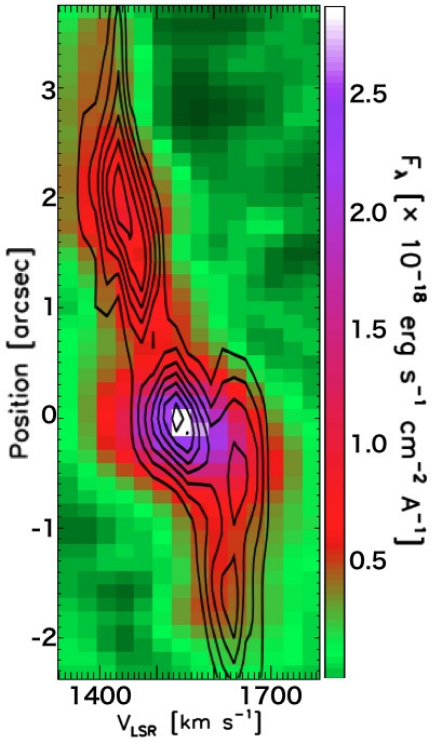

Figure 3.22: H_2 $1-0$ S(1) position-velocity diagram across SGMC 2, crossing PCC1, with CO$(3-2)$ emission shown as contours in steps of 0.02 Jy beam^{-1} starting at 0.03 Jy beam^{-1}. Position zero defined the location of PCC1.

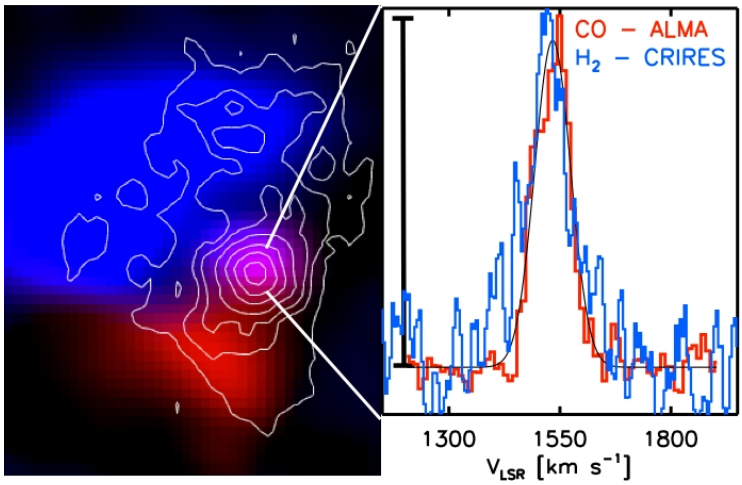

Figure 3.23: (*Left*) CO(3 − 2) emission from SGMC 2, where emission between 1350−1540 km s^{-1} and between 1540−1750 km s^{-1} are shown in blue and red, respectively. Contours show the H_2 1 − 0 S(1) morphology. (*Right*) CO(3 − 2) (red) and CRIRES H_2 1 − 0 S(1) (blue) spectrum of PCC1. The H_2 1 − 0 S(1) spectrum is smoothed to 18 km s^{-1} resolution. The bar corresponds to 77 mJy beam^{-1} for CO(3 − 2) and 4.4 ×10^{-17} erg s^{-1} cm^{-1} Å^{-1} for H_2 1 − 0 S(1). Solid black line represents the Gaussian fit to the CO(3 − 2) line emission.

emission from the two velocity components of SGMC 2 observed in its spectrum of Figure 3.14. I present in blue, the emission integrated over the range 1350−1540 km s^{-1}, and in red, over the range 1540−1750 km s^{-1}. The contours are the H_2 1 − 0 S(1) emission. PCC1 seems to be at the interface of blue and redshifted gas. Right panel in Figure 3.23 shows a comparison of the CO and CRIRES high-resolution (6 km s^{-1}) H_2 1 − 0 S(1) spectra of PCC1. The CO spectrum is the peak emission at the position of PCC1 corrected for the surrounding emission, measured over an annulus outside the source, to isolate the CO velocity component associated with PCC1. CO(3 − 2) and H_2 1 − 0 S(1) spectra are remarkably similar, with a line-width of ∼ 90 km s^{-1}. In Figure 3.23 I only present the Gaussian fit for the CO(3 − 2) line emission.

3.5 Summary

In this chapter, I presented the observations used in my thesis, which consist of near-IR imaging, spectroscopic, and imaging-spectroscopic observations obtained with the CFHT/WIRCam, VLT/CRIRES and VLT/SINFONI instruments, and on radio observations obtained with the ALMA interferometer. Data reduction of the near-IR observations was performed, ALMA observations were reduced by the ALMA team. For the spectroscopic observations, emission lines were measured by Gaussian fit to the lines. The main results of this Chapter are the following:

– K-band continuum emission correlates with the Brγ emission, and the CO with the H_2 emission. In the CO(3 − 2) flux map, I identified the SGMCs discovered

in $CO(1-0)$ by Wilson et al. (2000). All of the SGMCs in the overlap region have associated H_2 and $Br\gamma$ gas. Kinematics of H_2 and CO are well matched.

– Across the overlap region, SSCs are associated with SGMCs.

– There is only one SSC associated with an H_2 peak, which is located in SGMC 4/5. This source is the brightest $Br\gamma$ source. It is also the only source associated with continuum emission at 230 and 345 GHz.

– CO spectra of each SGMCs show that all SGMCs have two (or more) velocity components. Comparison between CO and H_2 $1-0$ S(1) spectra show that there are large variations in the H_2/CO ratio between SGMCs and between velocity components in the same SGMC.

– The high angular resolution of the SINFONI data revealed a bright compact (50 pc) molecular source located in SGMC 2, labeled as PCC1. It has a K-band spectrum showing only H_2 line emission, and it is not associated with any SSC. This source is also detected as an emission peak in the $CO(3-2)$ map. Its H_2 and CO line-width are similar ~ 90 $\mathrm{km\,s^{-1}}$. PCC1 is located in the SGMC with the largest velocity gradient, and where the gradient is the steepest. It seems to be located in the interface of red- and blue-shifted gas.

Chapter 4

Nature of the H_2 emission from the Antennae overlap region

Contents

One of the main questions I faced during my thesis years was to understand the nature of the H_2 emission from the Antennae overlap region with SINFONI observations. Haas et al. (2005) proposed, based on ISO observations, that H_2 line emission in the overlap region could probe shocks driven into molecular clouds. This was later called into question by Brandl et al. (2009), who found lower H_2 line fluxes with Spitzer-IRS, and suggested that the bulk of the warm molecular gas may be heated by star formation after all. I started my thesis working on the SINFONI observations with the idea that maybe some of the emission was associated with dissipation of gas turbulent kinetic energy. My research was motivated by results of earlier ISO and Spitzer observations. Bright H_2 line emission powered by shocks (rather than star formation) has been identified in the diffuse interstellar medium of the Milky Way (Falgarone et al. 2005), as well as in a significant number of extragalactic systems including many interacting galaxies (Appleton et al. 2006; Cluver et al. 2010; Zakamska 2010). This result shows that (1) dissipation of turbulent kinetic energy powers H_2 line emission, and (2) the kinetic energy of interacting galaxies drives turbulence in molecular gas. The difficulty in the Antennae is to be able to separate the H_2 emission associated with PDRs from that from energy dissipation. In this chapter, I explain how we convinced ourselves that the observations were

providing evidence that the H_2 emission from the overlap region is mainly coming from shocked gas.

In this chapter of my thesis, I gather the work I did to assess the origin of the H_2 emission in the Antennae galaxies. This text borrows from what has been presented in Section 4 of my first article Herrera et al. (2011), which focuses on the SGMC 2, and Section 2 of my second article Herrera et al. (2012) which extends the previous results to the other SGMCs. I start this chapter by discussing the H_2 excitation diagram of the SGMCs. Then, I discriminate between PDRs and shocks as the sources powering the H_2 emission. Finally, I quantify the intrinsic H_2 luminosity from SGMC 2 and PCC1, which will be used in the next chapter.

4.1 H_2 excitation diagrams

In environments where the H_2 levels are excited by thermal collisional excitation and de-excitation (in the high-density limit, $n_{\rm gas} \gg n_{\rm crit}$[1]), the H_2 levels will be thermalized and populated as the Boltzmann distribution:

$$N_{\rm u} = N_{\rm H_2}\, g_{\rm u}\, \frac{e^{-E_{\rm u}/kT_{\rm exc}}}{\phi(T_{\rm exc})}, \tag{4.1}$$

where $N_{\rm u}$, $g_{\rm u}$ and $E_{\rm u}$ are the column density, degeneracy[2] and energy of the upper level of the transition, $N_{\rm H_2}$ is the total H_2 column density, $T_{\rm exc}$ is the excitation temperature and $\phi(T_{\rm exc})$ is the partition function. In this environment, where all H_2 levels are thermalized, the comparison between $ln(N_{\rm u}/g_{\rm u})$ and $E_{\rm u}$, the *H_2 excitation diagram*, is a measure of the kinetic temperature of the gas.

When are the H_2 levels thermalized? As mentioned before, if the gas density is larger than the critical density, then the levels will be thermalized. At a constant temperature, the critical density depends on the coefficient rate of spontaneous radiation, A_{ij}. This value is defined for each transition because it depends on the energy in the upper and lower levels. On one hand, the mid-IR H_2 lines have low A_{ij} values (see Table 4.1), implying that the critical densities will also be small ($\sim 10^2$ cm^{-3} for the lowest levels). In molecular clouds, where H_2 is found, densities are larger than 10^2 cm^{-3}. Therefore, mid-IR lines are always a result of collisional de-excitation (they are thermalized levels). The excitation temperature corresponds to the kinetic temperature of the gas. On the other hand, near-IR rovibrational H_2 lines have much higher critical densities, $n_{\rm crit} \sim 10^{4-5}$ cm^{-3}. To thermalize these lines, we require high densities and temperatures.

The H_2 excitation diagrams for SGMC 1, 2 and 4/5 are presented in Fig. 4.1. I complement my SINFONI observations of H_2 rovibrational lines with the H_2 pure-rotational lines observed with Spitzer (Brandl et al. 2009). Their Table 6 lists these values for 8 positions in the central part of the Antennae. Three out of

[1]The critical density $n_{\rm crit}$ is defined as the density at which the collisional de-excitation rate is equal to the spontaneous radiation rate.

[2]statistical weight of the level

Table 4.1: Mid- and near-IR H II lines properties used to construct the excitation diagrams.

	Transition lines	Wavelength [μm]	g_u	E_u [K]	A_{ij} [s^{-1}]
mid-IR	H_2 S(0)	28.2196	5	510	2.95×10^{-11}
	H_2 S(1)	17.0340	21	1015	4.77×10^{-10}
	H_2 S(2)	12.2780	9	1682	2.76×10^{-9}
	H_2 S(3)	9.6645	33	2504	9.86×10^{-9}
near-IR	H_2 1 − 0 S(0)	2.2233	5	6472	2.53×10^{-7}
	H_2 1 − 0 S(1)	2.1218	21	6952	3.48×10^{-7}
	H_2 1 − 0 S(2)	2.0338	9	7585	3.99×10^{-7}
	H_2 1 − 0 S(3)	1.9575	33	8365	4.22×10^{-7}
	H_2 2 − 1 S(1)	2.2477	21	12551	4.99×10^{-7}

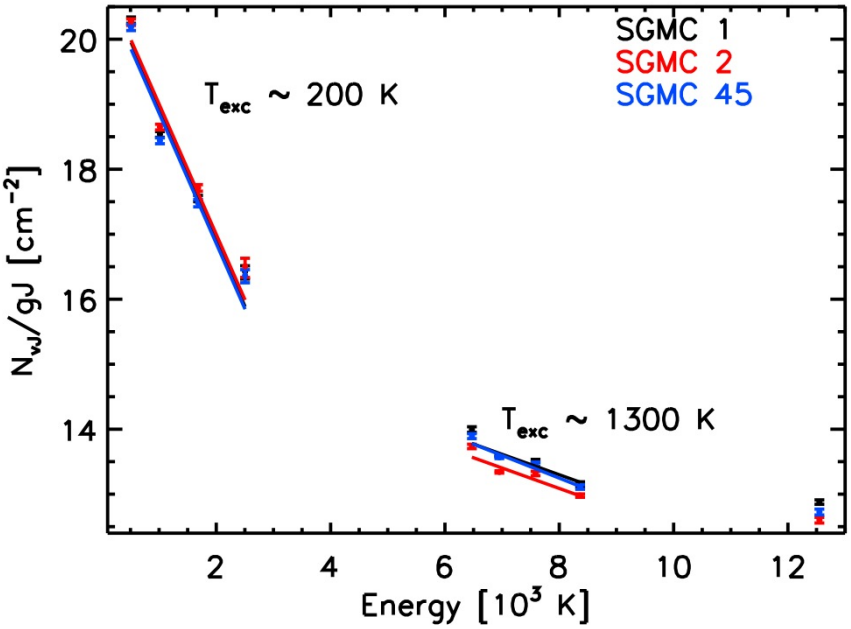

Figure 4.1: H_2 excitation diagrams of SGMC 1 (black), SGMC 2 (red) and SGMC 4/5 (blue), as seen by Spitzer and SINFONI. The color lines correspond to the fit excitation temperatures. Rotational lines are well fitted with excitation temperatures of about 200 K. Rovibrational excitation temperatures are much higher, about 1300 K.

these positions correspond to SGMCs observed with SINFONI. Fig 4.2 shows the location of these positions in the Antennae overlap region and their FOV (Brandl et al. 2009). The color image shows H_2 1 − 0 S(1) (in green), CO(3 − 2) (in blue) and the K-band continuum (in red). Peak 1, 3 and 5 correspond to SGMC 4/5, 1 and 2, respectively. To create the H_2 excitation diagram for the SGMCs, the H_2 rovibrational lines observed with SINFONI were measured from a similar area as the Spitzer observations. Since SGMC 6 is not included in the Spitzer observations

and is weak in the H_2 near-IR lines, I do not show its excitation diagram. Near-IR H_2 rovibrational lines are not corrected for extinction.

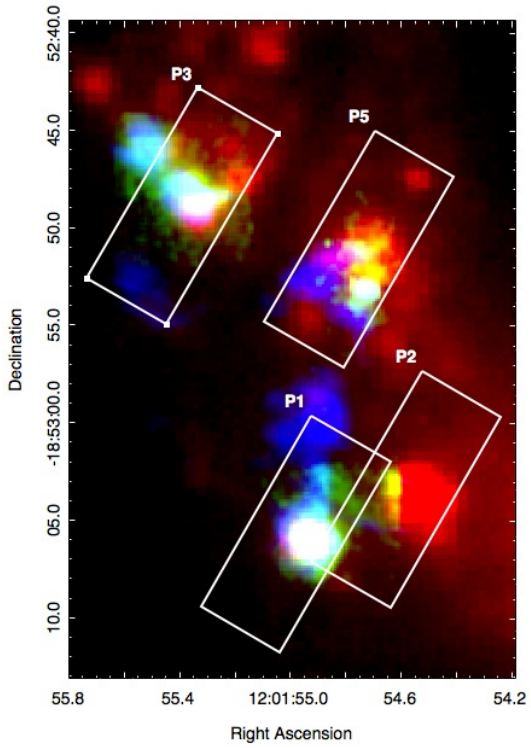

Figure 4.2: Positions of the Spitzer observations obtained with the IRS high-resolution instrument in the Antennae overlap region. The color image shows the K-band continuum emission in red, the H_2 $1-0$ S(1) emission line in green and the $CO(3-2)$ line in blue, respectively. Boxes represent the four Spitzer FOVs (Brandl et al. 2009). Peaks 1, 3 and 5 coincide with our SINFONI observations.

All of the SGMCs have similar H_2 excitation diagrams. I obtained two estimates of the gas temperature by fitting the H_2 population in the rotational states of the $v = 0$ vibrational state from J = 5 to 2 (S(3) to S(0), named rotational temperature) and the population in the $v = 1$ vibrational state from J = 5 to 2 (S(3) to S(0), named rovibrational temperature). I performed linear fits to the $ln(N_{\rm v,u}/g_{\rm u})$ and E_u values, which are listed in Table 4.2. The same table also gives the H_2 total column densities and masses inferred from the two fits and computed with Equation 4.1. The pure-rotational H_2 lines trace gas with kinetic temperatures of $\sim$ 200 K, cool H_2 gas, and the bulk of the H_2 mass where the masses are estimated to be larger than 10^6 $M_\odot$. Rovibrational lines trace less amount of gas, a few hundred solar masses, but much greater gas temperatures ($\sim$ 1300 K). The H_2 excitation diagrams show that a single temperature component cannot account for all the H_2 transition lines.

Table 4.2: Linear fit of the rotational and rovibrational excitation temperatures for the SGMCs, and the associated H_2 total column density and mass.

Source	Rotational			Rovibrational		
	T_{exc} [K]	N_{H_2} [cm^{-2}]	M_{H_2} [10^6 $M_\odot$]	T_{exc} [K]	N_{H_2} [cm^{-2}]	M_{H_2} [$M_\odot$]
SGMC 1	213 ± 5	2.4×10^{21}	7.0	1381 ± 107	1.0×10^{17}	304
SGMC 2	217 ± 7	2.5×10^{21}	7.7	1379 ± 83	6.5×10^{16}	195
SGMC 4/5	217 ± 5	1.8×10^{21}	6.2	1246 ± 89	1.6×10^{17}	527

4.2 Is the H_2 emission powered by shocks or UV radiation?

In molecular clouds, the excitation of H_2 is mainly produced by two mechanisms: far-UV heating of the gas (i.e. PDRs) and heating by shocks (see Section 1.4.2.2 for more details). To discriminate between shocks and UV radiation as the H_2 powering source, I combine complementary methods that make use of the observed gas line intensities and morphologies. In this section, I describe them and apply them to the SGMCs and to the compact source PCC1. I also include in tables and figures two other sources, PCC2 and B1, which are discussed in Appendix A and in Chapter 6.

Table 4.3 lists the H_2 $2-1/1-0$ S(1) and H_2 $1-0$ S(1)/ Brγ line ratios for each source, values that will be used for the diagnostics. H_2 $2-1/1-0$ S(1) values for the SGMCs and PCC1 are taken from Table 1 in Herrera et al. (2012). H_2 $1-0$ S(1)/ Brγ values for SGMC 2 and PCC1 are taken from Table 4 in Herrera et al. (2011). H_2 $1-0$ S(1)/ Brγ ratios for SGMC 1, 4/5 and 6 were estimated from the K-band total spectrum. The description of the H_2 and Brγ line measurements for PCC2 are given in Appendix A and for B1 in Section 6.2.

Table 4.3: Extinction-independent diagnostic line values for the different sources in the overlap region.

Source	H_2 $\frac{2-1}{1-0}$ S(1)	$\frac{H_2\ 1-0\ S(1)}{Br\gamma}$
SGMC 1	0.25±0.02	0.94±0.06
SGMC 2	0.25±0.03	0.73±0.04†/∼3.0‡
SGMC 4/5	0.17±0.03	0.34±0.01
SGMC 6	<0.3	0.35±0.08
PCC1	0.12±0.03	>126
PCC2	0.2±0.1	1.9±0.2
B1	0.37±0.04	0.09±0.01

† ratio obtained for the region where the H_2 $1-0$ S(1) and Brγ emission overlap, ‡ ratio obtained for the southern region in the SGMCs, which has no strong Brγ contribution (see Fig. 7 in Herrera et al. 2011, Appendix B).

4.2.1 Extinction-independent diagnostics: H_2 lines

One of the most widely used diagnostics to discriminate between gas heated by UV radiation and shocks, is the ratio between the H_2 rovibrational lines $2-1$ S(1) and $1-0$ S(1), $R_{2-1/1-0}$ (see section 1.4.2.2). Since both emission lines are close to each other, within the K-band, this ratio is independent of the extinction, which in the overlap region can reach very high values. The left image in Fig. 4.3, taken from Le Petit et al. (2006, their Fig. 27), displays the values of $R_{2-1/1-0}$ for different gas densities $n_{\rm H}$ and radiation fields χ[3]. PDR models estimate a range of $R_{2-1/1-0}$ values, typically 0.6 in PDRs, for radiation fields in the range of $\chi \sim 10^4 - 10^5$ and gas densities in the range of $n_{\rm H} \sim 10^3 - 10^5$ cm^{-3}. The observed values for the whole complexes SGMC 1, 2 and 4/5 are marked in the left panel of Fig. 4.3. These values can be accounted for by PDR models, but only for high UV fields ($\chi > 10^4$, in units of the mean value in the solar neighborhood) and high densities ($n_{\rm H} > 10^5$ cm^{-3}, Le Petit et al. 2006). These conditions exist near massive stars embedded in molecular clouds, but the extended H_2 emission is generally not observed to peak near the brightest SSCs. The notable exception is the embedded cluster in SGMC4/5, which, however, has a higher line ratio (Gilbert et al. 2000).

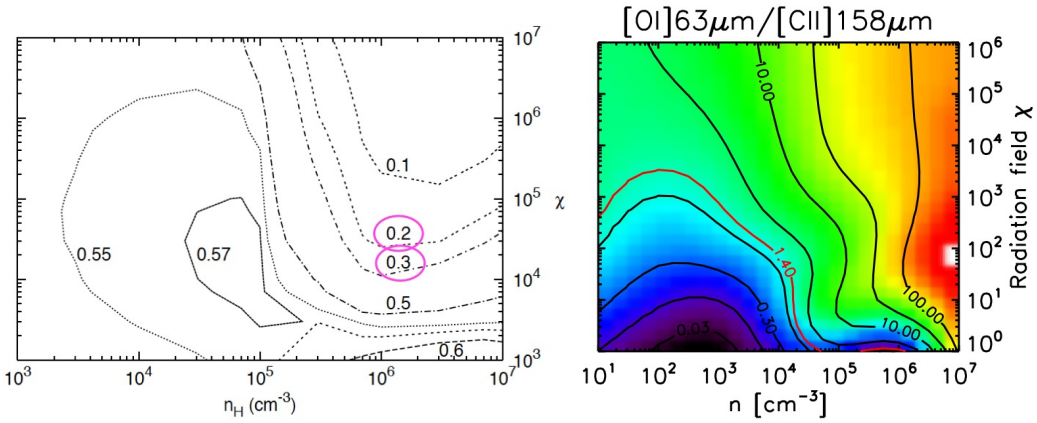

Figure 4.3: *Left*: H_2 $2-1/1-0$ S(1) ratio predicted from the PDR Meudon code. Observed values of the SGMCs are marked with a magenta circle. *Right*: [OI]63μm/[CII]158μm ratio predicted from the PDR code by Kaufman et al. (2006). The observed value of 1.4 (Fischer et al. 1996) is highlighted in red.

4.2.2 Extinction-independent diagnostics: Atomic lines

We can also constrain the physical properties of the gas by studying the ratio between atomic lines. The atomic fine-structure lines [C II]158μm and [O I]63μm are well known tracers of PDRs. They constrain the radiation field and density. The ratio $R_{\rm [OI]/[CII]}$ = [O I]63μm/[C II]158μm is very sensitive to the radiation field. The right image in Fig. 4.3 displays the $R_{\rm [OI]/[CII]}$ ratio for different radiation fields and

[3]Radiation field in Draine's units

gas densities, for PDR models by Kaufman et al. (2006, extracted from the PDR Toolbox[4]). Fischer et al. (1996) measured a ratio of $R_{[OI]/[CII]} = 1.4$ across the central part of the Antennae. In Figure 4.3, I highlight the observed value with a red line. This value is reached for radiation fields weaker than $\chi = 3 \times 10^3$ and for densities lighter than 10^4 cm^{-3}. Schulz et al. (2007) argued that the $R_{[OI]/[CII]}$ ratio measured for the whole galaxy pair is representative for the overlap region. They showed that the PDR fit of the $^{12}CO/^{13}CO$ and [C II]/ CO(1 − 0) line ratios, observed in the overlap region, agree with a radiation field of $\chi = 10^3$, the same for the PDR fit of the [C II]158μm and [O I]63μm lines. Therefore, the PDR contribution is defined for this radiation field.

Now I can compare the results from the analysis of the atomic lines with the H_2 lines. The $R_{[OI]/[CII]}$ ratio indicates that the mean radiation field in the overlap region is $\chi \sim 10^3$. The $R_{2-1/1-0}$ ratio associated with this value is ~ 0.6 (see left panel in Fig. 4.3), which corresponds to the typical ratio measured in PDRs. However, as mentioned before, the observed $R_{2-1/1-0}$ ratios require higher radiation fields of at least one order of magnitude. This is the first indication that the H_2 line intensities are not powered by UV-heating in PDRs. Except for the SSC in SGMC 4/5, the other luminous SSCs have already dispersed most of their gas and dust. Thus, the brightest UV-heated gas would come from clouds away from the clusters. Outside the clusters the intensity of the radiation field is not very high. For a $5{\times}10^6$ $M_\odot$ SSC, the UV field is $\chi > 10^4$ only out to a distance of <100 pc from the cluster and less if we include extinction.

4.2.3 Extinction-independent diagnostics: H_2 and Brγ

Another diagnostic is the ratio between H_2 1 − 0 S(1) and Brγ lines $R_{H_2\ 1-0\ S(1)/Br\gamma}$ (Puxley et al. 1990). These diagnostics provide additional evidence of shock excitation of H_2 in my data. Fig. 4.4 presents the H_2 1 − 0 S(1) and Brγ fluxes measured in 44 star-forming regions within 30 galaxies (Fig. 3 in Puxley et al. 1990, references therein), where, typically, the H_2 1 − 0 S(1) line is weaker than the Brγ line. Only 4 regions have a ratio higher than 1. Their flux ratios range between 0.1 and 1.5 with a mean of 0.5 and a dispersion of 0.3. Puxley et al. (1990) present models for a number of different scenarios and conclude that the line emission is most likely from H II/PDR gas in massive star forming regions, for most of their sources. Their estimated range is $R_{H_2\ 1-0\ S(1)/Br\gamma} = 0.4 - 0.9$, which is represented in the figure as a shaded area. A few sources such as the merger remnants NGC 6240 and Arp 220 show a much higher $R_{H_2\ 1-0\ S(1)/Br\gamma}$ value, highlighted in Fig. 4.4. Observations have shown that their H_2 emission lines are powered by non-thermal sources (Larkin et al. 1995; van der Werf et al. 1993).

Table 4.3 lists the values measured with SINFONI for the SGMCs and compact sources. They are represented in Fig. 4.4 as the colored lines. Since H_2 1 − 0 S(1) and Brγ lines can suffer from high extinction, the ratio is better represented by a line and not just a point in the graph. The magenta line with an arrow represents

[4] http://dustem.astro.umd.edu/pdrt/index.html

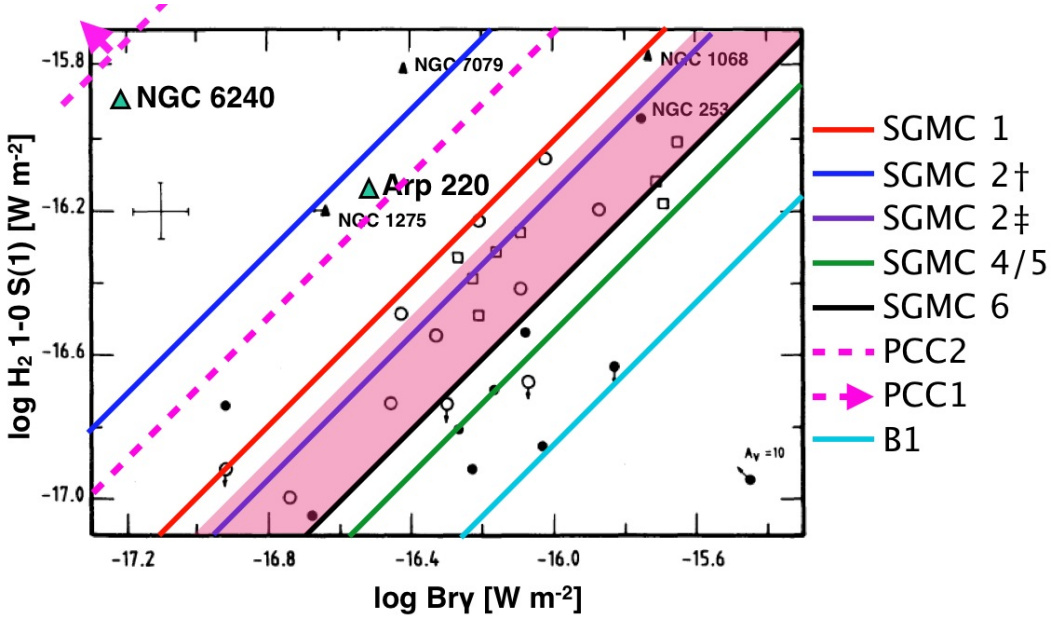

Figure 4.4: This figure shows the H_2 $1-0$ S(1) and Brγ fluxes observed in 44 star-forming regions in 30 galaxies (Puxley et al. 1990). The shaded zone represents the typical values of the H_2 $1-0$ S(1)/Brγ ratio for H II/PDR gas in massive star forming regions. The lines overlaid in the figure represent the H_2 $1-0$ S(1)/Brγ ratio observed for the different sources in the Antennae overlap region listed in Table 4.3. Since the lines intensites of H_2 and Brγ are not corrected for extinction, I prefer to show lines, instead a single point. The red, green and black lines correspond to SGMC 1, 4/5 and 6, respectively. The blue and purple lines correspond to the two measures in SGMC 2 (see Tab. 4.3 and Herrera et al. 2011). The light blue line is the ratio observed for the SSC B1 in SGMC 4/5 (presented in Chapter 6). Finally, dashed magenta lines correspond to PCC1, for the shortest line, and PCC2 (Appendix A).

PCC1 whose ratio is located beyond the scale of the figure. Almost all of the sources are located outside the H II/PDR region, suggesting that most of the H_2 emission is not excited by UV-heating in PDRs.

4.2.4 Morphology of the gas as a diagnostic

It is observed that the H_2 emission from PDRs correlates spatially with the stellar source that is producing the UV radiation (emblematic examples are the galactic star-forming regions Orion (Beckwith et al. 1978) and the Horsehead nebula (Habart et al. 2005)). If we observe this phenomenon at spatial resolutions larger than 60 pc, we cannot spatially resolve the H_2 emission from the stellar source. This size corresponds to the seeing of the H_2 observations presented in this work. Thus, the most powerful indicator that the H_2 emission is not powered by the UV-heating of the gas produced by nearby massive stars, is that H_2 emission does not peak around SSCs outside the embedded cluster in SGMC 4/5 (B1) which will be further studied in Chapter 6.

4.2.5 H_2 emission is shock powered

After contrasting all of these diagnostics, we can conclude that in this turbulent medium, shocks are the main heating mechanism of the H_2 molecule. Indeed, Fig. 4.5 presents the inverse of the $R_{2-1/1-0}$ ratio for shock models by Flower & Pineau des Forêts (2003), in a grid of velocities and pre-shocked gas densities. This figure was adapted from Kristensen (2007). The shaded area corresponds to the observed values for the SGMCs in the overlap $(0.1 - 0.3)$. As we can see, the values are reproduced by shock models at different velocities and densities.

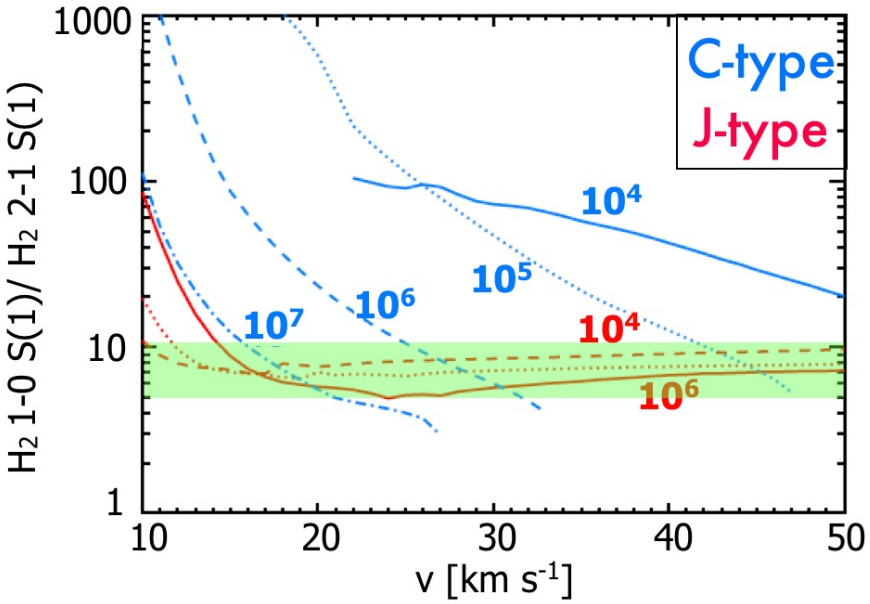

Figure 4.5: This figure presents the H_2 $1-0/2-1$ S(1) ratio estimated from models of C- and J-type shocks by Flower & Pineau des Forêts (2003). Figure adapted from Kristensen (2007). Lines represent the different density of the pre-shocked gas in cm^{-3}. The shaded area corresponds to the range of values observed in the SGMCs of the Antennae overlap region.

H_2 is the major cooling agent in shocks (i.e. Flower & Pineau des Forêts 2010). Other molecular lines (i.e. H_2O, CO, etc) can also contribute to the cooling of the gas, but at a minor rate (Flower & Pineau des Forêts 2010; Godard et al. 2010).

4.3 Bolometric H_2 luminosity of PCC1 and SGMC 2

The intrinsic flux of emission lines that emit in the near-IR can be underestimated by observations due to extinction. In this section, I will detail the calculations of the bolometric luminosity of PCC1 and the extended emission of SGMC 2, which, in Chapter 5, I will use as an example to discuss the H_2 emission as a coolant of the molecular gas.

To estimate the H_2 bolometric luminosities of PCC1 and SGMC 2, I combine the Spitzer and SINFONI H_2 line measurements. This is not straightforward to do

because, besides the near-IR H_2 being attenuated by dust extinction, the Spitzer angular resolution is too low to separate the contributions of the extended and compact source to the mid-IR rotational line emission. First, in Section 4.3.1, I estimate the near-IR extinction for both emission components. Second, I estimate the bolometric H_2 luminosities, under the assumption that the fraction of the H_2 luminosity in the H_2 $1-0$ S(1) line is the same for the extended emission and the compact source (Section 4.3.2).

4.3.1 Extinction correction

To quantify the extinction in the extended gas, I compare the number of ionizing photons $N_{\rm Lyc}$ obtained from the observed Brγ emission line with that computed from the fluxes in the mid-IR [Ne II]λ12.8μm and [Ne III]λ15.6μm fluxes (Brandl et al. 2009). The extinction corresponds to the ratio between the two estimated values of $N_{\rm Lyc}$. This ratio provides the effective extinction factor averaged over the entire FOV at the wavelength of Brγ because the dust extinction of the mid-IR neon lines is much smaller than in the near-IR. The observed $N_{\rm Lyc}$ in the FOV was measured by integrating the Brγ flux over the entire SINFONI cube.

I use the photoionization models of Hummer & Storey (1987) to compute the $N_{\rm Lyc}$ from the Brγ observed flux. Equation 4.2, which gives the $N_{\rm Lyc}$ value for a Brγ luminosity $L_{\rm Br\gamma} = F_{\rm Br\gamma}\, 4\pi D^2$, where $F_{\rm Br\gamma}$ is the flux of the Brγ line and D is the distance to the Antennae (22 Mpc). The value $\alpha_{rec}^{\rm tot} = 2.6\times10^{-13}$ cm^3 s^{-1} is the total recombination coefficient for the Case B approximation (where only Lyman lines are assumed to be optically thick) and $\varepsilon_{\rm Br\gamma}$ is the Brγ emissivity.

$$N_{\rm Lyc} = \frac{L_{\rm Br\gamma}\, \alpha_{rec}^{\rm tot}}{\varepsilon_{\rm Br\gamma}}. \tag{4.2}$$

I use emissivities and line ratios obtained for an ionized region with electron density $n_{\rm e} = 10^2$ cm^{-3} and electron temperature $T_{\rm e} = 10^4$ K (in the Case B approximation), listed in Table 8 of Hummer & Storey (1987). The estimated value is $N_{\rm Lyc} = 4.4\times10^{52}$ phot. s^{-1}. To compute the $N_{\rm Lyc}$ from the Ne fluxes, I use the equations in Ho & Keto (2007) and the [Ne II]λ12.8μm and [Ne III]λ15.6μm fluxes measured by Brandl et al. (2009, their Table 5). I further assume that $n_{\rm e}$ is smaller than the critical density, $\sim 10^5$ cm^{-3}, and adopt the galactic Neon abundance. From Equation 12 in Ho & Keto (2007),

$$N_{\rm Lyc} = 1.4\times10^{65}\, \frac{F_{\rm NeII} + F_{\rm NeIII}}{f_+ + 1.65\, f_{2+}}\ \text{phot. s}^{-1} \tag{4.3}$$

$F_{\rm NeII} = 3.33\times10^{-13}$ erg s^{-1} cm^{-2} and $F_{\rm NeIII} = 2.13\times10^{-13}$ erg s^{-1} cm^{-2} are the Neon fluxes (Brandl et al. 2009), and $f_+ = 0.7$ and $f_{2+} = 0.3$ are the fractional abundances of the Neon lines (computed using Eqs. 7, 8 and 9 from Ho & Keto 2007). I obtain $N_{\rm Lyc} = 6.6\times10^{52}$ phot. s^{-1}. Comparing with the result for Brγ this suggests an extinction factor of 1.5.

PCC1 has a very high column density, $N_H < 9 \times 10^{23}$ H cm^{-2} (Section 3.4.4), and therefore, the extinction must be much higher. An optical depth of $\tau_{ext} = 30$ in the K-band agrees with that value (using the Milky Way extinction curve for $R_V = 3.1$ in Weingartner & Draine 2001). I roughly estimate the extinction correction from $\tau_{ext}(K)$ with a simple toy model. I compute the attenuation due to the dust absorption for every point of a spherical and homogeneous cloud of constant density ρ and line emission per unit volume. The flux that reaches the surface of the cloud depends on the path length l, and is attenuated by a factor $e^{-\tau_\lambda(l)}$. The optical depth $\tau_\lambda(l) = \kappa_\lambda \rho \times l$ depends on the absorption coefficient at a given wavelength κ_λ and the mass density ρ. The κ_λ value is taken from the $R_V = 3.1$ curve in Weingartner & Draine (2001). I sum the attenuated emission over the cloud and compare the result with the total emission for zero opacity. I find a correction factor $e_c = 0.7 \times \tau_{ext}$. I also run the model with a density and emission profile $\rho \propto r^{-2}$ for which I find $e_c = 0.6 \times \tau_{ext}$. In the following I only apply this extinction correction ($e_c = 20$) to the narrow component of the H_2 line emission (50 km s^{-1}, Section 3.4.4). In our interpretation of the data, the broad component is likely to come from the surface of the cloud, for which the extinction correction should be about a factor of 2, because we do not see the emission behind the cloud.

4.3.2 Bolometric correction

The angular resolution of Spitzer/IRS is only 5″, too low to measure the total H_2 luminosity, H_2^{bol}, including the pure-rotational mid-IR lines, of PCC1 directly. To circumvent this difficulty, I need to make an assumption. I assume that the H_2^{bol}/ H_2 1 − 0 S(1) ratio, after extinction correction, is the same for PCC1 and for the extended emission. The total H_2 luminosity (extended emission and PCC1) is taken from the observations by Brandl et al. (2009), assuming that most of the H_2 emission is from the first four rotational lines:

$$\frac{H_2^{bol}(\text{SGMC 2})}{H_2\ 1-0\ \text{S(1)(SGMC 2)}} = \frac{H_2^{bol}(\text{PCC1})}{H_2\ 1-0\ \text{S(1)(PCC1)}} \tag{4.4}$$

$$H_2^{bol}(\text{SGMC 2}) + H_2^{bol}(\text{PCC1}) = \sum_{i=0}^{3} H_2\,\text{S(i)} \tag{4.5}$$

Within these simplifying assumptions, using Equations 4.4 and 4.5, I find bolometric H_2 luminosities of $L_{H_2} = 5.4 \times 10^6$ and 2.6×10^6 $L_\odot$ for the extended emission and PCC1, respectively.

The extinction correction introduces significant uncertainties to these luminosities, in particular for PCC1. The total H_2 luminosity (extended emission plus compact source) does not depend on extinction because most of the H_2 emission is from the mid-IR v=0 rotational lines measured by Spitzer for which extinction is negligible. It is the ratio between both luminosities which depends on the extinction correction. We set a lower limit of 8×10^5 $L_\odot$ on the luminosity of the

compact source by assuming that the extinction is the same for both components. The H_2 $1-0$ S(1) emission represents 3% of the bolometric H_2 emission for PCC1.

4.4 Summary

This chapter focused on the nature of the H_2 emission from the overlap region, which comes from different sources such as SGMCs and molecular compact sources (PCCs). The main results are:

- H_2 excitation diagrams of the SGMCs are similar, indicating that the excitation mechanism for all of them must be the same. Rotational H_2 lines have temperatures of about 200 K, which represents the bulk of the molecular mass, with typical masses of 7×10^7 $M_\odot$. Rovibrational H_2 lines have higher excitation temperatures, $\sim$ 1300 K, tracing smaller amounts of gas with masses of a few hundred of $M_\odot$.

- Spectral diagnostics show that the H_2 emission from most of the overlap region is powered by shocks rather than UV radiation as in PDRs. This H_2 emission traces the dissipation of the gas turbulent kinetic energy.

- For the extended emission from SGMC 2 and PCC1, I estimated the extinction factor in the K-band as 1.5 and 20, respectively. The estimated extinction factor for PCC1 allows to compute its bolometric H_2 luminosity. PCC1 is very luminous, with a bolometric luminosity of 2.6×10^6 $L_\odot$.

Chapter 5

From large scale gas compression to star formation

Contents

In the previous chapter, I argued that the H_2 line emission traces the dissipation of turbulent kinetic energy from SGMCs and PCC1. In this chapter, I propose that the H_2 emission may be accounted for by the loss of turbulent kinetic energy associated with the formation of gravitationally bound gas within convergent gas flows driven by the galaxy interaction. I discuss the general relevance of this interpretation to address the question which motivated my thesis, how do the large-scale dynamics of galaxy interactions trigger star formation?

This research was published in the second year of my thesis in Herrera et al. (2011), before the ALMA data were available. The text of this chapter borrows from Section 5 and 6 of this publication, where for SGMC 2 we refer to the $CO(1-0)$ data of Wilson et al. (2000). For PCC1, we make use of the ALMA results in Section 3 of my second paper Herrera et al. (2012).

Galaxy mergers play a pivotal role in the hierarchical evolution of galaxies building massive galaxies and triggering starbursts and AGN activity. Much of the star formation in mergers occurs in SSCs, as we observe in the Antennae galaxies. Our understanding of how the galaxy interaction may trigger gas collapse and the very early phases in the formation of SSCs is much less developed and relies mostly on theoretical arguments. For example, Scoville et al. (1986) suggested that the interaction between the two galaxies could trigger collisions between pre-existing GMCs.

Jog & Ostriker (1988) argued that shock-heated ambient gas may enhance star formation by increasing the pressure in embedded molecular clouds. Keto et al. (2005) discuss their high resolution interferometric observations of molecular gas and the formation of massive star clusters in the starburst galaxy M82 within this scenario. However, observations of the Antennae overlap region may not be accounted for by the collapse of pre-shock clouds. The large surface density of molecular gas and its fragmentation into complexes with masses of several 10^8 $M_\odot$ (Wilson et al. 2000), two orders of magnitude larger than masses of GMC in spiral galaxies, are evidence for cooling and gravitational fragmentation of the diffuse gas compressed in the galaxy collision.

The formation of SSCs in interacting galaxies must involve a complex interplay of merger-driven gas dynamics, turbulence fed by the galaxy interaction, and dissipation of the kinetic energy of the gas. Hydrodynamical simulations suggest that massive complexes of cold gas akin to SGMCs form where the flows trigger compression, cooling and gravitational fragmentation of the gas (Teyssier et al. 2010). Within SGMCs, a hierarchy of structures must be produced including dense and compact concentrations of molecular gas that are sufficiently massive to form SSCs, pre-cluster clouds (PCCs) (Weidner et al. 2010). To initiate the formation of a SSC, the mechanical energy of the galaxy collision must be radiated away to allow the self-gravity of the PCCs to locally win over their thermal and turbulent gas pressures.

The results presented in the previous chapters raise three questions, (1) how were the SGMCs and PCCs formed? (2) Why is this gas so H_2 luminous? (3) What is the nature of the observed PCC1? To address these questions, I focus on SGMC 2 and PCC1 for which I computed the bolometric luminosities (Section 4.3.2).

This chapter is structured as follows. In Section 5.1 I argue that the extended emission traces highly turbulent molecular gas formed where the galaxy interaction is driving a large scale convergent flow. I relate the H_2 emission to the dissipation of the gas turbulent kinetic energy and the formation of the SGMC 2 complex and PCC1 by gas accretion (Section 5.2). In Section 5.3 I argue that PCC1 is a massive core on its way to forming a SSC. In Section 5.2 I put my work in a more general context. Finally, Section 5.5 gives the conclusions.

5.1 Gas compression and gravitational fragmentation

The Antennae merger is close to pericenter passage when tidal forces are compressive (Renaud et al. 2008, 2009). Thus, I consider that the velocity gradient observed with the H_2 line emission across the SINFONI field of SGMC 2 is tracing a convergent flow driven by the galaxy interaction. The associated gas compression has created the conditions for the gas to cool and to become molecular like in numerical simulations of convergent flows (Hennebelle et al. 2008). As observed in the galaxy collision in Stefan's Quintet, the mechanical energy of the interaction is not fully thermalized in large scale shocks (Guillard et al. 2009). Due to the inhomogeneous, multi-phase,

nature of the interstellar medium much of the gas kinetic energy decays from large to small scales before it is dissipated. Thus, we consider that it is the galaxy interaction that drives the molecular gas turbulence. This interpretation is supported by the fact that the large velocity gradient ($\sim$ 200 km s^{-1}) has the same magnitude as the turbulent line width (Δv = 215 km s^{-1}), and by numerical simulations, which illustrate how dynamical and thermal instabilities lead to the formation of highly structured and turbulent molecular clouds where gas flows collide (Heitsch et al. 2005; Vázquez-Semadeni et al. 2007; Hennebelle et al. 2008).

In the overlap region, the gas surface density is high enough for the turbulent gas to gravitationally contract and fragment within the time scale over which the tidal forces are compressive ($\sim$10 Myr, Renaud et al. 2008). The Jeans length $R_{\rm Jeans}$ and mass $M_{\rm Jeans}$ in a disk are:

$$R_{\rm Jeans} = \frac{5\sigma^2}{2\pi G\Sigma}, \tag{5.1}$$

$$M_{\rm Jeans} = \pi\, R^2_{\rm Jeans}\, \Sigma = \frac{25}{4\,\pi} \times \frac{\sigma^4}{G\,\Sigma}, \tag{5.2}$$

where σ is the gas velocity dispersion and Σ is the surface gas density. I compute $R_{\rm Jeans}$ and $M_{\rm Jeans}$ for the overlap region using the CO(1 – 0) observations, which trace the cold molecular gas, of Wilson et al. (2000) to estimate the gas velocity dispersion and surface density. The value of σ is 30 km s^{-1}. The surface density Σ is obtained taking the ratio between the total virial mass and the total area of the overlap region $\Sigma \sim 500\ M_\odot$ pc^{-2}. I find $R_{\rm Jeans} \simeq 350$ pc and $M_{\rm Jeans} = 2 \times 10^8\ M_\odot$. To compute the free-fall time scale $\tau_{\rm ff} = \sqrt{3\pi/(32\rho G)}$ I determine the mean density ρ as:

$$\rho = \frac{M_{\rm Jeans}}{4/3\,\pi\, R^3_{\rm Jeans}} = \frac{3}{10}\,\frac{\pi\, G\, \Sigma^2}{\sigma^2}. \tag{5.3}$$

The free-fall time scale is $\tau_{\rm ff}$ = 8 Myr.

The Jeans length and mass are comparable to the size of SGMC 2. It is thus likely that this complex has formed by gravitational contraction out of the gas compressed by the galaxy interaction. This interpretation also holds for the other SGMCs. Their sizes and masses are also similar to the Jeans mass. This is supported by the CO ALMA observations. All clouds have two spatially separated velocity components as seen in the channel maps of SGMC 2 in Fig. 3.23 (or as we will see in the next chapter for SGMC 4/5 in Fig. 6.8). In the other clouds, the spatial offsets between velocity components are less obvious, possibly because of projection effects. The velocity difference between components within an individual SGMC is up to 150 km s^{-1} (Figure 3.14). Given the size and mass of SGMCs, this is too large to be accounted only for by the gas self-gravity. The gas kinematics are most likely driven by the galaxy interaction.

In particular for SGMC 2, the gravitational contraction could contribute to the observed H_2 velocity gradient (see the position-velocity diagram for SGMC 2 Fig. 3.22). An estimate of the motions driven by the self-gravity of SGMC 2 is obtained taking the ratio between the free-fall velocity $v_{\rm ff} = 2\ R_{\rm Jeans}/\tau_{\rm ff} \simeq 90$

km s^{-1} and the Jeans radius, 0.26 km s^{-1} pc^{-1}. This value is comparable to the velocity gradient measured with the H_2 line emission (200 km s^{-1} over 600 pc). This calculation provides an upper limit to the velocity gradient from the cloud contraction since it is unlikely that the complex is free-falling. The cloud contraction must occur at a slower rate than free-fall because it takes time to dissipate turbulent energy (Elmegreen 2007; Huff & Stahler 2007).

Thus, we propose that the SGMCs are formed by convergent gas flows driven by the galaxy interaction and the gas self-gravity. Wilson et al. (2000) find that the gas mass inferred from the CO line luminosity matches the virial mass estimated from the CO line width and conclude that the SGMCs are gravitationally bound. In the remainder of this Chapter we keep the term "CO complexes" to refer to gravitationally bound gas within the SGMCs. In my first paper, based on the OVRO data and the interpretation by Wilson et al. (2000), we thought that the CO emission was tracing gravitationally bound gas. The CO line-width was a factor 2 smaller than the H_2 line-with and it was assumed to be the virial line-width. The higher-sensitivity ALMA data have since taught us that the CO and H_2 kinematics are very similar. To be consistent with our first publication, we keep the OVRO CO line-with of SGMC 2 as the virial line-width of the complex. Within this interpretation, the velocity gradient and line width of the H_2 and CO emission arise from gas that is unbound.

In the next two sub-sections we will interpret our H_2 data of SGMC 2 within this scenario. We associate the H_2 emission with the formation of gravitationally bound CO-emitting gas (hereafter CO complex) through gas accretion. We argue that the H_2 emission traces the dissipation of kinetic energy, which is required for gas that is driven by the galaxy interaction to become gravitationally bound.

5.2 The energetics and formation of the SGMC 2 complex

From observations of the Milky Way (Falgarone et al. 2005), and, more recently, of extragalactic sources (Guillard et al. 2009; Nesvadba et al. 2010; Ogle et al. 2010), we know that H_2 line emission is a major coolant of the ISM associated with the dissipation of interstellar turbulence. The H_2 line emission may arise from shocks, as quantified by models such as Flower & Pineau des Forêts (2010), and from friction betweens ions and neutral species in vortices (Godard et al. 2010). Models show that other emission lines contribute to the gas cooling but that they do not change the order of magnitude of the cooling rate (Flower & Pineau des Forêts 2010; Godard et al. 2010). Based on this earlier work, I focus on the SGMC 2, the SGMC with the steepest velocity gradient, and consider the extended H_2 emission from SGMC 2 as a quantitative tracer of the dissipation rate of the kinetic energy of the gas.

Since the H_2 line widths and the velocity gradient across SGMC 2 is twice the CO line width (see Table 3.3), the H_2 emission does not come solely from the dissipation of the turbulent kinetic energy of the CO complex. A significant fraction

of the emission must come from the dissipation of bulk and turbulent kinetic energy of gas driven by the galaxy interaction. Such a loss of kinetic energy is a required step for this gas to become gravitationally bound.

In the following, I quantify this interpretation which connects the energetics of the H_2 gas to the formation of the CO complex. I consider that the CO complex evolves in a quasi-static way assuming that virial equilibrium applies at all times. The virial equation relates the gravitational and turbulent kinetic energy, $E_{\rm grav}$ and $E_{\rm turb}$, and includes the external pressure $P_{\rm ext}$:

$$E_{\rm grav} + 2\,E_{\rm turb} = 3\,P_{\rm ext}\,V, \tag{5.4}$$

where V is the volume. The turbulent energy is $E_{\rm turb} = 3/2\,M_{\rm CO}\,\sigma^2_{\rm CO}$, where $M_{\rm CO}$ is the mass of the CO complex and $\sigma_{\rm CO}$ is the velocity dispersion along the line of sight derived from the integrated CO spectrum of SGMC 2. For a fixed $P_{\rm ext}$, the exchange of energy associated with gas accretion and radiation is associated with the derivative of the enthalpy H of the complex (Huff & Stahler 2007):

$$\dot{H} = \dot{E}_{\rm grav} + \dot{E}_{\rm turb} + P_{\rm ext}\,\dot{V} = -\dot{E}_{\rm turb} + 4\,P_{\rm ext}\,\dot{V} = \dot{E}_{\rm in} - \frac{L_{\rm H_2}}{f_{\rm H_2}}, \tag{5.5}$$

where $\dot{E}_{\rm in}$ is the energy input from gas accretion, $L_{\rm H_2}$ the H_2 luminosity, and $f_{\rm H_2}$ the fraction of the gas bolometric luminosity that is radiated in the H_2 lines used to compute $L_{\rm H_2}$. This fraction is smaller than 1 because some cooling occurs in lines which have not been measured. Combining H_2 and far-IR observations, Maret et al. (2009) find that $f_{\rm H_2}$ is in the range $\sim 0.25 - 0.5$ for shocks associated with gas outflow from low mass stars. I assume that the kinetic energy of the accreted gas is the main source of energy that balances radiative losses (Klessen & Hennebelle 2010). In doing this I neglect the energy that comes from stellar feedback. The fact that the H_2 emission shows no enhancement around the SSC is an indication that stellar feedback does not have a significant contribution to the H_2 emission (Section 4.2).

We follow Klessen & Hennebelle (2010) in introducing the efficiency factor ε which represents the fraction of the accretion energy that drives turbulence. The turbulent energy dissipates over a time scale $t_{\rm dis}({\rm CO}) \simeq R/\sigma_{\rm CO}$ where $R \simeq 300\,{\rm pc}$ is the radius of the SGMC 2 complex (McKee & Ostriker 2007). The balance equation between energy input and dissipation is:

$$\varepsilon \times \dot{E}_{\rm in} = \frac{3}{2}\,M_{\rm CO} \times \frac{\sigma^3_{\rm CO}}{R}. \tag{5.6}$$

We compute the mass accretion rate necessary to drive the gas turbulence by equating the energy input and the radiative losses. This corresponds to a solution of equation (5.5) where the derivative of the gas kinetic energy $\dot{E}_{\rm turb}$ and the term associated with $\dot{V}$ are both small with respect to the right-hand terms. Thus, I write:

$$\dot{E}_{\rm in} = \frac{3}{2}\,\dot{M}_{\rm acc}\,\sigma^2_{\rm H_2} \simeq \frac{L_{\rm H_2}}{f_{\rm H_2}}, \tag{5.7}$$

where $\sigma_{\rm H_2}$ is the velocity dispersion along the line of sight derived from the H_2 data. To quantify $\dot{M}_{\rm acc}$ and ε, I consider only the turbulent component of the velocity field (FWHM(H_2) $\sim 150\,{\rm km\,s^{-1}}$), assuming that accretion occurs from turbulent gas with a mean velocity equal to that of the CO complex. For $\sigma_{\rm H_2} = 65\,{\rm km\,s^{-1}}$ and $\sigma_{\rm CO} = 30\,{\rm km\,s^{-1}}$, we find $\dot{M}_{\rm acc} = 5.3/f_{\rm H_2}\ M_\odot\,{\rm yr^{-1}}$ and $\varepsilon = 1.8 \times f_{\rm H_2}$. For this interpretation to hold we must have $\varepsilon < 1$, and thus $f_{\rm H_2} < 0.5$. The fact that the H_2 line width is larger than that of CO shows that this holds. In our following calculations we will adopt $f_{\rm H_2} \sim 0.25$.

We scale $\dot{M}_{\rm acc}$ by the turbulence dissipation time scale to estimate the mass of gas from which accretion is occurring: $M_{\rm acc} = \dot{M}_{\rm acc} \times t_{\rm dis}({\rm H_2})$, where $t_{\rm dis}({\rm H_2}) \simeq R/\sigma_{\rm H_2}$ is the turbulent dissipation time scale. The large scale flow can feed this mass reservoir, compensating for what is accreted onto the CO complex, because the dissipation time scale is comparable to the dynamical time scale associated with the velocity gradient across SGMC 2 ($\tau_{\rm dyn} = 3 \times 10^6\,{\rm yr}$). We find $M_{\rm acc} = 2.4 \times 10^7/f_{\rm H_2}\ M_\odot$. For $f_{\rm H_2} \sim 0.25$, $M_{\rm acc}$ is 25% of $M_{\rm CO}$. Thus, the mean density in the CO complex may only be a few times larger than that of the accreted gas. This agrees with our estimate of the efficiency factor ε. Based on their numerical simulations and theoretical arguments, Klessen & Hennebelle (2010) argue that the efficiency factor ε is roughly equal to the ratio between the density of the accreting gas to the mean density of the bound system.

Computing the ratio between the CO mass of SGMC 2 and the mass accretion rate, we obtain a time scale $t_{\rm acc} = 7 \times 10^7 \times f_{\rm H_2}$ yr. For $f_{\rm H_2} \sim 0.25$, this is slightly longer than the 10 Myr time scale over which the dynamics of the interaction may have been driving the convergent flow (Renaud et al. 2008). However, within the uncertainties in this rough calculation, we consider that the present accretion rate is close to the mean rate needed to account for the formation of the SGMC 2 complex as a result of gravitational fragmentation and gas accretion driven by the galaxy interaction.

Our interpretation introduces a dynamical view of the present state of the SGMC 2 complex. The virialized CO complex is physically associated with gas which is too turbulent to be bound. This unbound gas is dynamically fed by the convergent flow. It contributes an accretion flow onto the CO complex, which has the necessary magnitude to drive the gas turbulence, i.e. to balance the dissipation of the gas turbulent kinetic energy. Klessen & Hennebelle (2010) have proposed a similar interpretation to account for the formation and subsequent growth of turbulent molecular clouds in the LMC. Now, in the next section, we move from the SGMC 2 complex to a smaller scale to discuss the nature of PCC1.

5.3 The nature of PCC1

In this section we discuss the nature of PCC1. First, we compute the mass of PCC1 with two methods, assuming virial equilibrium and from the dust continuum emission. Second, we demonstrate that there is no (or a little) star formation within PCC1. Third, we discuss the dynamical state of this source, by proposing that its H_2 emission traces gas accretion, as in SGMC 2.

5.3.1 PCC1 mass

The compactness of PCC1 suggests that it may be gravitationally bound, and that we can estimate the gas mass using the virial theorem. For a homogeneous spherical cloud the balance between gravitational and kinetic energy gives the virial mass as

$$M_{\rm vir} = 5\frac{R\sigma^2}{G}, \tag{5.8}$$

where R is the radius, σ the velocity dispersion of the gas, and G the gravitational constant. Using the velocity dispersion of $\mathrm{CO}(3-2)$, we obtain a virial mass of $M_{\rm vir} = 4.6 \times 10^7 \times (\sigma_v/40\ \mathrm{km\ s^{-1}})^2\ M_\odot$. Since ALMA does not spatially resolve the PCC, we instead used the 50 pc size measured with SINFONI.

Dust continuum emission can also be used as an estimator of the molecular gas mass. Fig. 3.10 shows the continuum emission at 230 and 345 GHz, with overlaid contours of $\mathrm{CO}(2{-}1)$ and $\mathrm{CO}(3-2)$, respectively. PCC1 does not have an obvious counterpart in the continuum emission. To obtain an upper limit for the gas mass, we measure the standard deviation in a region away from the CO emitting sources. The gas mass was estimated as:

$$M_{\rm gas} = \frac{S_\nu\, D^2}{\varepsilon_{\rm H}(\nu)\, B_\nu(T_{\rm d})}. \tag{5.9}$$

where S_ν is the dust continuum emission, D is the distance the Antennae, $\varepsilon_{\rm H}(\nu)$ is the dust emissivity per hydrogen atom and $B_\nu(T_{\rm d})$ is the black body emission at a dust temperature $T_{\rm d}$. For that, we used a typical dust temperature of 15 K and the emissivity per hydrogen measured in the Taurus molecular cloud by Planck Collaboration et al. (2011a). This value is twice the value measured for the atomic medium in the solar neighborhood (Planck Collaboration et al. 2011b). The gas mass associated with 3σ is $M_{\rm gas} = 2.0 \times 10^7\ M_\odot$. This upper limit is lower than the virial mass estimated from the CO line-width and the H_2 size. The column density derived from the gas mass upper limit is very high, $N_{\rm H} = 9 \times 10^{23}$ H cm^{-2}.

5.3.2 Is there star formation within PCC1?

The characteristics of PCC1 are very different from H II regions (star-forming regions). Its spectrum shows prominent H_2 lines and negligible ionized lines and continuum emission (Figure 3.19).

We quantify the star formation within PCC1 by comparing the Brγ intensity with the radio continuum emission. Neff & Ulvestad (2000) presented the radio emission maps at 4 and 6 cm for the whole Antennae pair. PCC1 has no clear radio counterpart. The maps show a slight excess (50 μJy,) at the position of PCC1 (Figures 4 in Neff & Ulvestad 2000). Assuming that this radio flux is entirely thermal, we estimate the number of ionizing photons as (Roman-Lopes & Abraham 2004):

$$N_{\rm Lyc} = 5.59 \times 10^{48}\, T_{\rm e}^{-0.45} \left(\frac{\nu}{5\ {\rm GHz}}\right)^{0.1} \left(\frac{S_\nu}{\rm Jy}\right) \left(\frac{D}{\rm kpc}\right)^2. \qquad (5.10)$$

where $T_{\rm e}$ is the electronic temperature assumed to be 10^4 K, ν the frequency of the observations, S_ν the thermal radio emission in Jansky and D the distance in kiloparsecs. This yields an ionizing photon rate of $N_{\rm Lyc} = 2 \times 10^{51}\,{\rm s}^{-1}$, which corresponds to a Brγ flux of $\sim 5 \times 10^{-16}$ erg s^{-1} cm^{-2} (Equation 4.2). This value is a factor 5 larger than the upper limit on the observed Brγ flux in Table 3.3 after scaling by our estimate of the extinction correction (a factor 20, see Section 4.3.1). This slight discrepancy could indicate that the newly formed stars are concentrated at the center of the cloud. In this case their emission could be more attenuated than the H_2 emission.

The $N_{\rm Lyc}$ value computed from the radio continuum observations yields, for a young (1 − 2 Myr) burst, a stellar mass of $\sim 4 \times 10^4\ M_\odot$ based on Starburst99 models. This stellar mass is 0.2% of the PCC1 gas mass derived from the dust continuum emission.

5.3.3 PCC1, forming by gas accretion

PCC1 appears to be located at the interface between blue and redshifted gas (see Figure 3.23 in Section 3.4.4) where CO shows a steep velocity gradient ($\sim$1 km s^{-1} pc^{-1} in the position-velocity diagram in Figure 3.22). The observed properties of PCC1 are consistent with a scenario where the formation of SSCs is triggered by interactions between two gas flows. In SGMC 2, depending on the full 3-D geometry, the flows could either be colliding or creating a large velocity shear, and most likely a combination of both. In either case, the interaction drives a turbulent energy cascade in which kinetic energy is being dissipated. This is where we would expect the highest energy dissipation rate.

Can the H_2 emission from PCC1 be powered by protostellar outflows as observed in our Galaxy? The bolometric luminosity of the PCC is $\sim 10^7\,L_\odot$. Observations of, e.g., NGC 1333 (Maret et al. 2009) show that the bolometric luminosity of protostellar outflows is on the order of $10^5\ L_\odot \times \dot{M}_{\rm wind}$, where $\dot{M}_{\rm wind}$ is the stellar mass loss rate in M$_\odot$ yr^{-1}. To account for the observed H_2 luminosity, the stellar mass loss rate has to be $\dot{M}_{\rm wind} = 100\ M_\odot$ yr^{-1}. The small embedded stellar mass of $M_\star = 4 \times 10^4\,M_\odot$ (Section 5.3.2) leads to an age for PCC1 of 400 yr, which makes protostellar winds an implausible energy source.

Is PCC1 a bound cloud formed through gravitational fragmentation? The cloud luminosity may be accounted for by the dissipation of the cloud kinetic energy for

a cloud mass of a few $10^7\,M_\odot$ – a value comparable to the virial mass $5\times10^7\,M_\odot$ – and a dissipation timescale of 1 Myr. This is comparable to the cloud crossing time $\tau_{\rm cross}$, and also the dynamical time scale $\tau_{\rm dyn}$ associated with the velocity gradient of $1\,{\rm km\,s^{-1}\,pc^{-1}}$ at the position of the cloud. The similarity of both time-scales indicates that the cloud may still be forming by accreting gas, and therefore that a significant part of the cloud luminosity may be powered by gas accretion. This interpretation is supported by the ALMA continuum observations which sets an upper limit on the PCC1 mass lower than the virial mass (Section 5.3.1).

The H_2 luminosity associated with the dissipation of the turbulent energy driven by the gas accretion is:

$$L_{\rm diss} \simeq 10^7\,L_\odot \times \left(\frac{\dot{M}_{\rm acc}}{10\ M_\odot\ {\rm yr}^{-1}}\right) \times \left(\frac{\Delta V/2}{100\ {\rm km\ s^{-1}}}\right)^2, \qquad (5.11)$$

where ΔV is the velocity gradient across the field 200 $\rm km\,s^{-1}$(the difference in velocities of the colliding flows). To account for the observed H_2 luminosity, the mass accretion rate has to be $\dot{M}_{\rm acc} \sim 10\ M_\odot\ {\rm yr}^{-1}$.

5.4 Discussion

The observations of my thesis are related to two main questions in the field of star formation. How do super star clusters form? What are the roles of turbulence and stellar feedback in regulating the star formation efficiency in galaxy mergers? I discuss how our observations and interpretation may be of general relevance for these fields.

5.4.1 The formation of super-star clusters

Star formation is the result of the hierarchical structure of the molecular interstellar medium established by turbulent compression and gravitational contraction (Mac Low & Klessen 2004). The available gas fragments over a range of masses and time scales. Massive clusters form at different times from the densest and most massive gas concentrations. For SGMC 2, this view is supported by the presence of two massive clusters (the near-IR SSC-C and the compact ionized source H II1, see Figure 3.17 in Section 3.4.3), which have formed before PCC1. More clusters, too small to be identified individually, are likely to have formed or to be in the process of being formed. Thus, the formation of SSCs in SGMC 2 can be understood within the same framework as the formation of smaller clusters in disk galaxies like the Milky Way.

This work highlights three physical parameters which may contribute to account for the formation of exceptionally massive clusters in the overlap region of the Antennae. These may be of general relevance for the formation of SSCs in other extragalactic objects: other interacting/merging galaxies, and also starbursts and irregular dwarf galaxies (Keto et al. 2005; Weidner et al. 2010).

(1) The presence of compressive motion on large scales which collects the gas. The formation of the SGMC 2 complex and that of PCC1 is driven by the galaxy interaction. The large scale dynamics trigger the gas compression necessary for their formation and their subsequent growth by gas accretion.

(2) As discussed in earlier studies (Escala & Larson 2008; Weidner et al. 2010), shear is the second key parameter in the formation of massive clusters because it sets the maximum mass that the gas self-gravity can collect. In the Antennae, the present geometry of the interaction, which temporarily makes the tidal forces compressive (Renaud et al. 2008), is favorable to the formation of massive clusters. As discussed by Renaud et al. (2009) such conditions occur repeatedly in galaxy mergers.

(3) High turbulence is an additional key parameter. Since the Jeans mass is proportional to σ^4 (see Section 5.1), a high value of the velocity dispersion σ scales up the masses of the clouds formed by gravitational fragmentation. To form a SSC, it is not sufficient to bind a large mass of gas. It is also necessary that the star formation efficiency becomes high when the gas mass is highly concentrated. It is likely that high turbulence is a key factor which prevents star formation to be efficient before the cloud mass has been concentrated by gravity. This is a prerequisite to form a dense, potentially bound, cluster rather than a loose OB association (Elmegreen 2008).

5.4.2 The impact of turbulence

The impact of turbulence on the star formation efficiency is a long standing topic of research (Mac Low & Klessen 2004). Krumholz & McKee (2005) and Padoan & Nordlund (2011) used numerical simulations to quantify the dependence of the star-formation rate per free-fall time on the Mach number of turbulence. Both agree that, independent of the mean cloud density, for a cloud near virial equilibrium, the fraction of the gas mass that is unstable to collapse is small. If this is correct, then the formation of dense clusters within a cloud supported by turbulence must occur over several cloud crossing times as argued by Tan et al. (2006) and Krumholz et al. (2006). Elmegreen (2008) expresses a different view point by proposing that star formation becomes efficient within cores with a mean density $> 10^4$ H cm^{-3} independent of turbulence.

These ideas are being tested against observations of galactic star forming regions and cores, which are far more detailed than the present information we have on PCC1. High angular resolution observations of high density gas and shock tracers would be needed for a detailed study of the formation of SSCs on the example of this source, and if it is consistent with present ideas based on observations of lower mass and less turbulent cores. Here we only make preliminary remarks that can soon be tested with ALMA (hopefully in Cycle 1, see Section 7.2). The mean density of the compact H_2 source is $\sim 9 \times 10^4$ H cm^{-3}. We estimate its formation time scale to at least 10^6 yr, but the star-formation efficiency is still very small (stellar to gas

mass ratio $\sim 0.2\%$). This remarkable result may indicate that the high turbulence (1-D velocity dispersion $\Delta v_{CO} \sim 40\,km\,s^{-1}$) has been very effective at preventing star formation. Star formation may occur rapidly once the rate of mass accretion becomes insufficient to drive the present amplitude of turbulence. The fact that stars may be forming out of gas which has lost the turbulent energy it had during the initial gravitational contraction reduces the requirement on the star formation efficiency to form a bound stellar cluster.

5.5 Conclusions

In this chapter, I have combined my H_2 and CO observations to study how the large-scale gas dynamics of the Antennae galaxy interaction triggers the formation of SGMCs and SSCs. I presented a quantitative interpretation of the H_2 emission from the SGMC 2 and PCC1. I have also discussed how these observations are of general relevance for the formation of massive clusters and the efficiency of star formation in mergers. The main conclusions of this chapter are:

– I argue that the extended emission from SGMC 2 traces a convergent turbulent flow driven by the interaction.

– The virial mass of PCC1 is larger than the mass estimated from the dust continuum emission. The absence of Brγ emission and of some obvious counterpart in the radio continuum set a low limit on the mass of newly formed stars (stellar mass fraction $\sim 0.2\%$). To our knowledge, this is the first time that an extragalactic source with such characteristics is found.

– The line-width of the H_2 spectra show that the SGMC 2 complex and the compact source are both associated with gas which is too turbulent to be bound. We argue that this suggests that the H_2 emission is powered by gas accretion. We show that the required accretion rate is of the right order of magnitude to drive the gas turbulence and to account for the formation of both the SGMC 2 complex and PCC1 by accretion.

– By observing gas cooling through H_2 lines, we may have discovered a massive cloud on its way to form an SSC within the next few Myr. However, this conclusion is only tentative, and will remain incomplete, until we obtain the missing information about the mass, the density structure and the kinematics of the bulk of the gas. The H_2 line emission provides this information only for the warm shock excited fraction. PCC1 was detected in the CO ALMA data, but this optically thick line does not probe the inner structure of this cloud. The fact that the CO and H_2 line-widths are similar suggests that both emissions come from the same gas which is not gravitationally bound. The missing information can be obtained by observing high density gas tracers and optically thin isotopes of CO with ALMA.

– We propose that the strong turbulence observed in the extended emission and PCC1 is of general relevance for the formation of SSCs in two ways. A high value of the gas velocity dispersion increases the masses of the clouds formed by gravitational fragmentation. It may also prevent star formation to be efficient before the cloud is fully formed, i.e. as long as turbulence is driven by accretion. Clusters may form out of gas which has lost much of the turbulent energy it had during gravitational formation of the pre-stellar cloud. If this is correct, then it reduces the requirement on the star-formation efficiency to form a bound stellar cluster.

– Our observations highlight the role of merger-driven turbulence in regulating the star-formation efficiency in interacting galaxies. Within the field of view of our SINFONI observations, about 2% of the molecular gas has been turned into stars. We relate this small efficiency to the fact that the gas turbulence does not dissipate because it continues to be driven by on-going accretion.

Chapter 6

Stellar Feedback

Contents

Stellar clusters are formed in virialized molecular clouds. In these clouds, self-gravity is balanced by internal turbulent kinetic energy which together regulate the energetics of the cloud and thereby star formation. Within a molecular cloud, where gravity locally wins over turbulence, the matter collapses to form stars. In the absence of a source of energy to drive turbulence, star formation proceeds to efficiencies of order unity within a few crossing times (a few dissipation time-scales), that is, all the gas in the molecular cloud is used as fuel to form stars. However, observations of GMCs in the Milky Way indicate that the star formation efficiency $\varepsilon_{\rm SF}$ is a few up to 20%, for GMCs with masses of a few 10^4 to 10^7 $M_\odot$ (Murray 2011). Many studies have considered *stellar feedback*, i.e. the interaction of stars with the ISM, as a main energy source to maintain turbulence as stellar clusters are formed (Tan et al. 2006; Krumholz et al. 2006). In these models star formation and feedback are concurrent. Eventually, stellar feedback will unbind and disperse the matter around the stars. How quickly this occurs is key to the star formation efficiency.

The newly formed stars affect their surrounding matter in several ways, which have been quantified analytically. Matzner & McKee (2000) discuss the ability of winds from low mass stars to drive turbulence and balance dissipation. Matzner (2002) discuss the disruption of clouds by photoionization and expansion of the H II region by the thermal gas pressure. More recent studies have included the impact of the radiation pressure on the expansion of the H II region and the disruption of the

parent molecular clouds (Murray et al. 2010; Fall et al. 2010). Radiation pressure is the dominant mechanism for massive stellar clusters, such as those observed in the Antennae, where the escape velocity is larger than the sound speed of the H II gas (Krumholz & Matzner 2009; Murray et al. 2010). The mechanical energy associated with SN explosions and winds from massive stars are also potentially able to disrupt clouds. In this scenario, the mechanical energy is thermalized in shocks producing high pressure hot plasma. This plasma can drive the expansion of the surrounding matter, provided it remains within the cloud. Observations and theoretical work indicate that this may not be as efficient as originally proposed (Castor et al. 1975), because the plasma is able to flow out through holes in the bubbles very early in the expansion (Harper-Clark & Murray 2009). Observations suggest that embedded clusters manage to break apart their parent cloud within a time scale shorter than the main sequence life time of their most massive stars (Murray & Rahman 2010; Lopez et al. 2011), thus before SN explosions become significant.

Numerical simulations provide an additional point of view on stellar feedback. Dale & Bonnell (2011) have modeled the formation of massive stellar clusters from turbulent gas taking into account the ionization by newly formed stars. They find that contagious star formation occurs but it is not a dominant process. The velocity field of the turbulent cloud produces a filamentary structure. The radiation from star clusters ionizes the voids, where the density is low. Stars are formed were the gas density is high, in the filaments. The star formation process within such a turbulent molecular cloud produces several stellar clusters of different masses, born at different ages. Within these simulations, star formation is concurrent to cloud formation. Turbulence is not uniquely driven by feedback. On-going accretion of gas from the surrounding medium can contribute to balance energy dissipation (Vázquez-Semadeni et al. 2010; Klessen & Hennebelle 2010).

Lopez et al. (2011) have used observations of the 30 Doradus star-forming region in the LMC to compare the relative values of the pressures associated with radiation, ionized gas and hot plasma, as a function of position in the nebula. Within the shells close to the core of the central R136 super star cluster, radiation pressure dominates. In this chapter of my thesis, I am using observations of the Antennae to carry out a similar study for the most massive SSC across the overlap region. The chapter is organized as follows. In section 6.1, I present the search for SSCs lying in the SINFONI fields which are associated with molecular and ionized gas on scales of their parent GMC. I used my data and data from the literature to look for H_2 and Brγ emission lines. Section 6.2 focuses on the most massive SSC, located in SGMC 4/5, which has associated ionized and molecular gas emission. This cluster is still embedded in its parent cloud. I present its physical characteristics and measurement of their gas emission lines. From these parameters, I do a detailed analysis of this source by modeling the H II region and PDR. I use the model to compare the pressures associated with radiation, turbulence, warm ionized gas and stellar winds finding that turbulence balances gravity, allowing radiation pressure to disrupt the cloud. Within this scenario, I compute the expansion of the molecular gas, which is exposed to the radiation pressure from the central cluster. Finally,

Section 6.3 gives the conclusions of this chapter.

6.1 Search for SSCs within their parent clouds

Young and massive SSCs found in the Antennae overlap region are observed to emit in the $K-$band continuum. But how many of them are associated with molecular and/or ionized gas? All clusters younger than about 10 Myr have significant ionizing flux. If the cluster is still embedded in its parent cloud, the H II region will be compact ($\sim$100 pc) and barely resolved by the arcsecond spatial resolution of near-IR ground-based observations. For older SSCs, the Brγ emission will be more extended because the ionizing photons will travel into the SGMCs and the more diffuse ISM, over distances larger than the size of their parent cloud.

In this work I have selected a few SSCs identified in the literature which lie within the four SINFONI fields. For each of these SSCs, I search in the SINFONI data for compact (diameter $\sim1''$) gas emission associated with SSCs. The goal of this search is to identify which SSCs are still embedded in their parent clouds. First, I indicate how I selected the clusters. Second, I explain how I used the SINFONI data to search for compact line emission.

6.1.1 Known SSCs within SINFONI fields

Several young ($<$8 Myr) and massive ($>10^5$ $M_\odot$) SSCs lie within the four fields observed with SINFONI (see Fig. 3.17). I have compiled three studies to identify them. First, I included the SSCs observed by Gilbert & Graham (2007) with the NIRSPEC (Near-IR SPECtrograph) at the Keck II telescope. Second, I used the SSCs observed with the NICMOS (Near Infrared Camera and Multi-Object Spectrometer) mounted at the HST, listed by Whitmore et al. (2010, Table 8). Last, I searched the SSCs list of Christopher (2008, Table 2.4) based on near-IR observations from the Wide-Field Infrared Camera (WIRC) at Palomar Observatory, from which a selection of clusters were observed with NIRSPEC. At the end I have six objects listed in Table 6.1.

Figure 6.1 shows the K-band continuum as seen by WIRCAM and the positions of the SSCs across the Antennae overlap region. Blue squares correspond to the SSCs listed in Table 6.1; green diamonds highlight the position of other young IR clusters, observed with WIRC imaging and listed in Table 2.4 of Christopher (2008), but not observed with the spectrometer NIRSPEC and not detected in the SINFONI data-cube. Red circles indicate the position of the PCCs and black triangles show the position of three ionized sources that are presented in Section 6.1.2. The ages and masses provided in Table 6.1 are taken from these three publications. Gilbert & Graham (2007) estimated the ages from the Brγ equivalent width, and the masses from the K-band magnitude without extinction correction. Whitmore et al. (2010) computed the ages and masses by comparing the fluxes in the UBVIHα filters with population synthesis models. The ages estimated by Christopher (2008)

are computed from the Brγ and/or CO bandheads[1] equivalent widths, and the masses correspond to the photometric masses based on HST high resolution observations. Most of the SSCs were observed with more than one instrument. In that case, I select the age and mass given by Gilbert & Graham (2007), which is the most reliable because they are based on high resolution spectroscopy. The fourth column gives the reference being used with its ID in the original publication. My nomenclature is that of Gilbert & Graham (2007). The SSC not observed by them is labeled as S.

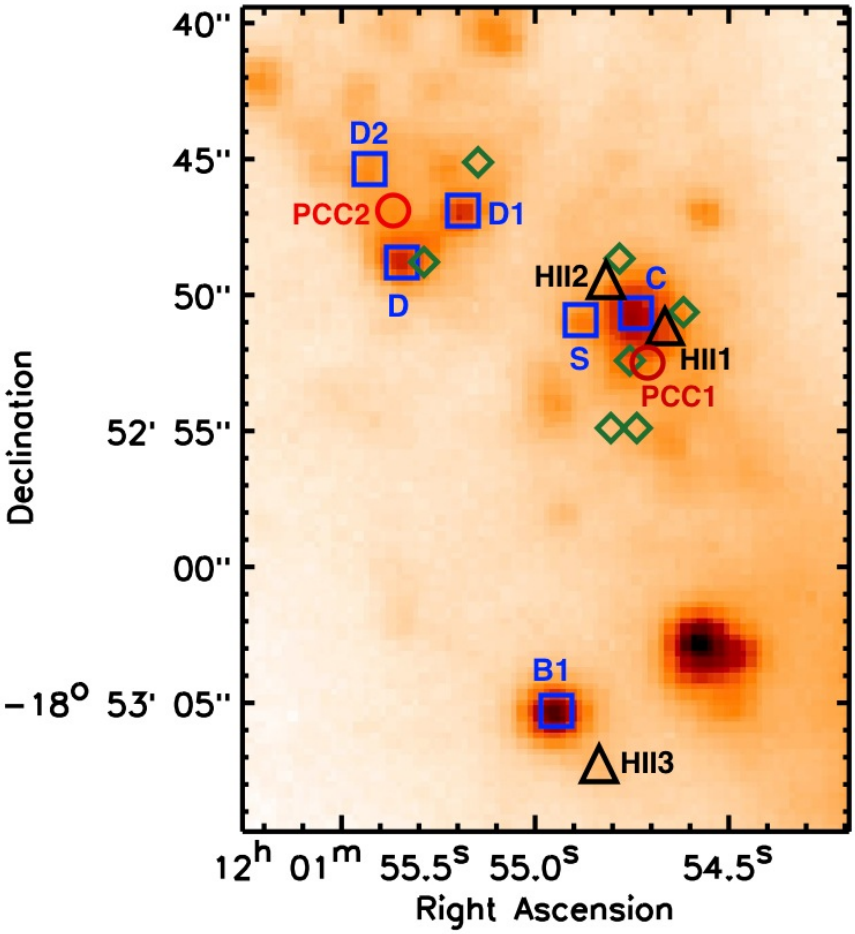

Figure 6.1: Positions of the SSCs lying within the four SINFONI fields and listed in Table 6.1 (blue squares). Green diamonds represent young IR clusters listed in Christopher (2008), not included in my selected SSCs because they were not observed with NIRSPEC and not detected in the SINFONI data-cubes. Red circles and black triangles show the position in the overlap region of the two PCCs (Section 3.4.4 and Appendix A) and the three ionized sources (Section 6.1.2).

[1] CO rovibrational overtone bands, which have $\Delta v = 2$. The first CO overtone bandhead is at 2.3 μm (CO $v = 2 - 0$).

6.1.2 SINFONI measurements of SSCs

The detection of line emission associated with SSCs in the SINFONI data-cube is not straightforward because the SGMCs, where SSCs are found, show complex velocity structures and some of them have several sources (see Fig. 3.13 and 3.17). I face two main difficulties. The first one is to isolate the emission associated with the SSC from the extended gas where the SSC is embedded, and the second is to isolate the different sources within the SGMCs. I focus on secure detections, for SSCs which are isolated.

For each SSC detection, I obtain the K-band spectrum by circular aperture photometry. The aperture diameter is $\sim 1\farcs3$ (140 pc), twice the observed FWHM size. This is appropriate to quantify compact emission from clusters still embedded in their parent clouds. I subtract the nearby background measured within an annulus of $0\farcs65$ width, the seeing of my SINFONI data. Within the SINFONI spectra, I measure the molecular and ionized emission line fluxes. Tab. 6.1 also lists the K-band continuum emission of the SSCs, and, if the Brγ line was detected, its flux, central velocity and line-width. Three sources in the table have Brγ emission, and only in one of them I detect H_2 and Brγ. For the other sources, upper limits for H_2 $1-0$ S(1) and Brγ are estimated. To obtain these upper limits, I apply aperture photometry in the integrated intensity line images per SGMC to all the pixels, after masking the detected sources within each SGMC. The upper limits in the table are the 1-σ standard deviation of the Gaussian distribution.

I also search for ionized compact sources in the Brγ line emission. In total, three ionized compact sources are identified in SGMC 2 and 4/5. All of them have a K-band continuum counterpart, but they do not have associated molecular gas. It is likely that the compact ionized sources young and dense H II regions ionized by internal sources (embedded stellar clusters) which have photo-ionized most of their surrounding gas, but not cleared it out. Figure 6.1 shows their positions in the overlap region. The H II1 source in SGMC 2 was already introduced in Herrera et al. (2011). I estimate the extent of the emission (FWHM) from cuts across the sources in the integrated Brγ image. I obtain their spectra by circular aperture photometry, integrating the emission within a diameter twice the measured FWHM, and subtracting the nearby background estimated from an annulus of width equal to the SINFONI seeing. Table 6.2 lists the Brγ and continuum fluxes. It also includes the ages of these sources, inferred from the Brγ equivalent width (EW), i.e. the ratio between the line intensity and the continuum emission. Since the Brγ emission traces the young, ionizing stellar population, and the continuum emission comes from all the stellar population, the Brγ EW is an age indicator. This value depends neither on the extinction nor on the cluster stellar mass, which are the two main sources of uncertainty. I compare the observed Brγ EW with the population synthesis model Starburst99[2] (Leitherer et al. 1999). This model lists spectrophotometric properties of star clusters as a function of age, metallicity and IMF. I assume an instantaneous stellar burst, solar metallicity and a Salpeter initial mass function with lower and

[2] http://www.stsci.edu/science/starburst99

Table 6.1: Properties of SSCs within the area observed with SINFONI

SGMC	SSC	Age [Myr]	Mass [$\times 10^5\ M_\odot$]	ID in references	Continuum erg s^{-1} cm^{-2} A^{-1}	H_2 $1-0$ S(1) Flux^d erg s^{-1} cm^{-2}	Brγ line Flux^a erg s^{-1} cm^{-2}	Brγ line Δv^b km s^{-1}	Brγ line V_{LSR} km s^{-1}
1	D	3.9	14.3	#30 [1], D [2], #29 [3]	$1.4\pm0.3 \times 10^{-17}$	$< 2.9 \times 10^{-16}$	$2.1\pm0.1 \times 10^{-15}$	120±4	1430±2
	D1	6.1	16.2	#3 [1], D1 [2], #32 [3]	$1.4\pm0.1 \times 10^{-17}$	$< 1.1 \times 10^{-16}$	$< 1.5 \times 10^{-16}$		
	D2	5.4	8	D2 [2]	$2.6\pm0.5 \times 10^{-18}$	$< 1.1 \times 10^{-16}$	$6.7\pm0.3 \times 10^{-16}$	104±3	1524±2
2	C	5.72	41.3	#28 [1], C [2], #26 [3]		$< 1.0 \times 10^{-16}$	$< 9.9 \times 10^{-17}$		
	S	8.7	-	#25 [3]		$< 1.0 \times 10^{-16}$	$< 9.9 \times 10^{-17}$		
4/5^c	B1	3.5	42.3	#16 [1], B1 [2], #15 [3]	$7.4\pm1.5 \times 10^{-17}$	$2.9\pm0.2 \times 10^{-15}$	$2.2\pm0.1 \times 10^{-14}$	132±5	1512±2

For the SSCs I kept the nomenclature given by Gilbert & Graham (2007). The other SSC, I labeled S.
References indicate the identification of the SSC in each paper: [1] IR Luminous SSCs from Table 8 in Whitmore et al. (2010), [2] IR SSC from Table 1 in Gilbert & Graham (2007), [3] SSCs observed with WIRC/NIRSPEC from Table 2.4 in Christopher (2008).[a] Uncorrected for extinction. [b] Observed line-width (FWHM). [c] Measurements of the H_2 lines for this source are made in section 6.2. [d] The upper limits for the H_2 lines were estimated as the standard deviation of aperture photometry of several positions in the integrated line image.

upper mass cutoffs of 1 and 100 $M_\odot$, respectively. The H II1 source has an EW slightly higher than the values provided by Starburst99. For this source, I set an upper limit of the age of 1 Myr. The Brγ emission measures the flux of ionizing photons $N_{\rm Lyc}$, listed in Table 6.2. For a cluster of a given age and IMF, $N_{\rm Lyc}$ depends only on the stellar mass. I estimate these masses by comparing the $N_{\rm Lyc}$ values with the Starburst99 models. Since the Brγ fluxes are not corrected by extinction, $N_{\rm Lyc}$ and the stellar mass are lower limits.

Table 6.2: Characteristics of the ionized compact sources within the SINFONI fields.

Source	Brγ^a erg s^{-1} cm^{-2}	Continuum^a erg cm^{-2} s^{-1} Å^{-1}	EW^b Å	Age Myr	$N_{\rm Lyc}$ phot. s^{-1}	Mass 10^5 $M_\odot$
H II1	$1.9 \pm 0.1 \times 10^{-15}$	$3.6{\times}10^{-18}$	538	<1	8.5×10^{51}	1.6
H II2	$1.4 \pm 0.1 \times 10^{-15}$	$1.1{\times}10^{-18}$	131	5.3	6.1×10^{51}	8
H II3	$7.5 \pm 0.3 \times 10^{-16}$	$2.2{\times}10^{-18}$	336	3.3	3.3×10^{51}	1.3

^{a}Not corrected for extinction. ^{b} Brγ equivalent width.

6.1.3 The early evolution of SSCs

The observations show that most of the SSCs do not have associated molecular nor ionized compact line emission. The three clusters with detections of Brγ have ages $\lesssim$5 Myr and masses $\gtrsim 10^6$ $M_\odot$. The young and massive SSC C in SGMC 2, has an ionized nebula larger than the aperture size used to search for compact emission (Gilbert & Graham 2007; Herrera et al. 2011). Other clusters may not be detected in the gas emission due to the difficulty of isolating their emission from the background. This is a problem for the less massive clusters. For instance, we can contrast D and S1 in SGMC 1, and D2 and S2 in the same cloud. Each one of this sample pairs has similar ages, but masses about one order of magnitude different. Those SSCs with higher masses have associated ionized emission, while the others do not. The comparison between D and D1 in SGMC 1 gives us a clue of the time-scale for the disruption of H II regions in the overlap region. Both clusters have similar masses (10^6 $M_\odot$) but only D, which is 2 Myr younger, is associated with compact ionized gas emission. Clusters, with ages and masses larger than ∼6 Myr and a few times 10^5 $M_\odot$, respectively, have already cleared out all or most of their parent molecular clouds.

Figures 6.2 and 6.3 show the ratio between the line fluxes (both H_2 $1-0$ S(1) and Brγ) and cluster masses versus cluster ages for seven and nine sources, respectively. The figures include all of the SSCs listed in Table 6.1, but SSC S, and the molecular compact sources PCC1 and 2 presented in Section 3.4.4 and Appendix A. Figure 6.2 shows that the H_2 emission per unit of stellar mass decreases sharply, by more than one order of magnitude for ages of about 3.5 Myr. Only the PCCs and B1 show clear H_2 emission. Sources without an obvious H_2 detection are older than B1. This suggests that the disruption of the parent clouds by the newly formed stars occurs within a few Myr. Figure 6.3 also includes the three ionized compact sources

presented in the previous section. It shows much scatter in the Brγ emission per unit of stellar mass with no striking trend versus cluster ages. The Brγ emission does not decrease as fast as the H_2 emission.

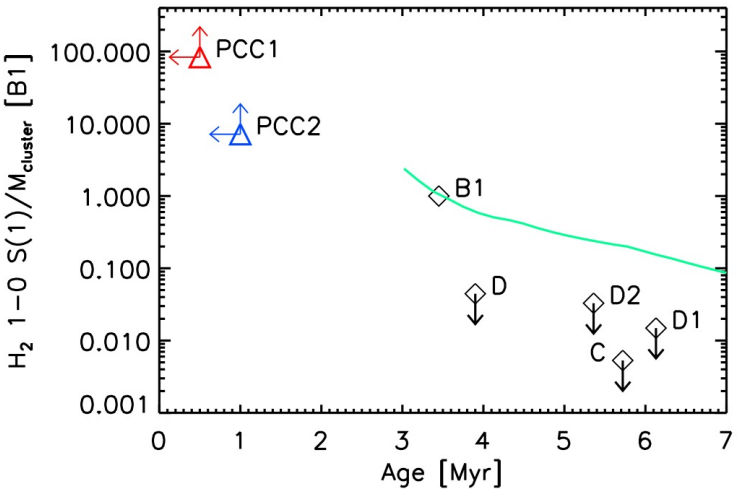

Figure 6.2: H_2 $1-0$ S(1) emission over the stellar cluster mass, for SSCs with different ages and compact molecular sources PCC1 and 2, observed in the SINFONI fields. Since both the masses and H_2 $1-0$ S(1) fluxes depend on the extinction in the same way, the H_2-to-stellar mass ratio is independent of extinction. The two PCCs have upper limits for their ages. The H_2-to-stellar mass ratio is normalized to the value for B1. The green line represents a PDR model for B1, which is discussed in Section 6.2.5.

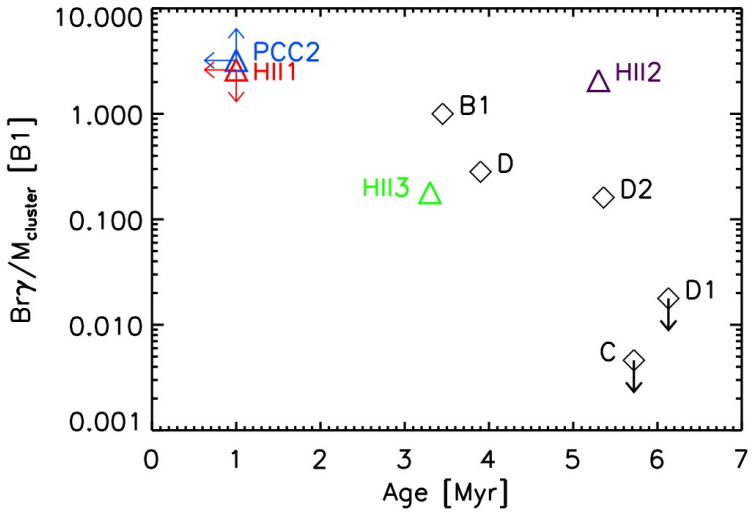

Figure 6.3: Brγ emission over the stellar cluster mass, for the SSCs, ionized compact sources and PCCs in the SINFONI fields. As for H_2, the Brγ-to-stellar mass ratio is extinction free. The ratio is normalized to the value for B1.

Within each SGMC there are a variety of sources. For instance, SGMC 1 and 2 harbor molecular and ionized compact sources and more evolved SSCs. These

observations show that star formation within SGMCs occurs over a range of ages. It proceeds in different positions within the SGMC and yields SSCs with a range of masses. In the next section, I focus on the B1 SSC, which is still embedded in its parent cloud and therefore allows us to study the physical process involved in the cloud disruption. The evolution of the molecular gas sets the time-scale of the disruption of the bound parent cloud by the newly formed stars.

6.2 SSC still embedded in its parent molecular cloud

The SSC B1 in SGMC 4/5 is associated with bright compact ionized and molecular emission. This indicates that B1 is still associated with its parent molecular cloud. With this source, we are witnessing the action! It is a bright target to study how massive SSCs disperse their parent molecular clouds. First, I use multi-wavelength data on this source, including the SINFONI and ALMA observations of my thesis, to characterize its physical properties. Second, I present a model to quantify the emission from the H II region and associated PDR heated by SSC B1. Finally, I use the data to estimate the pressure for the different feedback mechanisms to identify how the gas is being pushed away from the cluster.

6.2.1 Physical properties

I start with the description of the available data. SSC B1 coincides with a bright emission peak in the mid-IR discovered by ISO (Mirabel et al. 1998). It accounts for 15% of the mid-IR flux from the whole Antennae. SSC B1 is the brightest compact radio source at 4 and 6 cm in the overlap region (Neff & Ulvestad 2000). It is also one of the brightest sources in the K-band and Brγ emission, in the near-IR observations presented by Gilbert et al. (2000) and my SINFONI data (Section 3.3). The ALMA maps published by Herrera et al. (2012) show that it coincides with a CO emission peak. It is also a continuum source at 230 and 345 GHz. In this section, I use these data to characterize the B1 cluster and the matter around it.

6.2.1.1 SSC B1 cluster

The radio flux of SSC B1 at 4 and 6 cm has a thermal spectral index (Neff & Ulvestad 2000). This thermal radio emission is directly associated with the ionization flux of the cluster $N_{\rm Lyc}$. Both thermal radio emission and hydrogen recombination lines originate within ionized regions and are proportional to $N_{\rm Lyc}$, but the radio emission, unlike the Brγ emission, is not affected by dust extinction. Thus I am using the radio emission to estimate $N_{\rm Lyc}$. The radio fluxes at 4 and 6 cm are listed in Tables 4 and 3 in Neff & Ulvestad (2000), respectively. The fluxes are 5161$\pm$21 μJy at 4 cm and 4704$\pm$22 μJy at 6 cm. I used Equation 5.10, in section 5.3, to derive the $N_{\rm Lyc}$ values. I obtained similar values of $N_{\rm Lyc}$ from the emission at 4 and 6 cm. The mean value is $N_{\rm Lyc} = 2.2 \pm 0.1 \times 10^{53}$ phot. s^{-1}.

The mass of the B1 stellar cluster can also be derived from $N_{\rm Lyc}$ if we know the age of the cluster. To do that, I use the equivalent width of the Brγ line provided by Gilbert et al. (2000), and the Starburst99 population synthesis model. The Brγ EW is 255 ± 8 Å which yields an age of 3.5 Myr. Starburst99 provides $N_{\rm Lyc}$ values for stellar populations at different ages, for a stellar mass of 10^6 $M_\odot$. I selected the $N_{\rm Lyc}$ value associated with the estimated age of the cluster. The comparison between $N_{\rm Lyc}$ obtained from the models with that computed from the thermal radio emission, gives the stellar mass of the cluster $M_{\rm cluster} = 9.8 \pm 0.5 \times 10^6$ $M_\odot$. The mass, age and $N_{\rm Lyc}$ values of the B1 cluster, are listed in Table 6.3.

Table 6.3: Estimated properties of the B1 cluster in SGMC 4/5

$N_{\rm Lyc}$	$2.2 \pm 0.1 \times 10^{53}$ phot. s^{-1}
Stellar mass	$9.8 \pm 0.5 \times 10^6$ $M_\odot$
Stellar age	3.5 Myr
$A_{\rm K}$	0.8 mag
Brγ emission size	70 pc
H_2 $1-0$ S(1) emission size	<210 pc
GMC size[a]	120 pc
GMC gas mass $M_{\rm H}$	$9.7 \pm 0.5 \times 10^7$ $M_\odot$
Mean gas density $n_{\rm H}$	4350 cm^{-3}
$N_{\rm H}^b$	1.1×10^{24} H cm^{-2}

[a] Size (FWHM) measured from continuum emission at 345 GHz. [b] Column density at the center of the GMC, computed as $N_{\rm H} = M_{\rm H}/{\rm Area}$.

6.2.1.2 Spatial extent of the ionized and molecular gas associated with SSC B1

I use the SINFONI and ALMA data to determine the spatial extent of the gas associated with B1. I use the Brγ line to measure the extent of the ionized gas and the continuum emission at 345 GHz for the molecular gas. This emission is optically thin and, unlike the near-IR H_2 line emission, a tracer of the column density.

Fig. 6.4 displays the Brγ emission profiles of the SSC across the x and y axis. The color images show the Brγ emission from SGMC 4/5, black and red lines correspond to the cuts along the x and y axis, respectively. To measure the size of the source, I fitted Gaussian curves to both emission profiles. The observed size is $0\farcs8 \times 1\farcs0$ (FWHM), which after correction by the seeing gives a geometric size of $0\farcs67$ (FWHM = 70 pc, listed in Table 6.3).

The ALMA continuum images were presented in the previous chapter. Figure 3.10 presents the CO$(3-2)$ emission overlaid with the continuum emission at 345 GHz. It shows that the SSC B1 has a clear counterpart in the continuum. I fitted a 2-D Gaussian function to the continuum source. The angular sizes and fluxes derived from the fit are listed in Table 6.3. The source size (FWHM), after beam correction, is $0\farcs8 \times 1\farcs6$ (85 pc×170 pc), which gives a geometrical size of $1\farcs1$ (120 pc, listed in Table 6.3). This is the spatial extent of the parent molecular

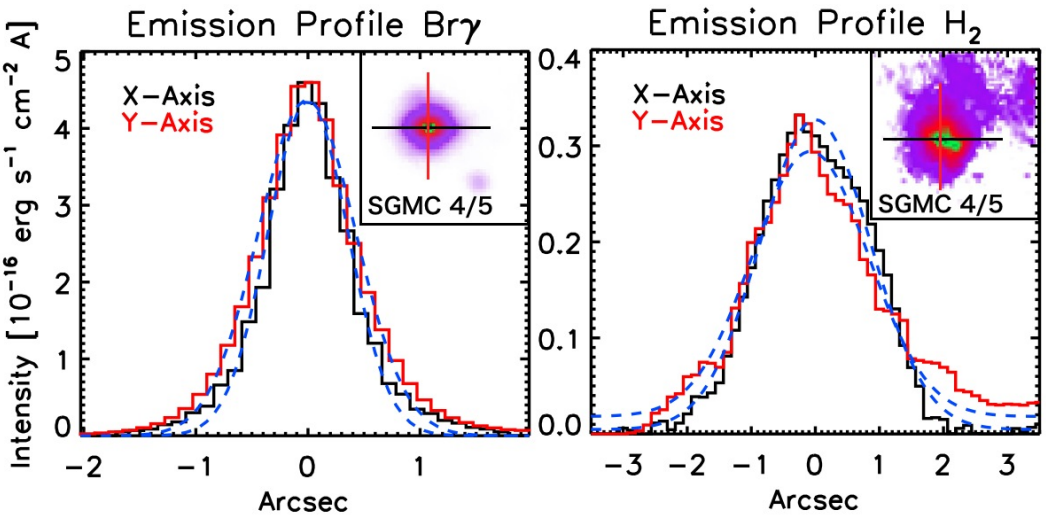

Figure 6.4: Left and right panels show the line profiles along the x and y axis of the SSC B1 in SGMC 4/5 for the Brγ and H_2 $1-0$ S(1) lines, respectively. The two color images are the Brγ and H_2 $1-0$ S(1) emission line fluxes of SGMC 4/5, and they show the cuts across both axis.

cloud of SSC B1. It is larger than the Brγ extent, which suggests that the ionizing emission comes from within the cloud.

In Fig. 6.4 I present the H_2 $1-0$ S(1) emission profile. Gaussian fits to these profiles yield a size of $2\farcs0\times2\farcs1$ (FWHM), which after correction by the seeing gives a geometric size of $2''$(FWHM = 210 pc, listed in Table 6.3). This value is larger than the GMC size. This indicates that part of the H_2 emission is coming from the SGMC and is not directly associated with SSC B1. In the absence of velocity information, it is hard to isolate the specific contribution from the SSC.

6.2.1.3 Intensities of the ionized and molecular gas associated with SSC B1

Now I describe how I obtain the CO and near-IR line fluxes (H_2, Brγ, He I and Brδ), listed in Table 6.4.

The K-band spectrum of SSC B1 is presented in Fig. 6.5. Several ionized and molecular lines are detected and I have highlighted the main ones. This spectrum is obtained integrating the flux within an aperture of twice the FWHM observed in Brγ ($1\farcs9$ diameter), and subtracting a background estimated within an annulus of $0\farcs65$ width (the size of the seeing disk of the SINFONI data). The same figure shows a zoom on the Brγ and H_2 $1-0$ S(1) lines, where we can see that the Brγ is one order of magnitude brighter than the H_2 $1-0$ S(1) line. The H_2 fluxes have been measured with the same apertures for the source and background. These fluxes represent a rough estimate on the H_2 emission associated with SSC B1. For a larger aperture of $4\farcs2$ diameter, twice the FWHM of the H_2 emission profile (Fig. 6.4), I measure a H_2 $1-0$ S(1) flux four times larger, which is likely to be dominated by the SGMC (conservative upper limit).

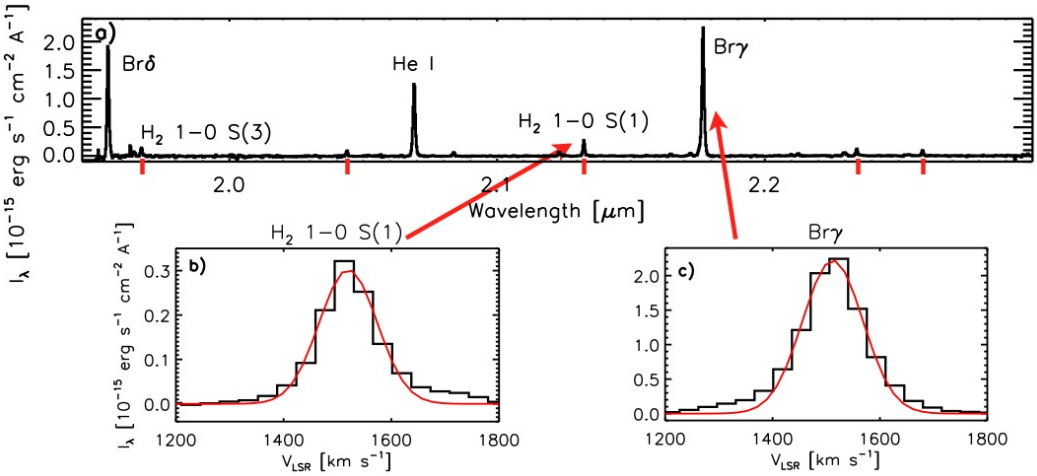

Figure 6.5: Upper figure displays the K-band spectrum of the SSC B1 located in SGMC 4/5, obtained from aperture photometry based on the Brγ line. Ionized lines are the brightest lines across the spectrum. Lower figures correspond to a zoom in the H_2 $1-0$ S(1) and Brγ lines. H_2 $1-0$ S(1) spectrum was measured within an aperture based on the H_2 size of the source (see Fig. 6.4). Red lines represent the fitted Gaussian curves.

Measurements of the line intensities are done by fitting Gaussians to each line emission, which are listed in Table 6.4. Fluxes are not corrected for extinction. Velocities are given with respect to the LSR. Line widths correspond to the FWHM of the Gaussian fit, without correction for the spectral resolution (107 $\mathrm{km\,s^{-1}}$). The effective extinction for the Brγ emission may be estimated by comparing the Brγ and thermal radio fluxes. I use Equation 4.2 in Section 4.3.1 to compute the intrinsic Brγ flux from the N_{Lyc} derived from the radio emission, assuming case B recombination, an electron density $n_{\mathrm{e}} = 10^4$ cm^{-3} and an electron temperature of $T_{\mathrm{e}} = 10^4$ K (see Table 6 of Hummer & Storey 1987). I obtain a value of Brγ= 5×10^{-14} erg s^{-1} cm^{-2}. The ratio between the observed (see Table 6.4) and intrinsic Brγ fluxes, gives an effective extinction for Brγ of 0.8 magnitudes (a factor 2 extinction in the K-band), listed in Table 6.3. Gilbert et al. (2000) reported a slightly higher value of 1.2 mag. Their Brγ flux, measured from slit spectroscopy is 1.5 times smaller than mine. They also do not use the same Starburst99 model.

The ALMA images of the CO emission lines have been presented in the previous chapters. In Fig. 3.17 I have overlaid the CO, H_2 and Brγ line emission. Within the uncertainty between the astrometry, the emission peaks coincide. I measure the CO line fluxes by aperture photometry within a diameter of $2\farcs8$, twice the observed FWHM size in the CO$(3-2)$ emission flux map. The background is estimated within an annulus of width equals to the beam of the ALMA observations ($0\farcs8$). Fig. 6.6 illustrates the measurement of the CO$(3-2)$ spectrum. The color image corresponds to the integrated CO$(3-2)$ emission from the SGMC 4/5. The inner circle of the white ring delimits the aperture used to measure the emission, which is shown as a black line in the spectrum. The ring itself is the annulus used to estimate the background emission. The background contribution corresponds to the

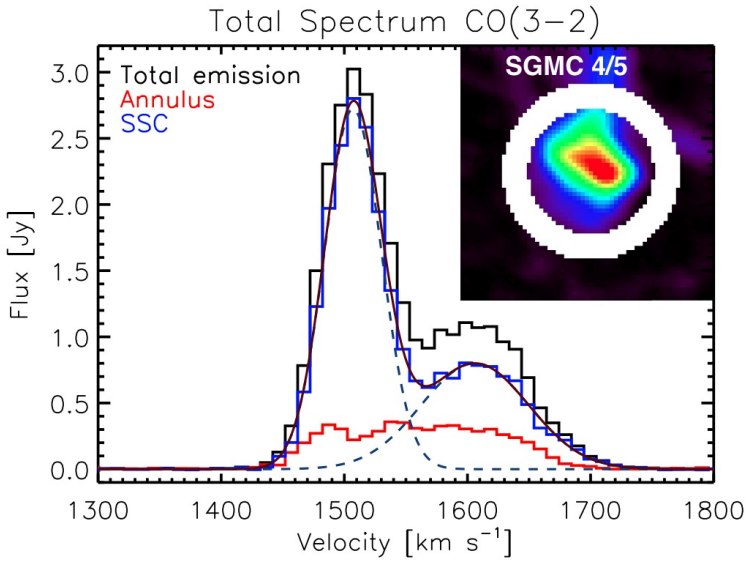

Figure 6.6: CO(3 − 2) spectrum of the SSC B1 in SGMC 4/5. Image color corresponds to the CO(3 − 2) integrated emission from the whole SGMC 4/5. The rings in the image represent the apertures used to compute the SSC spectrum. The inner circle defines the source emission and the outer circle the annulus used for background subtraction. The black line is the total emission inside the inner circle, without any subtraction. The red line is the background contribution. The blue line is the SSC spectrum, after subtraction of the background. Dashed lines are the fitted Gaussian curves to the velocity components. Solid line corresponds to the final fitted curve, the addition of the two Gaussian curves.

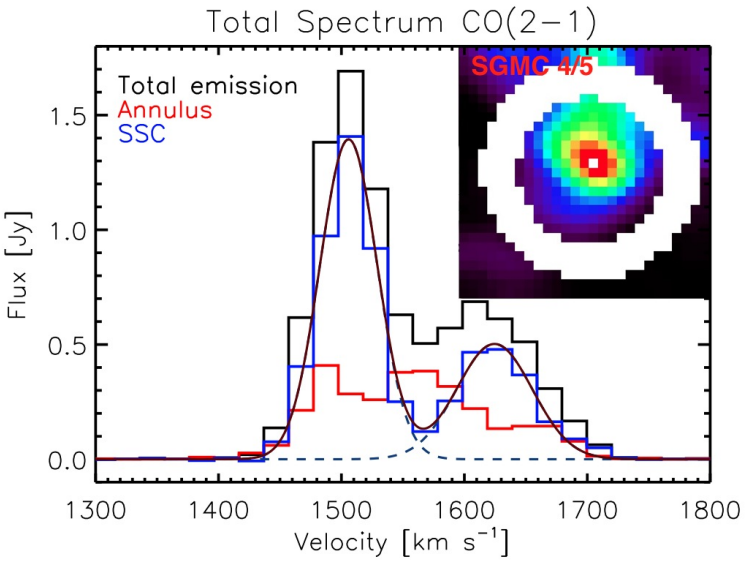

Figure 6.7: CO(2 − 1) spectrum of the SSC B1 in SGMC 4/5. Image color corresponds to the CO(2 − 1) integrated emission from the whole SGMC 4/5. Same caption as Figure 6.6.

spectrum in red. Finally, the spectrum in blue is the emission from the SSC, that is the total emission after background subtraction. The CO(2−1) spectrum, displayed

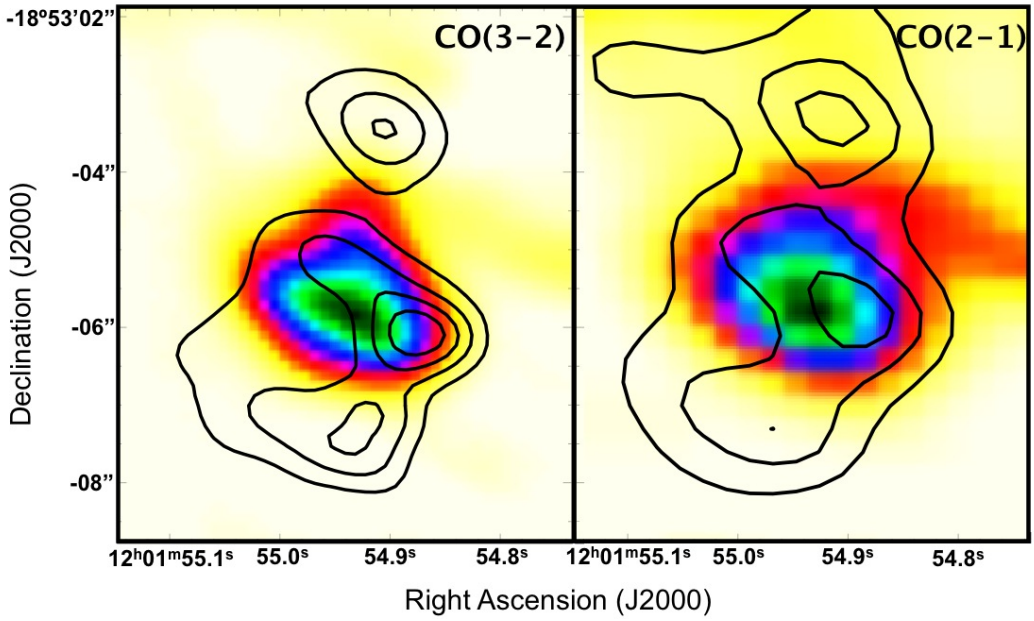

Figure 6.8: CO velocity components in SGMC 4/5. Left and right panels correspond to the $CO(3-2)$ and $CO(2-1)$ line emission, respectively. The color images are the first velocity component, which is integrated in the range $1440-1540$ km s^{-1}, and contours are the second component, integrated in $1580-1660$ km s^{-1}.

in Figure 6.7, is obtained in a similar way. Aperture photometry was done for a diameter of $4\farcs6$ (twice the observed FWHM in $CO(2-1)$), with the subtraction of the nearby background within an annulus of width equals to the beam of the $CO(2-1)$ ALMA observations ($1\farcs2$). The apertures used for the photometry include the emission of almost the whole SGMC.

Both CO spectra reveal more than one velocity component. Figures 6.6 and 6.7 display the fit of the $CO(3-2)$ and $CO(2-1)$ spectra, respectively, each of them with two Gaussians (dashes lines). The addition of these curves are the purple lines. The parameters of the Gaussians are listed in Table 6.4. Figure 6.8 presents the two velocity components in the SGMC 4/5, left and right panels for $CO(3-2)$ and $CO(2-1)$, respectively. In both images, the background images correspond to the integrated emission between 1440 and 1540 km s^{-1}, and the contours the emission between 1580 and 1660 km s^{-1}. The left panel shows a spatial offset between the two velocity components. The low velocity emission is that which is mainly associated with the SSC, while the higher velocity component has the spatial extent of the SGMC. However, this second component also peaks at the position of the SSC B1. This indicates that some of the high velocity gas may be associated with the cluster. This observational fact is reminiscent of what I and collaborators reported for PCC1 located in SGMC 2 (Fig. 3 in Herrera et al. 2011). In this complex, we find that the PCC1 source is located in a region with a step velocity gradient (1 km s^{-1} pc^{-1}). This may also apply to the B1 cluster within SGMC 4/5, which is a more evolved source. This suggests that the GMC that gave birth to the B1 cluster, is still

physically connected with the SGMC. This cloud may still be accreting matter from the SGMC, as proposed for PCC1.

Table 6.4: Line parameters measured from SSC B1 in SGMC 4/5

Line	Rest wavelength μm	Flux[a] erg s^{-1} cm^{-2}	V_{LSR} km s^{-1}	FWHM[b] km s^{-1}
Brδ	1.9451	$1.67\pm0.05\times10^{-14}$	1492±1	131±3
HeI	2.05869	$1.28\pm0.02\times10^{-14}$	1521±1	145±2
Brγ	2.16612	$2.2\pm0.1\times10^{-14}$	1512±2	132±5
HeI	2.1127	$6.7\pm0.8\times10^{-16}$	1509±5	146±13
H_2 1−0 S(3)	1.95756	$1.02\pm0.08\times10^{-15}$	1486±3	120±7
H_2 1−0 S(2)	2.03376	$5.8\pm0.9\times10^{-16}$	1516±5	103±12
H_2 1−0 S(1)	2.12183	$1.93\pm0.08\times10^{-15}$	1515±1	110±3
H_2 1−0 S(0)	2.22329	$9.4\pm1.2\times10^{-16}$	1514±5	124±12
H_2 2−1 S(1)	2.24772	$7.1\pm0.1\times10^{-16}$	1516±3	109±8
CO(2 − 1)	230 GHz	$6.3\pm0.1\times10^{-16}$	1505.8±0.3	55±1
		$3.0\pm0.1\times10^{-16}$	1624±1	73±3
CO(3 − 2)	345 GHz	$1.82\pm0.02\times10^{-15}$	1507.0±0.2	54±1
		$1.01\pm0.03\times10^{-15}$	1606±1	102±2

[a] Near-IR fluxes are not corrected for extinction. [b] Observed line-widths, without correction for the spectral resolution.

The mass of the GMC, in which the SSC B1 is embedded, is also estimated. I proceed like in section 3.4.4, where I estimated the mass of the PCC1 from the continuum emission at 345 GHz. At the beginning of this section, I explained how I computed the GMC size. I use this size, based on the continuum emission at 345 GHz, to measure the dust continuum flux from the GMC associated with B1. To derive the gas mass, I use the Equation 5.9, by assuming the same dust properties as for PCC1. The mass of the giant molecular cloud is $M_{\rm GMC} = 9.7\pm0.8\times10^7\ M_\odot$, which is given in Table 6.3. The error is estimated from the $1-\sigma$ standard deviation of the continuum image measured with the same aperture over nearby regions free of sources. The $N_{\rm H} = 1.1\times10^{24}$ H cm^{-2} gas column density was estimated assuming spherical symmetry. This value is twice larger than the threshold $\sigma = 1$ g cm^{-2} to allow the formation of massive stars our of a molecular cloud (Krumholz & McKee 2008).

6.2.2 Modeling of the H II region and PDR

Now that the physical properties of the SSC and the size and mass of the GMC have been estimated, I can model the source. In this section I introduce a simple geometrical model that I use to quantify and compare the action of stellar winds with the thermal, turbulent and radiation pressure. The geometrical model is combined with a PDR model to quantify the H_2 and CO line emission. I introduce the model in two parts. First, I model the H II region and then the PDR.

Fig. 6.9 displays the spherical model that I use. This 1-D model describes a segment of the shell. It does not assume that the cluster is fully embedded in

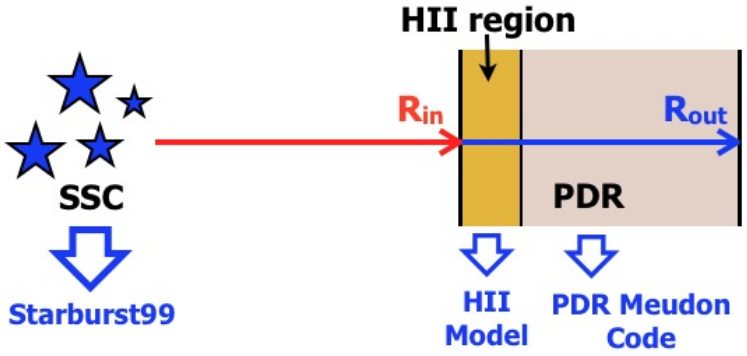

Figure 6.9: This diagram illustrates the GMC associated with SSC B1. I include the ionizing source represented by stars, the H II region defined by the inner radius $R_{\rm in}$ and the PDR. I also specify the model used to represent each component.

a spherical shell. The matter around the SSC is likely to be clumpy, with some radiation escaping in some directions. This is in agreement with the fact that the mean extinction of the shell is moderate (a factor 2, section 6.2.1.1). The H II region is directly receiving the UV radiation from the SSC and the incident radiation on the PDR is the output radiation from the H II gas layer. The internal radius $R_{\rm in}$ is unknown, the external radius is the GMC radius observed in the continuum emission, $R_{\rm out} = 60$ pc. The stellar radiation was chosen to be that from the Starburst99 models, for an age of 3 Myr scaled by the cluster age. This SED was used for the H II region modeling as the ionizing radiation.

– **H II Region**

I model the H II region as an ionized hydrogen nebula with dust grains. I compute the radiative transfer equation for this nebula in the plane-parallel approximation.

The luminosity radiated by the central cluster at the wavelength λ per unit wavelength is $\mathrm{L}^{\star}(\lambda)$. As we move away, the flux is decreasing due to geometric dilution. Thus, the incident intensity in the nebula (at a distance $R_{\rm in}$) is $I(R_{\rm in}, \lambda) = I^{\star}(\lambda)/(4\,\pi\,R_{\rm in}^2)$, where $R_{\rm in}$ is the radius of the inner shell. The hydrogen atoms and dust grains in the H II region will absorb all of the ionizing photons and some of the non-ionizing photons. Therefore, the specific intensity will decrease as $I(\lambda) = I(R_{\rm in}, \lambda)\, e^{-\tau_\lambda}$ where $\mathrm{e}^{-\tau_\lambda}$ is the attenuation of the radiation due to absorption by the gas and extinction by the dust along the nebula, and τ_λ is the optical depth. In this nebula, the radiative transfer will be defined by the absorption produced by the ionization of the hydrogen atoms and light absorption and scatting by dust grains,

$$\frac{dI(\lambda)}{ds} = -n_{\rm H}\sigma_{\rm H}(\lambda)\, I(\lambda) - n_{\rm d}\sigma_{\rm d}(\lambda)\, I(\lambda), \tag{6.1}$$

where s is the position in the nebula from $R_{\rm in}$ at which the absorption occurs, $n_{\rm H}$ and $n_{\rm d}$, and $\sigma_{\rm H}$ and $\sigma_{\rm d}$ are the hydrogen and dust densities and cross sections,

respectively. $\sigma_{\rm H}$ is zero for non ionizing photons. We assume that the nebula extent is small compared to $R_{\rm in}$. The ionization rate ($N_{\rm ion} = n_H \bar{\sigma}\, S$) equals the recombination rate ($N_{\rm rec} = n_{\rm e}\, n_+\, \alpha_2$), where $\bar{\sigma}$ is the mean photoionization cross section, $S = S_0\, e^{-\tau}$ is the number of ionizing photons per unit time and unit area, $n_{\rm e}$ is the electron density, n_+ is the density of protons and α_2 is the recombination coefficient. Then, we can re-write Equation 6.1 as:

$$\frac{d\, e^{-\tau_\lambda}}{ds} = -\frac{\alpha_2}{S_0} n^2 - n\, x_d\, \sigma_d(\lambda)\, e^{-\tau_\lambda}, \tag{6.2}$$

where n is the gas density and x_d is the dust-to-gas mass ratio. I assume that all the protons and electrons come from the same atoms ($n = n_{\rm e} = n_+$). The dust cross section is taken from the DUSTEM model (Desert et al. 1990; Compiègne et al. 2011). I include the extinction cross sections of the very small grains and big grains (there is no observational evidence for PAHs in H II regions).

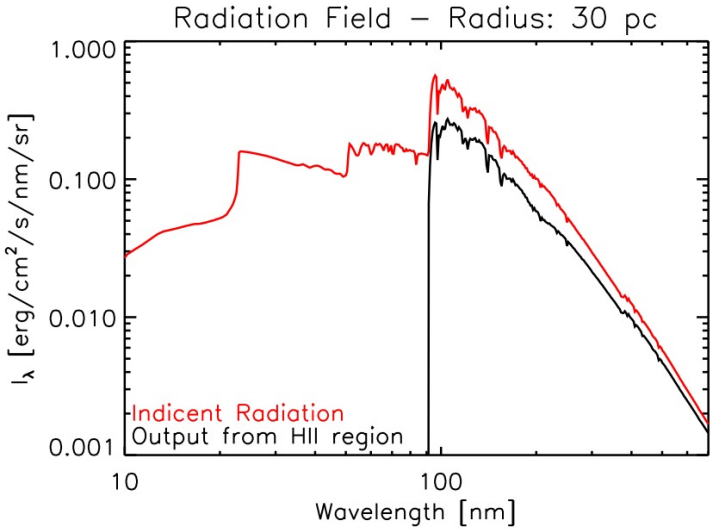

Figure 6.10: Stellar radiation field from the SSC B1 in SGMC 4/5. The incident radiation in the H II region is represented by a red line, while the outgoing radiation by a black line, for a H IIregion radius of $R_{\rm in}$ = 30 pc.

I solve Eq. 6.2 for different values of incident radiation, such that $I_{\rm incident} = L^\star/(4\,\pi\, R_{\rm in}^2)$, with $R_{\rm in}$ equals from 30 to 100 by spacings of 10 pc. This range is distributed around the GMC radius (60 pc), from the radius of the Brγ line emission to that of H_2. Fig. 6.10 displays the incident and outgoing radiation field of the H II region for $R_{\rm in}$ equals to 30 pc. The hydrogen atoms in the H II region absorb the radiation with wavelengths <91.2 nm. Dust grains in the nebula, absorb non-ionizing photons. I compute the output flux in units of the Mathis radiation field (Mathis et al. 1983), which corresponds to the stellar radiation in the solar neighborhood. It is composed of three black bodies at temperatures of 3000, 4000 and 7500 K, with dilution factors of 4.0×10^{-13}, 1.0×10^{-13} and 1.0×10^{-14}, respectively. The comparison between the radiation field obtained

from the H II model and the Mathis radiation field was done by integrating both of them between 91.2 to 200 nm. Table 6.5 lists the radiation field in Mathis units for the different internal radii. I also compute the radiation pressure exerted at the surface of the PDR from photons absorbed or scattered across the layer of the H II gas,

$$P_{\rm rad}({\rm HII}) = \frac{L_{\rm HII}}{4\,\pi\,R_{\rm in}^2\,c}. \tag{6.3}$$

The luminosity $L_{\rm HII}$ is the luminosity incident onto the H II region minus the output luminosity. $P_{\rm rad}$(HII) is the pressure produced by the ionizing photons and the non-ionizing photons which are absorbed by dust and gas in the H II layer. This is the minimum value of the pressure at the surface of the PDR. At the radii relevant to this study and for the mass of SSC B1, the radiation pressure is the dominant pressure (Krumholz & Matzner 2009), as we will see in section 6.2.3. Table 6.5 lists the estimated values of $P_{\rm rad}$.

Table 6.5: Radiation fields and gas pressures exerted at the surface of the PDR, for different values of $R_{\rm in}$.

$R_{\rm in}$ pc	χ Mathis	$P_{\rm rad}/k_{\rm B}$ K cm^{-3}
30	1.6×10^{4}	1.5×10^{8}
40	1.1×10^{4}	8.6×10^{7}
50	7.5×10^{3}	5.5×10^{7}
60	5.5×10^{3}	3.8×10^{7}
70	4.2×10^{3}	2.8×10^{7}
80	3.3×10^{3}	2.1×10^{7}
90	2.7×10^{3}	1.7×10^{7}
100	2.2×10^{3}	1.4×10^{7}

– **PDR**

To describe the PDR, I use the online tables of outputs from the PDR Meudon Code[3] (Le Bourlot et al. 2012). I chose to use results from isobaric, rather than isochoric, models to relate line intensities to the radiation pressure. Model results are available for a range of values of the incident radiation field and gas pressures. The model grid ranges are $P/k_{\rm B} = n\,T_{\rm K} = 1\times10^{5} - 1\times10^{8}$ K cm^{-3}, for the gas pressure and $\chi = 1$ to 1×10^{6} for the radiation field in Mathis units.

Fig. 6.11 shows the model results for the CO$(3-2)$/CO$(2-1)$ and the H_2 $2-1/1-0$ S(1) line ratios. The red contours indicate the ratios for the fluxes in Table 6.4. In the CO plot, I include the ratio for the main velocity component (2.9), the second component (3.4) and the total CO emission (3.0). The range of possible combinations of radiation fields and pressures given in Table 6.11 are

[3] http://pdr.obspm.fr/PDRcode.html

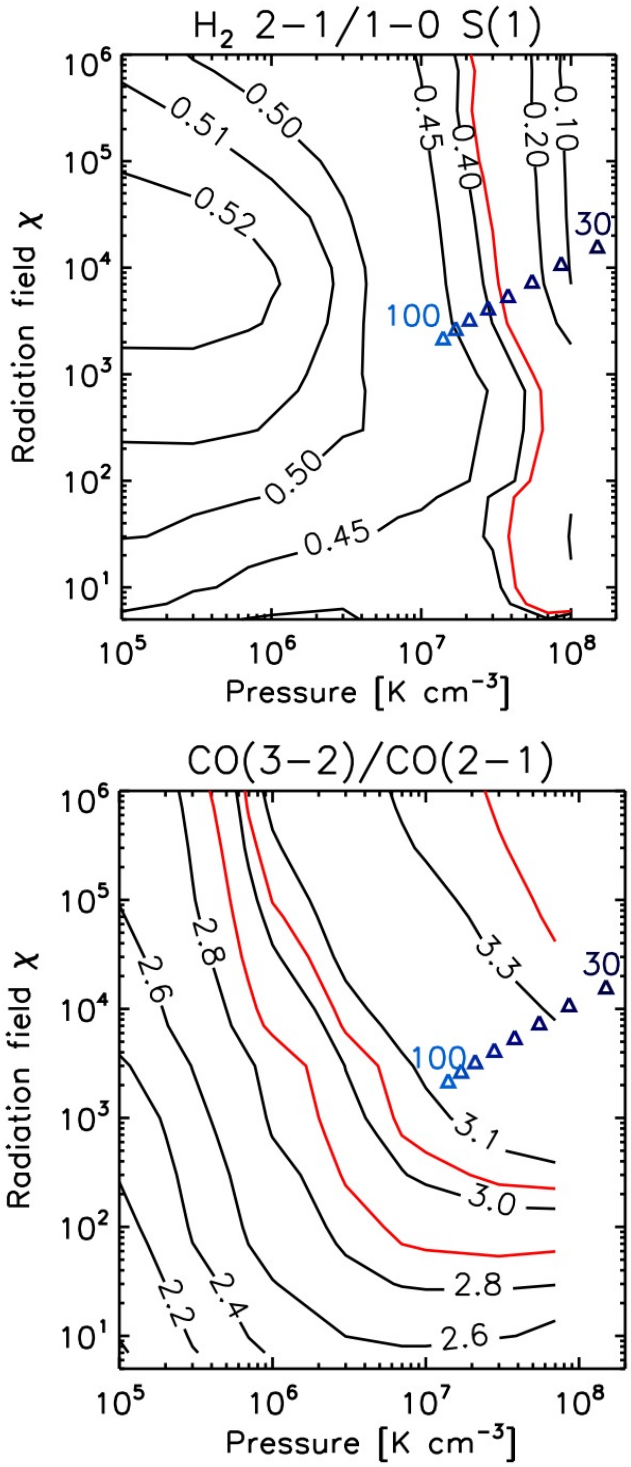

Figure 6.11: Emission lines estimated from the PDR Meudon code, for a grid of radiation fields and gas pressures. Upper figure, H_2 $2-1/1-0$ S(1) intensity line ratio. Lower figure, $CO(3-2)/CO(2-1)$ intensity ratio. Red lines indicate the observed values listed in Table 6.4. For CO, I include the ratio measured for the two velocity components (2.9 and 3.4 for the first and second component, respectively) and for the total emission. Triangles represent the values given in Table 6.5, estimated from the H II/PDR model for radii from 30 to 100 pc.

marked by triangles. From this figure it is clear that PDR models can account for the observed intensity ratios within the constrains on physical parameters set by the spatial extent of the emission lines.

6.2.3 Comparison of feedback mechanisms

Lopez et al. (2011) compare the different pressures acting on the gas of the star-forming region 30 Dor in the LMC, finding that the radiation pressure dominates in the central part of the nebula. In this section, I proceed in a similar way. I quantify the radiation pressure, the thermal pressure of the ionized gas and X-ray emitting plasma, and turbulent pressure of the molecular gas.

a. Radiation Pressure

The radiation pressure $P_{\rm rad}$ is the pressure exerted by the stellar radiation over the molecular gas that surrounds the cluster. It can be written as

$$P_{\rm rad} = (1+\tau_{\rm rad})\frac{L}{4\,\pi\,R_{\rm in}^2\,c}, \tag{6.4}$$

where L is the luminosity of the cluster, $R_{\rm in}$ is the H II radius and $\tau_{\rm rad}$ accounts for the trapping of the IR photons in the cloud ($\tau_{\rm rad} \geq 0$). UV and visible photons emitted by the stellar cluster are absorbed by the dust grains in the cloud, and re-emitted in the IR. If the shell is optically thick, then these IR photons will be trapped within the shell before escaping, interacting more than once with the dust grains in the shell. The number of interactions will depend on the opacity of the shell. Trapping may significantly enhance the momentum given by the cluster to the cloud and thereby accelerate the expansion of the cloud (Murray et al. 2010).

The radiation pressure was estimated from the bolometric luminosity emitted by the SSC, $L_{\rm bol} = 1.8 \times 10^{10}\ L_{\odot}$, and the H II region radius, $R_{\rm in} = 35$ pc. I compute $P_{\rm rad}/k_{\rm B} = 1.1 \times 10^{8} \times (1+\tau_{\rm rad}) \times ([35\ {\rm pc}]/R_{\rm in})^2$ K cm^{-3}.

b. Stellar Winds

Main sequence O stars produce high velocity winds (higher than thousand km s^{-1}) with mass loss rates of about $10^{-6}\,M_{\odot}$ yr^{-1}. The interaction between the expanding winds and the surrounding matter creates shocks where the mechanical energy of the wind is thermalized producing hot plasma (Castor et al. 1975). If the hot plasma is confined within a closed shell of interstellar matter, the thermal energy of the plasma increases with time as

$$E_{\rm hot} = \frac{3}{2}\,P_{\rm hot}\,V_{\rm cavity} = L_{\rm wind}\,\Delta t, \tag{6.5}$$

where $P_{\rm hot}$ is the hot gas pressure, $V_{\rm cavity} = 4/3\,\pi\,R_{\rm in}^3$ is the volume of the inner cavity in Figure 6.9, $L_{\rm wind}$ is the mechanical luminosity (mechanical energy loss)

of the wind and Δt the age of the star-forming region. The pressure exerted by the hot plasma is:

$$\begin{aligned} P_{\rm hot} &= \frac{2}{3}\frac{L_{\rm wind}\,\Delta t}{V_{\rm cavity}} \\ &= \frac{L_{\rm wind}\,\Delta t}{2\,\pi\,R_{\rm in}^3}. \end{aligned} \tag{6.6}$$

To estimate this pressure I use for Δt the age of the SSC of 3.5 Myr and for $R_{\rm in}$ the radius of the H II region of 35 pc. The value of $L_{\rm wind}$ (2.4×10^7 $L_\odot$) is taken from the Starburst99 synthesis population model. The estimated pressure is $P_{\rm hot}/k_{\rm B} = 9 \times 10^9 \times ([35\ {\rm pc}]/R_{\rm in})^3$ K cm^{-3}. This pressure is more than one order of magnitude higher than the radiation pressure listed in Table 6.5. If the plasma can flow out because the shell has burst, then Δt in Equations 6.5 and 6.6 is not the cluster age but the sound crossing time $\Delta t = R_{\rm in}/c_{\rm s}$, where $c_{\rm s} = 300$ km s$^{-1} \times \sqrt{10^7\ {\rm K}/T}$ is the sound speed. In this scenario, the time-scale is short:

$$\Delta t = 0.1 \times \sqrt{\frac{10^7\ {\rm K}}{T}} \times \left(\frac{R_{\rm in}}{35\ {\rm pc}}\right)\ {\rm Myr}, \tag{6.7}$$

and the associated pressure is $P_{\rm hot}/k_{\rm B} = 2.7 \times 10^8 \times ([35\ {\rm pc}]/R_{\rm in})^2$ K cm^{-3}. X-ray observations yield a value even smaller.

SSC B1 is a X-ray source (source number 88 in Table 5 of Zezas et al. 2006). The X-ray luminosity, integrated between $0.1 - 10$ keV, is $L_{\rm X} = 1.9 \times 10^{38}$ erg s^{-1}. This X-ray luminosity can be used to estimate the hot gas pressure. $L_{\rm X}$ is written as:

$$L_{\rm X} = \varepsilon(T) \int n_{\rm e}^2\, dl \times A, \tag{6.8}$$

where $n_{\rm e}$ is electron density, $\varepsilon(T) = 3 \times 10^{-23}$ erg s^{-1} cm^3 is the emission coefficient (assuming a temperature of $T = 10^7$ K, from figure B.1 in Guillard et al. 2009), $EM = \int n_{\rm e}^2\, dl \simeq n_{\rm e}^2 \times R_{\rm in}$ is the emission measure, and $A = \pi\, R_{\rm in}^2$ is the area where the pressure is exerted. The pressure of the hot plasma is:

$$P_{\rm hot} = 1.9\, n_e\, k_{\rm B}\, T. \tag{6.9}$$

For the observed X-ray luminosity we find an electron density of $\sim$1 cm^{-3}. For a temperature of $T = 10^7$ K, the hot plasma pressure is $P_{\rm hot}/k_{\rm B} = 2 \times 10^7 \times ([35\ {\rm pc}]/R_{\rm in})^{3/2}$ K cm^{-3}. This value is a lower limit because we did not correct the X-ray luminosity for absorption by the shell. However, the 3 orders of magnitude difference with the theoretical value cannot result from X-ray absorption by foreground matter. Figure 1 in Ryter (1996) shows that the absorption in the X-ray by the gas is comparable to the extinction in the K-band and it is thus a factor of about 2. Obviously, the hot gas must escape the cavity as it is produced, like what is observed in 30 Doradus (Lopez et al. 2011).

c. Internal turbulence

The line-width of the CO emission associated with SCC B1 is $\mathrm{FWHM_{CO}} = 55\ \mathrm{km\,s^{-1}}$. I argue that this is dominated by turbulence rather than by the expansion of the shell.

To support this statement, I can quantify the momentum given by the radiation to the shell of matter surrounding the SSC. I write the change of momentum ΔP produced by the radiation from SSC B1:

$$\Delta P = \frac{L(1+\tau_{rad})}{c}\,\Delta t. \tag{6.10}$$

where L is the bolometric luminosity $L = 1.8 \times 10^{10}\ L_\odot$ and $\Delta t = 3.5$ Myr is the time over which the SSC radiation has been pushing away its surrounding matter (the age of the cluster).

The expansion velocity $v_{\rm exp}$ of the shell is related to ΔP as

$$\Delta P = M\, v_{\rm exp}, \tag{6.11}$$

where $M = 10^8\ M_\odot$ is the mass of the shell swept up by radiation pressure (the mass of the parent molecular cloud).

I find $\Delta v = 13\times(1+\tau_{\rm rad})\ \mathrm{km\,s^{-1}}$. For small values of $\tau_{\rm rad}$, this expansion velocity is smaller than the observed line-width. The fact that the effective extinction in the K-band is moderate, precludes large values of $\tau_{\rm rad}$ because the dust IR radiation cannot be scattered many times before escaping the shell.

The dissipation time scale of the gas turbulence in the GMC is:

$$\tau_{\rm diss} = 2.6 \times \left(\frac{60\ \mathrm{pc}}{R_{\rm GMC}}\right) \times \left(\frac{\sigma_v}{23\ \mathrm{km\ s^{-1}}}\right)\ \mathrm{Myr}, \tag{6.12}$$

where $R_{\rm GMC}$ and σ_v are the radius of the GMC and 1-D velocity dispersion of the gas, respectively. The dissipation time scale of 2.6 Myr is smaller than the age of the cluster (3.5 Myr). Significant dissipation must thus have occurred since the formation of the pre-cluster cloud. The present level of turbulence requires an energy source to balance dissipation. This energy source can be the stellar winds. Alternatively, as mentioned before, as in PCC1, on-going gas accretion could still drive turbulence.

I now quantify the turbulent pressure. The turbulence produces an outward pressure that can be written as

$$P_{\rm turb} = \frac{3}{2}\rho_{\rm cloud}\,\sigma^2_{\rm turb}, \tag{6.13}$$

where $\rho_{\rm cloud} = M_{\rm GMC}/V_{\rm GMC}$ is the density of the GMC and $\sigma_{\rm turb}$ is the 1-D velocity dispersion of the cloud. The density was computed for the estimated

radius and mass of the GMC, $R_{\rm GMC}$ and $M_{\rm GMC}$, respectively. The turbulent pressure is:

$$P_{\rm turb} = 4.3 \times 10^8 \times \left(\frac{60 \text{ pc}}{R_{\rm GMC}}\right)^3 \times \left(\frac{\sigma_{\rm turb}}{[23 \text{ km s}^{-1}]}\right)^2 \text{ K cm}^{-3}. \quad (6.14)$$

d. Thermal Pressure

I compute the thermal pressure of the ionized gas, ignoring the radiation pressure, using a Strömgren sphere (Murray et al. 2010):

$$\begin{aligned} P_{\rm th} &= (n_{\rm e} + n_{\rm H} + n_{\rm He})\, k_{\rm B}\, T_{\rm HII} \\ &\simeq 1.9\, n_{\rm e}\, k_{\rm B}\, T_{\rm HII}, \end{aligned} \quad (6.15)$$

where $n_{\rm e}$, $n_{\rm H}$ and $n_{\rm He}$ are the electron, hydrogen and helium densities, respectively, and $T_{\rm HII}$ is the temperature of the H II region. The electron density is estimated from equating the ionization and recombination rates in the H II region:

$$N_{\rm Lyc} = \alpha_{\rm rec}\, n_{\rm e}^2\, V_{\rm HII}, \quad (6.16)$$

where $V_{\rm HII}$ is the volume of the H II region. The electron density is:

$$n_{\rm e} = \sqrt{\frac{N_{\rm Lyc}}{\alpha_2\, 4/3\, \pi\, R_{\rm in}^3}}. \quad (6.17)$$

For $N_{\rm Lyc} = 2.2 \times 10^{53}$ phot. s^{-1} and $R_{\rm in} = 35$ pc, the density is $n_{\rm e} = 426$ cm^{-3}. For a typical H II region temperature of 10^4 K, the resulting thermal pressure is $P_{\rm th}/k_{\rm B} = 8 \times 10^6 \times (35\ pc/R_{\rm in})^{3/2}$ K cm^{-3}.

Table 6.6: Derived values of pressures exerted by different mechanisms in the molecular cloud in SGMC 4/5, at a radious of the H II region of $R_{\rm in} = 35$ pc.

Mechanism	Pressure K cm^{-3}
Radiation[a]	2.2×10^8
Turbulence	4.3×10^8
Stellar winds	$2 \times 10^7 - 3 \times 10^8$
Thermal	8×10^6

[a] Radiation pressure assuming $\tau_{\rm rad} = 1$.

Table 6.6 lists the values for the radiation, turbulent, hot gas and thermal pressures for a radius of the H II region of $R_{\rm in}$. Fig. 6.12 illustrates the dependence of the pressures with the radius. The main mechanism that can balance gravity is turbulence.

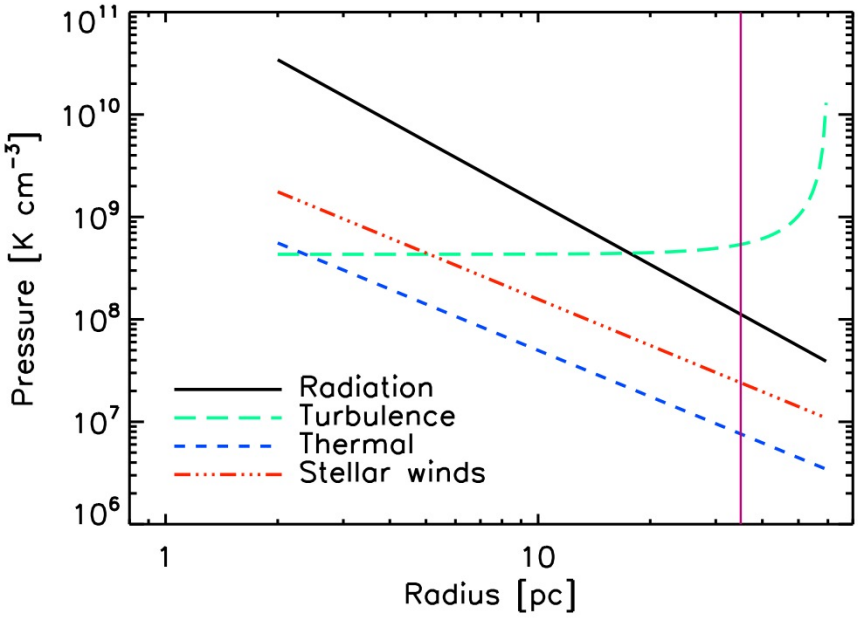

Figure 6.12: This figure illustrates the dependence of the different pressures on the radius of the GMC in SGMC 4/5. The black line corresponds to the radiation pressure, the green line to the turbulent pressure, the blue line to the thermal pressure and the red line to the thermal pressure of the X-ray emitting plasma (driven by stellar winds), respectively. The vertical line marks the radius measured from the Brγ emission of 35 pc.

6.2.4 Comparison with gravity

I can compare the outward forces which contribute to expand the shell with gravity that binds the cloud. Gravity is exerted by the central stellar cluster and the mass of the cloud itself. For a spherical distribution of matter, the gravitational pressure scales with the mass M within a radius r as:

$$P_{\rm grav} = \frac{1}{4\,\pi\,r^2}\left(\frac{G\,M\,M_\star}{r^2} + \frac{G\,M^2}{r^2}\right), \tag{6.18}$$

where $r = R_{\rm GMC}$ and $M = M_{\rm GMC}$ are the radius and mass of the GMC, and $M_\star = M_{\rm SSC}$ is the mass of the SSC. In this equation, the gravitational force is expressed as pressure which can be directly compared with the outward pressures from feedback and turbulence (Fig. 6.12). The first term in Equation 6.18 accounts for the gravity between the central SSC and the GMC, and the second term is the self-gravity of the cloud. Since in our source the molecular cloud is one order of magnitude more massive than the SSC, the self-gravity is the main force that binds the GMC. For our source, the global gravitational pressure was estimated to be $P_{\rm grav} = 1.3 \times 10^9 \times ([60\ {\rm pc}]/r)^4\ {\rm K\ cm^{-3}}$.

The pressure exerted by the turbulence is similar to that exerted by gravity. This implies that the turbulent pressure can balance gravity. If this balance holds, the radiation pressure may sweep-up the matter slowly. Without internal turbulence there are two possibilities. First, the cloud would still be collapsing because the

radiation pressure alone cannot support the cloud. Second, radiation pressure should be increased by $\tau_{\rm rad} \gtrsim 10$, which leads to the disruption of the GMC in less than 1 Myr. Obviously, the last possibility is unrealistic since we require a very high $\tau_{\rm rad}$ value which is excluded by the K-band opacity.

6.2.5 Expansion time-scale of the complex

To estimate the expansion time-scale of the shell, we assume that stellar winds and turbulence together balance gravity. I made a simple model for the evolution of the molecular cloud, where the shell momentum is driven by radiation pressure from the SSC. In this model, I assume that gravity is balanced by the internal turbulence of the cloud and thus radiation pressure is the only mechanism that sweeps-up the mass of the molecular cloud. I assumed that the total molecular cloud mass is constant at any time which means that hot gas is not carrying away significant interstellar mass. Thus, the change of momentum in time will be:

$$\frac{dP}{dt} = F_{\rm rad} = (1 + \tau_{\rm trap})\frac{L}{c}. \tag{6.19}$$

The momentum can be express as:

$$P = M\,\frac{dr}{dt}, \tag{6.20}$$

where dr/dt is the velocity of the expansion. Resolving Equations 6.19 and 6.20, for an expansion starting with zero velocity and keeping the $\tau_{\rm trap}$ value as a free parameter constant in time, the radius and velocity of the shell vary with time as:

$$r(t) = (1 + \tau_{\rm trap})\frac{L}{2\,M\,c}t^2 \tag{6.21}$$

$$v(t) = (1 + \tau_{\rm trap})\frac{L}{M\,c}t, \tag{6.22}$$

I constrain $\tau_{\rm trap}$ with the observed characteristics of the cloud: at $t = 3.5$ Myr (the observed age of the cluster) the expansion radius has to be 35 pc, the radius of the H II region. By doing that, I obtain $\tau_{\rm trap} = 0.5$ and a current velocity of the expansion of 20 $\mathrm{km\,s^{-1}}$. The value of $\tau_{\rm trap}$ is an effective value averaged over the whole expansion of the shell. This solution is not unique but it is a consistent solution. The expansion velocity is smaller than the observed line-width of 55 $\mathrm{km\,s^{-1}}$. This agrees with our hypothesis that the observed line-width is dominated by turbulence. The value of $\tau_{\rm trap}$ is small which agrees with the fact that the shell is not closed. I did not quantify alternative solutions where the expansion is faster and there is no turbulence, but such solutions will require unrealistic high values of $\tau_{\rm trap}$.

Figure 6.2, which shows the H_2 $1-0$ S(1)to-stellar mass ratio for SSCs at different ages, allows me to test the proposed scenario. I compute the H_2 emission along the expansion of the cloud. I estimate the H_2 flux from the PDR model described in Section 6.2.2. To do that, I write the radiation field and gas pressure in terms of the time. The radiation pressure is $P_{\rm rad}(r)/k_{\rm B} = 5.5 \times 10^7 \times$

$(35\ \mathrm{pc}/r)^2$ K cm^{-3}. From Equation 6.21 and for $\tau_{\mathrm{trap}} = 0.5$, the pressure is $P_{\mathrm{rad}}(t)/k_{\mathrm{B}} = 5.5 \times 10^7 \times (3.5\ \mathrm{Myr}/t)^4$ K cm^{-3}. Similarly, the radiation field depends on time as $\chi(t) = 7.5 \times 10^3 \times (3.5\ \mathrm{Myr}/t)^4$. Since I have PDR models for gas pressures smaller than 10^8 K cm^{-3}, I can compute the variation of the H_2 emission only for $t > 3$ Myr.

The results of this variation are presented as the green line in Figure 6.2. We see that the H_2 emission does not decrease as fast as the observations. This could imply that we are overestimating the expansion time scale. Alternatively, another factor contributes to the decrease of H_2 emission. In our calculation we assume that the surface covering factor of molecular gas is constant with time. This is unlikely to be true because the molecular gas is photodissociated and photoionized as it is expanding. It is difficult to quantify how much this reduces the observed H_2 emission. This interpretation fits with Fig. 6.3 which shows that the Brγ does not decrease as fast as the H_2. One other possibility to be quantify is that part of the H_2 emission can come from shocks associated with gas accretion and turbulent energy dissipation. If this contribution is significant for SSC B1, the PDR contribution will be lower. I am planning to do these calculations before submitting this work as a scientific article.

6.3 Conclusions

In this Chapter, I investigated the impact of stellar feedback from SSCs on GMC scales in the Antennae overlap region. I am using for this the SINFONI and ALMA data, together with published observations. The main results of this study are:

– It is difficult to isolate the molecular and ionized emission associated with SSCs. The SGMCs, where the SSCs are embedded, present extended emission with complex velocity structures. Moreover, they harbor several sources. We focus on six isolated massive SSC. Three of them are detected in Brγ, including one in both Brγ and H_2 $1-0$ S(1). In addition, we find in the SINFONI data three ionized compact sources, coinciding with continuum sources. These six sources point at SSCs still associated with their parent cloud.

– Most of the SSCs across the overlap region older than 5 Myr, have already cleared-out their surrounding gas. For a typical stellar cluster mass of 10^6 $M_\odot$, an upper limit for the time-scale of the disruption of the parent cloud is about 5 Myr.

– We study in detail the SSC B1, which is associated with both ionized and molecular gas, which is located in SGMC 4/5. The detection of molecular gas indicates that SSC B1 is still embedded in its parent molecular cloud. In this cluster, we witness the action. CO emission presents two velocity components, a compact one at the position of the SSC and are extended one of the scale of the SGMC. This second component also peaks at the position of the SSC. This suggests that the parent cloud of the SSC is still connected to the SGMC and, may still be forming by accreting gas.

– The CO line-width may not be explained by expansion of the parent cloud. It traces turbulent motions. Only turbulence produces enough pressure to balance the molecular cloud self-gravity. The expansion of the molecular cloud will occur slowly through momentum transfer due to the radiation pressure. We quantify the time-scale of the cloud expansion driven by radiation pressure. The present inner radius of 35 pc (the radius of the H II emission), will reach 60 pc (the present size of the GMC) in 1.5 Myr.

Chapter 7

Conclusions and Perspectives

Contents

In this Chapter, I first give an overview of the results and the conclusions of my thesis work. These include the formation of super-giant molecular clouds (SGMCs), the formation of pre-cluster clouds (PCCs) within SGMCs, and the disruption of parent molecular clouds by newly formed stars. I put them together in a broader context to have a full picture of the star formation process in the Antennae overlap region. More detailed results are given in every chapter of this thesis. Second, I outline a research project based on the results of my PhD work.

7.1 Conclusions

More than 10 years ago, IRAS observations demonstrated that galaxy mergers are high IR luminous sources powered by bursts of star formation. Furthermore, HST observations showed that most stars in the Antennae galaxies are formed in massive stellar clusters (up to 10^7 $M_\odot$) dubbed super-star clusters (SSCs). However, our understanding of how the molecular gas is converted into stars is still incomplete. My thesis addresses this question in an observational way, being guided by these two following questions:

(1) **How do the large-scale dynamics of galaxy interactions trigger star formation on much smaller scales?**

(2) **What is the impact of the stellar feedback from super-star clusters on their surrounding matter?**

My thesis work is based on observations with the SINFONI spectro-imager at the VLT in the K-band, which includes H_2 rovibrational and Brγ line emission, and with the ALMA interferometer which gives us information on the CO$(3-2)$ line emission

and dust continuum. Both data-sets have sub-arcsecond angular resolutions, which is enough to resolve the scales of stellar cluster formation (> 60 pc) in the Antennae galaxies (at a distance of 22 Mpc). Also, the spectral resolutions are sufficient to resolve motions within SGMCs. These observations were complemented with ancillary data at other wavelengths. The main results of my thesis are:

1. **H_2 emission from the overlap region is powered by shocks rather than UV heating in PDRs.**

   H_2 emission was first identified as a tracer of the dissipation of the turbulent kinetic energy in the diffuse Galactic ISM based on ISO observations (Falgarone et al. 2005). With Spitzer, this was extended to extragalactic sources. Spitzer observations revealed a diverse set of sources with H_2-to-PAH flux ratios which cannot be accounted for by UV heating in PDRs (Appleton et al. 2006; Ogle et al. 2010). Guillard et al. (2009) and Nesvadba et al. (2010) discuss two archetype sources, the Stephan's Quintet galaxy-wide shock and the H_2 luminous radio galaxy 3C 326. In the first source, the turbulence is powered by the galaxy interaction. In the second one, turbulence is induced by the interaction between the radio jet and the ISM. In both sources the star-formation efficiency of the gas is low.

   In the Antennae galaxies, like in the Stephan's Quintet, the kinetic energy of the merging gas is high, but nevertheless the star formation rate is high. Brandl et al. (2009) analyzed the Spitzer observations of rotational H_2 lines, at an angular resolution of $5''$ that corresponds to the typical sizes of SGMCs. They found that the ratio between mid-IR H_2 and both far-IR and PAH fluxes, as well as the line ratios between mid-IR rotational lines, are compatible with UV heating in PDRs. They discarded shocks as the origin of H_2 excitation. They also claimed that there is no evidence for large-scale shocks in the overlap region, as reported for Stephan's Quintet (Appleton et al. 2006).

   In my thesis, I present near-IR observations that provide extinction-independent diagnostics to discriminate between UV and shock heating of the gas, the H_2 $1-0/2-1$ S(1) and Brγ/ H_2 $1-0$ S(1) line ratios. From these diagnostics, I proved that most of the H_2 emission in the Antennae overlap region is shock powered (Chapter 4). This holds true for SGMCs and for PCC1, but not for the SSC embedded in its parent cloud (see Chapter 6).

2. **H_2 emission may trace turbulent energy dissipation associated with the formation of gravitationally bound clouds.**

   Earlier studies of the star formation in the Antennae focus on the analysis of CO and H I line emission to trace molecular and atomic mass (Wilson et al. 2000; Hibbard et al. 2001; Ueda et al. 2012). In Zhang et al. (2001), CO and H I maps are compared with common tracers of the star formation rate (i.e. far-UV radiation, dust IR continuum, Hα, radio continuum). They find that

the Kennicutt-Schmidt law applies across the Antennae. My ALMA and SINFONI data provide more detailed information since they resolve SGMCs, both spatially and kinematically. The combination of observations of CO, tracer of the molecular mass, and warm H_2, tracer of energy dissipation, line emission is crucial to characterize the morphology and kinematics of the molecular gas from where stars form and, thus, to characterize the star formation process. These observations allow me to address the question of the energetics of the molecular gas: how does the gas driven by the large-scale galaxy dynamics lose its kinetic energy to form bound clouds where stars can form?

I find that SGMCs in the Antennae overlap region have at least two broad (linewidths in the range of 50 to 100 $\mathrm{km\,s^{-1}}$) CO velocity components separated by more than 50 $\mathrm{km\,s^{-1}}$. After convolution to the lower spectral resolution of the H_2 SINFONI data, the CO and near-IR H_2 lines display similar emission profiles, which suggests that the warm molecular gas traced by the H_2 emission shares the kinematics of the bulk of the gas traced by CO. The broad width and non-Gaussian line profiles suggest that SGMCs are not globally bound. Some SGMCs show steep velocity gradients which I interpret as converging gas flows driven by the large-scale dynamics of the galaxy interaction. This large-scale motions will drive a turbulent energy cascade within SGMCs. Turbulence and gravity triggers the fragmentation of SGMCs in substructures including massive PCCs. Turbulence connects the large-scale galaxy dynamics to scales where clusters form. Since the Jeans mass scales as the velocity dispersion to the fourth power, large concentrations of masses are required to form bound clouds. The formation of such massive bound clouds must be concurrent with the dissipation of turbulent energy and thereby H_2 emission. In Chapter 5, I propose this interpretation for the H_2 line emission of both SGMCs and PCC1. This is supported by the association of PCC1 in the SGMC with the largest velocity gradient, where the gradient is the steepest.

3. **In a SSC embedded in its parent molecular cloud, radiation pressure does not support gravity. Turbulence does, even after the formation of stars.**

   In a molecular cloud that has formed a massive stellar cluster, the newly formed stars will eventually disrupt their parent cloud. How does this occur in the most massive SSCs in the Antennae? Since, in such clusters, the escape velocity is larger than the sound speed of the ionized gas, there are two possible mechanisms. The disruption can be driven by the expansion of shock-heated plasma or by the radiation pressure. In the nearby massive star cluster 30 Doradus in the LMC, Lopez et al. (2011) compared the different mechanisms through observations at different wavelengths, finding that, in the central part of the cluster, radiation pressure is the main mechanism driving the expansion of the parent molecular cloud. Murray et al. (2010) quantified the main feedback mechanisms for the disruption of the molecular clouds with analytical models. They modeled GMCs located in various en-

vironments from normal spirals to the densest starbursts. They found that in rapidly star-forming galaxies, radiation pressure is the dominant feedback mechanism. GMCs in starburst galaxies have very high surface densities, thus IR radiation produced by dust is trapped within the internal cavity of the cloud. The very high values of $\tau_{\rm trap}$ (> 10) in the models greatly enhance the action of radiation pressure.

With the SINFONI and ALMA observations, I identify in the Antennae overlap region a massive ($\sim 10^7$ $M_\odot$) and young (3.4 Myr) SSC, B1, which is still embedded in its parent molecular cloud. Like in Lopez et al. (2011), the data allows me to quantify the feedback mechanisms. I conclude that radiation pressure cannot support gravity, unless IR photons are highly trapped in the H II cavity before escaping the cloud to balance gravity, $\tau_{\rm trap} > 10$. Such a high value of $\tau_{\rm trap}$ is excluded for SSC B1 since the extinction correction estimated from the comparison between the radio continuum emission and the Brγ line is only a factor 2. The shell around the cluster must be clumpy with moderate column density lines-of-sight through which radiation can escape. The X-ray flux is weak which indicates that the pressure of shock-heated plasma is small.

I estimate the expansion velocity of the gas to be smaller than the observed CO line-width. Therefore, I argue that the CO line-width is turbulence dominated. ALMA observations with higher angular resolution would be needed to validate this interpretation. If I am right, turbulence has enough strength to balance the gravity of the massive parent cloud. The outward momentum provided by radiation pressure is thus fully converted in expansion of the cloud. This expansion is not fast. It cannot alone account for the time-scale of 5 Myr over which H_2 emission from SSCs is observed to decrease (Chapter 6).

My thesis focuses on diverse sources in the overlap region which trace different stages of star formation: the gathering of mass necessary to form SGMCs, the formation of PCCs within SGMCs and the disruption of parent clouds by newly formed SSCs. At each stage turbulence plays a key role. (1) Turbulence in SGMCs, which is driven by the large-scale dynamics of the merger, has an amplitude much larger than that observed in GMCs within normal galaxies. The high turbulence scales up the mass of clouds which are formed by gravitational fragmentation. (2) The characteristics of PCC1 suggest that the formation of gravitationally bound clouds massive enough to form SSCs is initiated by dissipation of the gas turbulent kinetic energy in regions of large velocity shear. The dissipation of turbulence may allow gravity to become locally dominant. (3) Turbulent energy in the parent cloud of SSC B1 is comparable to its gravitational energy. This implies that all feedback mechanism providing outward momentum contribute to disrupt the cloud.

These results are based on only one specific environment, the Antennae overlap region, where we have only one example of PCC within a SGMC, and where we witness the disruption of only one molecular cloud. Obviously, the ideas presented in my thesis have to be confirmed by additional observations. I have started think-

ing about this. In the following section, I discuss three projects which have been submitted to obtain telescope time.

7.2 Quantifying turbulence and searching for more PCC-like sources in diverse environments

In this section, I present three projects. In Section 7.2.1, I propose to image the emission of the Antennae galaxies in the mid-IR H_2 S(2) line (at 12.28μm rest wavelength) with the VISIR/VLT camera. In Section 7.2.2, I propose to observe molecular tracers of shocks in the Antennae overlap region with ALMA. In Section 7.2.3, I propose to extend the near-IR observations to other extragalactic sources in particular mergers at different stages of evolution.

7.2.1 Searching for PCC-like sources in the mid-IR

The analysis of the SINFONI data shows that it is difficult to separate the compact PCC-like sources from the extended H_2 emission from SGMCs. Since PCCs have very large column densities $\sim 10^{24}$ H cm^{-2} (see Section 5.3.1), the H_2 emission from PCCs must be more attenuated by extinction than that of SGMCs. In the mid-IR for the H_2 S(2) line the dust extinction is one order of magnitude smaller than that in the near-IR. Thus, I expect the contrast between PCCs and SGMCs to be higher for the mid-IR lines. This is the idea which motivated a search for PCC-like sources in the mid-IR with VISIR in the Antennae galaxies.

If H_2 luminous PCCs represent an early stage in the formation of SSCs where gravitationally bound clouds are being formed by gas accretion, we can estimate the expected number of PCC-like sources from the observed number of SSCs and the accretion time-scale. This time-scale is assumed to be the time-scale of the H_2 luminous phase. In the Antennae pair, Mengel et al. (2005) showed that there are $\sim$ 36 SSCs with masses larger than 10^6 $M_\odot$ and ages less than 6 Myr. This yields a formation rate of $\sim$6 SSCs per Myr with a mass larger than 10^6 $M_\odot$. If the accretion time-scale of the turbulent energy of PCC-like sources is $\sim$1 Myr, the number of PCC-like sources has to be $\sim$6. The number of H_2 luminous sources increases with the accretion time scale, but the luminosity for a given mass decreases (Figure 7.1). To prepare the VISIR proposal, I have quantified this dependance using Equation 5.7. Numerically, the equation is:

$$L_{H_2} = 3.9 \times 10^6 \; L_\odot \times \left(\frac{\dot{M}_{\rm acc}}{10 \; M_\odot \; {\rm yr}^{-1}} \right) \times \left(\frac{\Delta {\rm v}}{80 \; {\rm km \; s}^{-1}} \right)^2 \frac{f_{H_2}}{0.25}. \qquad (7.1)$$

where $\dot{M}_{\rm acc}$ is the gas accretion rate and the value Δv is the amplitude of the velocity gradient observed across the SGMCs with ALMA, which have a typical value of 80 km s^{-1}. From the Spitzer observations (Brandl et al. 2009) we can estimate the H_2 S(2) contribution to the bolometric H_2 luminosity. For all the SGMCs, the ratio between the H_2 S(2) emission line and the sum of the S(0) to

S(3) H_2 lines is 0.17. This value yields a H_2 S(2) luminosity of $6.6{\times}10^5$ $L_\odot$ to form a 10^7 $M_\odot$ cloud in 1 Myr. We assume that this is the required mass to form a SSC of 10^6 $M_\odot$. This 10% efficiency is what we observe in SSC B1. Thus, we can write Equation 7.2 for the H_2 S(2) line as:

$$L_{\mathrm{H_2S(2)}} = 6.6 \times 10^5\ L_\odot \times \left(\frac{M_{\mathrm{PCC}}/\tau_{\mathrm{acc}}}{10\ M_\odot\ \mathrm{yr}^{-1}}\right) \times \left(\frac{\Delta \mathrm{v}}{80\ \mathrm{km\ s}^{-1}}\right)^2 \frac{f_{\mathrm{H_2}}}{0.25}. \qquad (7.2)$$

In Figure 7.1, I highlight the detection limit (sensitivity) of our proposed mid-IR observation of 3×10^5 $L_\odot$. This observation may reveal the existence of other PCCs in the Antennae. The number of sources that we will find, will give us a constraint on the time-scale of the luminous H_2 phase of the PCCs. It will also test our interpretation of the origin of the H_2 emission from PCCs. We hope to detect new sources, but the results will be significant even if we do not detect any new PCC. In both cases, the observations will provide us with additional information that can allow us to be more specific in our interpretation of the H_2 luminosity of PCC1 observed with SINFONI. The non-detection of any new H_2 luminous source may have two interpretations. First, PCC1 may be an exceptional object which traces a very short ($\lesssim$ 1 Myr) phase in the evolution of PCCs. Second, the mean formation time-scale is larger than 2 Myr.

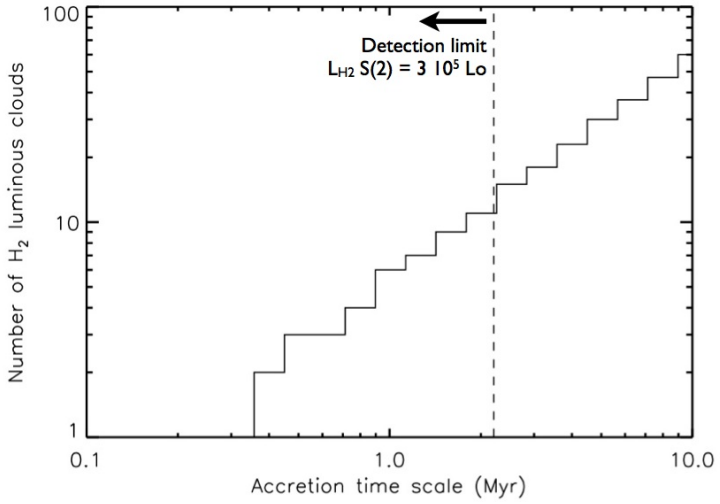

Figure 7.1: Estimate of the number of the detected sources for the proposed H_2 S(2) luminosity detection limit. The number of detected sources will change according to the accretion time-scale over which PCCs are formed (the time-scale over which they are assumed to be H_2 luminous sources). Based on statistics of young and massive SSCs in the Antennae, we estimate that we should detect several new H_2 luminous sources if the formation time-scale of the pre-SCC clouds is smaller than 2 Myr.

7.2.2 Observing molecular shock tracers with ALMA

High spatial and spectral resolution observations are needed to separate PCCs from SGMCs. Our near-IR H_2 SINFONI observations are limited by the seeing ($0\farcs65$) and the instrumental spectral resolution (~ 100 km s^{-1}). The mid-IR H_2 imaging VISIR observations are limited by diffraction to an angular resolution of about $0\farcs4$ and do not provide spectral information. ALMA observations can provide both better angular and spectral resolution that is essential to test and complement our interpretation of H_2 observations. I prepared a proposal for Cycle1 where we want to explore the possibility of replacing H_2 as a tracer of mechanical energy dissipation with molecular shock tracers observable with ALMA.

Specifically, we proposed to observe SiO, J = 2 − 1 and J = 5 − 4, HNCO, and CH_3OH, within Bands 3 and 6, with an angular resolution of $\sim 0\farcs5$ at the highest frequencies. With these observations, we plan to address the two following questions.

(a) Is H_2 radiation powered by shocks or not?
SiO is commonly used as a shock tracer in the environment of YSOs and Galactic molecular clouds (Martin-Pintado et al. 1997; Martín et al. 2008). SiO has also been imaged in nearby galaxies, like in the spiral galaxy IC 342, where SiO is observed away from the nuclear starburst. This is interpreted as evidence of dissipation, on the scale of GMCs, of turbulent energy driven by the large-scale galaxy dynamics (Usero et al. 2006). With ALMA, we can extend this pioneering work to the Antennae merger. The sub-arcsecond resolution will allow us to assess whether the energy source powering the H_2 emission comes from embedded SSCs (UV and stellar winds) or the large-scale dynamics of the merger. We will observe the shock tracers SiO, CH_3OH and HNCO, testing our interpretation of H_2 radiation powered by shocks. The detection of these molecules from the SGMCs and PCCs can be uniquely related to shock chemistry. It will be an unambiguous evidence of energy dissipation in shocks driven by the large-scale merger dynamics.

(b) Tracing energy dissipation from SGMCs to PCCs.
ALMA gives us the combination of spectral and spatial resolution needed to describe the dynamical state of the sources, not provided by Spitzer nor SINFONI H_2 observations. From the MHD shock code of Flower & Pineau des Forêts (2010, Fig. 7.2), we know that the SiO line emission correlates with the H_2 S(3) line, which is a main cooling line of shocks with velocities larger than 10 km s^{-1}. This indicates that SiO (and CH_3OH & HNCO) can be used as a tracer of energy dissipation in shocks. We will validate this by correlating the emission from these shock tracers with the H_2 line emission among SGMCs, obtained with both Spitzer and VLT/SINFONI, and within SGMCs, for the SINFONI near-IR lines. Besides, the intensity ratio between SiO(5−4) and (2−1) will constrain the gas density (Fig. 7.2). We expect SiO(2−1) to be best suited to detect the extended emission from SGMCs while SiO(5−4) will be best to detect emission from denser gas in PCC-like sources.

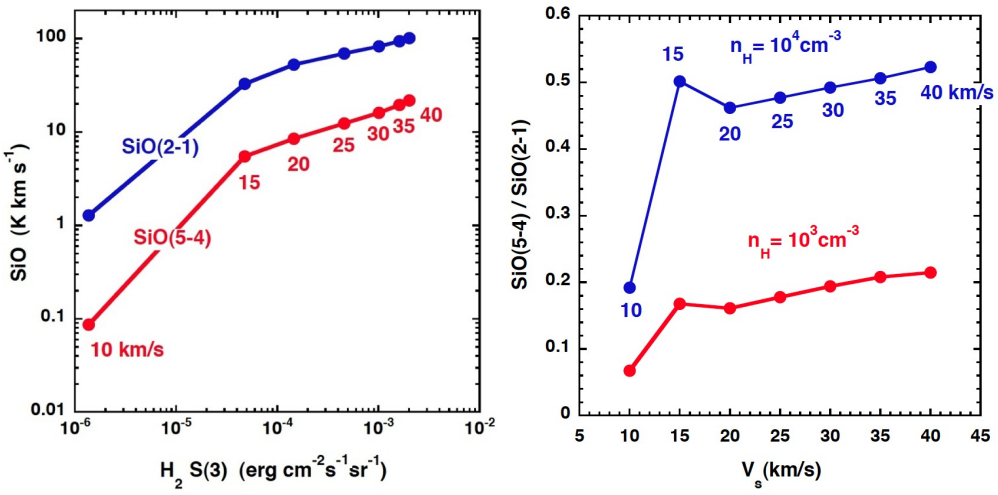

Figure 7.2: Predictions for the SiO and H_2 molecules by the MHD shock model of Flower & Pineau des Forêts (2010). *Left panel.* Intensities of the SiO$(2-1)$ and $(5-4)$ lines in comparison with the intensity of the H_2 S(3) line for a gas density of $n_{\rm H} = 10^3$ cm^{-3}. Values are given for velocity shocks from 10 to 40 km s^{-1} by 5 km s^{-1}. The SiO lines correlates with the H_2 line emission for shock velocities larger than 15 km s^{-1}. *Right panel.* Estimated ratio between the SiO$(5-4)$ and $(2-1)$ lines, for two different values of density, $n_{\rm H} = 10^3$ and 10^4 cm^{-3}. This ratio depends on the gas density but not on the shock velocity. This figure was provided to me by G. Pineau des Forêts.

7.2.3 Observing other galaxies

The results of my thesis, which are uniquely based on the Antennae galaxies, must hold true in other galaxies. However, with only one example in a specific merger, I am presently unable to generalize these results. I plan to expand my work to mergers that are in different evolutionary stages, from the first encounters to coalescence. It will be also interesting to observe and/or analyze archival data on starbursts and other nearby galaxies.

The first step I have already done is to obtain imaging observations of the near-IR H_2 $1-0$ S(1) and Brγ emission. These lines give us an extinction-independent diagnostic to discriminate between UV and shock heated gas. I will start this investigation by analyzing recently obtained CFHT near-IR narrow-band imaging of H_2 $1-0$ S(1) and Brγ for four nearby galaxy mergers, NGC 520, NGC 2207, NGC 6050, and NGC 3395. These galaxies are at a distance comparable to the Antennae. Their morphologies suggest that they are in a similar evolutionary stage as the Antennae galaxies, near pericenter passage. In these mergers, like in the Antennae, the galaxy interaction injects kinetic energy rapidly into the ISM. Figure 7.3 illustrates what we expect to observe with the CFHT observations. These observations will allow us to identify the locations of possible detections of PCC-like sources. They will guide follow-up observations with spectro-imagers in the near-IR and with ALMA.

My thesis work may open a new observational avenue towards understanding

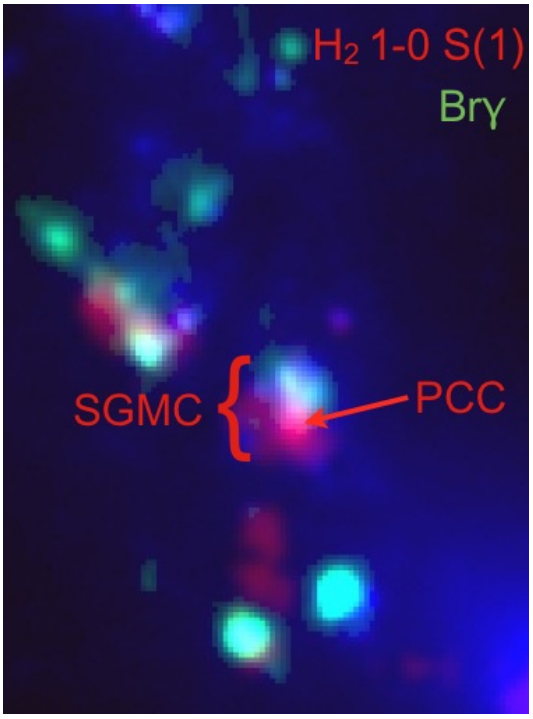

Figure 7.3: The Antennae overlap region as seen by CFHT. This figure is a zoom of Figure 3.2. The color image is composed by the K-band continuum in blue, Brγ line emission in green and H_2 $1-0$ S(1) line emission in red. PCC1 is observed as an emission peak within SGMC 2.

the evolutionary link between galaxy interactions and star formation, a link which has important implications for our understanding of galaxy evolution overall. More follow-up observations than those I have already been working on, will certainly materialize in my future research.

Appendix A

An additional molecular compact source, PCC2

A few months before writing this manuscript, I came back to the data to prepare an ALMA Cycle1 proposal. After an inspection through each SGMC/SINFONI data-cube, I found another compact molecular source. I did not identify this source before because it was *hidden* by the bright H_2 emission associated with SGMC 1. In this section, I introduce it and measure its physical properties.

PCC2 is a compact molecular source located in SGMC 1, between the SSCs D and D2 (see Fig. 3.17). Fig A.1 shows the x and y axis profiles of SGMC 1 at the position $\alpha : 12^{h}01^{m}55\overset{s}{.}34, \delta : -18°52'48\overset{''}{.}0$, where the PCC2 peaks. Since this source is embedded in the extended emission from SGMC 1, it is difficult to isolate. I measure the size from the emission profile in the y-axis, which rather than the x-axis profile has less contribution from the extended emission (black spectrum in Fig. A.1). The observed FWHM was obtained from a 1-D Gaussian fit, and it gives an observed size of $1\overset{''}{.}2$. After correction by the seeing of the SINFONI observations, the size of the source is $0\overset{''}{.}99$ (106 pc).

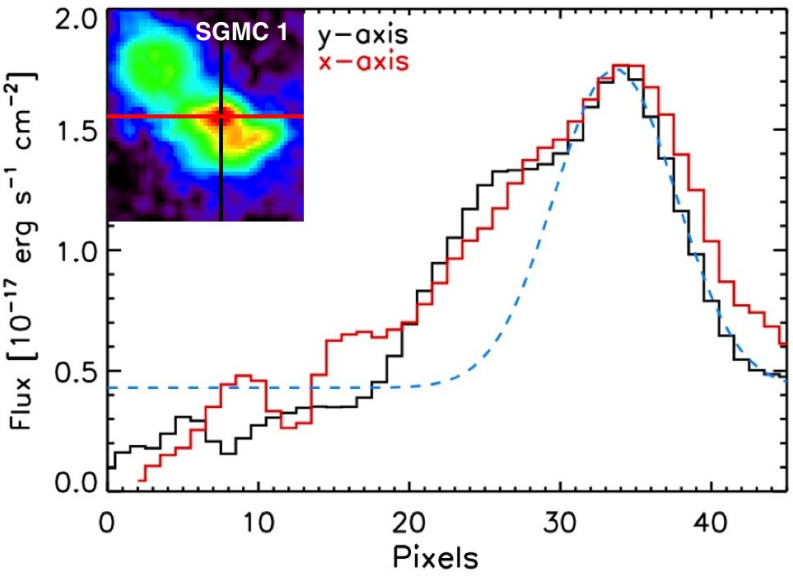

Figure A.1: Emission profile of the compact molecular source located in SGMC 1, PCC2. Color image on the top-left corresponds to the H_2 $1-0$ S(1) integrated line emission of SGMC 1. Black and red lines represent the cuts through the y and x axis, respectively, from where the spectra were taken. The blue dashed line is the 1-D Gaussian fit to the y-axis.

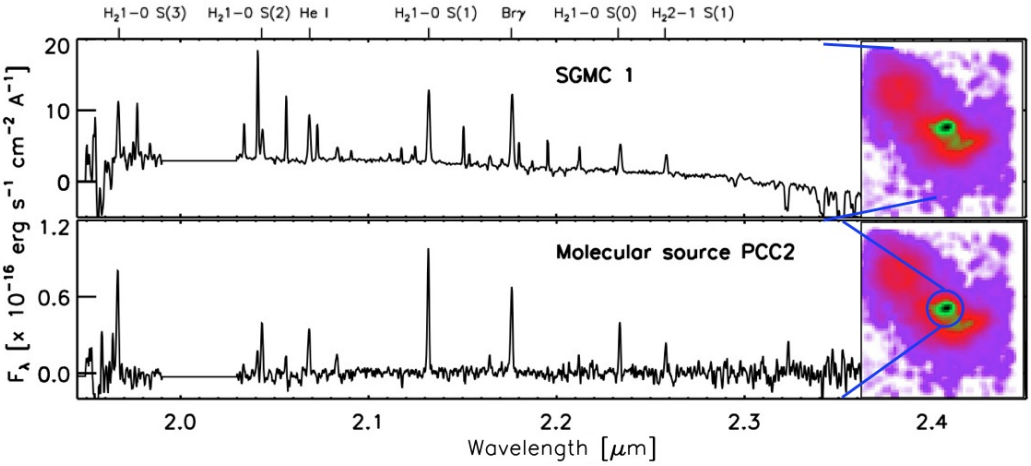

Figure A.2: Integrated SINFONI spectra for the extended emission from the SGMC 1 and the compact source PCC2. The spectra are smoothed by 3 bins in wavelength. Around 2.0 μm the atmospheric transmission is very low so we did not plot this part of the spectra. Small color images to the right are the H_2 $1-0$ S(1) integrated emission where we highlight PCC2.

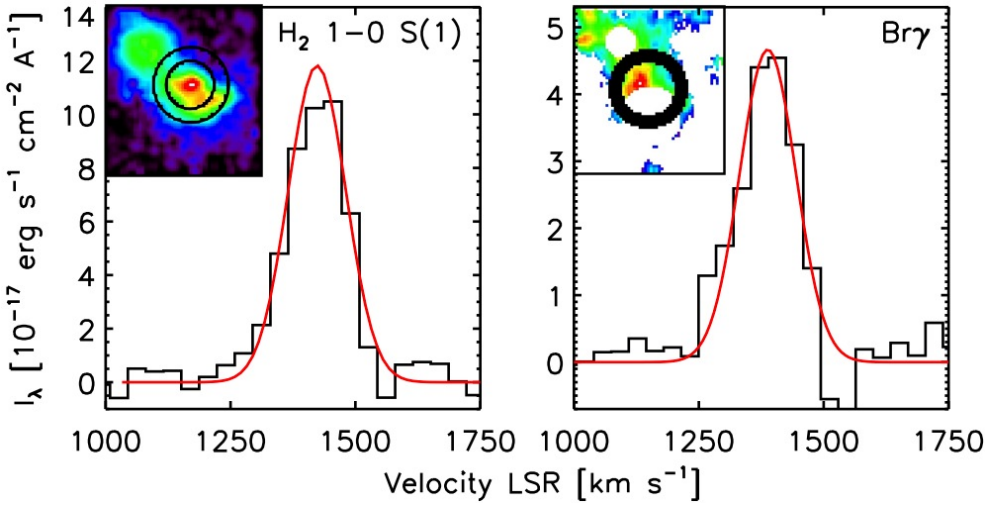

Figure A.3: H_2 $1-0$ S(1) and Brγ spectra of PCC2. Small color images show the intensity map for each line. The Brγ image presents the mask used to exclude the emission from the SSCs D and D2. The circles represent the apertures used for photometry, emission and annulus. The red lines correspond to the Gaussian fit.

Figure A.2 shows the integrated K-band spectra, on the top, for the whole SGMC 1 and, on the bottom, for PCC2. The spectrum for the whole SGMC 1 is obtained by integrating the emission over the whole area where the gas is emitting, without any subtraction. The spectrum for PCC2 is measured by aperture photometry of diameter twice the observed FWHM, subtracting the background within an annulus of $0\farcs65$ width, the SINFONI seeing. In particular, to measure the ionized line fluxes I masked the emission from the nearby SSCs, D and D2. The emission

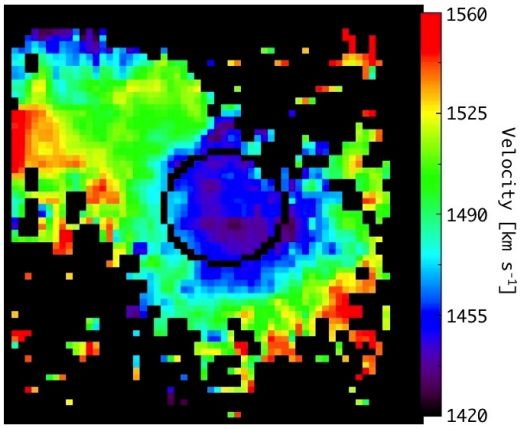

Figure A.4: H_2 $1-0$ S(1) velocity map of SGMC 1. The circle mark the position of PCC2, which coincides with the lowest velocity across SGMC 1.

profiles of H_2 $1-0$ S(1) and Brγ are given in Fig. A.3. Small color images correspond to the SGMC 1 emission in each line. The Brγ image shows the masking. I fit Gaussian curves to all the molecular and ionized lines in the near-IR to measure their intensities, line-widths and velocities. These values are listed in Table A.1. Figure A.4 presents the H_2 $1-0$ S(1) velocity map of the SGMC 1. The black circle indicates the position of PCC2, where the H_2 $1-0$ S(1) velocity is the lowest, surrounded by higher velocity gas.

Figure A.5 presents the CO$(3-2)$ spectrum of PCC2. The color image is the CO$(3-2)$ intensity map, and the circles represent the apertures used to do the photometry, where the inner circle delimits the emission and the outer circle the annulus used for background subtraction. The black line corresponds to the total emission without any subtraction. The red line is the annulus and the blue line is the PCC2 emission. The annulus emission shows a component at a larger velocity (~ 1500 km s^{-1}) not associated with PCC2. I did a Gaussian fit to the main velocity component at $v = 1389$ km s^{-1}, obtaining a flux of $F_{\mathrm{CO}(3-2)} = 71$ Jy km s^{-1} and a line-width of $\Delta v = 65$ km s^{-1}.

I computed the contribution of the two velocity components in SGMC 1. Figure A.6 shows the H_2 $1-0$ S(1) intensity map as the color image. Black and white contours are the CO$(3-2)$ emission integrated between 1300 and 1415 km s^{-1}, and between 1415 and 1490 km s^{-1}, respectively. PCC2 is directly associated with the component with lower velocity.

PCC2, as PCC1, is not detected in the continuum emission at 230 nor at 345 GHz. The upper limit of its mass correspond to the same upper limit for PCC1, 2×10^7 $M_\odot$. From Equation 5.8, I compute the virial mass of PCC2 using its H_2 size and CO line-width of the main velocity component $\Delta v = 65$ km s^{-1}, $M_{\mathrm{vir}} = 4.8 \times 10^7$ $M_\odot$, which is more than twice higher than the upper limit estimated from the dust emission.

I also infer its stellar mass, following the method presented in Section 5.3.2.

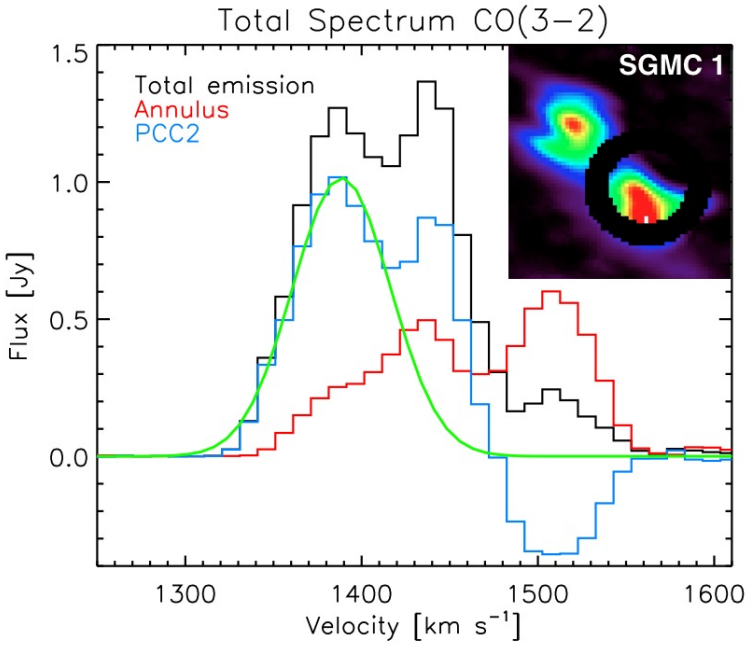

Figure A.5: This figure displays the CO(3 − 2) emission from the PCC2. The color image is the CO(3 − 2) intensity map, where I marked the aperture sizes used for photometry. The inner circle defines the source emission and the outer circle the annulus used for background subtraction. The black, red and blue lines correspond to the total, annulus and PCC2 emission. The green line correspond to the Gaussian fit of the main velocity component.

PCC2 is not a compact source in the radio maps at 4 nor 6 cm of Neff & Ulvestad (2000). I estimate an upper limit of for its radio continuum emission at 6 cm of 175 μJy, which yields an ionizing photon rate of $N_{\rm Lyc} = 7.5 \times 10^{51}\,{\rm s}^{-1}$, and a stellar mass of $M_\star \sim 1 \times 10^5\ M_\odot$. This value corresponds to a 0.5% of the mass estimated from the dust continuum emission.

The observed characteristics and estimated properties of PCC2 suggest that this source, as PCC1, is still accreting gas mass and its H_2 emission is tracing the dissipation of the turbulent kinetic energy driven by this accretion. As I mentioned before, this is a preliminary result that has to be deeper studied.

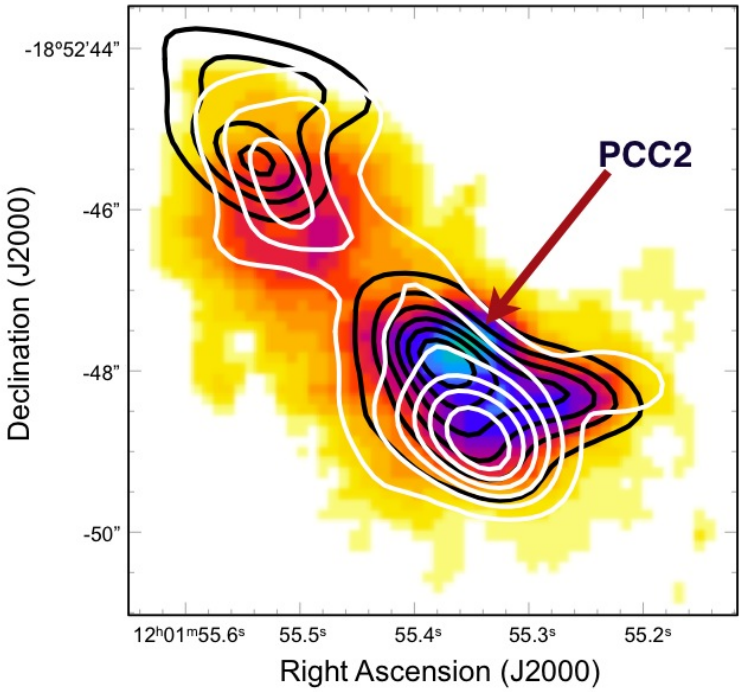

Figure A.6: The color image is the H_2 $1-0$ S(1) flux map from SGMC 1. Black and white contours are the $CO(3-2)$ emission integrated in the velocity range $1300-1415$ $km\,s^{-1}$and $1415-1490$ $km\,s^{-1}$, respectively. I highlight PCC2.

Table A.1: Line parameters measured for PCC2 in SGMC 1

Line	Flux$\times 10^{16}$	Velocity	FWHM
H_2 $1-0$ S(3)	11.0 ± 0.9	1383 ± 5	175 ± 11
H_2 $1-0$ S(2)	4.6 ± 0.9	1423 ± 8	137 ± 20
H_2 $1-0$ S(1)	12.1 ± 0.6	1422 ± 3	135 ± 5
H_2 $1-0$ S(0)	4.5 ± 0.7	1410 ± 6	117 ± 13
H_2 $2-1$ S(1)	2.8 ± 0.8	1404 ± 11	128 ± 27
Brγ	6.2 ± 0.6	1393 ± 6	144 ± 11
HeI	2.7 ± 0.4	1400 ± 7	139 ± 16

Fluxes are given in erg s^{-1} cm^{-2}, and velocities and FWHM in km s^{-1}.

Appendix B

Articles published in Astronomy & Astrophysics

Contents

A&A 534, A138 (2011)
DOI: 10.1051/0004-6361/201117324

Astronomy & Astrophysics

From large scale gas compression to cluster formation in the Antennae overlap region⋆

C. N. Herrera, F. Boulanger, and N. P. H. Nesvadba

Institut d'Astrophysique Spatiale, UMR 8617 CNRS, Université Paris-Sud 11, 91405 Orsay Cedex, France
e-mail: cherrera@ias.u-psud.fr

Received 23 May 2011 / Accepted 1 September 2011

ABSTRACT

We present a detailed observational analysis of how merger-driven turbulence may regulate the star-formation efficiency during galaxy interactions and set the initial conditions for the formation of super star clusters. Using VLT/SINFONI, we obtained near-infrared imaging spectroscopy of a small region in the Antennae overlap region, coincident with the supergiant molecular cloud 2 (SGMC 2). We find extended H_2 line emission across much of the 600 pc field-of-view, traced at sub-arcsecond spatial resolution. The data also reveal a compact H_2 source with broad lines and a dynamical mass $M_{\rm dyn} \sim 10^7\ M_\odot$, which has no observable Brγ or K-band continuum emission, and no obvious counterpart in the 6 cm radio continuum. Line ratios indicate that the H_2 emission of both sources is powered by shocks, making these lines a quantitative tracer of the dissipation of turbulent kinetic energy. The turbulence appears to be driven by the large-scale gas dynamics, and not by feedback from star formation. We propose a scenario where the H_2 emission is related to the formation of bound clouds through accretion. The kinetic energy of the accreted gas drives the turbulence and powers the H_2 emission. Broad H_2 line widths of-order 150 km s^{-1}, similar to the velocity gradient of the gas across the field of view, support this idea. Within this interpretation, the compact H_2 source could be a massive cloud on its way to form a super star cluster within the next few Myr. This scenario can be further tested with ALMA observations.

Key words. galaxies: ISM – galaxies: interactions – galaxies: starburst – galaxies: star formation

1. Introduction

Detailed observations of the nearby Antennae galaxy merger NGC4038/4039 at a distance of only 22 Mpc (Schweizer et al. 2008) provide important benchmarks for our understanding of how the large-scale dynamics of galaxy interactions trigger star formation on much smaller scales. Contrary to the "canonical" scenario of merger-induced star formation, which predicts intense starbursts in the nuclear regions (e.g., Barnes & Hernquist 1996), most stars in the Antennae are formed off-nucleus, in a heavily obscured, gas-rich, infrared-luminous region where both galaxies permeate each other, the "overlap region" (e.g., Vigroux et al. 1996; Klaas et al. 2010).

Most of the star formation in the overlap region of 20 $M_\odot$ yr^{-1} (Zhang et al. 2001) occurs in massive super-star clusters (SSCs) with masses larger than 10^4 and up to a few $10^6\ M_\odot$ (Whitmore & Schweizer 1995; Zhang & Fall 1999; Whitmore et al. 2010). Detailed studies of SSCs constrain the recent star formation history of the overlap region. At typical ages of few 10^6 yrs, many SSCs have already expelled most of the gas and dust from their immediate surroundings, and they may be becoming unbound themselves (Fall et al. 2005; Mengel et al. 2005; Gilbert & Graham 2007; Fall et al. 2010).

Our understanding of how the galaxy interaction may trigger gas collapse and the very early phases in the formation of SSCs, is much less developed and relies mostly on theoretical arguments. For example, Scoville et al. (1986) suggested that the collision between the two galaxies could trigger collisions between pre-existing giant molecular clouds. Jog & Ostriker (1988) argued that shock-heated ambient gas may enhance star formation by increasing the pressure in embedded molecular clouds. Keto et al. (2005) discuss their high resolution interferometric observations of molecular gas and the formation of massive star clusters in the starburst galaxy M 82 within this scenario. However, observations of the Antennae overlap region may not be accounted for by the collapse of pre-shock clouds. The large surface density of molecular gas and its fragmentation in complexes with masses of several $10^8\ M_\odot$ (Wilson et al. 2000), two orders of magnitude larger than masses of giant molecular clouds in spiral galaxies, are evidence for cooling and gravitational fragmentation of the diffuse gas compressed in the galaxy collision.

First attempts to quantify the impact of the interaction on gas cooling and fragmentation have been made with numerical simulations (Teyssier et al. 2010; Karl et al. 2011, 2010), but their description of the energy dissipation of the post-shock, turbulent multiphase ISM is still schematic. The simulations follow the turbulent energy of the gas over a limited range of scales. The mechanical energy of the galaxy collision is thermalized in large-scale shocks and radiated away by the shock compressed post-shock gas. Observations of the galaxy-wide shock in Stephan's Quintet (Appleton et al. 2006; Cluver et al. 2010) show that a dominant fraction of the collision energy is not thermalized in such shocks, but cascades to smaller scales into turbulent motion within molecular gas. This results from the clumpy multi-phase structure of the pre-shock interstellar medium (Guillard et al. 2009). The fact that most of the collision energy is transferred to the molecular gas has consequences for the energy dissipation and the gravitational fragmentation of the post-shock gas, and thereby for induced star formation, which

⋆ Based on observations with the VLT/SINFONI, Program ID 383.B-0789, with the VLT/CRIRES, Program ID386.B-0942, and with the CFHT/WIRCAM, Program ID 09AF98.

A&A 534, A138 (2011)

have yet to be understood. It is the motivation of this paper to investigate how gas compression and turbulence driven by the large-scale dynamics of the two interacting galaxies trigger and regulate star formation in the Antennae overlap region.

Bright H_2 line emission powered by shocks (rather than star formation) has been identified in the diffuse interstellar medium of the Milky Way (Falgarone et al. 2005), as well as in a significant number of extragalactic systems including many interacting galaxies (Appleton et al. 2006; Cluver et al. 2010; Zakamska 2010). This makes emission-line observations of warm H_2 an interesting tracer of the dissipation of turbulent energy in the molecular gas. Haas et al. (2005) proposed, based on ISO observations, that H_2 line emission in the overlap region could probe large-scale shocks driven into molecular clouds. This was later called into question by Brandl et al. (2009), who found lower H_2 line fluxes with Spitzer-IRS, and suggested that the bulk of the warm molecular gas may be heated by star formation after all. However, at a spatial resolution of ∼5″, and a spectral resolution of $R = 600$ (∼500 km s^{-1}) Spitzer-IRS does not allow to study the molecular gas at the scales relevant for the fragmentation of the molecular gas, ≤100 pc and ∼100 km s^{-1}, respectively.

We use near-infrared spectroscopy obtained with the imaging spectrograph SINFONI and the echelle spectrograph CRIRES (both on the ESO Very Large Telescope) to quantify the dissipation of kinetic energy in the molecular gas on scales of few 10 s to 100 s of pc. To this end we observed the region around "knot 5" of Brandl et al. (2009), the brightest H_2 peak in the overlap region. This knot, which is near the massive and IR-bright cluster No. 28 of Whitmore et al. (2010), coincides with the super-giant molecular cloud SGMC 2 observed by Wilson et al. (2000) in CO. SGMC 2 is one of the most massive molecular clouds in the overlap region, with a mass of $4 \times 10^8\,M_\odot$. Our pointing also coincides with knot K2a in the Herschel dust imaging of Klaas et al. (2010). Thus, overall, by selecting an area with particularly bright line emission of warm molecular hydrogen, we observed one of the main sites of molecular gas and star formation in the Antennae overlap region.

The paper is organized as follows. The observations and data reduction are described in Sect. 2. In Sect. 3 we focus on the structure and kinematics of the warm H_2 gas. We identify two components of H_2 emission: diffuse emission extended over the 600 pc wide field of view of SINFONI, and a compact source. We show that, for the compact and diffuse extended emission, the H_2 emission is powered by shocks rather than UV heating, and estimate the bolometric H_2 luminosity of each component combining Spitzer and SINFONI observations (Sect. 4). In Sect. 5 we propose an interpretation of the observations which relates the H_2 emission to the formation of bound clouds through gas accretion. In Sect. 6 we discuss the observations and our interpretation within a broader astrophysical context, highlighting the role of turbulence for the formation of super star clusters and the regulation of the star formation efficiency in galaxy mergers. Section 7 gathers the main conclusions.

2. Observations

2.1. VLT/SINFONI imaging spectroscopy

Our analysis is based on observations carried out with the near-infrared integral-field spectrograph SINFONI (Eisenhauer et al. 2003; Bonnet et al. 2004) on the ESO Very Large Telescope. Data were obtained in service mode under Program ID 383.B-0789 (PI Nesvadba). SINFONI is an image slicer with a field of view of $8'' \times 8''$ and a pixel scale of 250 mas in the seeing-limited mode. The spectral resolution is $R = 4000$ at $\lambda = 2.2$ μm. We observed three regions in the Antennae galaxy merger in the K-band, one near each nucleus and one region in the overlap region. These pointings were selected based on their bright pure-rotational H_2 line emission detected with Spitzer/IRS. This paper presents an analysis of molecular emission of the pointing in the overlap region.

All data were taken in June and July 2009 under good and stable atmospheric conditions. We obtained a total of 1800 s of exposure time split into individual exposures of 600 s. We adopted a dither pattern where one sky frame was taken in-between two object frames to allow for an accurate subtraction of the night sky. Data reduction was done with the standard IRAF tools to reduce longslit spectroscopy (Tody 1993), which we extended with a set of SINFONI-specific IDL routines. For details see, e.g., Nesvadba et al. (2007, 2008). The telluric correction was done using bright ($K \sim 6$–8 mag) stars observed at a similar air mass as our target. We used the light profiles of these stars to measure the PSF of our data, $FWHM = 0\farcs7 \times 0\farcs6$. Comparison with high-resolution HST/NICMOS imaging of Whitmore et al. (2010) shows that our PSF estimate is robust.

2.2. CRIRES high-resolution spectroscopy and CFHT narrow-band imaging

To complement our SINFONI observations we also obtained a high-resolution longslit spectrum with CRIRES on the VLT (program ID 386.B-0942; PI Herrera) and near-infrared imaging of the Antennae through the H_2 1−0 S(1) and the Brγ filters with WIRCAM at the Canada-France Hawaii Telescope (CFHT program ID 09AF98; PI Nesvadba).

With CRIRES we obtained a total of 5 h of integration time of the H_2 1−0 S(1) line at 2.12 μm in the rest-frame for one pointing centered on the compact molecular source (Sect. 3.3) and at position angle PA = 67°. Atmospheric conditions were good and stable. We nodded our target along the slit to ensure a robust sky subtraction. Data were dark-subtracted, flat-fielded, and sky subtracted. The wavelength calibration was done on telluric OH lines straddling the wavelength of the H_2 1−0 S(1) line. Using a 0.4″ wide slit, we reached a spectral resolution of 6 km s^{-1}, a factor ∼20 higher than the effective resolution of our SINFONI data. This allowed us to analyze the line profile of the compact molecular source at a spectral resolution which is comparable to that reached by Wilson et al. (2000) for CO.

We determined the astrometry of the near-IR CFHT images through cross-correlation with the 2MASS K-band image of NGC 4038/39. We give a short description of these data in Sect. 3.1. They have also been used to improve the astrometric accuracy of the SINFONI observations (Sect. 2.4).

2.3. Ancillary data sets

We complement our near-IR spectro-imaging data with CO(1−0) observations obtained with the Caltech Millimeter Array. C. Wilson generously shared her zeroth and first-moment maps of NGC 4038/4039 with us. For a full discussion of these observations, see Wilson et al. (2000, 2003). Our SINFONI pointing in the overlap region coincides with their super-giant molecular cloud 2 (SGMC 2). Within the spatial resolution of the CO data, the peak of SGMC 2 coincides with the warm H_2 peak #5 in Brandl et al. (2009). In our analysis we adopt the mass, size and line width of SGMC 2 listed in Table 1 of Wilson et al. (2000).

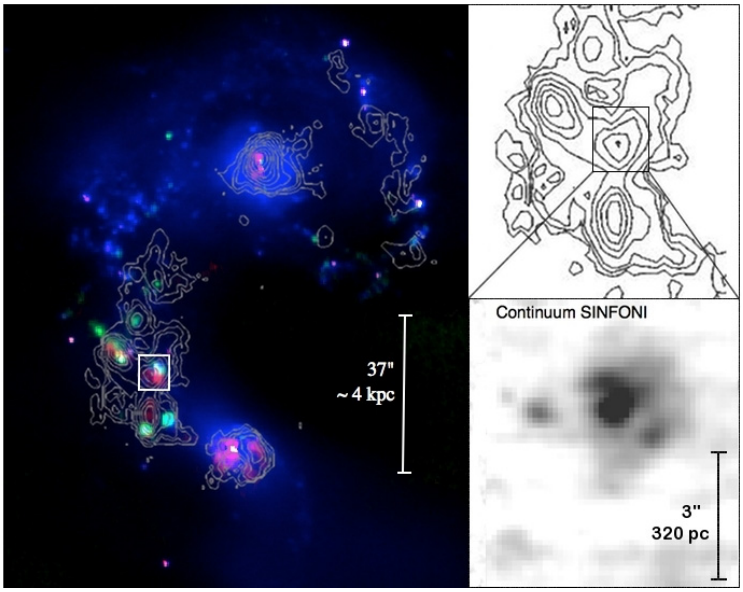

Fig. 1. *Left panel*: central regions of the Antennae galaxy merger including both nuclei. The *K*-band continuum, H_2 1−0 S(1), and Brγ line emission are shown in blue, red, and green, respectively. All data were taken with WIRCAM on the CFHT. Grey contours show the CO(1−0) line emission from Wilson et al. (2000). The white square represents our SINFONI pointing. The H_2 1−0 S(1) emission has the same morphology as the Spitzer IR emission in Brandl et al. (2009, their Fig. 4). The H_2 morphology does not follow the continuum morphology, however, the Brγ does. *Right panel*: zoom onto the CO map of the overlap region (top, the square shows our SINFONI field of view) and the line-free *K*-band continuum morphology seen with SINFONI (bottom). North is up, and east to the left in all panels.

In addition, we use published results from Spitzer/IRS mid-infrared spectroscopy by Brandl et al. (2009). Our pointing corresponds to their Peak #5. In Sect. 4.2 we will use the rotational H_2 line fluxes from their Table 5 to compute the bolometric H_2 luminosity. The integrated S(2) flux measured with the Short-High (SH) module is a factor 1.4 higher than that measured with the Short-Low (SL) module. Brandl et al. (2009) attribute this difference to the different apertures used for the SH and SL flux measurements. Since the aperture of the SH module (4.″4 × 11.″3) is best matched to the SINFONI field of view, we scale the S(3) flux, which was measured only with the SL module, by a factor 1.4.

2.4. Astrometry of the SINFONI images

The SINFONI field-of-view is too small to register these data directly with astrometric catalogues. Therefore, to ensure that the absolute positional accuracy of our data is better than 1″, we collapsed the SINFONI cube over the wavelength range of our CFHT *K*s-band image, which we previously registered relative to the USNO catalog of astrometric standards, and matched the coordinates of both images. This gives a positional accuracy of ∼0.″5 for the SINFONI data. The position of the super-star cluster, the brightest continuum source in the SINFONI field of view, is within 0.″5 of archival HST/NICMOS images (taken through the *F187N* and *F160W* filters). Curiously, we find a 2″ offset relative to the coordinates of the super star cluster given by Whitmore et al. (2010, cluster #28 in their Table 8)

3. Observational results

In Sect. 3.1, we present the morphology and kinematics of the molecular and ionized gas. In the two following sections, we highlight the presence of extended H_2 emission throughout the field (with broad *FWHM* ∼ 150–200 km s^{-1}, Sect. 3.2), and the discovery of a compact molecular source, with bright H_2 line emission, which shows no Brγ, nor continuum emission in the *K*-band (Sect. 3.3).

3.1. Identification of individual components

The left panel of Fig. 1 shows the overall morphology of the continuum-subtracted H_2 1−0 S(1) and Brγ line emission in the Antennae. H_2 emission is found in the two nuclei and in the overlap region. Brγ is found in the overlap region with a different morphology than the molecular gas. Our SINFONI observations targeted the brightest peak in pure-rotational molecular line emission by Brandl et al. (2009). The field-of-view of our observations is marked by the white box. The right panel of Fig. 1 shows two zooms into this region.

In the SINFONI data cube we identify several emission lines from molecular (H_2 1−0 S(0)→S(3), H_2 2−1 S(1)), and ionized (Brγ, He) gas. Figure 2 shows the maps of emission-line surface brightnesses, velocities, and *FWHM*s for H_2 1−0 S(1) and Brγ. A position-velocity diagram is shown in Fig. 3. Mean velocity and line widths were measured with Gaussian fits, carefully masking bad pixels. We also constructed a line-free continuum map (lower right panel of Fig. 1) by averaging the flux across the full band in each spatial pixel after masking emission lines, bad pixels, and wavelengths affected by strong night-sky lines.

We identify 4 components in these maps: a compact continuum source (hereafter the super star cluster, SSC), two compact emission line sources (hereafter the molecular, and the ionized compact source, respectively) and diffuse extended emission. The three compact sources are labelled in Fig. 4. The SSC has previously been identified with HST and Keck. The main parameters of the cluster are listed in Table 1. We estimated the stellar mass to 6 × 10^6 $M_\odot$ from the *K*-band and Brγ fluxes corrected for extinction (see Sect. 4.2.1), using Starburst99 (Leitherer et al. 1999), assuming solar metallicity, an instantaneous burst of age 4.5 Myr, and a Salpeter initial mass function with lower and upper mass cutoffs of 1 and 100 $M_\odot$, respectively. Our upper age limit of 6 Myr is based on the absence of CO band-heads in the

A&A 534, A138 (2011)

Table 1. Parameters of the super star cluster in our field.

Obs	Size $''$	Age Myr	A_K mag	Mass $\times 10^6\ M_\odot$	$N_{\rm ion}$ $\times 10^{52}$ s^{-1}	K mag	Reference
HST	–	4.8[a]	0.8[a,b]	1.2[a]	–	–	#28 from Table 8 in [1]
Keck + VLT	0.″46[c]	5.7[d]	–	4.1[e]	1.3[e]	15.2[f]	SSC-C in [2]
VLT/SINFONI	0.″6[g]	<6 4.5	0.4	6.0	4.4[e,h] 6.6[i]	15.0[f]	Our work [3]

Notes. [(a)] From the comparison of integrated photometry UBVIHα with population synthesis models, [(b)] estimated from measured $E(B-V) = 2.20$ and assuming $R_V = 3.1$ extinction curve (Weingartner & Draine 2001), [(c)] deconvolved *FWHM* from Lorentzian fit, [(d)] based on the Brγ equivalent width as an age indicator comparing it with Starburst99 (Leitherer et al. 2010) models, [(e)] not corrected for extinction, [(f)] K-band apparent magnitude for an aperture of 2″, [(g)] it is unresolved. The angular size (*FWHM*) measured from a Gaussian fit corresponds to the size of the seeing disk, [(h)] from observed Brγ luminosity, [(i)] from the fluxes of the [Ne] and [Ne] lines at 12.81 and 15.56 μm.

References. [1] Whitmore et al. (2010) based on ACS and NICMOS observations, [2] Gilbert & Graham (2007) based on Keck/NIRSPEC-SCAM and VLT/ISAAC observations, [3] for details see Sect. 3.1.

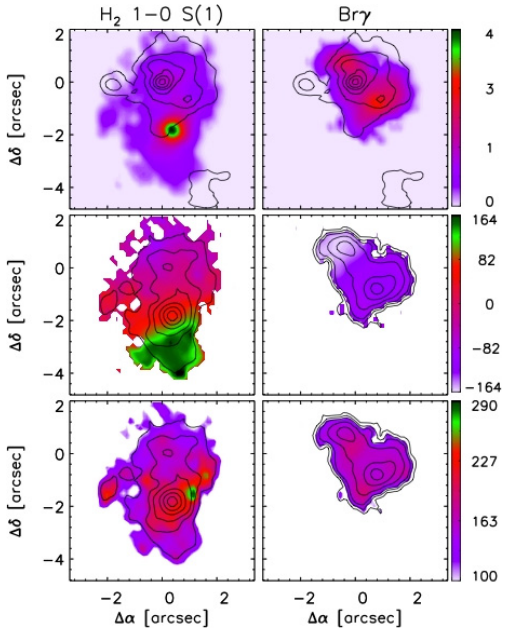

Fig. 2. H_2 1−0 S(1) and Brγ morphologies and kinematics. North is up, and East to the right in all panels. *Top*: line surface brightnesses in units of $\times 10^{-17}$ erg s^{-1} cm^{-2}. The contours show the K-band continuum in steps of 15%, starting at 10% of the peak intensity, 45 $\times$ 10^{-20} erg s^{-1} cm^{-2} Å^{-1}. *Center*: velocities in km s^{-1} relative to the mean recession velocity in our field-of-view of 1556 km s^{-1}. *Bottom*: measured *FWHM*s in km s^{-1}. All maps are spatially smoothed by averaging the original data over 3 pixels × 3 pixels (0.″4 × 0.″4 pix^{-1}). The contours in the mid and lower images show the line surface brightness. Levels are 0.1, 0.2, 0.3, 0.5, 0.7, and 0.9 the peak intensity (3.8×10^{-17} erg s^{-1} cm^{-2} for H_2 and 2.6×10^{-17} erg s^{-1} cm^{-2} for Brγ). Offsets are relative to the peak in the K-band continuum map, α(J2000): 12$^{\rm h}$01$^{\rm m}$54$^{\rm s}$.753, δ(J2000): −18°52′51.″44.

K-band spectrum and is consistent with previous measurements (Table 1). This cluster is one of the most massive clusters in the overlap region, and one of the brightest in the near-IR. The characteristics of the molecular and ionized compact sources are presented in Table 3.

The integrated spectra of each of the four components are presented in Fig. 4. In Table 2, we list line fluxes, mean velocities and line widths for the extended emission, and the molecular and ionized compact sources. To construct the spectrum of the extended emission, we integrated over the full spatial extent where H_2 1−0 S(1) emission is observed, and subtracted the contribution from the compact sources. For the compact sources, we integrated within circular apertures of 0.″6, 0.″8, and 0.″7 (for the stellar cluster, the molecular and ionized sources, respectively) matched to their sizes. For the molecular and ionized sources we subtract the nearby background using an outer annulus. For the SSC, we do not see a distinct emission-line component that could be separated from the surrounding line emission. Therefore, we did not subtract background line emission from the spectrum of the SSC. Had we done so, we would have obtained a pure continuum spectrum with no evidence of emission lines (not shown).

The spectra suggest that the astrophysical nature of these sources must be very different. For the extended line emission, we observe emission lines from both molecular and ionized gas. The molecular source shows only H_2 lines and the ionized source only the Brγ and He emission lines. Figure 5 presents a zoom onto the Brγ and H_2 1−0 S(1) lines for the extended emission-line region and the compact molecular source to illustrate the differences in line intensities and kinematics. For the extended emission, the velocities of the molecular and ionized gas are offset by ∼100 km s^{-1}. Throughout the rest of the paper we focus on the molecular emission, i.e., the H_2 extended emission and the compact H_2 source. The analysis of the ionized gas will be presented in a future publication.

3.2. Extended molecular emission

Figure 2 shows extended H_2 line emission over most of the field-of-view, with a morphology that is very different from that of Brγ which is more concentrated around the SSC. The velocity field shows a systematic gradient of ∼200 km s^{-1} from north-east to south-west over a projected distance of 600 pc, giving an average velocity gradient of 0.35 km s^{-1} pc^{-1}. Figure 3 shows the position-velocity diagram for the H_2 1−0 S(1) line, along the direction of the velocity gradient (PA 15°). The diagram is centered on the compact H_2 source and reveals the velocity gradient and the high turbulence in the field. The H_2 line widths of *FWHM* = 150–200 km s^{-1} are comparable to the total gradient over the SINFONI field-of-view. The H_2 line width is larger than those measured in Brγ for the ionized gas (Fig. 5).

Table 2. Emission-line characteristics.

Line	Rest Wavelength	Extended emission			Molecular compact source			Ionized compact source		
		V_{LSR}	Flux $\times 10^{15}$	*FWHM*[a]	V_{LSR}	Flux $\times 10^{16}$	*FWHM*	V_{LSR}	Flux $\times 10^{17}$	*FWHM*
H_2 1−0 S(3)	1.95756	1490 ± 17	6.1 ± 0.4	225 ± 14	1515 ± 16	6.5 ± 0.2	167 ± 7			
H_2 1−0 S(2)	2.03376	1461 ± 18	3.3 ± 0.3	234 ± 18	1538 ± 17	2.3 ± 0.1	140 ± 11			
H_2 1−0 S(1)	2.12183	1493 ± 17	6.9 ± 0.3	215 ± 9	1547 ± 16	7.6 ± 0.1	146 ± 2	1481 ± 18	3.1 ± 0.6	<136
H_2 1−0 S(0)	2.22329	1465 ± 18	2.8 ± 0.2	188 ± 16	1554 ± 18	1.6 ± 0.2	140 ± 22			
H_2 2−1 S(1)	2.24772	1450 ± 18	1.7 ± 0.2	146 ± 20	1530 ± 26	0.9 ± 0.2	243 ± 44		<0.36	
Brγ	2.16612	1408 ± 16	9.5 ± 0.2	133 ± 4	1443	<0.06		1404 ± 16	25.8 ± 1.1	20 ± 29
He I	2.05869	1410 ± 16	5.2 ± 0.2	131 ± 7				1400 ± 16	16.3 ± 1.0	35 ± 27
Continuum[b]			0.06						0.1	

Notes. Wavelengths are given in μm, fluxes in erg s^{-1} cm^{-2}, and velocities and *FWHM* in km s^{-1}. Error bars include the uncertainties in the wavelength calibration. [(a)] Intrinsic *FWHM* after deconvolution with the instrumental resolution of ~136 km s^{-1}, [(b)] line-free *K*-band continuum flux in units of erg s^{-1} cm^{-2} Å^{-1}.

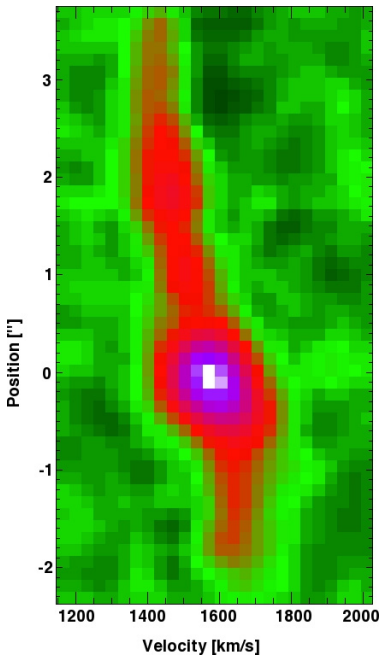

Fig. 3. H_2 1−0 S(1) position-velocity diagram from north to south, at the position of the compact H_2 source. The peak corresponds to the compact H_2 source (Sect. 3.3). Positions are relative to this source.

The H_2 rotational lines observed with Spitzer (Brandl et al. 2009) are not spectrally resolved, the highest spectral resolving power of these data is $R = 600$, corresponding to *FWHM* = 500 km s^{-1}. The CO(1−0) velocity (V_{LSR} = 1470 km s^{-1}) agrees with the mean, luminosity weighted, velocity of the H_2 extended emission (Table 2). CO shows a velocity gradient as large as that of H_2 but over larger distances. CO observations with a higher angular resolution are needed to resolve this gradient at the same scale as H_2. The warm H_2 gas traced by the near-IR emission lines has line widths more than twice as large as those measured in CO at the same position (73 km s^{-1} in Wilson et al. 2000).

3.3. Compact molecular source

The H_2 flux map in Fig. 2 reveals a compact source without a counterpart in the ionized gas and continuum emission. The spectrum of this source in Figs. 4 and 5 is unlike that of the other emission components. To our knowledge, this is the first time that an extragalactic source with a *K*-band spectrum showing only H_2 lines is discovered. Similar spectra are seen in the Milky Way towards low-mass stars embedded in molecular clouds, which do not produce enough ionizing photons to power bright Hydrogen recombination lines (Giannini et al. 2006). In these sources the H_2 emission traces shock heating of H_2 associated with the interaction of the stellar jet with the molecular cloud.

Table 2 gives the H_2 line fluxes and an upper limit on the Brγ flux. The H_2 1−0 S(1) flux of the molecular compact source accounts for 10% of the total emission from SGMC 2 in this line. To estimate the size of this source, we fit the azimuthally-averaged emission-line surface brightness profile along right ascension and declination with Gaussian curves. The *FWHM* size, geometrically averaged over the two axes, is 0.″8. Correcting for the seeing we obtain an intrinsic source size of 0.″5 corresponding to 50 pc.

We obtained high spectral resolution measurements of the line profile of the compact source with CRIRES (Fig. 6). Fitting this profile requires two Gaussian components with different line widths at a common velocity, with *FWHM* = 50 km s^{-1} and *FWHM* = 160 km s^{-1}, respectively. We illustrate this by showing fits with one and two Gaussians in Fig. 6. In the two-Gaussian fit, the narrow component contributes 25% to the total H_2 line flux. We verified that we recover the line profile measured with SINFONI after convolution with the line spread function of SINFONI.

The compactness of the H_2 source suggests that it is gravitationally bound, and that we can estimate the gas mass using the virial theorem. For a homogeneous spherical cloud the balance between gravitational and kinetic energy gives the virial mass as $M_{vir} = 5\ R\ \sigma^2/G$, where R is the radius, σ the velocity dispersion of the gas, and G the gravitational constant. In this formula, we estimate the diameter using the *FWHM* size of the near-IR H_2 emission. We obtain a virial mass of $1.3 \times 10^7 \times (\sigma/21\ \mathrm{km\ s^{-1}})^2\ M_\odot$ using the line width of the narrow component detected with CRIRES for σ. The CO data do not have the required angular resolution to separate the compact source from the extended emission. High angular resolution observations with ALMA are required to estimate the virial mass from CO. The mass of the compact H_2 source is a factor

A&A 534, A138 (2011)

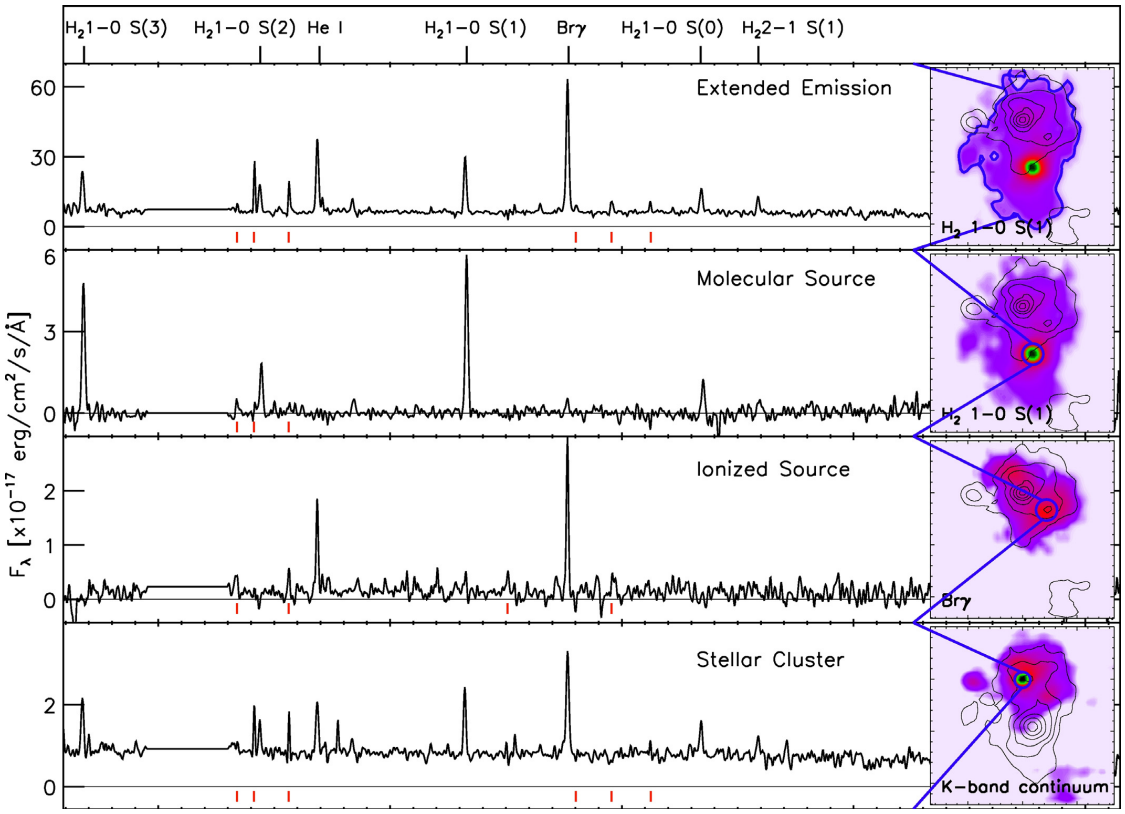

Fig. 4. Integrated SINFONI spectra for the four different components in our pointing of the overlap region of the Antennae. All spectra are smoothed by 3 bins in wavelength. Around 2.0 μm the atmospheric transmission is very low so we did not plot this part of the spectra. We mark in red the wavelengths of the strong night sky lines seen in the spectra (OH lines). In the right panel, blue contours mark the aperture from which each spectrum was extracted.

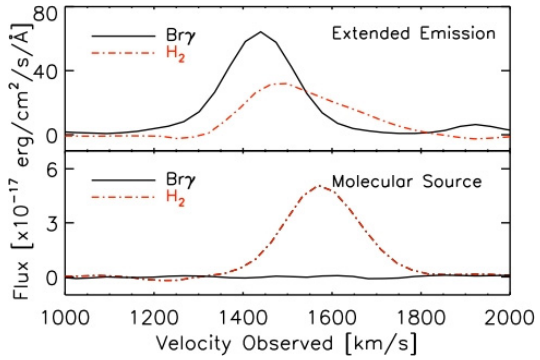

Fig. 5. Emission line profiles of molecular and ionized gas. Solid lines correspond to Brγ and dot-dashed lines to H_2 1−0 S(1). The kinematics of the extended molecular and ionized gas are different with an offset of ~100 km s^{-1}. The molecular source shows broad H_2 line emission and no Brγ emission.

~30 smaller than the mass derived from CO observations for the SGMC 2 molecular complex (Wilson et al. 2000). From the virial mass and size, we derive the column density of the molecular source and we obtain $N_H = 6 \times 10^{23}$ H cm^{-2}. This corresponds to a mean density of 6000 H cm^{-3}.

Radio continuum maps at 6 cm show a slight excess (50 μJy) at the position of our molecular source (see Figs. 5 and 9 in Neff & Ulvestad 2000). Assuming that this radio flux is entirely thermal emission from ionized gas, it corresponds to a Brγ flux of ~5×10^{-16} erg s^{-1} cm^{-2}. This value is a factor 5 larger than the upper limit on the observed Brγ flux in Table 2 after scaling by our estimate of the extinction correction (a factor 20, see Table 3 and Sect. 4.2.1). This slight discrepancy could indicate that the newly formed stars are concentrated at the center of the cloud. In this case their emission could be more attenuated than the H_2 emission. From the radio flux, we compute an ionizing photon rate of 2×10^{51} s^{-1}, which, for a young (1–2 Myr) burst corresponds to a stellar mass of ~4×10^4 $M_\odot$ based on Starburst99 models. This stellar mass is 0.3% of the virial mass of the compact H_2 source.

4. The nature of the compact and diffuse H_2 emission

In this section we argue that, for both the extended emission and the compact molecular source, the H_2 line emission is shock

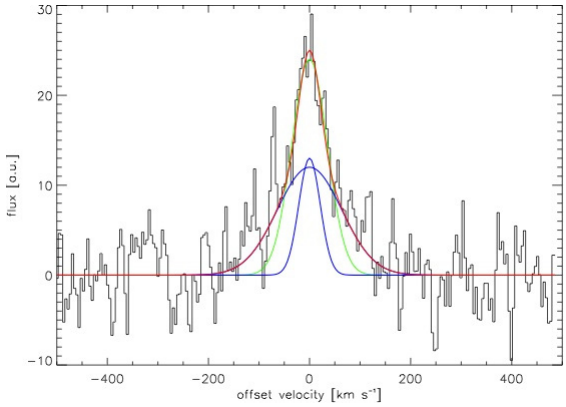

Fig. 6. Integrated spectra of the compact H_2 source observed with CRIRES. Fitting the data with a single Gaussian (green line) shows significant residuals. An adequate fit (red line) requires 2 Gaussian curves (blue lines), corresponding to a narrow and a broad component, respectively.

Table 3. Observed characteristics of the compact sources.

Parameters	H_2 source	H source
Size	0.″5	0.″4
e_c	~20	–
n_e [cm^{-3}]	–	58[a]
Mass [$M_\odot$]	1.3×10^{7}[b]	4.8×10^{4}[c]
N_{ion} [phot. s^{-1}]	$<2.6\times10^{49}$[d]	8.5×10^{50}[e]
L_{bol} [$L_\odot$]	2.6×10^{6}[f]	5×10^{7}[g]

Notes. [(a)] Assuming ionization balance, and not correcting for extinction, scales as $e_c^{0.5}$; [(b)] virial mass estimated from the intrinsic S(1) size and the CO line width; [(c)] mass of the H gas uncorrected for extinction, scales as $e_c^{0.5}$; [(d)] from the upper limit of the Brγ emission, uncorrected for extinction; [(e)] derived from the Brγ luminosity, scales as e_c; [(f)] H_2 bolometric luminosity corrected for extinction (Sect. 3.3); [(g)] from the age and N_{ion}. Uncorrected for extinction, scales as e_c.

powered. We also estimate the bolometric H_2 luminosity for both emission components.

4.1. Spectral diagnostics: PDR or shocked gas?

In this section, we discuss the excitation of the H_2 gas and the nature of the H_2 emission for the extended emission and the compact source. We focus on the near-IR lines within the K-band using spectral diagnostics that do not depend on extinction.

The H_2 excitation diagrams for the extended emission and the compact H_2 source are presented in Fig. 8. We obtain two estimates of the gas temperature, the first by fitting the H_2 population in the rotational states of the $v = 1$ vibrational state, and the second from the ratio between the $J = 1$ level of the $v = 1$ and $v = 2$ states. For the compact H_2 source we find 1700 K and 2300 K, respectively, and for the extended emission 900 K and 2700 K. The molecular gas has a range of temperatures. Most of the molecular gas is too cold to emit in the near-IR. The mass of warm gas seen in the near-IR is several orders of magnitude smaller than that observed in the mid-IR rotational lines by Brandl et al. (2009), and also much smaller than the virial mass given in Sect. 3.3. However, even though the mass is small, the energies are very large as we will see in Sect. 4.2.

Table 4. H_2 line emission: spectral diagnostics.

Component	H_2 2−1/1−0 S(1)	H_2 1−0 S(1)/Brγ
Extended emission		
Full area	0.2	0.72
Southern part		3
H_2 compact source	0.1	>100

The ratio $R_{2-1/1-0} \equiv H_2$ 2−1 S(1)/H_2 1−0 S(1) is often used to discriminate between UV heating of H_2 in photodissociation regions (PDRs) and shock heating. The observed values of the extended emission and compact molecular source are 0.2 and 0.1, respectively. We compare these values with the Meudon PDR code described in Le Petit et al. (2006). Their Fig. 27 shows that PDRs typically have $R_{2-1/1-0} = 0.5$–0.6. Values of $R_{2-1/1-0}$ in the range 0.1 to 0.2 are only reached for very high densities and strong radiation fields ($n \gtrsim 10^5$ cm^{-3}, $\chi \gtrsim 10^5$). Such conditions do exist in massive star-forming regions, but only close to massive stars. This solution does not apply here because the compact H_2 source is far away from the SSC, and has no strong ionized line emission indicating the absence of massive young stars. For the compact source PDR emission is also ruled out by the ratio H_2 1−0 S(0)/H_2 1−0 S(1) (see Fig. 28 of Le Petit et al. 2006). The extended H_2 emission-line region extends over the whole field-of-view and does not peak at the position of the SSC. We therefore discard UV heating and favor shocks as main heating mechanism for the extended emission as well. Using the models of Kristensen (2007), we find that J- and C-shocks match the observed values over a wide range of densities (10^4–10^6 cm^{-3}) and shock velocities (15–50 km s^{-1}).

The ratio $R_{S(1)/Br\gamma} \equiv H_2$ 1−0 S(1)/Brγ is an additional, more empirical diagnostics to identify the origin of the H_2 excitation. These diagnostics provide additional evidence of shock excitation of H_2 in our data. We compare our results for the Antennae overlap region with data presented by Puxley et al. (1990). Their data include 44 star-forming regions in 30 galaxies, where, typically, the H_2 1−0 S(1) line is weaker than the Brγ line (only 4 regions have a ratio higher than 1). Their flux ratios range between 0.1 and 1.5 with a mean of 0.5 and a dispersion of 0.3. A few sources such as the merger NGC 6240 show a much higher $R_{S(1)/Br\gamma}$ value. Puxley et al. (1990) present models for a number of different scenarios and conclude that the line emission is most likely from H /PDR gas in massive star forming regions, for most of their sources. With our data, we obtain $R_{S(1)/Br\gamma} = 0.72$ and >100 for the extended emission and the compact source, respectively. The compact source shows a very high ratio, which is far from the typical range in star-forming galaxies. The ratio of the extended emission is within the range of observed and modeled values by Puxley et al. (1990). However, this is not true for all of the extended gas. In the region South of the bright Brγ line emission (Fig. 7), we measure a ratio of 3. This value suggests that at least parts of the extended H_2 emission is excited by shocks.

4.2. H_2 bolometric luminosity

Before discussing the H_2 emission as a coolant of the molecular gas in Sect. 5, we need to estimate the H_2 bolometric luminosity of the extended emission and the compact source. This will be used in Sects. 5.2 and 5.3 to discuss what may power the H_2 emission. To achieve this we combine the Spitzer and SINFONI H_2 line measurements. This is not straightforward to

A&A 534, A138 (2011)

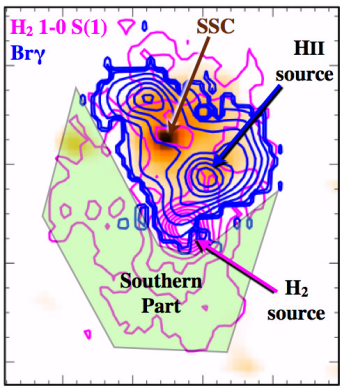

Fig. 7. The color image shows the K-band continuum, which peaks at the SSC. Pink and blue contours show the H_2 1−0 S(1) and Brγ emission, respectively. We also mark the compact ionized and molecular source (H source and H_2 source, respectively). The green area corresponds to the gas which is likely not influenced by the SSC, we call it "Southern part".

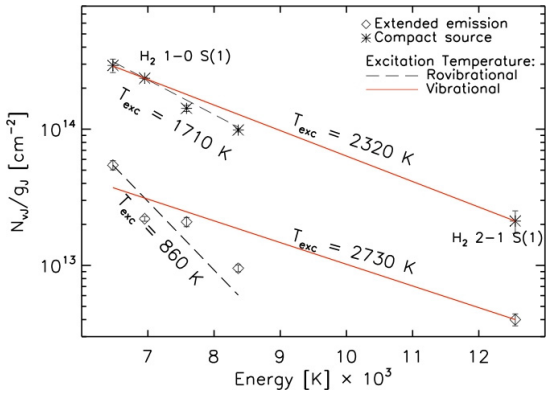

Fig. 8. H_2 excitation diagram of the extended emission-line region and the compact source (Sect. 3.1). The dashed and solid red lines show the gas excitation temperature derived from fitting the H_2 population in the rotational states of the $v = 1$ vibrational state, and from the ratio between the $J = 1$ level of the $v = 1$ and $v = 2$ states, respectively.

do because the near-IR H_2 is attenuated by dust extinction and the Spitzer angular resolution is too low to separate the contributions of the extended and compact source to the mid-IR rotational line emission. First, we estimate the near-IR extinction for both emission components (Sect. 4.2.1). Second, we estimate the bolometric H_2 luminosities, under the assumption that the fraction of the H_2 luminosity in the H_2 1−0 S(1) line is the same for the extended emission and the compact source (Sect. 4.2.2).

4.2.1. Extinction correction

To quantify the extinction in the extended gas, we compare the number of ionizing photons $N_{\rm ion}$ obtained from the observed Brγ emission line with that computed from the fluxes in the mid-IR [Ne]λ12.8 μm and [Ne]λ15.6 μm fluxes (Brandl et al. 2009). The extinction corresponds to the ratio between the two estimated values of $N_{\rm ion}$. This ratio provides the effective extinction factor averaged over the entire field-of-view at the wavelength of Brγ because the dust extinction of the mid-IR neon lines is much smaller than in the near-IR. The observed $N_{\rm ion}$ in the field-of-view was measured by integrating the Brγ flux over the entire SINFONI cube. Assuming case B recombination, an electron density $n_{\rm e} = 10^2$ cm^{-3} and an electron temperature of $T_{\rm e} = 10^4$ K (see Table 8 of Hummer & Storey 1987), $N_{\rm ion} = 4.4 \times 10^{52}$ phot. s^{-1}. To compute the $N_{\rm ion}$ from the Ne fluxes, we use the equations in Ho & Keto (2007) and the [Ne]λ12.8 μm and [Ne]λ15.6 μm fluxes. We further assume that $n_{\rm e}$ is smaller than the critical density, $\sim 10^5$ cm^{-3}, and adopt the galactic Neon abundance. We obtain $N_{\rm ion} = 6.6 \times 10^{52}$ phot. s^{-1}. Comparing with the result for Brγ this suggests an extinction factor of 1.5.

The compact source has a very high column density, $N_{\rm H} = 6 \times 10^{23}$ H cm^{-2} (Sect. 3.3), and therefore, the extinction must be much higher. Using the Milky Way extinction curve for $R_V = 3.1$ in Weingartner & Draine (2001) this column density corresponds to $\tau_{\rm ext} = 30$ in the K-band. We roughly estimate the extinction correction from $\tau_{\rm ext}(K)$ with a simple toy model. We compute the attenuation due to the dust absorption for every point of a spherical and homogeneous cloud of constant density and line emission per unit volume. The flux that reaches the surface of the cloud depends on the path length l, and is attenuated by a factor $e^{-\tau_\lambda(l)}$. The optical depth $\tau_\lambda(l) = \kappa_\lambda \rho \times l$ depends on the absorption coefficient at a given wavelength κ_λ and the mass density ρ. The κ_λ value is taken from the $R_V = 3.1$ curve in Weingartner & Draine (2001). We sum the attenuated emission over the cloud and compare the result with the total emission for zero opacity. We find a correction factor $e_{\rm c} = 0.7 \times \tau_{\rm ext}$. We also run the model with a density and emission profile $\rho \propto r^{-2}$ for which we find $e_{\rm c} = 0.6 \times \tau_{\rm ext}$. In the following we only apply this extinction correction ($e_{\rm c} = 20$) to the narrow component of the H_2 line emission. In our interpretation of the data, the broad component is likely to come from the surface of the cloud, for which the extinction correction should be about a factor of 2, because we do not see the emission behind the cloud.

4.2.2. Bolometric correction

The angular resolution of Spitzer/IRS is only 5″, too low to measure the total H_2 luminosity, $H_2^{\rm bol}$, including the pure-rotational mid-IR lines, of the compact source directly. To circumvent this difficulty, we need to make an assumption. We assume that the $H_2^{\rm bol}$ /H_2 1−0 S(1) ratio, after extinction correction, is the same for the compact source and for the extended emission. The detailed shock modelling which would be needed to support or refine this assumption is beyond the scope of this observational paper. The total H_2 luminosity (extended and compact source) is taken from the observations by Brandl et al. (2009), assuming that most of the H_2 emission is from the first four rotational lines. Within these simplifying assumptions, we find bolometric H_2 luminosities of $L_{H_2} = 5.4 \times 10^6$ and 2.6×10^6 $L_\odot$ for the extended and compact emission, respectively.

The extinction correction introduces significant uncertainties to these luminosities, in particular for the compact source. The total H_2 luminosity (extended emission + compact source) does not depend on extinction because most of the H_2 emission is from the mid-IR $v = 0$ rotational lines measured by Spitzer for which extinction is negligible. It is the ratio between both luminosities which depends on the extinction correction. We set a lower limit of 8×10^5 $L_\odot$ on the luminosity of the compact source by assuming that the extinction is the same for both components. The H_2 1−0 S(1) emission represents 3% of the bolometric H_2 emission.

5. From large scale gas compression to star formation

The results presented in the previous sections raise three questions. How were the extended molecular gas component and the compact H_2 source formed? Why is this gas so H_2 luminous? What is the nature of the compact H_2 source? In this section, we argue that the extended emission traces highly turbulent molecular gas formed where the galaxy interaction is driving a large scale convergent flow. We relate the H_2 emission to the dissipation of the gas turbulent kinetic energy and the formation of the SGMC 2 complex and the compact H_2 source by gas accretion (Sect. 5.2). In Sect. 5.3 we argue that the compact H_2 source is a massive core on its way to forming a super star cluster.

5.1. Gas compression and gravitational fragmentation

The Antennae merger is close to pericenter passage when tidal forces are compressive (Renaud et al. 2008, 2009). Thus, we consider that the velocity gradient observed with the H_2 line emission across the SINFONI field is tracing a convergent flow driven by the galaxy interaction. The associated gas compression has created the conditions for the gas to cool and to become molecular, like in numerical simulations of convergent flows (Hennebelle et al. 2008). As observed in the galaxy collision in Stefan's Quintet, the mechanical energy of the interaction is not fully thermalized in large scale shocks (Guillard et al. 2009). Due to the inhomogeneous, multi-phase, nature of the interstellar medium much of the gas kinetic energy decays from large to small scales before it is dissipated. Thus, we consider that it is the galaxy interaction that drives the molecular gas turbulence. This interpretation is supported by the fact that the large velocity gradient has the same magnitude as the turbulent line width, and by numerical simulations, which illustrate how dynamical and thermal instabilities lead to the formation of highly structured and turbulent molecular clouds where gas flows collide (Heitsch et al. 2005; Vázquez-Semadeni et al. 2007; Hennebelle et al. 2008).

The gas surface density is high enough for the turbulent gas to gravitationally contract and fragment within the time scale over which the tidal forces are compressive (~10 Myr, Renaud et al. 2008). We compute the Jeans length ($R_{\rm Jeans} = 5\sigma^2/(2\pi G\Sigma)$) and mass ($M_{\rm Jeans} = \pi R^2_{\rm Jeans}\Sigma$) using the CO(1−0) observations of Wilson et al. (2000) to estimate the gas velocity dispersion (σ) and surface density (Σ). The value of σ is 30 km s^{-1}. The surface density Σ is obtained taking the ratio between the total virial mass and the total area of the overlap region $\Sigma \sim 500\ M_\odot\ {\rm pc}^{-2}$. We find $R_{\rm Jeans} \simeq 350$ pc and $M_{\rm Jeans} = 2 \times 10^8\ M_\odot$. To compute the free-fall time scale $\tau_{\rm ff} = \sqrt{3\pi/(32\rho G)}$ we determine the mean density ρ from $R_{\rm Jeans}$ and $M_{\rm Jeans}$. We find $\tau_{\rm ff} = 8$ Myr.

The Jeans length and mass are comparable to the size of the super giant molecular complex SGMC 2. It is thus likely that the complex has formed by gravitational contraction out of the gas compressed by the galaxy interaction. The gravitational contraction could contribute to the H_2 velocity gradient. An estimate of the motions driven by the self gravity of the complex is obtained taking the ratio between the free-fall velocity $v_{\rm ff} = 2\ R_{\rm Jeans}/\tau_{\rm ff} \simeq 90$ km s^{-1} and the Jeans radius. We find a value comparable to the velocity gradient measured with the H_2 line emission (200 km s^{-1} over 600 pc). This calculation provides an upper limit to the velocity gradient from the cloud contraction since it is unlikely that the complex is free-falling. The cloud contraction must occur at a slower rate than free-fall because it takes time to dissipate turbulent energy (Elmegreen 2007; Huff & Stahler 2007).

Thus, we propose that the SGMC 2 complex is formed by convergent gas flows driven by the galaxy interaction and the gas self-gravity. Wilson et al. (2000) find that the gas mass inferred from the CO line luminosity matches the virial mass estimated from the the CO line width and conclude that the SGMC 2 complex is gravitationally bound. In the remainder of this paper we use "CO complex" to refer to gravitationally bound gas in the SGMC 2 complex. The velocity gradient and line width of the H_2 emission are both larger than the CO line width, suggesting that not all gas in the SGMC 2 complex is gravitationally bound. Most of the H_2 emission arises from gas that is unbound.

In the next two sub-sections we will interpret our H_2 data within this scenario. We associate the H_2 emission with the formation of the CO complex through gas accretion. We argue that the H_2 emission traces the dissipation of kinetic energy, which is required for gas that is driven by the galaxy interaction to become gravitationally bound.

5.2. The energetics and formation of the SGMC 2 complex

From observations of the Milky Way (Falgarone et al. 2005), and, more recently, of extragalactic sources (Guillard et al. 2009; Nesvadba et al. 2010; Ogle et al. 2010), we know that H_2 line emission is a major coolant of the ISM associated with the dissipation of interstellar turbulence. The H_2 line emission may arise from shocks, as quantified by models such as Flower & Pineau Des Forêts (2010), and from friction betweens ions and neutral species in vortices (Godard et al. 2010). Models show that other emission lines contribute to the gas cooling but that they do not change the order of magnitude of the cooling rate (Flower & Pineau Des Forêts 2010; Godard et al. 2010). Based on this earlier work, we consider the extended H_2 emission from SGMC 2 as a quantitative tracer of the dissipation rate of the kinetic energy of the gas.

Since the H_2 line widths and the velocity gradient across SGMC 2 is twice the CO line width, the H_2 emission does not come solely from the dissipation of the turbulent kinetic energy of the CO complex. A significant fraction of the emission must come from the dissipation of bulk and turbulent kinetic energy of gas driven by the galaxy interaction. Such a loss of kinetic energy is a required step for this gas to become gravitationally bound.

In the following, we quantify this interpretation which connects the energetics of the H_2 gas to the formation of the CO complex by gas accretion. We consider that the CO complex evolves in a quasi-static way assuming that virial equilibrium applies at all times. The virial equation relates the gravitational and turbulent kinetic energy, $E_{\rm grav}$ and $E_{\rm turb}$, and includes the external pressure $P_{\rm ext}$:

$$E_{\rm grav} + 2\,E_{\rm turb} = 3\,P_{\rm ext}\,V \qquad (1)$$

where V is the volume. The turbulent energy is $E_{\rm turb} = 3/2\,M_{\rm CO}\,\sigma^2_{\rm CO}$, where $M_{\rm CO}$ is the mass of the CO complex and $\sigma_{\rm CO}$ is the velocity dispersion along the line of sight derived from the integrated CO spectrum of SGMC 2. For a fixed $P_{\rm ext}$, the exchange of energy associated with gas accretion and radiation is associated with the derivative of the enthalpy H of the complex (Huff & Stahler 2007):

$$\dot{H} = \dot{E}_{\rm grav} + \dot{E}_{\rm turb} + P_{\rm ext}\,\dot{V} = -\dot{E}_{\rm turb} + 4\,P_{\rm ext}\,\dot{V} = \dot{E}_{\rm in} - L_{\rm H_2}/f_{\rm H_2} \qquad (2)$$

A&A 534, A138 (2011)

where $\dot{E}_{\rm in}$ is the energy input from gas accretion, $L_{\rm H_2}$ the H_2 luminosity, and $f_{\rm H_2}$ the fraction of the gas bolometric luminosity that is radiated in the H_2 lines used to compute $L_{\rm H_2}$. This fraction is smaller than 1 because some cooling occurs in lines which have not been measured. Combining H_2 and far-IR observations, Maret et al. (2009) find that $f_{\rm H_2}$ is in the range ~0.25–0.5 for shocks associated with gas outflow from low mass stars. We assume that the kinetic energy of the accreted gas is the main source of energy that balances radiative losses (Klessen & Hennebelle 2010). In doing this we neglect the energy that comes from stellar feedback. The fact that the H_2 emission shows no enhancement around the SSC is an indication that stellar feedback does not have a significant contribution to the H_2 emission (Sect. 6.4).

We follow Klessen & Hennebelle (2010) in introducing the efficiency factor ϵ which represents the fraction of the accretion energy that drives turbulence. The turbulent energy dissipates over a time scale $t_{\rm dis}({\rm CO}) \simeq R/\sigma_{\rm CO}$ where $R \simeq 300$ pc is the radius of the SGMC 2 complex (McKee & Ostriker 2007). The balance equation between energy input and dissipation is:

$$\epsilon \times \dot{E}_{\rm in} = 3/2\, M_{\rm CO} \times \sigma^3_{\rm CO}/R. \quad (3)$$

We compute the mass accretion rate necessary to drive the gas turbulence by equating the energy input and the radiative losses. This corresponds to a solution of Eq. (2) where the derivative of the gas kinetic energy $\dot{E}_{\rm turb}$ and the term associated with $\dot{V}$ are both small with respect to the right-hand terms. Thus, we write:

$$\dot{E}_{\rm in} = 3/2\, \dot{M}_{\rm acc}\, \sigma^2_{\rm H_2} \simeq L_{\rm H_2}/f_{\rm H_2} \quad (4)$$

where $\sigma_{\rm H_2}$ is the velocity dispersion along the line of sight derived from the H_2 data. To quantify $\dot{M}_{\rm acc}$ and ϵ, we consider only the turbulent component of the velocity field ($FWHM_{\rm H_2} \sim 150\,{\rm km\,s^{-1}}$), assuming that accretion occurs from turbulent gas with a mean velocity equal to that of the CO complex. For $\sigma_{\rm H_2} = 65\,{\rm km\,s^{-1}}$ and $\sigma_{\rm CO} = 30\,{\rm km\,s^{-1}}$, we find $\dot{M}_{\rm acc} = 5.3/f_{\rm H_2}\, M_\odot\,{\rm yr^{-1}}$ and $\epsilon = 1.8 \times f_{\rm H_2}$. For our interpretation to hold we must have $\epsilon < 1$, and thus $f_{\rm H_2} < 0.5$. The fact that the H_2 line width is larger than that of CO shows that this holds. In the following, for numerical calculations, we consider that $f_{\rm H_2} \sim 0.25$.

We scale $\dot{M}_{\rm acc}$ by the turbulence dissipation time scale to estimate the mass of gas from which accretion is occurring: $M_{\rm acc} = \dot{M}_{\rm acc} \times t_{\rm dis}({\rm H_2})$, where $t_{\rm dis}({\rm H_2}) \simeq R/\sigma_{\rm H_2}$ is the turbulent dissipation time scale. The large scale flow can feed this mass reservoir, compensating for what is accreted by the CO complex, because the dissipation time scale is comparable to the dynamical time scale associated with the velocity gradient across SGMC 2 (3×10^6 yr). We find $M_{\rm acc} = 2.4 \times 10^7/f_{\rm H_2}\, M_\odot$. For $f_{\rm H_2} \sim 0.25$, $M_{\rm acc}$ is 25% of $M_{\rm CO}$. Thus, the mean density in the CO complex may only be a few times larger than that of the accreted gas. This agrees with our estimate of the efficiency factor ϵ. Based on their numerical simulations and theoretical arguments, Klessen & Hennebelle (2010) argue that the efficiency factor ϵ is roughly equal to the ratio between the density of the accreting gas to the mean density of the bound system.

Computing the ratio between the CO mass of SGMC 2 and the mass accretion rate, we obtain a time scale $t_{\rm acc} = 7 \times 10^7 \times f_{\rm H_2}$ yr. For $f_{\rm H_2} \sim 0.25$, this is slightly longer than the 10 Myr time scale over which the dynamics of the interaction may have been driving the convergent flow (Renaud et al. 2008). However, within the uncertainties in this rough calculation, we consider that the present accretion rate is close to the mean rate needed to account for the formation of the SGMC 2 complex as a result of gravitational fragmentation and gas accretion driven by the galaxy interaction.

Our interpretation introduces a dynamical view of the present state of the SGMC 2 complex. The virialized CO complex is physically associated with gas which is too turbulent to be bound. This unbound gas is dynamically fed by the convergent flow. It contributes an accretion flow onto the CO complex, which has the necessary magnitude to drive the gas turbulence, i.e. to balance the dissipation of the gas turbulent kinetic energy. Klessen & Hennebelle (2010) have proposed a similar interpretation to account for the formation and subsequent growth of turbulent molecular clouds in the LMC. In Sect. 6.3, we discuss the impact of this interpretation on the star formation efficiency within SGMC 2.

5.3. The nature of the compact H_2 source

In this section we extend our interpretation of the extended H_2 emission to the compact H_2 source. Like for the SGMC 2 complex we propose an interpretation where the H_2 luminosity traces the dissipation of the turbulent energy of the gas and gas accretion.

As a first test whether this is a plausible interpretation, we compare the dissipation rate of the turbulent energy of the gas with the H_2 luminosity of the source. Combining Eqs. (3) and (4), we obtain an equation that we can use to estimate the mass of the compact source, $M_{\rm cloud}$, from the H_2 luminosity.

$$3/2\, M_{\rm cloud} \times \sigma^3_{\rm v}/R = \epsilon \times L_{\rm H_2}/f_{\rm H_2} \quad (5)$$

where $\sigma_{\rm v} = 20\,{\rm km\,s^{-1}}$ based on the width of the narrow component in the CRIRES spectrum ($FWHM = 50\,{\rm km\,s^{-1}}$). We find

$$M_{\rm cloud} = 2.7 \times 10^7 \times \epsilon/f_{\rm H_2} \times (L_{\rm H_2}/2.6 \times 10^6\, L_\odot)\, M_\odot. \quad (6)$$

This mass estimate depends on the ratio $\epsilon/f_{\rm H_2}$. Assuming that this ratio is ~1 as estimated for the CO complex, we find a mass slightly larger than the virial mass $M_{\rm vir} = 1.3 \times 10^7\, M_\odot$ derived for the same velocity dispersion in Sect. 3.3. We conclude from this comparison that the H_2 emission from the compact source may be accounted for by the dissipation of turbulent kinetic energy if the source is a gravitationally bound cloud with a mass in the range 1 to a few $10^7\, M_\odot$. With this interpretation, the compact H_2 source is a gravitationally bound cloud, massive enough to form a super star cluster.

Like what we have done in the previous section for the CO complex, we can use Eq. (4) to estimate the mass accretion rate and thereby the cloud formation time scale. For $\sigma_{\rm H_2}$, we use the width of the broad component ($FWHM = 160\,{\rm km\,s^{-1}}$) in the line profile of the 1–0 H_2 S(1) measured with CRIRES. We find:

$$\dot{M}_{\rm acc} = 9.2 \times \left(\frac{f_{\rm H_2}}{0.25}\right)^{-1} \times \left(\frac{L_{\rm H_2}}{2.6 \times 10^6\, L_\odot}\right) M_\odot\,{\rm yr^{-1}}. \quad (7)$$

The ratio between $M_{\rm cloud}$ and $\dot{M}_{\rm acc}$ yields a cloud formation time scale by accretion of $t_{\rm acc} = 2.9 \times 10^6 \times (\epsilon/0.25)$ yr. This value is about twice the cloud dynamical time $R/\sigma_{\rm v}$. We would thus be observing a pre-cluster cloud early in its evolution. Even at this early stage it is remarkable that the fraction of the cloud mass that has been transformed into stars is very small (~0.3%, Sect. 3.3). We observe that the cloud has formed and become gravitationally bound without having formed massive stars.

If our interpretation is correct, by observing the gas cooling through H_2 lines, we may have discovered a massive cloud on its way to form a SSC within the next few Myr. However, this conclusion is only tentative, and will remain incomplete, until

we obtain the missing information about the mass, the density structure and the kinematics of the bulk of the gas. The H_2 line emission provides this information only for the fraction of warm, shock-heated gas. The missing information can be obtained with ALMA.

6. Discussion

Our observations are related to two main questions in the field of star formation. How do super star clusters form? What are the roles of turbulence and stellar feedback in regulating the star formation efficiency in galaxy mergers? We discuss how our observations and interpretation may be of general relevance for these questions.

6.1. The formation of super-star clusters

Star formation is the result of the hierarchical structure of the molecular interstellar medium established by turbulent compression and gravitational contraction (Mac Low & Klessen 2004). The available gas fragments over a range of masses and time scales. Massive clusters form at different times from the densest and most massive gas concentrations. For SGMC 2, this view is supported by the presence of two massive clusters (the near-IR SSC and the compact ionized source), which have formed before the compact H_2 source. More clusters, too small to be identified individually, are likely to have formed or to be in the process of being formed. Thus, the formation of super star clusters in SGMC 2 can be understood within the same framework as the formation of smaller clusters in disk galaxies like the Milky Way.

Our work highlights three physical parameters which may contribute to account for the formation of exceptionally massive clusters in the overlap region of the Antennae. These may be of general relevance for the formation of super star clusters in other extragalactic objects: other interacting/merging galaxies, and also starbursts and irregular dwarf galaxies (Keto et al. 2005; Weidner et al. 2010). (1) The presence of compressive motion on large scaleswhich collects the gas. The formation of the SGMC 2 complex and that of the compact H_2 source is driven by the galaxy interaction. The large scale dynamics triggers the gas compression necessary for their formation and their subsequent growth by gas accretion. (2) As discussed in earlier studies (Escala & Larson 2008; Weidner et al. 2010), shear is the second key parameter in the formation of massive clusters because it sets the maximum mass that the gas self-gravity can collect. In the Antennae, the present geometry of the interaction, which temporarily makes the tidal forces compressive (Renaud et al. 2008), is favorable to the formation of massive clusters. As discussed by Renaud et al. (2009) such conditions occur repeatedly in galaxy mergers. (3) High turbulence is an additional key parameter. Since the Jeans mass is proportional to σ^4 (see Sect. 5.1), a high value of the velocity dispersion σ scales up the masses of the clouds formed by gravitational fragmentation. To form a super star cluster, it is not sufficient to bind a large mass of gas. It is also necessary that the star formation efficiency becomes high when the gas mass is highly concentrated. It is likely that high turbulence is a key factor which prevents star formation to be efficient before the cloud mass has been concentrated by gravity. This is a prerequisite to form a dense, potentially bound, cluster rather than a loose OB association (Elmegreen 2008).

6.2. The impact of turbulence

The impact of turbulence on the star formation efficiency is a long standing topic of research (Mac Low & Klessen 2004). Krumholz & McKee (2005) and Padoan & Nordlund (2011) used numerical simulations to quantify the dependence of the star-formation rate per free-fall time on the Mach number of turbulence. Both agree that, independent of the mean cloud density, for a cloud near virial equilibrium, the fraction of the gas mass that is unstable to collapse is small. If this is correct, then the formation of dense clusters within a cloud supported by turbulence must occur over several cloud crossing times as argued by Tan et al. (2006) and Krumholz et al. (2006). Elmegreen (2008) expresses a different view point by proposing that star formation becomes efficient within cores with a mean density $>10^4$ H cm^{-3} independent of turbulence.

These ideas are being tested against observations of galactic star forming regions and cores, which are far more detailed than the present information we have on the compact H_2 source. High angular resolution observations of molecular lines at mm wavelengths, which unlike the near-IR H_2 lines will trace the kinematics of the bulk of the gas and the source density structure, would be needed for a detailed study of the formation of super star clusters on the example of this source, and if it is consistent with present ideas based on observations of lower mass and less turbulent cores. Here we only make preliminary remarks that can soon be tested with ALMA. The mean density of the compact H_2 source is $\sim 10^4$ H cm^{-3}. We estimate its formation time scale to at least 10^6 yr, but the star-formation efficiency is still very small (stellar to gas mass ratio $\sim$0.3%). This remarkable result may indicate that the high turbulence (1D velocity dispersion $\sim$20 km s^{-1}) has been very effective at preventing star formation. Star formation may occur rapidly once the rate of mass accretion becomes insufficient to drive the present amplitude of turbulence. The fact that stars may be forming out of gas which has lost the turbulent energy it had during the initial gravitational contraction reduces the requirement on the star formation efficiency to form a bound stellar cluster.

6.3. Star formation efficiency

The star formation rate (SFR) in the Antennae merger has been estimated to 20 $M_\odot$ yr^{-1} for a total molecular gas mass $\sim 10^{10}$ $M_\odot$. Local values measured from CO and Hα images of the Antennae agree with the general correlation between the SFR and molecular gas surface densities, the Schmidt-Kennicutt law (Kennicutt 1998; Zhang et al. 2001). The burst of star formation observed in the overlap region follows mainly from the high surface density of molecular gas with only a small (a factor $\sim$3) enhancement of the star formation efficiency with respect to the Galactic value. This enhancement comes from the non-linear dependence of the SFR on the surface density of gas. The star formation rate per unit gas mass in the SINFONI field of view is similar to the global value. Based on their Spitzer and Herschel data, Brandl et al. (2009) and Klaas et al. (2010) find an SFR of $\sim$0.7 $M_\odot$ yr^{-1} for a molecular mass of 4×10^8 $M_\odot$.

To compute the star formation efficiency, we consider that star formation is triggered by gas compression and occurs over the characteristic time, $\sim$10 Myr, over which the tidal interaction is compressive (Renaud et al. 2008). This is also the crossing time across the SINFONI field of view for the CO line width. Over this time the gas mass converted into stars is 7×10^6 $M_\odot$, which yields a star formation efficiency of 2%. The SSC accounts for a significant fraction of this stellar mass (see estimates of the cluster mass in Table 1). For the SGMC 2 complex, like for the compact H_2 source, the low star-formation efficiency may result from the strong, driven turbulence. For the molecular complex, the star-formation efficiency may remain low until it is

A&A 534, A138 (2011)

disrupted by the tidal interaction. If turbulence continues to be driven by on-going accretion, it is possible that the CO complex will be dispersed without losing its turbulent energy. It will be interesting to extend the present study to other complexes in the overlap region to test this idea.

6.4. Stellar feedback

It is interesting to compare this analysis and interpretation of observational data with numerical simulations. In their Fig. 1, Karl et al. (2011) compare the star-formation rates in recent numerical simulations of the Antennae. All simulations predict a significant enhancement of the star-formation efficiency, relative to its value in the two spirals prior to interaction, after pericenter passage. In the simulations, the enhancement in the star formation efficiency is triggered by the gas compression and subsequent gas cooling. For several runs the enhancement is one order of magnitude or more, i.e. larger than that derived from observations. Karl et al. (2011) present new simulations that quantify the impact of stellar feedback on the star formation efficiency, and argue that it is necessary to invoke stellar feedback to compensate for the gas cooling. They claim that the observations are best reproduced with weak feedback.

In Sect. 5, we argue that the gas turbulence is driven by the galaxy interaction. Stellar feedback is energetically significant but not a key contributor to the turbulent energy of the molecular gas. This holds for the SGMC 2 complex and the compact H_2 source. We start discussing feedback on the scale of the SGMC 2 complex using Starburst99 models. For a Salpeter IMF and continuous star formation over 10 Myr, the mechanical energy associated with stellar winds and supernovae explosions is $L_{\rm Mech}({\rm SF}) \sim 4{\times}10^7{\times}\,({\rm SFR}/0.7\,M_\odot\,{\rm yr}^{-1})\,L_\odot$. Most of this energy is released by the stars in the SSC. The non-thermal component of the radio flux from the SSC (Neff & Ulvestad 2000) indicates that the SSC has evolved to an age where the most massive stars are exploding as supernovae. For a stellar mass of a few $10^6\,M_\odot$, the mechanical power from stellar winds and supernovae is also a few $10^7\,L_\odot$. This value is one order of magnitude larger than the H_2 luminosity of the extended emission, but the lack of enhancement of the H_2 line width towards the SSC is evidence that stellar feedback does not contribute significantly to driving the turbulent kinetic energy of the H_2 gas. The energy from stellar feedback must be mostly transferred to the hot X-ray emitting plasma (Baldi et al. 2006). We plan to test this tentative conclusion with additional SINFONI data towards other super star clusters in the overlap region.

For the compact source, we estimate the star formation rate by dividing the stellar mass of $4 \times 10^4\,M_\odot$ (from Sect. 3.3) by the formation time scale $t_{\rm acc} \sim 3 \times 10^6$ yr (from Sect. 5.3). We find $SFR \sim 10^{-2}\,M_\odot\,{\rm yr}^{-1}$. For this rate, the mechanical energy from stellar winds is two orders of magnitude smaller than the H_2 luminosity of the compact source. Using formula (6) in Matzner (2002) we verified that the contribution from protostellar winds around low mass stars is also much smaller than the H_2 luminosity.

7. Conclusions

We presented an analysis of VLT/SINFONI near-IR imaging spectroscopy of the region with the brightest H_2 rotational line emission in the Antennae overlap region, which has previously been identified with Spitzer/IRS spectroscopy. The region encompasses one of the supergiant molecular complexes, SGMC 2, discovered through CO interferometric observations. It corresponds to one of the brightest FIR knots in the overlap region, and is near a young (~5 Myr) super star cluster previously identified in NIR imaging including HST imaging. Our imaging spectroscopy provides us with constraints on the spatial distribution, kinematics and excitation of the H_2 and H gas out to a radius of 300 pc from this cluster. Based on these observations, we investigated how the large-scale gas dynamics may trigger the formation of the SSC and regulate the star formation efficiency. We have also discussed how the observations and our interpretation may be of general relevance for the formation of dense massive clusters and the efficiency of star formation in mergers. We list our main results.

- We find extended near-IR H_2 line emission across much of our SINFONI field-of-view with broad line widths ($FWHM \sim 200\,{\rm km\ s}^{-1}$), larger than those measured from CO and Brγ at the same position (which are 70 and 130 km s^{-1}, respectively). The line width is commensurate with a large-scale velocity gradient across the field. We argue that this extended emission component traces a convergent turbulent flow driven by the galaxies interaction. Spectral diagnostics show that the H_2 emission is shock powered and traces the dissipation of the gas turbulent kinetic energy.

- The data reveal a compact H_2 source (50 pc diameter) with a K-band spectrum showing only H_2 line emission. The H_2 lines are spectrally resolved with a width ~150 km s^{-1} ($FWHM$). The H_2 emission from this source is also shock excited. The cloud virial mass is $\sim 1 \times 10^7\,M_\odot$. The absence of Br$\gamma$ emission and of some obvious counterpart in the radio continuum set a low limit on the mass of newly formed stars (stellar mass fraction ~0.3%). To our knowledge, this is the first time that an extragalactic source with such characteristics is identified.

- The width of the H_2 spectra show that the SGMC 2 complex and the compact source are both associated with gas which is too turbulent to be bound. We argue that this suggests that the H_2 emission is powered by gas accretion. We show that the required accretion rate is of the right order of magnitude to drive the gas turbulence and to account for the formation of both the SGMC 2 complex and the compact source by accretion.

- By observing gas cooling through H_2 lines, we may have discovered a massive cloud on its way to form an SSC within the next few Myr. However, this conclusion is only tentative, and will remain incomplete, until we obtain the missing information about the mass, the density structure and the kinematics of the bulk of the gas. The H_2 line emission provides this information only for the warm shock excited fraction. The missing information can be obtained with ALMA.

- We propose that the strong turbulence observed in the extended emission and the compact H_2 source is of general relevance for the formation of SSCs in two ways. A high value of the gas velocity dispersion increases the masses of the clouds formed by gravitational fragmentation. It may also prevent star formation to be efficient before the cloud is fully formed, i.e. as long as turbulence is driven by accretion. Clusters may form out of gas which has lost much of the turbulent energy it had during gravitational formation of the pre-stellar cloud. If this is correct, then it reduces the

requirement on the star-formation efficiency to form a bound stellar cluster.

- Our observations highlight the role of merger-driven turbulence in regulating the star-formation efficiency in interacting galaxies. Within the field of view of our SINFONI observations, about 2% of the molecular gas has been turned into stars. We relate this small efficiency to the fact that the gas turbulence does not dissipate because it continues to be driven by on-going accretion.

Acknowledgements. The authors wish to thank the staff at the VLT and at the CFHT for making these observations. We are grateful to C. Wilson for providing us with her OVRO CO data. We would like to thank the anonymous referee for the detailed and constructive report that helped us in the interpretation of our data. We thank B. Elmegreen, P. Guillard, P. Hennebelle and G. Pineau des Fôrets for helpful discussions at an early stage in the writing of this paper. C.H. acknowledges support from a CNRS-CONICYT scholarship. This research is funded by CONICYT and CNRS, in accordance with the agreement written on December 11, 2007.

References

Appleton, P. N., Xu, K. C., Reach, W., et al. 2006, ApJ, 639, L51
Baldi, A., Raymond, J. C., Fabbiano, G., et al. 2006, ApJ, 636, 158
Barnes, J. E., & Hernquist, L. 1996, ApJ, 471, 115
Bonnet, H., Abuter, R., Baker, A., et al. 2004, The Messenger, 117, 17
Brandl, B. R., Snijders, L., den Brok, M., et al. 2009, ApJ, 699, 1982
Cluver, M. E., Appleton, P. N., Boulanger, F., et al. 2010, ApJ, 710, 248
Eisenhauer, F., Abuter, R., Bickert, K., et al. 2003, in SPIE 4841, ed. M. Iye, & A. F. M. Moorwood, 1548
Elmegreen, B. G. 2007, ApJ, 668, 1064
Elmegreen, B. G. 2008, ApJ, 672, 1006
Escala, A., & Larson, R. B. 2008, ApJ, 685, L31
Falgarone, E., Verstraete, L., Pineau Des Forêts, G., & Hily-Blant, P. 2005, A&A, 433, 997
Fall, S. M., Chandar, R., & Whitmore, B. C. 2005, ApJ, 631, L133
Fall, S. M., Krumholz, M. R., & Matzner, C. D. 2010, ApJ, 710, L142
Flower, D. R., & Pineau Des Forêts, G. 2010, MNRAS, 406, 1745
Giannini, T., McCoey, C., Nisini, B., et al. 2006, A&A, 459, 821
Gilbert, A. M., & Graham, J. R. 2007, ApJ, 668, 168
Godard, B., Falgarone, E., Gerin, M., Hily-Blant, P., & de Luca, M. 2010, A&A, 520, A20
Guillard, P., Boulanger, F., Pineau Des Forêts, G., & Appleton, P. N. 2009, A&A, 502, 515
Haas, M., Chini, R., & Klaas, U. 2005, A&A, 433, L17
Heitsch, F., Burkert, A., Hartmann, L. W., Slyz, A. D., & Devriendt, J. E. G. 2005, ApJ, 633, L113
Hennebelle, P., Banerjee, R., Vázquez-Semadeni, E., Klessen, R. S., & Audit, E. 2008, A&A, 486, L43
Ho, L. C., & Keto, E. 2007, ApJ, 658, 314
Huff, E. M., & Stahler, S. W. 2007, ApJ, 666, 281
Hummer, D. G., & Storey, P. J. 1987, MNRAS, 224, 801
Jog, C. J., & Ostriker, J. P. 1988, ApJ, 328, 404
Karl, S. J., Naab, T., Johansson, P. H., et al. 2010, ApJ, 715, L88
Karl, S. J., Fall, S. M., & Naab, T. 2011, ApJ, 734, 11
Kennicutt, Jr., R. C. 1998, ApJ, 498, 541
Keto, E., Ho, L. C., & Lo, K.-Y. 2005, ApJ, 635, 1062
Klaas, U., Nielbock, M., Haas, M., Krause, O., & Schreiber, J. 2010, A&A, 518, L44
Klessen, R. S., & Hennebelle, P. 2010, A&A, 520, A17
Kristensen, L. E. 2007, Ph.D. Thesis, LERMA, Observatoire de Paris-Meudon, LAMAP, Université de Cergy-Pontoise
Krumholz, M. R., & McKee, C. F. 2005, ApJ, 630, 250
Krumholz, M. R., Matzner, C. D., & McKee, C. F. 2006, ApJ, 653, 361
Le Petit, F., Nehmé, C., Le Bourlot, J., & Roueff, E. 2006, ApJS, 164, 506
Leitherer, C., Schaerer, D., Goldader, J. D., et al. 1999, ApJS, 123, 3
Leitherer, C., Ortiz Otálvaro, P. A., Bresolin, F., et al. 2010, ApJS, 189, 309
Mac Low, M.-M., & Klessen, R. S. 2004, Rev. Mod. Phys., 76, 125
Maret, S., Bergin, E. A., Neufeld, D. A., et al. 2009, ApJ, 698, 1244
Matzner, C. D. 2002, ApJ, 566, 302
McKee, C. F., & Ostriker, E. C. 2007, ARA&A, 45, 565
Mengel, S., Lehnert, M. D., Thatte, N., & Genzel, R. 2005, A&A, 443, 41
Neff, S. G., & Ulvestad, J. S. 2000, AJ, 120, 670
Nesvadba, N. P. H., Lehnert, M. D., De Breuck, C., Gilbert, A., & van Breugel, W. 2007, A&A, 475, 145
Nesvadba, N. P. H., Lehnert, M. D., Davies, R. I., Verma, A., & Eisenhauer, F. 2008, A&A, 479, 67
Nesvadba, N. P. H., Boulanger, F., Salomé, P., et al. 2010, A&A, 521, A65
Ogle, P., Boulanger, F., Guillard, P., et al. 2010, ApJ, 724, 1193
Padoan, P., & Nordlund, Å. 2011, ApJ, 730, 40
Puxley, P. J., Hawarden, T. G., & Mountain, C. M. 1990, ApJ, 364, 77
Renaud, F., Boily, C. M., Fleck, J., Naab, T., & Theis, C. 2008, MNRAS, 391, L98
Renaud, F., Boily, C. M., Naab, T., & Theis, C. 2009, ApJ, 706, 67
Schweizer, F., Burns, C. R., Madore, B. F., et al. 2008, AJ, 136, 1482
Scoville, N. Z., Sanders, D. B., & Clemens, D. P. 1986, ApJ, 310, L77
Tan, J. C., Krumholz, M. R., & McKee, C. F. 2006, ApJ, 641, L121
Teyssier, R., Chapon, D., & Bournaud, F. 2010, ApJ, 720, L149
Tody, D. 1993, in Astronomical Data Analysis Software and Systems II, ed. R. J. Hanisch, R. J. V. Brissenden, & J. Barnes, ASP Conf. Ser., 52, 173
Vázquez-Semadeni, E., Gómez, G. C., Jappsen, A. K., et al. 2007, ApJ, 657, 870
Vigroux, L., Mirabel, F., Altieri, B., et al. 1996, A&A, 315, L93
Weidner, C., Bonnell, I. A., & Zinnecker, H. 2010, ApJ, 724, 1503
Weingartner, J. C., & Draine, B. T. 2001, ApJ, 548, 296
Whitmore, B. C., & Schweizer, F. 1995, AJ, 109, 960
Whitmore, B. C., Chandar, R., Schweizer, F., et al. 2010, AJ, 140, 75
Wilson, C. D., Scoville, N., Madden, S. C., & Charmandaris, V. 2000, ApJ, 542, 120
Wilson, C. D., Scoville, N., Madden, S. C., & Charmandaris, V. 2003, ApJ, 599, 1049
Zakamska, N. L. 2010, Nature, 465, 60
Zhang, Q., & Fall, S. M. 1999, ApJ, 527, L81
Zhang, Q., Fall, S. M., & Whitmore, B. C. 2001, ApJ, 561, 727

A&A 538, L9 (2012)
DOI: 10.1051/0004-6361/201118317

Astronomy & Astrophysics

Letter to the Editor

ALMA CO and VLT/SINFONI H_2 observations of the Antennae overlap region: mass and energy dissipation⋆

C. N. Herrera[1,⋆⋆], F. Boulanger[1], N. P. H. Nesvadba[1], and E. Falgarone[2]

[1] Institut d'Astrophysique Spatiale, UMR 8617 CNRS, Université Paris-Sud 11, 91405 Orsay Cedex, France
e-mail: cherrera@ias.u-psud.fr
[2] LERMA, UMR 8112 CNRS, École Normale Supérieure and Observatoire de Paris, Paris, France

Received 21 October 2011 / Accepted 28 December 2011

ABSTRACT

We present an analysis of super-giant molecular complexes (SGMCs) in the overlap region of the Antennae galaxy merger, based on ALMA CO(3−2) interferometry and VLT/SINFONI imaging spectroscopy of H_2 1−0 S(1) at angular resolutions of 0.9″and 0.7″, respectively. All but one SGMC have multiple velocity components offset from each other by up to 150 km s^{-1}. H_2 line emission is found in all SGMCs and the kinematics of H_2 and CO are well matched. H_2/CO line ratios vary by up to a factor of 10 among SGMCs and different velocity components of the same SGMCs. We also identify the CO counterpart of a bright, compact source of near-IR H_2 line emission, which shows no Brγ, and was first identified with SINFONI. This source has the highest H_2/CO line ratio, and coincides with the steepest CO velocity gradient of the entire overlap region. With a size of 50 pc and a virial mass of a few 10^7 $M_\odot$ it is perhaps a pre-cluster cloud that has not yet formed significant numbers of massive stars. We present observational evidence that the H_2 emission is powered by shocks, and demonstrate how the H_2 1−0 S(1) and the CO(3−2) lines can be used as tracers of energy dissipation and gas mass, respectively. The variations in the H_2/CO line ratio may indicate that the SGMCs are dissipating their turbulent kinetic energy at different rates. The compact source could represent a short (∼1 Myr) evolutionary stage in the early formation of super-star clusters.

Key words. galaxies: individual: Antennae – galaxies: ISM – radio lines: ISM – infrared: ISM

1. Introduction

Major gas-rich mergers are important sites of star formation and galaxy evolution in the Universe. The Antennae galaxy merger (NGC4038/4039) is an ideal target for studying in detail how galaxy interactions affect the interstellar medium and star formation. Most stars in the Antennae form in super-star clusters (SSCs) with stellar masses up to a few 10^6 $M_\odot$ (Whitmore et al. 2010) located where the two galaxies permeate each other, the "overlap region". Super-giant molecular complexes (SGMCs) with masses of several 10^8 $M_\odot$ and sizes of ∼500 pc have been identified in CO(1−0) in the overlap region with the OVRO interferometer (Wilson et al. 2000). Ueda et al. (2012) have recently reported higher resolution (∼100 pc), CO(3–2) observations of the Antennae obtained with the SMA.

The formation of SSCs involves a complex interplay of merger-driven gas dynamics, turbulence fed by the galaxy interaction, and dissipation of the kinetic energy of the gas. Hydrodynamic simulations suggest that massive complexes of cold gas, akin to SGMCs, form where gas flows trigger compression, cooling and gravitational fragmentation (Teyssier et al. 2010). Within SGMCs, a hierarchy of structures must form including clouds that are sufficiently massive to form SSCs (Weidner et al. 2010).

Recent VLT/SINFONI imaging spectroscopy of the peak of pure-rotational H_2 emission in the overlap region previously observed with *Spitzer* (Herrera et al. 2011, H11 hereafter) revealed bright diffuse H_2 line emission associated with an SGMC and a compact (∼0.6″, ∼50 pc) source. H11 proposed that the compact source may be a massive cloud on its way to form a SSC within the next few Myr. The H_2 lines are powered by shocks and trace energy that is being dissipated and radiated away as the cloud complex, and a pre-cluster cloud (PCC) within, grow through gas accretion.

Herrera et al. (2011) had sub-arcsecond resolution SINFONI data of shocked gas, but lacked CO observations at similar resolution, which are required to probe the bulk of the gas on the relevant scales of ≤100 pc. In this letter, we take advantage of the recently released ALMA science verification observations of CO(3−2) in band 7 (∼345 GHz) at ∼1″ angular resolution to compare the morphology and kinematics of CO(3−2) and H_2 line emission in the Antennae overlap region. We show that together the ALMA and VLT observations provide the complementary (mass and energetics) data needed to characterize the dynamical state of SGMCs and to search for pre-cluster clouds.

2. Comparison of ALMA and SINFONI observations

Our analysis relies on two data sets. First, CO(3−2) line emission was obtained during ALMA science verification. These data are part of a mosaic of the Antennae obtained in 10 h of observing time in band 7 (345 GHz) between May and June 2011, with 10 to 13 antennae and baselines from 25 to 200 m. This gives an angular resolution of 0.″6 × 1.″1 (66 pc × 115 pc, at a distance of 22 Mpc) and covers the entire overlap region. The data have an

⋆ Based on ALMA Science Verification data and observations with the VLT/SINFONI, Program IDs 383.B-0789 and 386.B-0942.
⋆⋆ Supported by a CNRS-CONICYT grant.

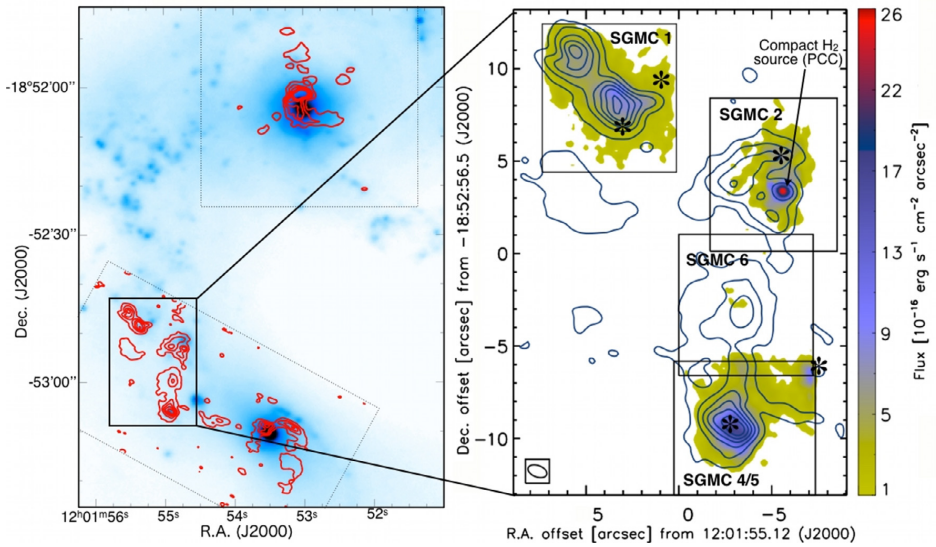

Fig. 1. *Left.* ALMA CO morphology shown on top of our CFHT *K*-band continuum image (H11). Dotted boxes mark the two ALMA mosaics, the solid box marks the overlap region. *Right.* H_2 1−0 S(1) morphology as seen with SINFONI. Boxes mark individual SINFONI fields-of-view, contours show CO(3−2) from 2 to 42 Jy km s^{-1} beam^{-1} in steps of 8 Jy km s^{-1} beam^{-1}. The inset at the bottom left of the right panel shows the ALMA beam. We also mark massive and young SSCs (asterisks), and the compact H_2 source PCC discussed in Sect. 3.

intrinsic spectral resolution of 0.85 km s^{-1} and were binned into channels of 10 km s^{-1}. We used the reduced data cubes publicly available on the ALMA website[1], which we corrected for the primary beam attenuation. Low spatial frequencies were filtered out because of missing short spacings that cause a loss of extended structures >4″ and negative sidelobes adjacent to bright emission. To measure fluxes we used a clipped cube where all pixel values <2σ (6 mJy beam^{-1}) were set to zero. To quantify the missing flux, we constructed spectra at the center of the overlap region with the angular resolution of the single-dish JCMT and HHT CO(3−2) observations of Zhu et al. (2003) and Schulz et al. (2007), respectively. We found about half the total flux of the single-dish data. The total flux of the SGMCs in the overlap region agrees with the SMA observations (Ueda et al. 2012). Second, we used VLT/SINFONI imaging spectroscopy of rovibrational H_2 lines in the near-infrared *K*-band at $R = 3000$ in four regions each 8″ × 8″ in size (Fig. 1). They were observed in February 2011 with on-source integration times of 40 min per pointing. Our previous observations of SGMC 2 have been discussed by H11. We obtained and reduced the data of the three additional fields in a similar way.

Figure 1 shows the spatial distribution of the H_2 and CO emission in the Antennae overlap region at a spatial resolution of ≤1″ (100 pc). The right panel displays the color image of the H_2 1−0 S(1) emission with CO(3−2) contours for comparison. Intensity maps were obtained from the SINFONI and ALMA data cubes by fitting Gaussian profiles to the spectra in each spatial pixel, using one component for SINFONI and up to three components for the higher spectral resolution ALMA data. In Fig. 2 we compare the velocity fields of these two lines. For the CO velocities we computed the first moment map, and for H_2 we constructed the velocity map from Gaussian fits.

[1] http://almascience.eso.org/alma-data/science-verification

The ALMA channel maps are very similar to the SMA observations in Ueda et al. (2012). We identified all SGMCs discovered by Wilson et al. (2000) except for SGMC 3, which is not covered by ALMA. The new data show two velocity components in SGMC 1 and 2. We also decomposed SGMC 4/5 into two smaller complexes at positions (−3, −9.5) and (−3, −3.5) in Fig. 1, each of which has two velocity components. We kept the name SGMC4/5 for the first complex, and labeled the northern extension SGMC 6. CO and H_2 spectra of each SGMC are displayed in Fig. 2. The CO spectra were integrated over each box in Fig. 1 using the clipped cube.

Table 1 lists the CO line properties of each SGMC and each velocity component, named a and b. Fluxes, velocities and line widths of all components are measured from Gaussian fits to the spectra in Fig. 2. Error bars include only fit uncertainties, not the systematic errors owing to the missing short spacings. We estimated the $R_{3-2/1-0} = I_{CO(3-2)}/I_{CO(1-0)}$ ratios of the SGMCs by comparing the ALMA and OVRO data, after smoothing to a common resolution. I_{CO} is the integrated intensity in K km s^{-1}. This ratio varies from source to source between 0.3−0.8, with a mean value of 0.5, consistent with what Schulz et al. (2007) found from single-dish data for the entire overlap region, as well as the peak line ratios measured with the SMA for each individual SGMC (Ueda et al. 2012).

We estimated gas masses from the CO fluxes, where the X_{CO} factor is the main source of uncertainty. To be consistent with previous studies, we used the same X_{CO} factor for CO(1−0) as Wilson et al. (2000), $X_{CO} = 3 \times 10^{20}$ H_2 cm^{-2} (K km s^{-1})$^{-1}$, and adopted the scaling $R_{3-2/1-0} = 0.59$ of Schulz et al. (2007). Our mass estimates (Table 1) are comparable to those of Wilson et al. (2000). Similar to H11, our data show that most of the H_2 emission away from SSCs is powered by shocks, not UV heating in PDRs. The observed H_2 2−1/1−0 S(1) ratios, 0.1−0.2 (Table 1) can be accounted for by PDR models, but only for high UV fields ($\chi > 10^4$, in units of the mean value in the

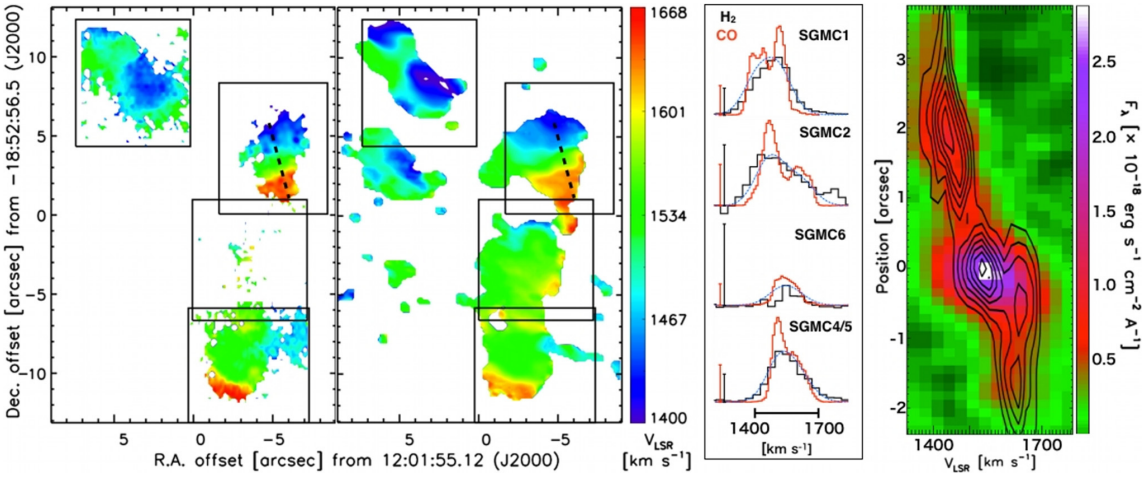

Fig. 2. *Left panel*: velocity map of H_2 1−0 S(1) (*left*) and first-moment map of CO(3−2) (*right*). Dotted lines mark the position-velocity cut shown in the right panel. *Mid panel*: integrated line profiles of CO(3−2) (red) and H_2 1−0 S(1) (black) for each SGMC. Blue spectra show the CO(3−2) lines convolved to the spectral resolution of SINFONI. Black bars correspond to 5×10^{-16} erg s^{-1} cm^{-2} Å^{-1} for H_2 1−0 S(1) and red bars to 1.5 Jy for CO(3−2), for all SGMCs. Offsets between the black and blue spectra indicate variations in the CO-to-H_2 ratio between velocity components. *Right panel*: H_2 1−0 S(1) position-velocity diagram of SGMC 2 (H11), with CO(3−2) emission shown as contours in steps of 0.02 Jy beam^{-1} starting at 0.03 Jy beam^{-1}.

Table 1. CO(3−2) properties of the SGMCs (top) and PCC (bottom).

Source	Velocity component	V_{LSR} km s^{-1}	Δv km s^{-1}	S_{CO} Jy km s^{-1}	M_{mol} $M_\odot$	$F_{H_2\ 1-0\ S(1)}$ erg s^{-1} cm^{-2}	$\frac{F_{H_2\ 2-1\ S(1)}}{F_{H_2\ 1-0\ S(1)}}$	$\frac{H_2\ 1-0\ S(1)}{CO(3-2)}$
SGMC 1	a	1417 ± 2	105 ± 6	380 ± 24	$5.6 \pm 0.3 \times 10^8$	1.6×10^{-14}	0.2	2.1
	b	1521 ± 1	63 ± 3	289 ± 16	$4.2 \pm 0.2 \times 10^8$			
SGMC 2	a	1469 ± 1	90 ± 2	289 ± 8	$4.2 \pm 0.1 \times 10^8$	8.3×10^{-15}	0.2	1.6
	b	1613 ± 2	114 ± 5	176 ± 10	$2.6 \pm 0.1 \times 10^8$			
SGMC 4/5	a	1505 ± 1	58 ± 2	171 ± 9	$2.5 \pm 0.1 \times 10^8$	1.3×10^{-14}	0.3	2.6
	b	1586 ± 3	126 ± 6	256 ± 12	$3.7 \pm 0.2 \times 10^8$			
SGMC 6	a	1506 ± 2	50 ± 8	48 ± 12	$0.7 \pm 0.2 \times 10^8$	6.7×10^{-16}	<0.5[a]	0.2
	b	1561 ± 5	113 ± 6	216 ± 15	$3.2 \pm 0.2 \times 10^8$			
H_2 source (PCC)	–	1534 ± 2	93 ± 4	7.6 ±0.4	$1.0 \pm 0.1 \times 10^7$	7.6×10^{-16}	0.1	8.7

Notes. We include the integrated H_2 1−0 S(1) fluxes, and the H_2 1−0/2−1 S(1) and H_2/CO flux ratios. For PCC, the line parameters are measured with a single-component Gaussian fit. [(a)] H_2 2−1 S(1) flux corresponds to an upper limit estimated from the noise.

solar neighborhood) and high densities ($n_H > 10^5$ cm^{-3}, Le Petit et al. 2006). These conditions exist near massive stars embedded in molecular clouds, but the extended H_2 emission is generally not observed to peak near the brightest SSCs. The notable exception is the embedded cluster in SGMC4/5, which, however, has a higher line ratio (Gilbert et al. 2000). In addition, the [CII]157 μm/[OI]63 μm line ratio indicates that the mean radiation field in the overlap region is $\chi \sim 10^3$ (Schulz et al. 2007), an order of magnitude smaller than that required to account for the H_2 2−1/1−0 S(1) ratios. The other luminous SSCs have already dispersed most of their gas and dust. Thus, the brightest UV-heated gas would come from clouds away from the clusters. Outside the clusters the intensity of the radiation field is not very high. For a 5×10^6 $M_\odot$ SSC, the UV field is $\chi > 10^4$ only out to a distance of <100 pc from the cluster and less if we include extinction.

Our analysis has three main results. (1) All SGMCs have H_2 1−0 S(1) line emission and the H_2 1−0 S(1) kinematics match those of CO(3−2) well. Zhu et al. (2003) and Schulz et al. (2007) found that the CO is emitted from gas at temperatures with $T \sim 30$–150 K. The excitation temperature of the warmer H_2 gas emitting in the near-IR is ~1000−2000 K (H11). The similarity of the gas kinematics of CO and H_2 indicates that warm and cold gas are closely associated. (2) Figues 1 and 2 show large variations in the H_2/CO ratio between SGMCs and between individual velocity components in the same SGMC (Table 1). Extinction is an unlikely cause, because the near- and mid-IR H_2 pure-rotational emission-line regions have similar morphologies (at least at the 5″ scales resolved by *Spitzer*-IRS; see Fig. 4 in Brandl et al. 2009, and the discussion in H11). In H11, we related the H_2 emission to the dissipation of kinetic energy. With this interpretation, the H_2/CO ratio traces differences in the energy dissipation rate per unit mass, which must be related to the dynamical evolution of the gas. (3) All clouds have two spatially separated velocity components as seen in the channel maps of SGMC 2 in Fig. 3. In the other clouds, the spatial offsets between velocity components are less obvious, possibly because of projection effects. The velocity difference between components within an individual SGMC is up to 150 km s^{-1} (Fig. 2). Given the size and mass of the SGMCs, this is too large to be accounted for by the gas self-gravity. The gas kinematics is most likely driven by the galaxy interaction. Single-dish observations

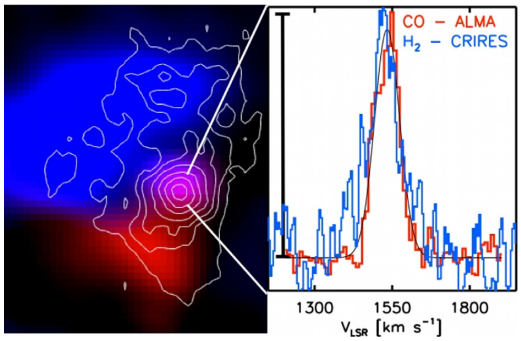

Fig. 3. (*Left*) CO(3−2) emission from SGMC 2, where emission between 1350−1540 km s^{-1} and between 1540−1750 km s^{-1} are shown in blue and red, respectively. Contours show the H_2 1−0 S(1) morphology. (*Right*) CO(3−2) (red) and CRIRES H_2 (blue) spectrum of PCC. The H_2 spectrum is smoothed to 18 km s^{-1} resolution. The bar corresponds to 77 mJy beam^{-1} for CO(3−2) and 4.4×10^{-17} erg s^{-1} cm^{-1} Å^{-1} for H_2 1−0 S(1).

found similar velocity gradients in the extended emission around the SGMCs, which further supports this idea. The two components in SGMC 2 are spatially separated and resolved by ALMA. We estimated their sizes and found their virial masses to be comparable to the molecular masses derived from the CO fluxes.

3. The compact H_2 source

The ALMA maps also give new insight into the nature of the bright, compact H_2 emitter associated with SGMC 2, PCC, recently discovered by H11. PCC is the brightest H_2 line emitter in the overlap region. It is not detected in the lower-resolution CO(1−0) data, but is an emission peak in the SMA and ALMA maps (Fig. 1). Isolating the PCC CO counterpart from the surrounding extended emission is difficult with an algorithm like CLUMPFIND because of the large velocity gradient across PCC (see right panel in Fig. 2). This may explain why the source is not specifically listed in Table B.1 of Ueda et al. (2012). There is no other CO peak in the SGMCs with an obvious counterpart in the near-IR, except for the embedded SSC in SGMC 4/5.

Figure 3 shows a comparison of the CO and CRIRES high-resolution (6 km s^{-1}) H_2 1−0 S(1) spectra of PCC (H11). The CO spectrum is the peak emission at the position of the PCC corrected for the surrounding emission, measured over an annulus outside the source, to isolate the CO velocity component associated with the PCC. CO(3−2) and H_2 1−0 S(1) spectra are remarkably similar. Table 1 lists the parameters of our Gaussian fit. The H_2-luminous PCC has a velocity dispersion (40 km s^{-1}) significantly higher than those of GMCs with the same sizes in the Milky Way (5 km s^{-1}; Falgarone et al. 2009; Heyer et al. 2009).

Using the velocity dispersion of CO(3−2), we obtain a virial mass of $M_{\rm vir} = 5R\sigma^2/G = 4.6 \times 10^7 \times (\sigma_v/40\ {\rm km\ s^{-1}})^2\ M_\odot$. Since ALMA does not spatially resolve the PCC, we instead used the 50 pc size measured with SINFONI. The exceptionally high H_2 1−0 S(1)-to-Brγ line ratio (>15, H11) provides unambiguous evidence that the H_2 emission of the PCC is powered by shocks (Puxley et al. 1990). The H_2/CO ratio, i.e. the energy dissipation rate per unit mass, is also exceptionally high, a factor 5 higher than that of the SGMC 2 complex overall.

PCC appears to be located at the interface between blue and redshifted gas (Fig. 3) where CO shows a steep velocity gradient (~1 km s^{-1} pc^{-1} in the position-velocity diagram in Fig. 2). The observed properties of PCC are consistent with a scenario where the formation of SSCs is triggered by interactions between two gas flows. In SGMC 2, depending on the full three-dimensional geometry, the flows could either be colliding or creating a large velocity shear, and most likely a combination of both. In either case, the interaction drives a turbulent energy cascade in which kinetic energy is being dissipated. This is where we would expect the highest energy dissipation rate.

The bolometric luminosity of the PCC is $\sim 10^7\ L_\odot$. Observations of, e.g., NGC 1333 (Maret et al. 2009) show that the bolometric luminosity of protostellar outflows is on the order of $10^5\ L_\odot \times \dot{M}_{\rm wind}$, where $\dot{M}_{\rm wind}$ is the stellar mass loss rate in $M_\odot$ yr^{-1}. The small embedded stellar mass of $M_* = 4 \times 10^4\ M_\odot$ (H11) makes protostellar winds an implausible energy source.

The cloud luminosity may be accounted for by the dissipation of the cloud kinetic energy for a cloud mass of a few $10^7\ M_\odot$ – a value comparable to the virial mass $5 \times 10^7\ M_\odot$ – and a dissipation timescale of 1 Myr. This is comparable to the cloud crossing time, and also the dynamical time scale associated with the velocity gradient of 1 km s^{-1} pc^{-1} at the position of the cloud. The similarity of both timescales indicates that the cloud may still be forming by accreting gas, and therefore that a significant part of the cloud luminosity may be powered by gas accretion. In any case, the time during which the PCC is a bright H_2 emitter is short, about 1 Myr.

This short timescale may explain why we do not find more bright compact sources in our new H_2 data. Whitmore et al. (2010) list five massive (>$10^5\ M_\odot$), young (<5 Myr) SSCs over the part of the overlap region covered with both ALMA and SINFONI (Fig. 1). This is consistent with finding only a single bright PCC with the SINFONI data if the H_2-luminous phase does not last longer than a few Myr.

Our analysis gives a foretaste of the power of combining mass and energy tracers to study the dynamical state of molecular gas in galaxy mergers and the early stages of the formation of SSCs. In the future, this approach can be extended with ALMA and VLT using additional tracers of energy dissipation and mass.

Acknowledgements. We wish to thank the staff at ALMA and the VLT for making these observations and are particularly grateful to the ALMA SV team for making the fully reduced and calibrated ALMA data available. We thank R. Kneissl for helping us in analyzing the ALMA SV maps, C. Wilson for providing us with her CO(1−0) OVRO data cube, and P. Guillard for his useful comments. We thank the referee for comments that improved our paper. The Atacama Large Millimeter/submillimeter Array (ALMA), an international astronomy facility, is a partnership of Europe, North America and East Asia in cooperation with the Republic of Chile. This paper makes use of the following ALMA Science Verification data: ADS/JAO.ALMA#2011.0.00003.SV.

References

Brandl, B. R., Snijders, L., den Brok, M., et al. 2009, ApJ, 699, 1982
Falgarone, E., Pety, J., & Hily-Blant, P. 2009, A&A, 507, 355
Gilbert, A. M., Graham, J. R., McLean, I. S., et al. 2000, ApJ, 533, L57
Herrera, C. N., Boulanger, F., & Nesvadba, N. P. H. 2011, A&A, 534, A138
Heyer, M., Krawczyk, C., Duval, J., & Jackson, J. M. 2009, ApJ, 699, 1092
Le Petit, F., Nehmé, C., Le Bourlot, J., & Roueff, E. 2006, ApJS, 164, 506
Maret, S., Bergin, E. A., Neufeld, D. A., et al. 2009, ApJ, 698, 1244
Puxley, P. J., Hawarden, T. G., & Mountain, C. M. 1990, ApJ, 364, 77
Schulz, A., Henkel, C., Muders, D., et al. 2007, A&A, 466, 467
Teyssier, R., Chapon, D., & Bournaud, F. 2010, ApJ, 720, L149
Ueda, J., Iono, D., Petitpas, G., et al. 2012, ApJ, 745, 65
Weidner, C., Bonnell, I. A., & Zinnecker, H. 2010, ApJ, 724, 1503
Whitmore, B. C., Chandar, R., Schweizer, F., et al. 2010, AJ, 140, 75
Wilson, C., Scoville, N., Madden, S., & Charmandaris, V. 2000, ApJ, 542, 120
Zhu, M., Seaquist, E. R., & Kuno, N. 2003, ApJ, 588, 243

Appendix C

Press Releases and Outreach

Contents

http://www.bbc.co.uk/news/science-environment-17539317

www.cnrs.fr

COMMUNIQUÉ DE PRESSE NATIONAL I PARIS I 9 février 2012

La naissance turbulente des super-amas d'étoiles dans les galaxies en fusion

Il s'agit de la première étude réalisée sur des données scientifiques collectées par le tout nouveau Atacama Large Millimeter Array (ALMA).En le couplant au Very Large Telescope (VLT) de l'Observatoire Européen Austral, des équipes françaises de l'Institut d'astrophysique spatiale (IAS-CNRS/Université Paris-Sud) et du Laboratoire d'étude du rayonnement et de la matière en astrophysique (LERMA- Observatoire de Paris/CNRS/Ecole normale supérieure/Université Pierre et Marie Curie/Université Cergy-Pontoise) ont pu pour la première fois retracer les prémices de la formation d'étoiles dans les galaxies des Antennes[1]. Parue le 9 février dans la revue européenne Astronomy and Astrophysics Letters, cette approche novatrice révèle l'origine des super-amas d'étoiles dans les galaxies en fusion.

La fusion de deux galaxies provoque de spectaculaires flambées de formation d'étoiles si lumineuses que les astronomes les voient loin dans le passé jusqu'au tout début de l'Univers. Ces feux d'artifice astronomiques associés à la naissance de gigantesques amas stellaires réunissent plusieurs millions d'étoiles dans un espace réduit à quelques dizaines d'années-lumière. Sur ce même volume, on ne trouve autour du Soleil que quelques étoiles.

Les astronomes ont découvert ces super-amas dans les galaxies des Antennes, il y a une vingtaine d'années avec le télescope spatial Hubble, mais les processus physiques qui conduisent à leur formation sont encore méconnus. Aujourd'hui, en combinant les premières données fournies par ALMA avec celles obtenues au préalable avec le VLT, les scientifiques mettent en évidence pour la première fois comment la fusion des galaxies déclenche la formation de super-amas stellaires. L'observation d'un tel phénomène s'intègre parfaitement aux objectifs de recherche d'ALMA.

Ce travail est au cœur de la thèse préparée par Cinthya Herrera, doctorante à l'Institut d'astrophysique spatiale (IAS) et titulaire d'une bourse de recherche dans le cadre de

[1] Les galaxies des Antennes ont déjà été observées par ALMA pour sa toute première image (cf. ALMA ouvre une nouvelle fenêtre sur l'Univers).

l'accord entre le CNRS et la CONICYT (Chili). Elle a suivi une nouvelle idée qui consiste non pas à observer des amas stellaires déjà formés, mais plutôt à observer l'énergie perdue par le gaz dans lequel seront formés les amas. En effet, les étoiles se forment dans des régions où le gaz est très dense et très froid. Or, la fusion de deux galaxies rend le gaz très turbulent. Celui-ci doit donc perdre cette énergie pour pouvoir se condenser, se refroidir, s'effondrer et ainsi former les amas de nouvelles étoiles.

Cette perte d'énergie considérable, prédite par la théorie, est aujourd'hui visible grâce aux observations conjointes des deux télescopes. Quand le gaz se calme et perd son énergie turbulente par radiation, la luminosité qu'il émet est observable dans l'infrarouge proche : elle est donc captée par le VLT. Quant aux observations d'ALMA, elles ont mis en évidence l'extrême agitation turbulente du gaz dans ces immenses nuages où les amas d'étoiles se forment. Cette turbulence est causée par l'énergie gravitationnelle libérée lors de l'interaction des deux galaxies.

Dans un seul de ces nuages, les observations ont révélé une concentration de gaz rayonnant une quantité considérable de son énergie turbulente. Cette région contient assez de gaz pour former son propre super-amas. Et là où ALMA ne voit qu'un nuage parmi d'autres, le VLT y voit l'objet le plus brillant de toute la région d'interaction des Antennes. Les calculs indiquent que dans quelques millions d'années – le temps d'un clin d'œil à l'échelle de l'univers – ce gaz aura perdu toute sa turbulence et un nouvel amas sera né. Ce premier résultat annonce de futures découvertes que les astronomes comme Cinthya Herrera se préparent à faire avec ALMA qui atteindra bientôt toute sa puissance.

Lien vers le résumé de l'article :
http://dx.doi.org/10.1051/0004-6361/201118317

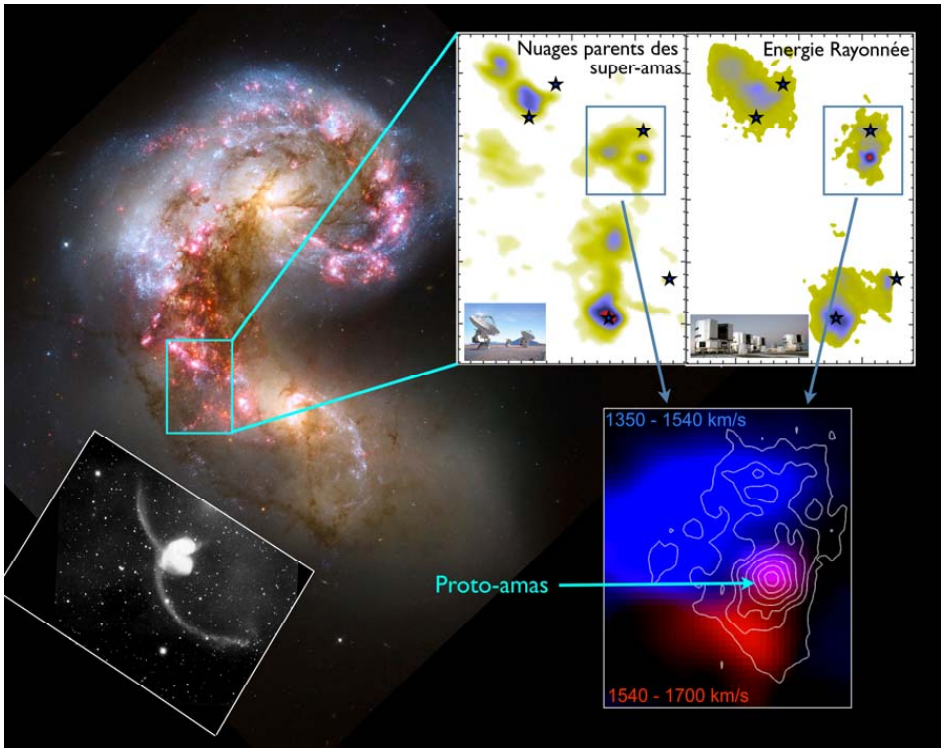

Montage illustrant la découverte d'un proto-amas stellaire dans les galaxies des Antennes.
L'image en bas à gauche est une image grand champ dans le visible qui montre les deux galaxies en interaction telles qu'elles ont été découvertes au siècle dernier.
L'image en haut à gauche montre un zoom sur la région centrale, là où les deux galaxies s'interpénètrent, obtenue par le télescope spatial Hubble (NASA).
Les images de droite, préparées par Cinthya Herrera, illustrent les observations faites par ALMA et le VLT. L'image ALMA, plus à gauche, montre les nuages où sont présents les amas stellaires les plus jeunes et de plus grande masse (symbolisés par des étoiles). L'image VLT à droite montre, elle, l'énergie rayonnée par les nuages. La source compacte brillante dans cette image (le pic de couleur rouge) est présente là où deux masses de gaz à des vitesses très différentes (couleurs rouge et bleue dans le cadre en bas à droite) se rencontrent. Les observations montrent que c'est là que la dissipation d'énergie est la plus forte et que les conditions sont réunies pour former un nouvel amas en quelques millions d'années.

Bibliographie

ALMA CO and VLT/SINFONI H2 observations of the Antennae overlap region: mass and energy dissipation. Herrera, C. N., Boulanger F., Nesvadba, N. P. H., Falgarone, E. 2012, A&A, volume 538, L9

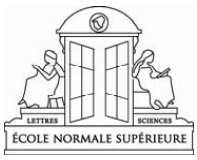

Contact

Chercheur CNRS
François Boulanger I **T 01 69 85 85 73** I francois.boulanger@ias.u-psud.fr
Edith Falgarone I **T 01 44 32 33 47** I edith.falgarone@lra.ens.fr

Presse CNRS I Marcelino Nuno I **T 01 44 96 43 90** I marcelino.nuno@cnrs-dir.fr

BBC NEWS

SCIENCE & ENVIRONMENT

30 March 2012 Last updated at 10:14 GMT

Chilean astronomer makes her mark

By Jonathan Amos
Science correspondent, BBC News, Manchester

Chilean researcher Cinthya Herrera has not quite achieved her PhD in astronomy yet, but already she has notched up a notable success in her career.

The 27-year-old student has the distinction of publishing the very first science paper to come out of the Alma radio telescope.

This huge facility, going up in Chile's Atacama Desert, is set to revolutionise our understanding of the cosmos.

Ms Herrera's efforts will be followed by thousands more publications.

"I was really excited to be told my work was the first refereed paper accepted for publication based on Alma observations, but also I was extremely proud because Alma is in Chile," the young astronomer told BBC News.

Ms Herrera has been describing her studies here in Manchester at the **UK National Astronomy Meeting (NAM)**.

Her investigations involved looking for star forming clusters resulting from the merger of a pair of spiral galaxies.

This collision, known as "The Antennae", lies about 70 million light-years away in the constellation of Corvus (The Crow).

It produces very turbulent regions of gas that must dissipate their energy if they are to condense and form new stars.

"With Alma and its wonderful resolution, we were able to trace the molecular mass of the gas and the structures that will form stars; and using another telescope run by the European Southern Observatory, we were able to trace the energy dissipation," Ms Herrera explained.

"The tracers we observe to do this are carbon monoxide in the case of Alma and molecular hydrogen in the case of the second telescope - the Very Large Telescope, also in the Atacama."

Details of the work have **appeared in Astronomy and Astrophysics**.

The data was acquired in the so-called science verification phase of Alma (Atacama Large Millimeter/submillimeter Array).

The co-operative venture that includes the scientific and engineering inputs of Europe, East Asia, North America, and the host nation, Chile, is still only half-built.

Week by week, new radio antennas are being added to the observing network sited 5,000m above sea level on Atacama's Chajnantor plateau.

Right now, there are 22 of its 12m dishes in place with another seven 7m dishes also observing the sky.

It is planned there should be a total of 66 antennas when Alma becomes fully operational in the next couple of years.

The observatory's capabilities are keenly awaited by astronomers.

The unprecedented resolution it will achieve at longer wavelengths of light will allow scientists to study extremely cold objects in space - such as the dense clouds of cosmic dust and gas from which stars and planets form.

It is expected also to see very distant objects in the early Universe, including some of the very first structures to form more than 13 billion years ago.

Ms Herrera is currently studying in Paris, France, at the Institute of Space Astrophysics (IAS), but her intention is to return home to work on all the telescopes that take advantage of the great observing conditions in the high, dry Atacama.

"For the next few decades, I think Alma will be one of the greatest telescopes on Earth," she told the BBC.

Jonathan.Amos-INTERNET@bbc.co.uk and follow me on **Twitter**

More Science & Environment stories

Stardust recycling mystery solved [/news/science-environment-17675163]
The mechanism by which stars spew out the raw ingredients for planets at the end of their lives is elucidated in a pioneering experiment.
UK 'saturated' by light pollution [/news/uk-17665397]
Indian Ocean tsunami alert lifted [/news/world-asia-17675399]

Appendix D

Definition of Constants

$\alpha_{\rm rec}$	2.6×10^{-13} cm^2 s^{-1}	Recombination rate
c	$2.99792458 \times^{10}$ cm/s	Speed of light
pc	3.08568×10^{18} cm	1 parsec in cm
$M_\odot$	1.98892×10^{33} g	Solar mass
$L_\odot$	3.839×10^{33} erg s^{-1}	Solar Luminosity erg/s
G	6.674×10^{-8} cm^3 gr^{-1} s^{-2}	Gravitational constant
$k_{\rm B}$	1.38065×10^{-16} erg K^{-1}	Boltzmann constant
$m_{\rm H}$	1.67×10^{-24} g	Hydrogen mass
μ	1.36	Helium abundance
h_p	$6.62606957 \times 10^{-27}$ erg s	Planck constant
σ_{SB}	5.57041×10^{-5} erg cm^{-2} s^{-1} K^{-4}	Stephan Boltzmann constant

Appendix E

Abbreviations

AGN	Active Galactic Nucleus
CMB	Cosmic Microwave Background
GMC	Giant Molecular Cloud
HST	Hubble Space Telescope
IRAS	Infrared Astronomical Satellite
ISM	Interstellar Medium
ISO	Infrared Space Observatory
LMC	Large Magellanic Cloud
ONC	Orion Nebula Cluster
PCC	Pre-Cluster Cloud
PDR	Photodissociation Region
SFE	Star Formation Efficiency
SFR	Star Formation Rate
SGMC	Super Giant Molecular Complex
SNR	Supernova Remnant
SSC	Super-Star Cluster
YSO	Young Stellar Object

Bibliography

Allen, C. W. 1973, Astrophysical quantities 53

Alpher, R. A., Bethe, H., & Gamow, G. 1948, Physical Review, 73, 803 2

Appleton, P. N., Xu, K. C., Reach, W., et al. 2006, *ApJ*, 639, L51 67, 119

Arab, H., Abergel, A., Habart, E., et al. 2012, *A&A*, 541, A19 15

Arzoumanian, D., André, P., Didelon, P., et al. 2011, *A&A*, 529, L6 15

Barnes, J. E. 1988, *ApJ*, 331, 699 39

Barnes, J. E. & Hernquist, L. E. 1991, *ApJ*, 370, L65 10, 11

Beckwith, S., Persson, S. E., Neugebauer, G., & Becklin, E. E. 1978, *ApJ*, 223, 464 74

Belokurov, V., Zucker, D. B., Evans, N. W., et al. 2007, *ApJ*, 654, 897 10

Bennett, C. L., Bay, M., Halpern, M., et al. 2003, *ApJ*, 583, 1 3

Bertoldi, F. & McKee, C. F. 1992, *ApJ*, 395, 140 26

Bigiel, F., Leroy, A., Walter, F., et al. 2008, *AJ*, 136, 2846 23

Birnboim, Y., Dekel, A., & Neistein, E. 2007, *MNRAS*, 380, 339 7

Black, J. H. & Dalgarno, A. 1976, *ApJ*, 203, 132 17

Black, J. H. & van Dishoeck, E. F. 1987, *ApJ*, 322, 412 17

Blitz, L. 1993, in Protostars and Planets III, ed. E. H. Levy & J. I. Lunine, 125–161 26

Bolatto, A. D., Leroy, A. K., Rosolowsky, E., Walter, F., & Blitz, L. 2008, *ApJ*, 686, 948 22, 27, 29

Bonnet, H., Abuter, R., Baker, A., et al. 2004, The Messenger, 117, 17 45

Bournaud, F., Daddi, E., Elmegreen, B. G., et al. 2008, *A&A*, 486, 741 6, 8

Bower, R. G., Benson, A. J., Malbon, R., et al. 2006, *MNRAS*, 370, 645 5

Brandl, B. R., Snijders, L., den Brok, M., et al. 2009, *ApJ*, 699, 1982 37, 44, 54, 55, 67, 68, 69, 70, 76, 77, 119, 122

Burkert, A. & Lin, D. N. C. 2000, *ApJ*, 537, 270 13

Castor, J., McCray, R., & Weaver, R. 1975, *ApJ*, 200, L107 92, 110

Chandrasekhar, S. 1949, *ApJ*, 110, 329 26

Christopher, M. H. 2008, "Young, massive star clusters in the Antennae", PhD thesis, California Institute of Technology 93, 94, 96

Clark, D. M., Eikenberry, S. S., Brandl, B. R., et al. 2011, *MNRAS*, 410, 890 36

Clowe, D., Gonzalez, A., & Markevitch, M. 2004, *ApJ*, 604, 596 5

Cluver, M. E., Appleton, P. N., Boulanger, F., et al. 2010, *ApJ*, 710, 248 67

Cole, S., Lacey, C. G., Baugh, C. M., & Frenk, C. S. 2000, *MNRAS*, 319, 168 5, 7

Colless, M., Dalton, G., Maddox, S., et al. 2001, *MNRAS*, 328, 1039 4

Compiègne, M., Verstraete, L., Jones, A., et al. 2011, *A&A*, 525, A103 107

Conselice, C. J., Bershady, M. A., Dickinson, M., & Papovich, C. 2003, *AJ*, 126, 1183 9

Croton, D. J., Springel, V., White, S. D. M., et al. 2006, *MNRAS*, 365, 11 7

Dale, J. E. & Bonnell, I. 2011, *MNRAS*, 403 92

Dame, T. M., Hartmann, D., & Thaddeus, P. 2001, *ApJ*, 547, 792 22

Dame, T. M., Ungerechts, H., Cohen, R. S., et al. 1987, *ApJ*, 322, 706 22

Darg, D. W., Kaviraj, S., Lintott, C. J., et al. 2010, *MNRAS*, 401, 1043 9

de Avillez, M. A. & Breitschwerdt, D. 2005, *A&A*, 436, 585 13

de Ravel, L., Le Fèvre, O., Tresse, L., et al. 2009, *A&A*, 498, 379 9

Dekel, A., Birnboim, Y., Engel, G., et al. 2009, *Nature*, 457, 451 7, 8, 9

Desert, F.-X., Boulanger, F., & Puget, J. L. 1990, *A&A*, 237, 215 107

Di Matteo, P., Bournaud, F., Martig, M., et al. 2008, *A&A*, 492, 31 9, 10

Eggen, O. J., Lynden-Bell, D., & Sandage, A. R. 1962, *ApJ*, 136, 748 7

Eisenhauer, F., Abuter, R., Bickert, K., et al. 2003, in SPIE, ed. M. Iye & A. F. M. Moorwood, Vol. 4841, 1548–1561 45

Elmegreen, B. G. 1989, *ApJ*, 342, L67 21

Elmegreen, B. G. 2007, *ApJ*, 668, 1064 82

Elmegreen, B. G. 2008, *ApJ*, 672, 1006 88

Elmegreen, B. G. 2011, in EAS Publications Series, Vol. 51, EAS Publications Series, ed. C. Charbonnel & T. Montmerle, 3–17 23

Elmegreen, B. G. 2012, in IAU Symposium, Vol. 284, IAU Symposium, 317–329 1

Escala, A. & Larson, R. B. 2008, *ApJ*, 685, L31 88

Fabbiano, G., Baldi, A., King, A. R., et al. 2004, *ApJ*, 605, L21 36

Falgarone, E., Verstraete, L., Pineau des Forêts, G., & Hily-Blant, P. 2005, *A&A*, 433, 997 67, 82, 119

Fall, S. M., Chandar, R., & Whitmore, B. C. 2005, *ApJ*, 631, L133 35

Fall, S. M., Krumholz, M. R., & Matzner, C. D. 2010, *ApJ*, 710, L142 92

Federrath, C. & Klessen, R. S. 2012, ArXiv e-prints 29

Federrath, C., Roman-Duval, J., Klessen, R. S., Schmidt, W., & Mac Low, M.-M. 2010, *A&A*, 512, A81 28

Field, G. B., Goldsmith, D. W., & Habing, H. J. 1969, *ApJ*, 155, L149 13

Fischer, J., Shier, L. M., Luhman, M. L., et al. 1996, *A&A*, 315, L97 72, 73

Flower, D. R. & Pineau des Forêts, G. 2003, *MNRAS*, 343, 390 19, 75

Flower, D. R. & Pineau des Forêts, G. 2010, *MNRAS*, 406, 1745 75, 82, 124, 125

Frieman, J. A., Turner, M. S., & Huterer, D. 2008, *ARA&A*, 46, 385 3

Fukui, Y. & Kawamura, A. 2010, *ARA&A*, 48, 547 22, 23, 24

Fukui, Y., Kawamura, A., Minamidani, T., et al. 2008, *ApJS*, 178, 56 22

Gerin, M., Pety, J., & Goicoechea, J. R. 2009, in Astronomical Society of the Pacific Conference Series, Vol. 417, Submillimeter Astrophysics and Technology: a Symposium Honoring Thomas G. Phillips, ed. D. C. Lis, J. E. Vaillancourt, P. F. Goldsmith, T. A. Bell, N. Z. Scoville, & J. Zmuidzinas, 165 15

Gilbert, A. M. & Graham, J. R. 2007, *ApJ*, 668, 168 58, 93, 94, 96, 97

Gilbert, A. M., Graham, J. R., McLean, I. S., et al. 2000, *ApJ*, 533, L57 72, 99, 100, 102

Godard, B., Falgarone, E., Gerin, M., Hily-Blant, P., & de Luca, M. 2010, *A&A*, 520, A20+ 28, 75, 82

Gott, III, J. R., Jurić, M., Schlegel, D., et al. 2005, *ApJ*, 624, 463 4

Guillard, P., Boulanger, F., Pineau des Forêts, G., & Appleton, P. N. 2009, *A&A*, 502, 515 80, 82, 111, 119

Haas, M., Chini, R., & Klaas, U. 2005, *A&A*, 433, L17 67

Habart, E., Abergel, A., Walmsley, C. M., Teyssier, D., & Pety, J. 2005, *A&A*, 437, 177 74

Harper-Clark, E. & Murray, N. 2009, *ApJ*, 693, 1696 92

Heitsch, F., Burkert, A., Hartmann, L. W., Slyz, A. D., & Devriendt, J. E. G. 2005, *ApJ*, 633, L113 81

Hennebelle, P., Banerjee, R., Vázquez-Semadeni, E., Klessen, R. S., & Audit, E. 2008, *A&A*, 486, L43 80, 81

Hennebelle, P. & Chabrier, G. 2011, *ApJ*, 743, L29 29

Herrera, C. N., Boulanger, F., & Nesvadba, N. P. H. 2011, A&A, 534, A138 44, 59, 61, 68, 71, 74, 79, 95, 97, 104

Herrera, C. N., Boulanger, F., Nesvadba, N. P. H., & Falgarone, E. 2012, *A&A*, 538, L9 58, 68, 71, 79, 99

Heyer, M., Krawczyk, C., Duval, J., & Jackson, J. M. 2009, *ApJ*, 699, 1092 26, 27

Hibbard, J. E., van der Hulst, J. M., Barnes, J. E., & Rich, R. M. 2001, *AJ*, 122, 2969 37, 38, 39, 41, 119

Ho, L. C. & Keto, E. 2007, *ApJ*, 658, 314 76

Hopkins, P. F., Somerville, R. S., Hernquist, L., et al. 2006, *ApJ*, 652, 864 10

Hubble, E. 1929, Proceedings of the National Academy of Science, 15, 168 2

Hubble, E. P. 1926, *ApJ*, 64, 321 4

Huff, E. M. & Stahler, S. W. 2007, *ApJ*, 666, 281 82, 83

Hughes, A., Wong, T., Ott, J., et al. 2010, *MNRAS*, 406, 2065 22

Hummer, D. G. & Storey, P. J. 1987, *MNRAS*, 224, 801 76, 102

Hunter, D. A., Shaya, E. J., Holtzman, J. A., et al. 1995, *ApJ*, 448, 179 34

Jarosik, N., Bennett, C. L., Dunkley, J., et al. 2011, *ApJS*, 192, 14 3

Jeans, J. H. 1902, Royal Society of London Philosophical Transactions Series A, 199, 1 25

Jog, C. J. & Ostriker, J. P. 1988, *ApJ*, 328, 404 80

Jog, C. J. & Solomon, P. M. 1984, *ApJ*, 276, 114 21

Johansson, P. H., Naab, T., & Burkert, A. 2009, *ApJ*, 690, 802 11

Kaeufl, H.-U., Ballester, P., Biereichel, P., et al. 2004, in Society of Photo-Optical Instrumentation Engineers (SPIE) Conference Series, Vol. 5492, Society of Photo-Optical Instrumentation Engineers (SPIE) Conference Series, ed. A. F. M. Moorwood & M. Iye, 1218–1227 47

Karl, S. J., Fall, S. M., & Naab, T. 2011, *ApJ*, 734, 11 39, 40

Karl, S. J., Naab, T., Johansson, P. H., et al. 2010, *ApJ*, 715, L88 39, 41, 42

Kauffmann, G., White, S. D. M., & Guiderdoni, B. 1993, *MNRAS*, 264, 201 7

Kaufman, M. J., Wolfire, M. G., & Hollenbach, D. J. 2006, *ApJ*, 644, 283 72, 73

Kennicutt, Jr., R. C. 1998a, *ARA&A*, 36, 189 1

Kennicutt, Jr., R. C. 1998b, *ApJ*, 498, 541 11, 22, 23

Kereš, D., Katz, N., Weinberg, D. H., & Davé, R. 2005, *MNRAS*, 363, 2 8

Keto, E., Ho, L. C., & Lo, K.-Y. 2005, *ApJ*, 635, 1062 80, 87

Klaas, U., Nielbock, M., Haas, M., Krause, O., & Schreiber, J. 2010, *A&A*, 518, L44 37

Klessen, R. S. 2011, in EAS Publications Series, Vol. 51, EAS Publications Series, ed. C. Charbonnel & T. Montmerle, 133–167 24, 25

Klessen, R. S. & Hennebelle, P. 2010, *A&A*, 520, A17+ 28, 83, 84, 92

Kolmogorov, A. 1941, Akademiia Nauk SSSR Doklady, 30, 301 27

Könyves, V., André, P., Men'shchikov, A., et al. 2010, *A&A*, 518, L106 15

Kristensen, L. E. 2007, "Observational analysis of the physical conditions in galactic and extragalactic active star forming regions", PhD thesis, LERMA, Observatoire de Paris-Meudon; LAMAP, Université de Cergy-Pontoise 75

Krumholz, M. R. & Matzner, C. D. 2009, *ApJ*, 703, 1352 24, 92, 108

Krumholz, M. R., Matzner, C. D., & McKee, C. F. 2006, *ApJ*, 653, 361 28, 88, 91

Krumholz, M. R. & McKee, C. F. 2005, *ApJ*, 630, 250 29, 88

Krumholz, M. R. & McKee, C. F. 2008, *Nature*, 451, 1082 105

Lacey, C. & Cole, S. 1993, *MNRAS*, 262, 627 5, 6

Larkin, J. E., Armus, L., Knop, R. A., Matthews, K., & Soifer, B. T. 1995, *ApJ*, 452, 599 73

Larson, R. B. 1981, *MNRAS*, 194, 809 27

Le Bourlot, J., Le Petit, F., Pinto, C., Roueff, E., & Roy, F. 2012, *A&A*, 541, A76 108

Le Fèvre, O., Abraham, R., Lilly, S. J., et al. 2000, *MNRAS*, 311, 565 9

Le Petit, F., Nehmé, C., Le Bourlot, J., & Roueff, E. 2006, *ApJS*, 164, 506 72

Lee, Y.-W., Joo, J.-M., Sohn, Y.-J., et al. 1999, *Nature*, 402, 55 11

Leitherer, C., Schaerer, D., Goldader, J. D., et al. 1999, *ApJS*, 123, 3 95

Lesaffre, P., Pineau des Forêts, G., Godard, B., et al. 2013, *A&A*, 550, A106 18, 20

Lopez, L. A., Krumholz, M. R., Bolatto, A. D., Prochaska, J. X., & Ramirez-Ruiz, E. 2011, *ApJ*, 731, 91 24, 92, 110, 111, 120, 121

Mac Low, M.-M. & Klessen, R. S. 2004, Reviews of Modern Physics, 76, 125 87, 88

Maret, S., Bergin, E. A., Neufeld, D. A., et al. 2009, *ApJ*, 698, 1244 83, 86

Markwardt, C. B. 2009, in Astronomical Society of the Pacific Conference Series, Vol. 411, Astronomical Society of the Pacific Conference Series, ed. D. A. Bohlender, D. Durand, & P. Dowler, 251–+ 53

Martín, S., Requena-Torres, M. A., Martín-Pintado, J., & Mauersberger, R. 2008, *ApJ*, 678, 245 124

Martin-Pintado, J., de Vicente, P., Fuente, A., & Planesas, P. 1997, *ApJ*, 482, L45 124

Martínez-Delgado, D., Peñarrubia, J., Gabany, R. J., et al. 2008, *ApJ*, 689, 184 10

Mathis, J. S., Mezger, P. G., & Panagia, N. 1983, *A&A*, 128, 212 107

Matzner, C. D. 2002, *ApJ*, 566, 302 91

Matzner, C. D. & McKee, C. F. 2000, *ApJ*, 545, 364 91

McKee, C. F. & Ostriker, E. C. 2007, *ARA&A*, 45, 565 28, 83

McKee, C. F. & Ostriker, J. P. 1977, *ApJ*, 218, 148 13

Mengel, S., Lehnert, M. D., Thatte, N., & Genzel, R. 2005, *A&A*, 443, 41 35, 40, 122

Mihos, J. C. & Hernquist, L. 1996, *ApJ*, 464, 641 11

Mirabel, I. F., Vigroux, L., Charmandaris, V., et al. 1998, *A&A*, 333, L1 32, 37, 58, 99

Moore, B., Ghigna, S., Governato, F., et al. 1999, *ApJ*, 524, L19 7

Mouschovias, T. C. 1991, *ApJ*, 373, 169 26

Murray, N. 2011, *ApJ*, 729, 133 26, 91

Murray, N., Quataert, E., & Thompson, T. A. 2010, *ApJ*, 709, 191 24, 92, 110, 113, 120

Murray, N. & Rahman, M. 2010, *ApJ*, 709, 424 92

Neff, S. G. & Ulvestad, J. S. 2000, *AJ*, 120, 670 37, 38, 86, 99, 130

Nesvadba, N. P. H., Boulanger, F., Salomé, P., et al. 2010, *A&A*, 521, A65+ 82, 119

Nesvadba, N. P. H., De Breuck, C., Lehnert, M. D., et al. 2011, *A&A*, 525, A43 46

Ogle, P., Boulanger, F., Guillard, P., et al. 2010, *ApJ*, 724, 1193 82, 119

Padoan, P. & Nordlund, Å. 2011, *ApJ*, 730, 40 29, 88

Penzias, A. A. & Wilson, R. W. 1965, *ApJ*, 142, 419 2

Pety, J., Goicoechea, J. R., & Gerin, M. 2008, in EAS Publications Series, Vol. 31, EAS Publications Series, ed. C. Kramer, S. Aalto, & R. Simon, 35–41 15

Planck Collaboration, Abergel, A., Ade, P. A. R., et al. 2011a, *A&A*, 536, A25 85

Planck Collaboration, Abergel, A., Ade, P. A. R., et al. 2011b, *A&A*, 536, A24 85

Press, W. H. & Schechter, P. 1974, *ApJ*, 187, 425 5

Putman, M. E., Gibson, B. K., Staveley-Smith, L., et al. 1998, *Nature*, 394, 752 9

Puxley, P. J., Hawarden, T. G., & Mountain, C. M. 1990, *ApJ*, 364, 77 73, 74

Renaud, F., Boily, C. M., Fleck, J., Naab, T., & Theis, C. 2008, *MNRAS*, 391, L98 iv, 39, 40, 80, 81, 84, 88

Renaud, F., Boily, C. M., Naab, T., & Theis, C. 2009, *ApJ*, 706, 67 80, 88

Richardson, L. F. 1922, in Weather Prediction by Numerical Process, ed. C. U. Press, xii+236 27

Riess, A. G., Filippenko, A. V., Challis, P., et al. 1998, *AJ*, 116, 1009 3

Robertson, B., Bullock, J. S., Cox, T. J., et al. 2006, *ApJ*, 645, 986 8

Robitaille, T. P. & Whitney, B. A. 2010, *ApJ*, 710, L11 11

Roman-Lopes, A. & Abraham, Z. 2004, *AJ*, 127, 2817 86

Rosolowsky, E. 2005, *PASP*, 117, 1403 22

Rubin, V. C., Ford, W. K. J., & . Thonnard, N. 1980, *ApJ*, 238, 471 5

Ryter, C. E. 1996, *Ap&SS*, 236, 285 111

Sanders, D. B. & Mirabel, I. F. 1985, *ApJ*, 298, L31 32

Sanders, D. B. & Mirabel, I. F. 1996, *ARA&A*, 34, 749 11

Schinnerer, E., Weiß, A., Aalto, S., & Scoville, N. Z. 2010, *ApJ*, 719, 1588 21

Schmidt, M. 1959, *ApJ*, 129, 243 22, 23

Schulz, A., Henkel, C., Muders, D., et al. 2007, *A&A*, 466, 467 50, 51, 73

Schweizer, F., Burns, C. R., Madore, B. F., et al. 2008, *AJ*, 136, 1482 32

Scoville, N. Z., Sanders, D. B., & Clemens, D. P. 1986, *ApJ*, 310, L77 79

Searle, L. & Zinn, R. 1978, *ApJ*, 225, 357 7, 10

Smail, I., Chapman, S. C., Blain, A. W., & Ivison, R. J. 2004, *ApJ*, 616, 71 7

Solomon, P. M. & Rivolo, A. R. 1989, *ApJ*, 339, 919 22

Solomon, P. M., Rivolo, A. R., Barrett, J., & Yahil, A. 1987, *ApJ*, 319, 730 22

Springel, V., Di Matteo, T., & Hernquist, L. 2005, *MNRAS*, 361, 776 11

Stanford, S. A., Sargent, A. I., Sanders, D. B., & Scoville, N. Z. 1990, *ApJ*, 349, 492 32

Stark, A. A. & Lee, Y. 2006, *ApJ*, 641, L113 21

Steinmetz, M. & Navarro, J. F. 2002, New A, 7, 155 7

Sternberg, A. & Dalgarno, A. 1989, *ApJ*, 338, 197 17

Tan, J. C., Krumholz, M. R., & McKee, C. F. 2006, *ApJ*, 641, L121 28, 88, 91

Teyssier, R., Chapon, D., & Bournaud, F. 2010, *ApJ*, 720, L149 6, 22, 40, 41, 80

Tielens, A. G. G. M. 2005, *The Physics and Chemistry of the Interstellar Medium, UK: Cambridge University Press* 13, 14, 17

Tody, D. 1993, in Astronomical Society of the Pacific Conference Series, Vol. 52, Astronomical Data Analysis Software and Systems II, ed. R. J. Hanisch, R. J. V. Brissenden, & J. Barnes, 173–+ 46

Toomre, A. & Toomre, J. 1972, *ApJ*, 178, 623 9, 11, 39

Toomre, A. & Toomre, J. 1977, *Violent Tides Between Galaxies*, ed. J. C. Brandt & S. P. Maran, 271 9

Trumpler, R. J. 1930, Lick Observatory Bulletin, 14, 154 12

Tyson, J. A., Wenk, R. A., & Valdes, F. 1990, *ApJ*, 349, L1 5

Ueda, J., Iono, D., Petitpas, G., et al. 2012, *ApJ*, 745, 65 32, 34, 55, 119

Usero, A., García-Burillo, S., Martín-Pintado, J., Fuente, A., & Neri, R. 2006, *A&A*, 448, 457 124

van der Werf, P. P., Genzel, R., Krabbe, A., et al. 1993, *ApJ*, 405, 522 73

Vázquez-Semadeni, E., Colín, P., Gómez, G. C., Ballesteros-Paredes, J., & Watson, A. W. 2010, *ApJ*, 715, 1302 92

Vázquez-Semadeni, E., Gómez, G. C., Jappsen, A. K., et al. 2007, *ApJ*, 657, 870 81

Wada, K., Meurer, G., & Norman, C. A. 2002, *ApJ*, 577, 197 29

Wei, L. H., Keto, E., & Ho, L. C. 2012, *ApJ*, 750, 136 33

Weidner, C., Bonnell, I. A., & Zinnecker, H. 2010, *ApJ*, 724, 1503 80, 87, 88

Weingartner, J. C. & Draine, B. T. 2001, *ApJ*, 548, 296 77

White, S. D. M. & Rees, M. J. 1978, *MNRAS*, 183, 341 5, 8

Whitmore, B. C., Chandar, R., Schweizer, F., et al. 2010, *AJ*, 140, 75 35, 47, 93, 96

Whitmore, B. C. & Schweizer, F. 1995, *AJ*, 109, 960 34

Whitmore, B. C., Zhang, Q., Leitherer, C., et al. 1999, *AJ*, 118, 1551 35

Wilson, C., Scoville, N., Madden, S., & Charmandaris, V. 2000, *ApJ*, 542, 120 32, 33, 54, 55, 66, 79, 80, 81, 82, 119

Wilson, C. D., Scoville, N., Madden, S. C., & Charmandaris, V. 2003, *ApJ*, 599, 1049 32

York, D. G., Adelman, J., Anderson, Jr., J. E., et al. 2000, *AJ*, 120, 1579 4

Zakamska, N. L. 2010, *Nature*, 465, 60 67

Zezas, A., Fabbiano, G., Baldi, A., et al. 2006, *ApJS*, 166, 211 36, 111

Zhang, Q., Fall, S. M., & Whitmore, B. C. 2001, *ApJ*, 561, 727 39, 119

Zhu, M., Seaquist, E. R., & Kuno, N. 2003, *ApJ*, 588, 243 50, 51